A MODELING APPROACH TO HYBRID ISOLATION OF STRUCTURE-BORNE SOUND

Clemens Beijers

De promotiecommissie is als volgt samengesteld:

Voorzitter en secretaris:	
Prof.dr.ir. H.J. Grootenboer	Universiteit Twente
Promotoren:	
Prof.dr.ir. A. de Boer	Universiteit Twente
Prof.dr.ir. J.W. Verheij	TNO
Leden:	
Prof.dr.ir. W. Desmet	Katholieke Universiteit Leuven
Prof.dr.ir. J.B. Jonker	Universiteit Twente
Prof.dr. H. Nijmeijer	Technische Universiteit Eindhoven
Prof.dr.ir. J.W.M. Noordermeer	Universiteit Twente
Prof.dr.ir. D.J. Rixen	Technische Universiteit Delft

This research was supported by the Knowledge Center '*Sound and Vibration UT-TNO*', programme '*Hybrid Isolation of Structure-borne Sound (HIC)*', a joint initiative of TNO, Delft, The Netherlands and the University of Twente, Enschede, The Netherlands.

A modeling approach to hybrid isolation of structure-borne sound
Beijers, Clementius Andreas Johannes
PhD thesis, University of Twente, Enschede, The Netherlands
June 2005

ISBN 90-365-2189-0
Subject headings: active isolation, passive isolation, hybrid isolation, actuators and sensors, active structural acoustic control, numerical modeling, structure-borne sound

Printed by PrintPartners Ipskamp B.V., Enschede, The Netherlands

Front cover: picture of the French Pyrenees during one of the hiking sessions, July 2003

A MODELING APPROACH TO HYBRID ISOLATION OF STRUCTURE-BORNE SOUND

PROEFSCHRIFT

ter verkrijging van
de graad van doctor aan de Universiteit Twente,
op gezag van de rector magnificus,
prof.dr. W.H.M. Zijm,
volgens besluit van het College voor Promoties
in het openbaar te verdedigen
op donderdag 2 juni 2005 om 15.00 uur

door

Clementius Andreas Johannes Beijers

geboren op 30 september 1976

te Bemmel

Dit proefschrift is goedgekeurd door de promotoren:

Prof.dr.ir. A. de Boer
Prof.dr.ir. J.W. Verheij

Summary

The tendency to design lighter structures and the increasing demands of customers for comfort, increases requirements of the resilient mounting of machinery (e.g. engines) in vehicles. The conventional passive vibration isolators might not be sufficient to reduce interior noise levels. Additionally, active isolation techniques can be used to obtain a better isolation performance. This research deals with the application of a combination of passive and active isolation (so-called hybrid isolation) for resilient mounting of machinery. Methods are introduced to model this kind of hybrid isolation system and in particular to investigate the different actuator configurations and sensor strategies of the active isolation part.

First the general theory is described to model hybrid isolation systems. The complete isolation system is considered to consist of three subcomponents: a source (e.g. an engine), a hybrid mounting system and a receiver structure (e.g. a vehicle). The hybrid mounting system consists of passive vibration isolators (for the passive resilient mounting of machinery, often rubber vibration isolators are used) and an active isolation part. The active isolation part is in turn composed of a set of actuators, sensors and a controller. The controller drives the actuators in such a way that the sensor response is minimized. For the considered applications, the sources are rotary or reciprocating machinery and the response is dominated by its rotational speed. For this reason a harmonic analysis is justified and a feedforward control strategy can be used to minimize the sensor response. Two types of sensor strategies are considered: the Active Vibration Control (AVC) approach where the sensors measure a structural response to be minimized and the Active Structural Acoustic Control (ASAC) where the actuators minimize an acoustic error sensor response.

As the next step two models of hybrid isolation are considered and analyzed with the described general theory. First a relatively simple model is analyzed where a rigid mass (the source) is isolated in a hybrid way from a simply supported receiver plate. The dynamics of the components are described analytically and simulation results are presented for different actuator

and sensor configurations.

The structures that are considered for the application of hybrid isolation techniques are light-weight vehicles like transport vehicles and luxury yachts. The second considered model is more representative for these applications and is a numerical model from a laboratory setup. The finite element method is used to describe the dynamic behavior. The goal of this model is not to obtain an accurate description, but to obtain a representative model with the same characteristics concerning the dynamic behavior as the considered applications. Furthermore, numerical tools are developed to simulate the vibrational and acoustic responses of the whole system. The software developed is used to investigate the effectiveness of different active control strategies. Important attention points are the sensor and actuator configurations. Procedures are derived to determine the optimal number and directions of the actuators for the considered practical applications.

Besides the analysis of different actuator concepts and error sensor strategies, attention is paid to the implementation. The actuator(s), the passive vibration isolator(s) and the possible sensors have to be integrated in one hybrid mount. An important issue for the design of such hybrid components are the isolation characteristics of the passive rubber vibration isolator. A procedure is presented to obtain a multi-directional characterization of the isolation behavior. The results are obtained with numerical finite element simulations and the influence of the frequency of excitation and the static deformation is considered. Further, an optimization procedure is described to derive rubber material parameters with the help of standardized measurements of an entire isolator.

Finally the concept of placing the sensors near the source of vibration is investigated. Normally, active isolation systems only make use of sensors at locations where the reduction is desired. The concept of placing the sensors near the source has some advantages: easier implementation, the possibility of obtaining a global response measure and less influence of flanking transmission paths or other disturbance sources as the considered disturbance. Two near-source error sensor strategies are investigated: minimization of the injected structural power and a technique to obtain a weighting matrix for the near-source sensors based on the off-line measured response of a well-chosen performance sensor set. An error-sensitivity analysis is performed to check the robustness of the near-source error sensor concepts and measurements at a representative laboratory setup were performed for validation. These measurements show that the use of such off-line weighting techniques is very doubtful for the considered applications of hybrid isolation.

Samenvatting

De tendens om steeds lichter te construeren en de hogere eisen van de consument met betrekking tot comfort, vereist dat er meer aandacht besteed moet worden aan het geluidsarm isoleren van machines (bijv. motoren) in voertuigen. Het gebruik van conventionele passieve trillingsisolatoren is vaak onvoldoende om het interieur geluid te reduceren. De isolatie kan verbeterd worden door ook gebruik te maken van actieve isolatie technieken. Dit proefschrift behandelt het toepassen van een combinatie van passieve en actieve isolatie technieken (hybride isolatie) voor het geluidsarm isoleren van machines. Verschillende methoden worden geïntroduceerd om dit soort isolatie systemen te modelleren en in het bijzonder om verschillende actuator configuraties en sensor strategieën met betrekking tot het actieve isolatie gedeelte te analyseren.

Eerst wordt de algemene theorie behandeld om hybride isolatie systemen te modelleren. Het gehele isolatiesysteem wordt onderverdeeld in drie componenten: een bron (bijv. een motor), een hybride ophanging en een ontvangstconstructie (bijv. een voertuig). De hybride ophanging bestaat uit passieve trillingsisolatoren (vaak worden rubberen trillingsisolatoren gebruikt) en een actief systeem. Het actieve systeem bestaat weer uit actuatoren, sensoren en een regelaar. De regelaar stuurt de actuatoren zodanig aan dat de sensor responsie geminimaliseerd wordt. Voor de beschouwde toepassingen is de verstoringsbron vaak een roterende of repeterende machine waardoor de responsie gedomineerd wordt door het toerental. Daarom is een harmonische analyse gerechtvaardigd en kan er gebruik gemaakt worden van feedforward regelstrategieën om de sensor responsie te minimaliseren. Twee typen sensor strategieën worden beschouwd: actieve trillings onderdrukking (ACV) waarbij de sensoren een structurele responsie meten en de actieve structurele akoestische onderdrukking (ASAC) waarbij de actuatoren een akoestische responsie van de fout sensoren minimaliseren.

Vervolgens worden twee modellen van hybride isolatie geanalyseerd met de beschreven algemene theorie. In eerste instantie wordt een relatief eenvoudig model geanalyseerd waarbij een starre massa (de bron) op een hybride manier

geïsoleerd wordt van de opgelegde ontvangstplaat. Het dynamisch gedrag van de componenten zelf wordt op een analytische manier beschreven en simulaties worden gepresenteerd voor verschillende actuator en sensor strategieën.

De ontvangstconstructies van de beschouwde toepassingen voor hybride isolatie technieken zijn licht-gewicht constructies zoals bijv. transport schepen en luxueuze jachten. Het tweede model dat wordt beschouwd is meer representatief voor dit soort applicaties en is een numeriek model van een laboratorium opstelling. Het dynamisch gedrag wordt bepaald met de Eindige Elementen Methode. Het doel is niet om een exacte beschrijving te verkrijgen maar om een model te hebben met dezelfde karakteristieken als de beschouwde applicaties. Verder zijn er numerieke methoden ontwikkeld om de structurele en akoestische responsie van het gehele systeem te bepalen. De ontwikkelde software wordt gebruikt om de effectiviteit van de verschillende actieve regelstrategieën te onderzoeken. Belangrijke aandachtspunten zijn de sensor en actuator configuraties. Er zijn procedures ontwikkeld om m.b.v. de ontwikkelde modellen het optimale aantal en richtingen van de actuatoren te bepalen.

Behalve de analyse van verschillende actuator concepten en sensor strategieën is er ook aandacht besteed aan de implementatie. De actuator(en), passieve trillingsisolator(en) en eventuele sensors moeten uiteindelijk geïntegreerd worden tot een hybride mount. Belangrijk voor het ontwerp van dergelijke hybride componenten zijn de isolatie karakteristieken van de passieve rubber trillingsisolatoren. Er wordt een methode gepresenteerd om deze multidimensionale isolatie karakteristiek te bepalen. Deze gebruikt eindige elementen analyses, waarbij de invloed van de excitatie frequentie en de statisch deformatie beschouwd wordt. Ook wordt er een optimalisatie procedure beschreven om de materiaal parameters te bepalen m.b.v. gestandaardiseerde metingen van een hele isolator.

Ten slotte is het concept van het plaatsen van de sensoren dicht bij de bron onderzocht. Normaal gesproken worden bij actieve isolatie de sensoren geplaatst op de locaties waar de reductie gewenst wordt. Het plaatsen van de sensoren dicht bij de bron heeft enkele voordelen: de implementatie is eenvoudiger, er is een mogelijkheid om een maat voor de gehele responsie van de ontvangstconstructie te verkrijgen en de flankerende transmissie paden of andere verstoringen dan de verstoringsbron die beschouwd wordt hebben minder invloed. Twee near-source sensor strategieën worden beschouwd: minimalisatie van het doorgeleid vermogen en een techniek waarbij de near-source sensoren worden gewogen met een off-line bepaalde weegmatrix gebaseerd op de responsie van een goed gekozen prestatie sensor set. Er is een fouten analyse uitgevoerd om de robuustheid te controleren en er zijn metingen aan de

laboratorium opstelling gedaan ter validatie. Deze metingen tonen aan dat de toepassing van off-line bepaalde weegmatrices onbruikbaar is voor de beschouwde applicaties van hybride isolatie.

Contents

Chapter 1

Introduction

1.1 Background

Sound can be experienced in different ways. The open-air performance of popular music causes a lot of sound which may be enjoyed by the visitors of the show, but at the same time can be experienced as unwanted sound, or noise, by the neighbors who would prefer an uninterrupted sleep. Due to the increasing growth of the human population, the noise problem is becoming more and more important. Noise and vibrations are also experienced in vehicles like cars, aeroplanes and ships. The tendency to reduce the weight of the construction to save material and production costs and to reduce fuel consumption leads to even more problems concerning the interior noise levels in vehicles. Also, the stricter demands of customers with respect to comfort require extra attention for the reduction of the interior noise.

Noise problems in vehicles may arise from different sources such as engines, gearing, exhaust, vehicle tyres and ship propellers. An example of the interior noise problem caused by an engine is shown in Figure 1.1. The structural vibrations of the engine and gearbox are transmitted to the cabin of a ship and cause interior noise. The present thesis concerns with resilient mounting of such machinery. The machinery is mounted with a combination of *active* and *passive isolation* techniques, so-called *hybrid isolation*, in such a way that the noise levels in the accommodations and cabins of the vehicle are reduced for a better comfort. The main goals are the development of models and tools for the analysis of such hybrid isolation systems and to investigate the aspects of active isolation near the noise source to reduce interior noise levels.

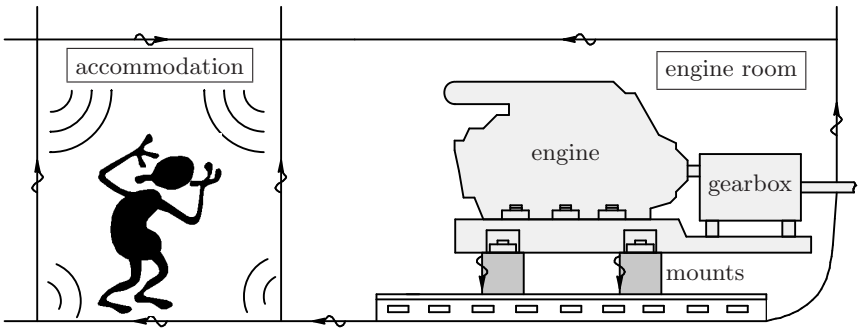

Figure 1.1: Interior noise in a ship caused by the structure-borne sound transmission from the engine to the ship hull.

1.2 Structure-borne sound

In general three types of sound sources are distinguished: sources that cause vibrations in solids (*structure-borne sound* such as excitation by rotating machinery), liquids (*fluidborne sound* such as cavitation) and gases (*airborne sound* such as a turbulent jet). The same distinction can be made for the sound transfer from the sound source to the surrounding environment, i.e. through solids, liquids and gases. Machinery in vehicles, like the engine, offer many sound transfer paths to the surrounding environment [134]. The engine radiates sound directly to the surrounding air, which is an example of an airborne sound path. The engine also transmits vibrations through the support mountings to the receiver structure. The vibrations of the receiver structure result in interior noise of the vehicle. This sound transfer path, which is also the source of the interior noise shown in Figure 1.1, is an example of a structure-borne sound path which is an important transfer path for lightweight vehicles with low damping. This sound transfer path is the main theme of this work and the isolation of the machinery is a possible solution for attenuation of the structure-borne sound.

Resilient mounting systems in vehicles contain several mounts with multi-directional vibration transmission paths. To describe the performance and response of the whole system, the concept of transmitted power is often used [46, 47, 48]. The transmitted power describes the vibrational energy flow through the whole mounting system due to the energy dissipation in the receiver structure. For this reason it is an interesting measure to determine the performance of an isolation system, but possibly also an interesting con-

trol strategy for active isolation purposes [86]. In Figure 1.2 the energy flow in an isolation system is depicted. The vibrating source injects power into the mounting system. The mounting system dissipates some of the injected power due to the structural damping and transmits a part to the receiver structure. The transmitted energy through the mounting system is the energy that is dissipated in the receiver structure and can be roughly subdivided into dissipated energy due to the internal damping of the structure and the radiated sound energy caused by the interaction with the surrounding environment (like air or water). If it is possible to measure the transmitted power, this might provide a useful quantity to use for active isolation purposes.

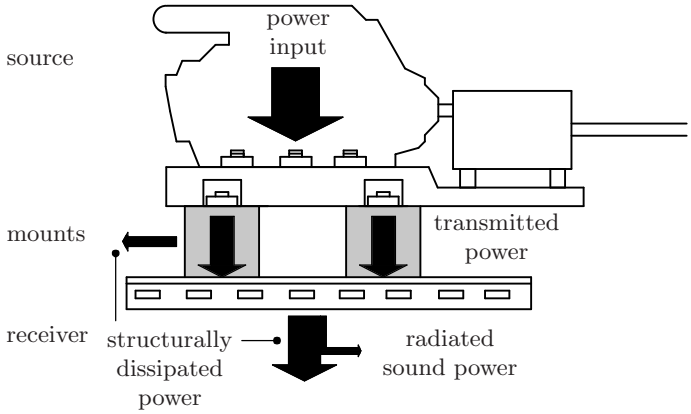

Figure 1.2: The energy flow in an isolation system.

1.3 Isolation of structure-borne sound

Broadly speaking there are two classes of isolation problems: cases where a vibrating body (a machine or engine) is isolated from a receiver structure (a car body, ship hull or aircraft fuselage) and cases where the body (such as sensitive equipment) is isolated from a vibrating source (such as ground vibrations). In both problems the source of vibrations may be deterministic or random. Generally speaking, problems of the first kind have a deterministic source of vibration when the source is a rotating or reciprocating machine. The second class of problems deals predominantly with vibration sources that are stochastic. An example is the design of active vehicle suspension systems. The body to be isolated is the passenger cabin and the source of excitation is the unknown and variable height of the road surface, being randomly distributed.

In this thesis problems of the first kind, which involve isolation of vibrating machinery from a receiver structure, are considered. These kinds of isolation systems can be subdivided into three subsystems or components: a source of vibration (e.g. an engine), a supporting mounting system (consisting of several mounts), and a receiver structure (the vehicle itself). In Figure 1.2 a typical isolation system is depicted and shows the different components. The vibrations transmitted by machines or other sources cause unwanted effects such as noise radiation. Generally speaking, the structure-borne sound transmission causes sound radiation, while low frequency vibrations cause fatigue and failure. The most simple solution to prevent these unwanted effects, is isolation of the source from the receiver structure. In this thesis it will be shown that a description of the dynamic behavior of the source, mounting system and receiver structure is needed for a correct modeling of the complete isolation systems.

1.3.1 Passive isolation and dissipation

Usually machinery is placed on a *resilient passive mounting system* to reduce the structure-borne sound [122]. In passive vibration isolation two basic phenomena play a role: isolation of the machinery and dissipation of the transmitted energy [135]. The first phenomenon follows from the impedance mismatch[1] introduced by the insertion of vibration isolators between the source and receiver. In general the source and the receiver are relatively heavy and stiff and have a high impedance. The mounts have a low stiffness resulting in a low impedance. In practice this is realized by placing the machinery on rubber isolators or metal springs. The energy remains in the source and the dynamic uncoupling results in a higher source vibration level. The larger the stiffness or impedance mismatch, the better the isolation. The second phenomenon is based on dissipation of the structure-borne sound energy in the mounts.

The mounting system is traditionally designed on low-frequency requirements: the mounting support has to be sufficiently stiff to limit low-frequency motions and static deformations (e.g. in the case of a ship engine the seaway motions and static deformations due to thrust forces and torques). This poses a lower limit on the static stiffness of the mounting system, so the effect that can be achieved with the concept of isolation is limited. Especially for flexible and lightweight receiver structures (i.e. structures with low stiffness), very flexible mounts are needed to create the stiffness mismatch needed for the isolation effect and to ensure passive isolation of the structure-borne sound

[1] The term impedance is the ratio of the force and the velocity and is explained in more detail in section 2.4.1.

at high frequencies. Clearly, there are conflicting demands for the design of passive resilient mounting systems.

1.3.2 Active isolation

The effectiveness of a passive resilient mounting system is limited due to conflicting design demands. To achieve additional attenuation in the low-frequency region *active isolation techniques* can be used. An active system typically consists of *sensors* to detect the response of the system, *actuators* as the external energy source to drive the system and a *controller* to process the sensor signals and to drive the actuators. The actuators (e.g. electrodynamic actuators) can be placed for example under the engine support and are driven by the controller in such a way that the response at the sensors (e.g. microphones or accelerometers) is minimized. The different components concerning the concept of active isolation of a ship engine are depicted in Figure 1.3.

Active control strategies can be divided into two categories: *feedforward* and *feedback*. Feedback strategies are necessary for systems without information about the disturbance of the system. The sensor signals for this kind of system are fed back to the controller. In lightweight vehicles the interior noise is often dominated by the structure-borne sound from the engine with the largest contributions originating from the engine orders. The engine orders are frequencies related with multiples of the number of revolutions of the engine. The rotary or reciprocating machinery in fact cause a deterministic excitation and for this reason feedforward control strategies can be used to tackle the control problem. The reference signal that is needed for such control strategies is determined by measuring the rotational speed of the engine. This reference signal is used as information by the controller after which the control signal is determined, hence the name feedforward strategy.

1.4 Hybrid isolation

Due to the limited isolation effect of passive resilient mounting systems in flexible and lightweight vehicles, extra attention might be required with respect to the reduction of the interior noise. For this reason the purpose of *hybrid isolation* is an interesting option: the isolation performance of a passive isolation system is enhanced by integration with active isolation techniques. The concept of active isolation is especially effective in the low-frequency region, whereas the passive vibration isolation techniques perform well at high frequencies.

1.4.1 Application of hybrid isolation

An interesting application of hybrid isolation techniques is in ships, because of their relatively lightweight construction. Heavy machinery like the engine and the gearbox are needed to drive the ship. These components are important sources of interior noise and the effect of passive isolation is limited due to the strict static requirements of suppressing seaway motions. For this kind of application it can be worthwhile to implement the relatively expensive equipment needed for active isolation. In this thesis, these kinds of applications are considered with respect to the implementation of hybrid isolation systems.

The components of a typical hybrid isolation system for a ship are shown in Figure 1.3. The engine is mounted on the passive vibration isolators, which are in most cases rubber mounts. Also an additional active isolation system is shown consisting of actuators (integrated with the passive mounts), sensors and a controller to determine the actuator signals. The goal is minimization of the structure-borne sound from the engine. This means that the other sound transmission paths are not considered in this thesis. The structure-borne sound from the engine is strongly related to the rotational speed of the engine. For this reason a multi-harmonic excitation of the receiver structure is assumed. This information can also be used for the controller (indicated by the reference signal) and a feedforward control strategy is used for this kind of isolation problem. An important factor to consider for the performance of the active isolation part is the choice of sensors and sensor locations that are used as input for the controller. The response of the (weighted) sensor signals minimized by the controller is called the *error criterion* or *cost function*.

It can be seen in Figure 1.3 that the actuators are situated near the source as part of the hybrid mounts. The sensors are depicted at two locations: at the receiver structure (e.g. the passenger accommodations) and near the mounting system. The first kinds of control strategies have already been analyzed in practice and their functioning has been proved successful. Winberg, Johansson and Lagö [80] presented experimental results of an active vibration isolation system in a boat with microphones as error sensors in the passenger accommodation. They showed that a good reduction could be obtained at the microphones. Their study provides a lot of insight as several problems arose with the implementation of the active isolation system. An important problem is the influence of the different disturbance sources and their transmission paths. The two main noise sources of the considered application were the propeller BPF (Blade Passage Frequency) and the engine orders. The engine mounts were the most important transmission path for the engine. The same transmission path is important for the noise caused by the propeller;

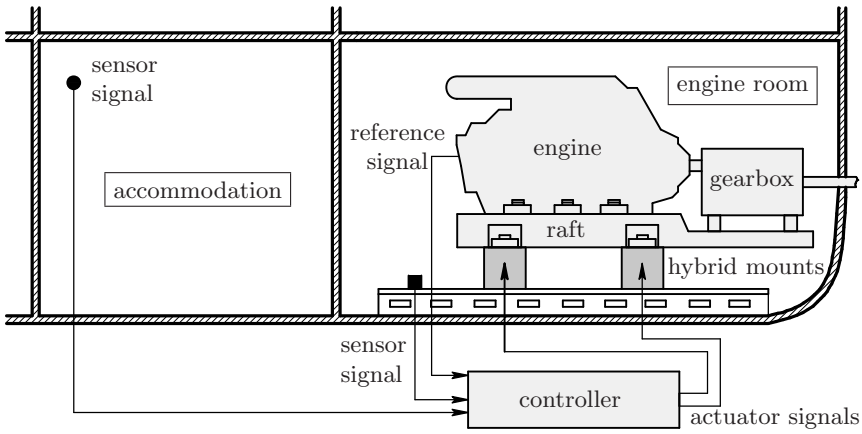

Figure 1.3: A schematic overview of a hybrid isolation system for a ship engine.

the propeller vibrations are also transmitted through the mounts to the ship hull. Reduction can only be obtained when the frequency components of the two disturbance sources are the same and when the actuators were placed at the locations of the mounts, meaning that only vibrations transmitted along these specific transmission paths can be attenuated effectively. However, the propeller vibrations, besides the transmission path through the propeller shaft and engine mounts, also excited the hull of the ship directly through the water. The latter transmission path is a so-called *flanking path* and its contribution was very difficult to attenuate by the actuators. The contribution from this flanking path was not dominant, so good reductions could still be obtained. This means that for an effective implementation of an active control system, the most dominant sources and flanking paths need to be identified.

1.4.2 Terminology

In this work various terms are used to define the different components with respect to the hybrid isolation of structure-borne sound. The term resilient mounting system is used to define the support of the source. This mounting system can be passive (passive mounting system), active (active mounting system) or a combination of both (hybrid mounting system). The hybrid mounting system consists of a combination of passive vibration isolators or mounts and actuators. The term *(hybrid) isolation system* describes the whole system including source, (hybrid) mounting system and receiver.

1.4.3 Models

In this thesis the design and performance of hybrid mounting systems is studied with the use of mathematical models. This has several advantages. First of all, the influence of the model complexity, like the number of natural modes in the frequency range of interest, can be more easily studied. Another advantage is that many of the complications concerning the practical implementation play no role or are more easily 'controlled' like flanking paths, other disturbance sources and convergence of the controller. Furthermore, the models allow a thorough investigation of all kinds of error sensor strategies. Even the performance of error sensor strategies which are difficult or impossible to implement in real applications (e.g. minimization of the kinetic energy) can be investigated. It is also possible to determine all kinds of dynamic and acoustic responses of each subcomponent at different locations (e.g. at other locations then the error sensors).

However, it is important to properly assess the use of mathematical models in this thesis. It is impossible to make an exact model to describe the dynamic behavior of complex structures such as a ship. The dynamic behavior of the model will always differ from the true behavior of the structure. However, when the model is representative for the considered applications, trends can be derived that are generally valid for this type of application. The practical implementation is of course another problem and may result in a decrease of the performance due to restrictions that are not considered in the model. It must be kept in mind that the available information for practical applications is very limited: normally only a limited set of measurements can be performed. This is the only information about the system that can be used (derived from the analyzed models) to deduce rules of thumb for the design of isolation systems in practice.

1.4.4 Near-source error sensor strategies

For the implementation of active isolation systems in vehicles it is advantageous to locate the sensors near the resilient mounting system for reasons of easier practical implementation and cost reduction. Another advantage of these so-called *near-source error sensor strategies*, is that the error sensor response is dominated by the disturbance source that has to be reduced. The influence of other disturbance sources and flanking paths have less influence on the error sensor response and the active control performance. This is explained in more detail in chapter 6. However, the use of sensor strategies near the source of vibration is not straightforward. Winberg *et al.* [80] presented

results with acceleration sensors in the axial direction of the mounts as error sensors. Although the vibration level was reduced at the error sensors, the interior noise was hardly affected. Besides that, the *robustness* of such strategies may be a problem; the error sensor response may be sensitive to small measurement errors.

The first concept of a near-source sensor strategy is the minimization of the transmitted power. This concept has already been analyzed with models and experiments by e.g. Pan and Hansen [102] and by Howard [53]. However, the considered models were relatively simple and cannot be compared with complex receiver structures like vehicles. A great disadvantage is that the error criterion of transmitted power is very sensitive to measurement errors at the sensors [41]. This means that relatively small measurement errors result in an unreliable measure for the transmitted power and consequently result in a bad active control performance.

An important topic in this work is the investigation of near-source error sensor strategies for hybrid isolation systems in complex receiver structures like ships. Besides the minimization of the transmitted power, another approach will be addressed in this thesis. This approach is based on an efficient weighting of a set of near-source sensor signals in such a way that the response at the receiver structure is reduced.

1.4.5 Hybrid mount

For the actual implementation of hybrid isolation, the passive and active isolation concepts will often be integrated into one module: the *hybrid mount*. The hybrid mount consists of a combination of passive vibration isolators (in most cases rubber vibration isolators are used for the considered applications), actuators and, possibly, sensors. For purposes of cost reduction, the number of actuators must be as small as possible. Also, the force that can be exerted with commercial actuators is limited. For performance and cost optimization of hybrid isolation modules, it is important to have a good characterization of the passive vibration isolators. The passive mounting system has a large influence on the actual performance and actuator configuration. In this work a numerical model is described to determine the multi-directional vibration transfer and isolation characteristics of rubber vibration isolators. Also, attention is paid to the characterization of the rubber material properties, which is very important for the passive isolation behavior. A procedure is introduced to derive the material parameters of the rubber material with the help of some standard measurements on the entire isolator. With help of the obtained material parameters, a complete description of the isolation behavior of the isolator

can be obtained with a numerical model.

1.5 Objectives

The objective of this study is to develop (numerical) models for hybrid isolation systems and to use these models for studying strategies for cost-effective system performances. The models are used as design tools to investigate the effectiveness of different control strategies. Another important aspect is the study of how to determine the number, location and direction of the actuators. From the viewpoint of cost-effective design, it is also important to reduce the number of actuators and sensors. With respect to the active isolation part, attention will also be paid to the use of near-source control strategies for practical applications with realistic receiver structures. The final step in the design of hybrid isolation concepts is the hybrid mount. An important point of attention for the design of the hybrid mount is the passive isolation characterization that is needed and this is analyzed in more detail for rubber vibration isolators.

1.6 Outline

The present chapter covers the general definitions in isolation and introduces the concept of the use of hybrid isolation of structure-borne sound. In the next chapter the general theory is described to analyze hybrid isolation systems. Both the modeling of the structural dynamic behavior as well as the acoustic behavior of the models are treated.

In chapter 3 the general theory is used to describe an example of a hybrid isolation system. The model describes the hybrid isolation of a rigid mass from a simply supported plate as receiver structure. The relatively simple configuration allows an analytical description of the dynamics of the subcomponents. However, general tendencies can still be shown using this model.

In chapter 4 a more representative system is treated for the considered applications of hybrid isolation. A model is made of a laboratory setup that has a dynamic behavior with the same characteristics as can be found in complex structures like for example ships and vehicles. This model is also analyzed with the theory described in chapter 2, but the dynamics of the subcomponents are determined from numerical models. Different error sensor strategies are analyzed and rules of thumb are presented to determine the number of actuators and the directions of the actuators for an effective active isolation.

Chapter 5 deals with the modeling of rubber vibration isolators. In this chapter a numerical model of a rubber vibration isolator is presented to determine its multi-directional passive isolation characteristics. The influence of the static pre-deformation of the isolator and the frequency dependent behavior are analyzed in more detail. Also attention is paid to the determination of the rubber material parameters with the help of standardized measurements of the entire isolator. A correct description of the material parameters is essential to obtain a reliable and complete description of the isolation behavior.

The use of near-source error sensor strategies has some advantages for the isolation systems that are considered in this study. This is explained in chapter 6 where two concepts of near-source error sensor strategies are studied. First, the minimization of the transmitted power to the receiver structure is considered. This error sensor strategy is known to be very sensitive to small measurement errors. For this reason another near-source error sensor strategy is introduced: weighting of a near-source error sensor set based on the response of a different sensor set that is actually desired to be minimized. Special attention is paid to the robustness of the near-source error sensor strategies. Experiments on the laboratory setup were performed to analyze the different procedures for determining the weighting matrices.

Finally, in chapter 7 the main results and conclusions are summarized and discussed.

Chapter 2

General theory of hybrid isolation systems

2.1 Introduction

In the first chapter it was explained that passive isolation may not sufficiently reduce the interior noise levels in lightweight structures. A solution is to improve the isolation performance in the low frequency region with the use of active isolation techniques. In this chapter the general theory is presented for modeling the vibrational and acoustic behavior of such combined passive and active isolation systems. The goal of these models is to enable the investigation of different hybrid isolation configurations.

The dynamics of the components and the complete isolation system can be analyzed with models or with measurements. In this thesis most attention is paid to the analysis of the complete isolation systems with models. As explained in chapter 1, models of the isolation system are made in such a way that their behavior is representative for the considered applications, though without modeling the dynamic behavior exactly. The general trends found are assumed to also be valid for practical applications. Performing measurements to determine the behavior of the isolation systems may be very time-consuming, whereas models can be easily used to determine the different responses for different actuator and sensor configurations. In this chapter, a general representation is used to model the complete hybrid isolation systems.

To put the models into perspective, first a short review of the literature regarding analytical models of active isolation systems is presented in section 2.2. The literature survey is split into two parts. First a review is given of analytical models to describe the structural transmitted power flow in isolation systems.

In the second part, a short overview of analytical models of active isolation systems is presented. Subsequently, some simple discrete dynamic models are analyzed and their shortcomings and restrictions are described in section 2.3. These models are quite simple but clearly show some basic physical principles of the dynamic behavior of isolation systems.

After the introduction of the basic terms and principles with the help of discrete analytical models, a general model description is given to calculate the dynamic response of the complete isolation system in section 2.4. A hybrid isolation system in its most general form consists of a source, a mounting system to support the source and a receiver structure. An approach is adopted that was also used by Gardonio [40, 41]. This approach distinguishes *ports* or *junctions* at the connection points between the hybrid isolation components (thus the source, mounting system and a receiver structure). The dynamics of the system are consistently described by the force and the velocity vectors at these junctions. An advantage of this way of modeling is that the models are solely described by the forces and velocities at the locations of interest, resulting in compact models. Another advantage is that the way to define the dynamics of the sub-components itself is not restricted: different techniques can be used such as analytical methods, numerical methods like the Finite Element Method, or measurements. Furthermore, the used port-description allows the description of the multi-directional vibration energy transmission and also allows the use of complex models of each component. These properties are important for the considered applications, because vibration transmission in vehicles occurs along several transmission paths of the mounting system (multi-directional vibration transmission by multiple mounts) into a receiver structure with a complex dynamic behavior. Another advantage is that the model properties of the components can be exchanged rather easily, for example by using mounting systems with different material properties. A requirement for the use of a port description is that linear models be used to describe the dynamic behavior. The use of this kind of model is justified because the dynamic displacements of the components are small, especially at the higher frequencies. The interior noise levels generated in the considered applications are mostly directly related to some discrete excitation frequencies of the source (for example the engine and the transmission in a ship). For this reason a harmonic analysis is allowed, resulting in frequency dependent forces and velocities at the junctions.

The structural vibrations of the receiver structure in the audible frequency region cause the interior noise. The surrounding medium is excited by the normal surface velocity distribution of (a part of) the structure, which causes

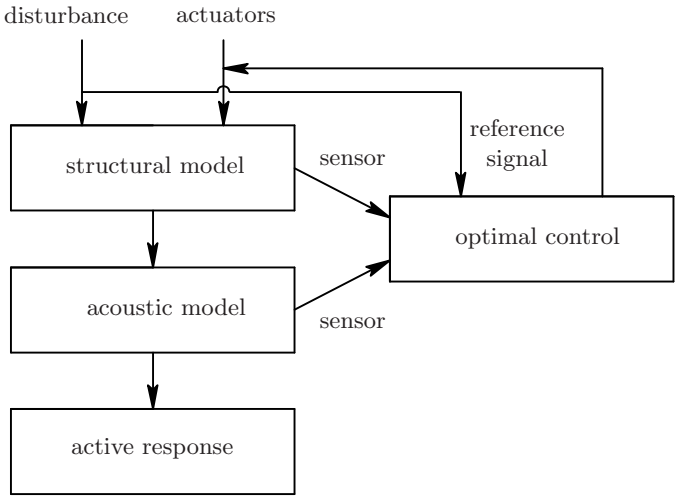

Figure 2.1: Analysis of hybrid isolation systems.

the pressure perturbations that are experienced as noise. For this reason, the structural dynamic models are extended with an acoustic analysis to have a more representative model of the considered applications of hybrid isolation. This is described in section 2.5. The normal surface velocity distribution of (a part of) the structure is used as input for the acoustic analysis. In this work, the free field radiation of a part of the receiver structure is modeled with the *Rayleigh integral method*. Besides free field radiation, the acoustic radiation of a part of the receiver structure into an acoustic enclosure is considered. The enclosure is a simple model for passenger accommodation in a vehicle and the acoustic response in the enclosure is determined with a modal superposition technique.

After the determination of the structural and the acoustic behavior of the isolation system caused by the disturbance mechanisms of the source and the actuators, the active isolation response can be calculated with the analysis of different error sensor strategies related to the acoustic and structural response of the receiver structure. For this purpose the *optimal control* procedure is used, implying that an ideal feedforward controller is used to tackle the controller problem (see section 2.6). A schematic overview of the whole procedure is shown in Figure 2.1.

Finally, some conclusions are drawn and presented in section 2.7.

2.2 Literature survey

This literature survey is subdivided into two parts. First a short overview is given of models that describe the structure-borne energy flow in structures and isolation systems. In the second part an overview of the models of complete active isolation systems is presented. The dynamics of most models are described analytically.

2.2.1 Dynamic modeling using power flow

In general an isolation system consists of several transmission paths, formed by the mounts that couple the source with the receiver structure in different directions. For this reason a large number of parameters is needed to describe the structural vibration transmission correctly. The transmitted energy flow through the mounting support to the receiver structure is a convenient measure to quantify the performance of multi-point mounting systems with multi-directional vibration transmission. Good results have been obtained by dividing the isolation system into individual components such as a source, a mounting system and a receiver structure. In this way the models can be kept relatively small, because a port description can be used to describe the dynamics at the connection or junction points of the different components only. The dynamic behavior is described by the transfer functions from the different excitation mechanisms (like the disturbance and actuator forces) to the responses (e.g. the velocity or forces) at the connection points between the different components for each degree of freedom. Goyder and White [46, 47, 48] used a novel approach by introduction of power flow techniques to describe the vibration isolation and power transmission. They showed results of this concept for complete isolator systems with a spring-like one-degree-of-freedom isolator and a receiver structure consisting of a beam, plate or a beam-stiffened plate. Only the out-of-plane vibration direction of the receiver structure is considered. Other authors have also used this approach like Pinnington and White [110] to describe the power flow to a resonant and non-resonant beam. They investigated when the beam structure can be considered as infinite for a correct prediction of the frequency-averaged power. Pinnington [109] also studied the vibrational power flow to a flexible seating by two one-degree-of-freedom mounts, by means of experimentally measured transfer matrices. The influence of the rotational degrees of freedom in addition to the translational motions were shown to be of importance for the power transmission to beam or plate-like structures (Koh and White [72, 73, 74], Petersson [105, 106] and Sanderson [114]). Pan, Pan and Hansen [103] studied the power flow in a

vibration isolation system with a rigid source, multiple vibration isolators and a rectangular plate as receiver structure. The isolators were each modeled as an assembly of six one-degree-of-freedom translational and rotational springs. Li and Lavrich [77] analyzed a similar vibration isolation system, except that a beam-reinforced plate was used as receiver structure. Li and Daniels [76] studied the power transmission of a vibration isolation system to a supporting cylindrical shell. Xiong, Xing and Price [141] introduced a generalized mobility/impedance[1] power flow model and considered a raft isolation system consisting of five subsystems (two rigid bodies as sources, each connected with four springs to a flexible raft. The raft was modeled as a free-free beam and connected with a clamped-clamped flexible beam as receiver structure, see also Figure 1.3). These articles only consider the power flow in the isolation system and not the influence of the active isolation control on the transmitted power. Also, the mounting systems are assumed to be linear. Further research has been done on the analysis of power flow through a nonlinear mounting system like Royston and Singh [113]. Generally speaking, it can be said that the transmitted power is an interesting measure to describe the global response of the whole dynamic system. This is especially interesting for the considered applications where the number of transmission paths to the receiver structure can be quite large. The response can still be characterized by just one measure: namely the transmitted power. A necessary condition is that the multi-directional vibration transmission is determined correctly for each transmission path.

2.2.2 Active isolation and power flow

In the preceding subsection a literature overview was given of transmitted power as a measure to describe the dynamic behavior of isolation systems. This section deals with models of active isolation systems.

Feedforward control in active vibration isolation systems

Besides a good description of the multi-directional vibration and sound radiation, the transmitted power flow was also be considered as an error criterion for active isolation purposes [86]. An overview of relevant papers concerning analytical models of active isolation systems is given in Table 2.1. Most earlier studies only deal with isolation systems having a single mount vibrating in one direction with a rigid source and a fixed base or a one-degree-

[1] The mobility y is defined as the ratio of the velocity v and the force f and the impedance z as the ratio of the force and the velocity, see also section 2.4.1.

of-freedom mass-damper-spring system as receiver structure for feedforward control strategies [38, 59]. More realistic models with a flexible receiver structure were studied by several authors. Pan, Hansen and Pan [102] presented a model that isolated a rigid body from a thin beam with a single mount and an actuator in the axial direction of the mount, and showed that it was possible to reduce the power transmission with feedforward control. They also considered a model with two active isolators and a flexible panel as receiver structure [100]. Experimental results were also included in these two papers. Koh and White [72, 73, 74] presented an isolation model consisting of a rigid seating block mounted on a flexible beam and plate. They considered only the out-of-plane DOF of the plate, caused by the normal force and in-plane moments. The influence of the moment introduced by the actuators (secondary moment) was investigated with a feedforward control strategy that minimized the transmitted power. Howard, Hansen and Pan adapted the models presented in [100] and [102] to an active isolation system with a flexible cylindrical shell as receiver structure [54]. The latter model was extended with an intermediate flexible plate as a raft model by Pan and Hansen [101]. Gardonio, Elliott and Pinnington [40, 41] presented an active isolation system consisting of a rigid source, two cylindrical beams as mounts and a flexible plate as receiver structure. Different feedforward control strategies were studied: besides minimization of transmitted power also minimization of (a combination of) forces and velocities were considered at the connection locations of the mounts with the receiver plate. The transfer matrices of the isolation system were described by mobility and impedance matrices, which makes it very flexible for analysis with other source, mount or receiver components. Gardonio and Elliott [39] used the same approach in another paper to describe the vibration transmission between two plates. Only the out-of-plane motion of the plates (source and receiver) was considered, and also experimental results were presented. The characteristic property that the transmitted power is closely connected to a global measure of the receiver response makes this measure very interesting as an error criterion of the global response. For this reason, the transmitted vibrational power is studied and analyzed as one of the error criteria in this thesis.

Feedback control in active vibration isolation systems

Feedback control strategies are also used for active isolation and many papers have been presented on this subject. Most earlier studies with feedback strategies (also active damping) only deal with isolation systems having a single mount vibrating in one direction with a rigid source and a fixed

base or a one-degree-of-freedom mass-damper-spring system as receiver structure [69, 81, 116, 126]. Sciulli and Inman [115] presented a one-degree-of-freedom model with a flexible beam receiver. Several (velocity and position) feedback strategies were considered with respect to their performance for different mount frequencies (the frequency of the rigid body mode of the source mass on the mount) with respect to the eigenfrequencies of the modes of the flexible receiver. Huang, Elliott and Brennan [55] studied an isolation system with a flexible or rigid source connected with four mounts to a flexible receiver structure. The flexible source and receiver are plates and the mounts were modeled as linear ideal springs with viscous dampers. Decentralized velocity feedback was considered and also experimental results were presented. Xiong, Xing, Price and Wang [142] presented a general model to examine the power flow in an isolation system with flexible substructures and with a force feedback control. They studied an isolation system with three substructures: a rigid mass as source and a flexible simply supported panel as receiver structure. The source was connected with two mounts to the receiver structure. The mounts were modeled as cylindrical tubes with structural damping. Only the bending vibration of the plate was considered. A more general formulation to analyze the power flow of active isolation systems with feedback control strategies was presented by Xiong, Xing and Price [140]. In their paper an example of an isolation system with three substructures was studied: two rigid masses as sources and a flexible panel as receiver structure. Each source was connected with two mounts to the receiver structure, which are modeled as linear springs with structural damping. Only the translational motion in the normal direction of the plate was considered. They used the same formulation in [141]. In this paper an example of an isolation system with three substructures is studied: two rigid masses as sources and a flexible panel as receiver structure. Each source is connected with two mounts to the receiver structure, which are modeled as cylindrical tubes with structural damping. Only the translational motion in the normal direction of the plate is considered. The performances of absolute velocity feedback, relative velocity feedback and a combination of these two were investigated.

However, for the applications considered in this work, feedback strategies are not the best solution. In the control of lightly damped structures, feedback control is mainly used for supplying *active damping* [112]. The closed loop response of the system, thus the behavior of the system including the controller, shows a reduction of the resonance peaks. When a reference signal is available, it is better to use *feedforward* control strategies. Unlike active damping, which can only attenuate the disturbances near the resonances, the

feedforward strategy works for any frequency and attempts to cancel the disturbance completely. Another advantage is that feedforward control can be used for higher frequencies and has therefore already been successfully applied in acoustics. The disadvantage is that the global response (thus also the response at locations where no error sensors are attached) is not necessarily reduced. More details about the implementation of feedforward control strategies can be found in references [127, 128].

In this thesis the main goal is suppression of structure-borne sound in complex vibrating structures caused by rotary or reciprocating machinery. The structure-borne sound transmission is dominated by the response at frequencies components that are directly coupled with the rotational speed of the machinery. For this reason the models described in this thesis assume harmonic excitation. As stated in the introduction chapter, the control effort for this type of problems is in general tackled by an adaptive feedforward strategy. The models from the literature in general have quite simple receiver structures. The applications that are considered to be interesting for hybrid isolation are e.g. vehicles or ships with quite complicated receiver structures. For this reason, a general model is introduced that makes use of a port description.

2.3 Discrete analytical models

To give the reader a first impression about isolation and the terminology used, some simple discrete dynamic models of isolation systems are analyzed as a start. Also some general tendencies can already be shown with these kinds of models.

The discrete models are composed of highly idealized components like masses, springs and dampers. The masses are assumed to have inertia without dimension (point masses) and the springs and dampers are assumed to be massless. The dynamic systems are excited by disturbance forces and isolated actively by actuator forces acting on the masses. The number of equations of motion describing the dynamic behavior of these discrete isolation systems is determined by the number of masses or the number of degrees of freedom (DOFs). First the passive isolation is treated. Then some basic active isolation concepts are analyzed in more detail. The last subsection treats the limitations of this kind of model.

2.3.1 Passive isolation and dissipation

A schematic picture of an idealized two-degree-of-freedom passive isolation system is given in Figure 2.2(a) [51]. The source is modeled by prescribing

Author	Year	Reference	Source	Mount	Receiver	DOF(s)	Remarks
Pan, Hansen and Pan	1993	[102]	rigid mass	1, spring-like	beam	2-dim bending	incl. experim. work
Pan and Hansen	1993	[100]	rigid mass	2, spring-like	plate	bending	incl. experim. work
Pan and Hansen	1994	[101]	rigid mass	6, spring-like	plate and cylindr. shell	6	
Koh and White	1996	[72, 73, 74]	-	rigid block	beam/plate	out-of-plane	influence of secondary moment
Howard, Hansen and Pan	1996	[54]	rigid mass	2, spring-like	cylindr. shell	6	
Gardonio, Elliott and Pinnington	1997	[40, 41]	rigid mass	2, cylindr. beams	plate	two-dim	different control strategies studied
Sciulli and Inman	1998	[115]	rigid mass	1,spring-like	beam	1	several feedback strategies
Xiong, Xing, Price and Wang	2000	[142]	rigid mass	2,cylindr. beams	plate	bending	several feedback strategies
Gardonio and Elliott	2000	[39]	plate	3, cylindr. beams	plate	out-of-plane	incl. experim. work
Huang, Elliott and Brennan	2003	[55]	plate	4, spring-like	plate	1	decentralized velocity feedback control
Xiong, Xing and Price	2003	[140]	2, rigid masses	4, cylindr. beams	plate	bending	velocity feedback control strategies
This thesis			rigid mass	4, cylindr. beams	plate	5	torsional DOF is not considered

Table 2.1: A selection of studies on analytical models of active isolation systems.

a harmonic displacement w at the top, the mount is a spring/damper combination and the receiver structure as a two-degree-of-freedom system without damping. The equations of motion of the two masses are [131]:

$$k\,(w - x_1) + c\,(\dot{w} - \dot{x}_1) - k_1\,(x_1 - x_2) = m_1\ddot{x}_1, \tag{2.1a}$$

$$k_1\,(x_1 - x_2) - k_2 x_2 = m_2\ddot{x}_2, \tag{2.1b}$$

where x_1 and x_2 are the displacements of the masses m_1 and m_2 respectively, k_1 and k_2 are the stiffness coefficients of the connecting springs related to the receiver structure and k and c are the stiffness and viscous damping coefficient of the mount respectively. Two damping mechanisms are considered: a *viscous* damper with damping coefficient c and *structural* damping in the mount defined by a loss factor η, which is described as a complex spring stiffness $k = k'(1 + \mathrm{j}\eta)$ [23]. The loss factor in fact indicates the ratio between the dissipated energy and the restoring mechanical energy during one vibration period. When it is assumed that the prescribed displacement is harmonic, a complex notation can be used:

$$w(t) = w\mathrm{e}^{\mathrm{j}\omega t}, \tag{2.2}$$

where t is the time, w is the amplitude of the source displacement, j is the imaginary unit and ω is the angular frequency. The damping force exerted by the viscous damper is proportional to the velocity. This means that for a harmonic excitation, the damping force is proportional to the frequency (when the amplitude of the displacements remains unchanged). This can be seen when the velocity is calculated by taking the time derivative of equation (2.2). Considering the structural damping model, the force exerted due to this damping mechanism is frequency independent. This damping mechanism is only defined in the frequency domain. In reality, the damping behavior of passive isolators is a combination of these two mechanisms.

In Figure 2.2(b) the transmissibility, which is defined as the displacement of mass m_2 divided by the displacement of the source w, is shown for a harmonic excitation of the source. The depicted reference solution is the transmissibility without damping (c and η are zero, so the peaks in the figure should be infinitely high). Besides the reference solution, transmissibilities are depicted for the case in which the mount has a certain amount of viscous damping c, structural damping η or a lower value of the stiffness k in comparison to the reference solution. In Figure 2.2(b) it can be seen that a reduction of the mount stiffness results in a lower transmissibility and thus a better isolation. The so-called *roll-off*, which is characterized by the decrease in transmissibility

with increasing frequency, starts at a lower frequency. However, at the eigenfrequencies the transmissibility is still infinitely high because of the absence of damping. When the mount contains some viscous or structural damping, the transmissibility is reduced at the eigenfrequencies. However, for *viscous* damping the roll-off decreases as well, thus being unfavorable for the transmissibility at high frequencies. The *structural* damping mechanism maintains the undamped roll-off and reduces the height of the peak responses at the resonance frequencies.

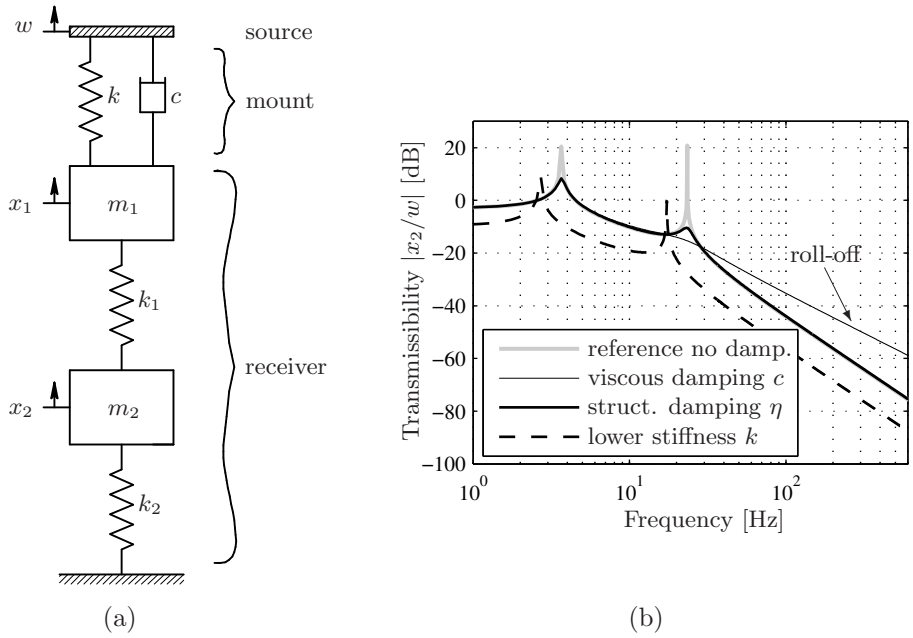

Figure 2.2: A two-DOF passive isolation system.

2.3.2 Active isolation

Passive isolation is only effective in the high frequency region because of the lower limit on the mount stiffness due to the static design requirements. To achieve a better performance of the isolation system in the low-frequency region, the concept of active isolation can be used. The components involved with active isolation are actuators, sensors and a controller. In Figure 2.3(a) the same isolation system is depicted as considered in the previous subsection,

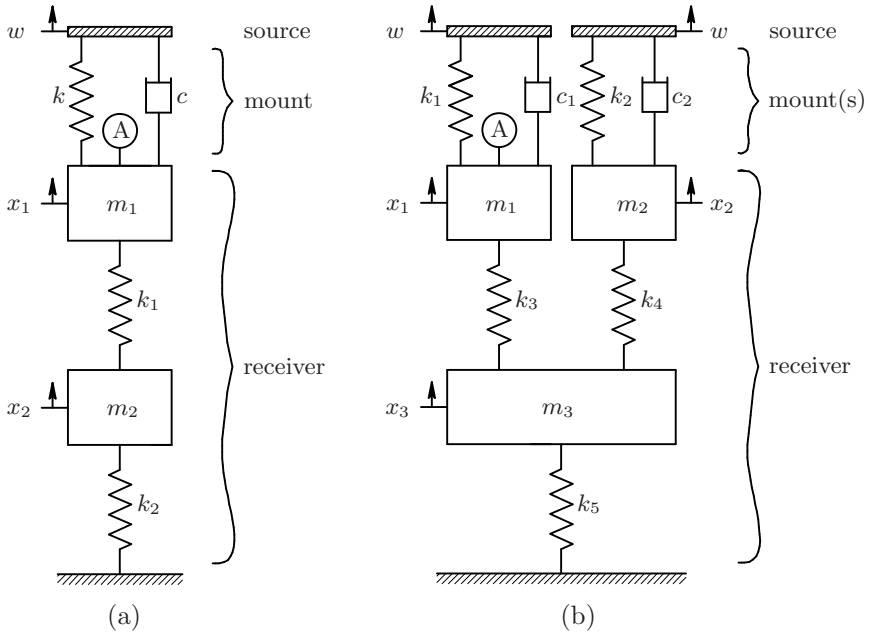

Figure 2.3: A two-DOFs (a) and a three-DOFs (b) hybrid isolation system, the actuators are assigned with the symbol Ⓐ.

but now extended with an actuator. This actuator is represented by an external force f_a acting on mass m_1 and the equations of motion now become:

$$f_a + k\,(w - x_1) + c\,(\dot{w} - \dot{x}_1) - k_1\,(x_1 - x_2) = m_1\ddot{x}_1, \tag{2.3a}$$

$$k_1\,(x_1 - x_2) - k_2 x_2 = m_2\ddot{x}_2. \tag{2.3b}$$

For this system with two degrees of freedom, the optimal actuator force f_a^{opt} can be determined in such a way that the displacement of mass m_2 is reduced to zero. With equations (2.3) the optimal actuator force for the harmonic case can be determined as:

$$f_a^{opt} = -\,(k + \mathrm{j}\omega c)\,w. \tag{2.4}$$

Besides a total reduction of the displacement of mass m_2, also the displacement of mass m_1 is totally canceled. This means a perfect isolation for the whole receiver structure resulting in a zero transmissibility, independent of the dynamics of the receiver structure. However, the considered example is a specific ideal case and is not representative for isolation systems in practice.

2.3.3 Limitations

Passive isolation

It was shown that passive isolation is a good concept for isolation of machinery at high frequencies. The discrete model showed that the roll-off is very important for a good isolation in the high-frequency region. It was also shown that a decrease of the mounting stiffness resulted in an overall decrease of the transmissibility. However, the passive mounting system must satisfy contradictory requirements. On the one hand it has to be sufficiently stiff to meet the static displacement requirements. On the other hand the stiffness of the mounting system has to be as small as possible to improve the isolation effect due to the impedance or stiffness mismatch, especially for lightweight structures. These demands may result in relatively stiff support mounting systems which are not effective in terms of structure-borne sound isolation. Also, the resilient mounting system must contain some damping to attenuate the response at the first rigid body eigenfrequencies of the source on the mounts. The transmissibility of mountings in practice will deviate considerably from the idealized two-degree-of-freedom model because of the resonances in the receiver structure and in the mount itself.

Active isolation

Active isolation is a good concept to improve the reduction of the transmissibility in the low frequency region. However, the example considered in the previous subsection was a special case of an active isolation system with only one transmission path. In actual multi-point mounting systems, a lot of structural transmission paths are present and it is difficult to place actuators in all the transmission paths.

To illustrate the effect of an extra transmission path without an actuator, consider the system depicted in Figure 2.3(b) with two transmission paths from the source to the receiver structure. In the considered system only on mass m_1 acts an actuator. The equations of motion for this three-degrees-of-freedom system are:

$$f_a + k_1 (w - x_1) + c_1 (\dot{w} - \dot{x}_1) - k_3 (x_1 - x_3) = m_1 \ddot{x}_1, \tag{2.5a}$$

$$k_2 (w - x_2) + c_2 (\dot{w} - \dot{x}_2) - k_4 (x_2 - x_3) = m_2 \ddot{x}_2, \tag{2.5b}$$

$$k_3 (x_1 - x_3) + k_4 (x_2 - x_3) - k_5 x_3 = m_3 \ddot{x}_3. \tag{2.5c}$$

When it is assumed that the source displacement is harmonic ($w(t) = w\mathrm{e}^{\mathrm{j}\omega t}$)

these equations can be rewritten as:

$$-\omega^2\mathbf{M}\cdot\mathbf{x}+\mathrm{j}\omega\mathbf{C}\cdot\mathbf{x}+\mathbf{K}\cdot\mathbf{x}=\mathbf{w_s}w+\mathbf{t}_a f_a, \tag{2.6}$$

where $\mathbf{M}$ is the mass matrix, $\mathbf{C}$ is the damping matrix, $\mathbf{K}$ is the stiffness matrix, $\mathbf{w_s}$ is a vector to apply the prescribed displacements at the masses and $\mathbf{t}_a$ is a vector to select the masses on which the actuator forces act. The matrices can be written as:

$$\begin{gathered}\mathbf{M}=\begin{bmatrix}m_1&0&0\\0&m_2&0\\0&0&m_3\end{bmatrix}\qquad\mathbf{C}=\begin{bmatrix}c_1&0&0\\0&c_2&0\\0&0&0\end{bmatrix},\\ \mathbf{K}=\begin{bmatrix}k_1+k_3&0&-k_3\\0&k_2+k_4&-k_4\\-k_3&-k_4&k_3+k_4+k_5\end{bmatrix},\\ \mathbf{w}_s=\begin{Bmatrix}k_1+\mathrm{j}\omega c_1\\k_2+\mathrm{j}\omega c_2\\0\end{Bmatrix}\qquad\mathbf{t}_a=\begin{Bmatrix}1\\0\\0\end{Bmatrix}.\end{gathered} \tag{2.7}$$

The response of mass m_3 is considered as a measure for the receiver response. The actuator force can be determined in such a way that the displacement of mass m_3 is reduced to zero, but the displacements of the other two masses are not zero. This means that total isolation is not achieved. It is also possible to minimize the response of more than one mass. For this reason it is useful to write the dynamics of the model (see equations (2.5)) in terms of transfer functions:

$$\mathbf{x}=\mathbf{h}_p w+\mathbf{h}_s f_a, \tag{2.8}$$

where $\mathbf{x}$ is a vector denoting the displacements of the three masses, $\mathbf{h}_p$ is a vector containing the transfers from the disturbance w to the displacements of the three masses (the so-called *primary transfer* or *primary path*) and $\mathbf{h}_s$ is a vector containing the transfers from the actuator force f_a to the displacements of the three masses (the so-called *secondary transfer* or *secondary path*). The transfers can be determined with equations (2.6) and (2.7) according to:

$$\mathbf{h}_p=\left(-\omega^2\mathbf{M}+\mathrm{j}\omega\mathbf{C}+\mathbf{K}\right)^{-1}\cdot\mathbf{w}_s, \tag{2.9}$$

$$\mathbf{h}_s=\left(-\omega^2\mathbf{M}+\mathrm{j}\omega\mathbf{C}+\mathbf{K}\right)^{-1}\cdot\mathbf{t}_a. \tag{2.10}$$

Now it is possible to define a vector with the displacements of the masses that are candidates for minimization, the so-called sensor set response $\mathbf{x}_s$. The response at the sensors in terms of harmonic transfer functions is:

$$\mathbf{x}_s=\mathbf{h}_{ps}w+\mathbf{h}_{ss}f_a, \tag{2.11}$$

where $\mathbf{h}_{ps}$ is the transfer from the disturbance displacement to the sensor displacements and $\mathbf{h}_{ss}$ is the transfer from the actuator force to the sensor displacements. It is now convenient to write the response as a Hermitian quadratic error criterion, see section 2.6.1 for more details. The quadratic cost function is written as:

$$J = \mathbf{x}_s^{\mathrm{H}} \cdot \mathbf{x}_s, \tag{2.12}$$

where J is the quadratic error sensor response or cost function in terms of the unknown actuator force. Note that $\mathbf{x}_s^{\mathrm{H}}$ denotes the complex conjugate transpose of $\mathbf{x}_s$. The optimum actuator force that minimizes the cost function J is consequently calculated by:

$$f_a^{opt} = -\left(\mathbf{h}_{ss}^{\mathrm{H}} \cdot \mathbf{h}_{ss}\right)^{-1} \cdot \left(\mathbf{h}_{ss}^{\mathrm{H}} \cdot \mathbf{h}_{ps} w\right). \tag{2.13}$$

The total response of the three-degrees-of-freedom model can be calculated with the optimal actuator force using equation (2.8). When the actuator force is determined in such a way that the displacement of mass m_1 is minimized, no perfect isolation occurs. The displacement of mass m_1 is perfectly reduced but the displacements of the other masses are not reduced. This is shown in Figure 2.4 where the transmissibility of mass m_3 is plotted. It is seen that the mass m_3 still vibrates with practically no reduction. Also, when both the displacements of masses m_1 and m_2 are minimized, no total isolation of the receiver structure occurs. In total two structural transmission paths transmit energy from the source to the receiver structure, which cannot be totally isolated with just one actuator. Total isolation is only obtained when an extra actuator is placed in the transmission path with mass m_2.

2.4 Dynamics of complex structures

The discrete models that have been described in the previous section are not suited for the applications of hybrid isolation that are considered in this work. For that reason a general model is introduced to determine the dynamic structural behavior of a hybrid isolation system with a multi-point and multi-directional mounting system. After this presentation, a reduced model is described consisting of a receiver structure and (a part of) the mounting system only. The latter model is suited for analysis of the influence of different actuator and sensor configurations on the behavior of the receiver structure.

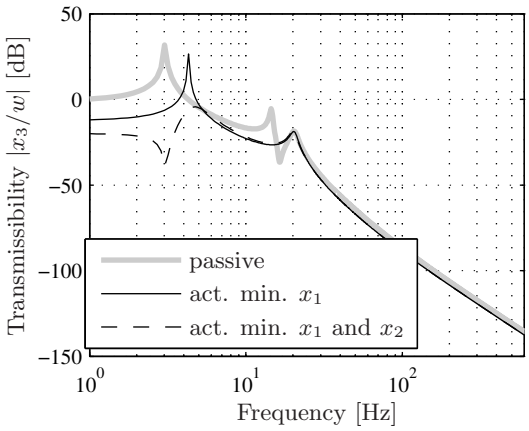

Figure 2.4: Transmissibility of mass m_3 for the three-dimensional simple hybrid isolation system.

2.4.1 Frequency Response Functions (FRF)

Generally speaking, the relation between the harmonic forces and velocities at point locations of the structure are described by steady-state Frequency Response Functions (FRFs). The FRFs describe the response at different locations of the structure due to sinusoidal (or harmonic) excitation forces. There are several ways to describe these functions, for example with the *mechanical impedance* [93]:

$$Z = \frac{f}{v}, \tag{2.14}$$

where Z is the impedance defined as the ratio of the force f divided by the velocity v. In practice the impedance is rarely measured directly. Instead, the *mobility* Y is often measured, being the velocity divided by the force [33, 93]:

$$Y = \frac{v}{f}. \tag{2.15}$$

Strictly speaking, also the mobility is rarely measured directly since it is common to use acceleration sensors for measurements, implying that the *accelerance* is measured. Mobility or admittance measurements are performed by exciting the structure with a known force resulting in a vibrating structure. Sensors (in most cases acceleration pickups or *accelerometers*) are attached to the structure to measure the response at different locations. During the measurement, the transfer between the accelerations at the sensor locations

and the force input is determined by means of an averaging procedure. When the measurements are performed for several excitations at different locations and/or at different DOFs, a transfer matrix can be composed. This frequency dependent matrix relates in fact the responses at different locations with the excitations at different (other) locations. For harmonic excitations, the *compliance*[2] can be determined by dividing the mobility by a factor $\mathrm{j}\omega$ respectively, when a complex notation is used. In the same way, the *dynamic stiffness*, which is defined as the ratio between the force divided by the displacement, can be determined by multiplying the impedance with a factor $\mathrm{j}\omega$. An overview of the different FRF matrices are shown in Table 2.2.

The different types of FRFs, like the impedance and the mobility description, are also used for the models considered in this thesis.

Response		**Force**	
receptance or compliance $\mathbf{H}$:	$\mathbf{x} = \mathbf{H} \cdot \mathbf{f}$	dynamic stiffness $\mathbf{K}$:	$\mathbf{f} = \mathbf{K} \cdot \mathbf{x}$
mobility or admittance $\mathbf{Y}$:	$\mathbf{v} = \mathbf{Y} \cdot \mathbf{f}$	impedance $\mathbf{Z}$:	$\mathbf{f} = \mathbf{Z} \cdot \mathbf{v}$
accelerance $\mathrm{j}\omega\mathbf{Y}$:	$\mathbf{a} = \mathrm{j}\omega\mathbf{Y} \cdot \mathbf{f}$	effective mass $\mathbf{M}$:	$\mathbf{f} = \mathbf{M} \cdot \mathbf{a}$

Table 2.2: Different types of FRF matrices that relate the displacement vector $\mathbf{x}$, velocity vector $\mathbf{v}$ and acceleration vector $\mathbf{a}$ to the excitation force vector $\mathbf{f}$ [93].

2.4.2 General multi-port model description

The dynamic port description for the dynamics of the whole hybrid isolation system has been adopted from Gardonio *et al.* [40, 41]. The source and receiver are connected by n mounts at the junctions as shown in Figure 2.5. The force vector $\mathbf{f}$ and velocity vector $\mathbf{v}$ at each junction consist of the following components for each frequency:

$$\mathbf{v} = \begin{Bmatrix} \dot{u} \\ \dot{v} \\ \dot{w} \\ \dot{\theta}_x \\ \dot{\theta}_y \\ \dot{\theta}_z \end{Bmatrix} \qquad \mathbf{f} = \begin{Bmatrix} f_x \\ f_y \\ f_z \\ m_x \\ m_y \\ m_z \end{Bmatrix}, \tag{2.16}$$

[2]The compliance is also known as the dynamic flexibility or receptance and defined as the ratio of the displacement divided by the force.

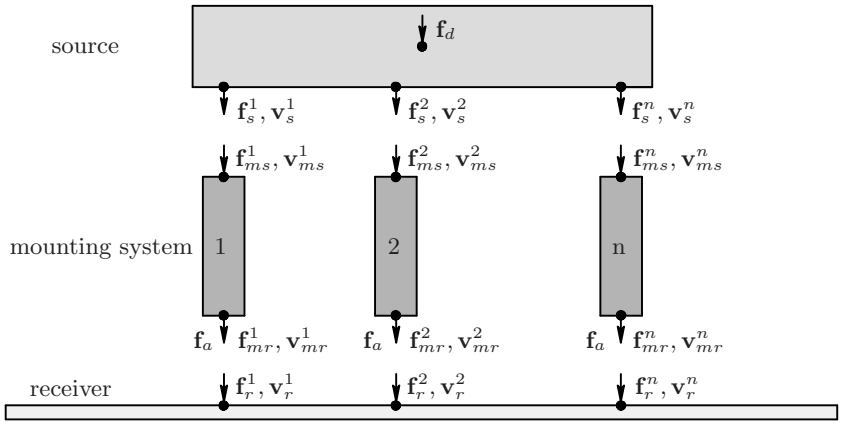

Figure 2.5: General model of a hybrid isolation system.

where u, v, w are the complex displacements in x, y and z direction respectively, θ_x, θ_y, θ_z are the angular displacements around the $x-$, $y-$ and $z-$ axes, f_x, f_y and f_z are the complex forces in x, y and z direction respectively and m_x, m_y and m_z are the complex moments around the $x-$, $y-$ and $z-$ axes. The dot symbol $\dot{(\,)}$ indicates the time derivative.

The velocity vectors and force vectors for all the connection points of the mounts can be combined in single vectors for each subsystem. This yields for the velocities and the forces at the source component:

$$\mathbf{v}_s = \begin{Bmatrix} \mathbf{v}_s^1 \\ \mathbf{v}_s^2 \\ \vdots \\ \mathbf{v}_s^n \end{Bmatrix} \qquad \mathbf{f}_s = \begin{Bmatrix} \mathbf{f}_s^1 \\ \mathbf{f}_s^2 \\ \vdots \\ \mathbf{f}_s^n \end{Bmatrix}, \tag{2.17}$$

for the mounts:

$$\mathbf{v}_m = \begin{Bmatrix} \mathbf{v}_{ms} \\ \mathbf{v}_{mr} \end{Bmatrix} = \begin{Bmatrix} \mathbf{v}_{ms}^1 \\ \mathbf{v}_{ms}^2 \\ \vdots \\ \mathbf{v}_{ms}^n \\ \mathbf{v}_{mr}^1 \\ \mathbf{v}_{mr}^2 \\ \vdots \\ \mathbf{v}_{mr}^n \end{Bmatrix} \qquad \mathbf{f}_m = \begin{Bmatrix} \mathbf{f}_{ms} \\ \mathbf{f}_{mr} \end{Bmatrix} = \begin{Bmatrix} \mathbf{f}_{ms}^1 \\ \mathbf{f}_{ms}^2 \\ \vdots \\ \mathbf{f}_{ms}^n \\ \mathbf{f}_{mr}^1 \\ \mathbf{f}_{mr}^2 \\ \vdots \\ \mathbf{f}_{mr}^n \end{Bmatrix}, \tag{2.18}$$

and for the receiver structure:

$$\mathbf{v}_r = \begin{Bmatrix} \mathbf{v}_r^1 \\ \mathbf{v}_r^2 \\ \vdots \\ \mathbf{v}_r^n \end{Bmatrix} \qquad \mathbf{f}_r = \begin{Bmatrix} \mathbf{f}_r^1 \\ \mathbf{f}_r^2 \\ \vdots \\ \mathbf{f}_r^n \end{Bmatrix}. \tag{2.19}$$

The vibration transmission of the isolation system is determined by the force and velocity vectors at the junctions of the different subsystems. The dynamics of each of the three subsystems are modeled using an impedance or mobility matrix approach [93]. The source and receiver are described by a mobility approach, so the relation between the velocities and the forces can be written in the form:

$$\mathbf{v}_s = \mathbf{Y}_{ss} \cdot \mathbf{f}_s + \mathbf{Y}_{sd} \cdot \mathbf{f}_d, \tag{2.20}$$

where $\mathbf{f}_d$ is the disturbance force vector acting on the source and $\mathbf{Y}_{ss}$ and $\mathbf{Y}_{sd}$ are the mobility matrices of the source. The dynamics of the receiver structure are described in the same way according to:

$$\mathbf{v}_r = \mathbf{Y}_r \cdot \mathbf{f}_r. \tag{2.21}$$

The dynamics of the mounts are modeled using an impedance matrix approach:

$$\begin{Bmatrix} \mathbf{f}_{ms} \\ \mathbf{f}_{mr} \end{Bmatrix} = \begin{bmatrix} \mathbf{Z}_{ss} & \mathbf{Z}_{sr} \\ \mathbf{Z}_{rs} & \mathbf{Z}_{rr} \end{bmatrix} \cdot \begin{Bmatrix} \mathbf{v}_{ms} \\ \mathbf{v}_{mr} \end{Bmatrix} + \begin{bmatrix} \mathbf{T}_{as} \\ \mathbf{T}_{ar} \end{bmatrix} \cdot \mathbf{f}_a, \tag{2.22}$$

where $\mathbf{Z}_{ss}$ and $\mathbf{Z}_{rr}$ are the driving point impedance matrices of the mounting system at the source and receiver side respectively, $\mathbf{Z}_{sr}$ and $\mathbf{Z}_{rs}$ are the transfer impedance matrices of the mounting system. $\mathbf{T}_{as}$ and $\mathbf{T}_{ar}$ are the actuator transformation matrices of the mounting system at the source side and receiver side respectively, which indicate the DOFs that are actuated at the bottom and top of the mounts and $\mathbf{f}_a$ is the vector with actuator forces. The coordinate systems chosen to derive the mobility or impedance matrices may differ from the global coordinate system of the whole hybrid isolation system. This is taken into account using a transformation matrix for each component:

$$\mathbf{f}_s^g = \mathbf{T}_s \cdot \mathbf{f}_s \qquad \mathbf{v}_s^g = \mathbf{T}_s \cdot \mathbf{v}_s, \tag{2.23a}$$

$$\mathbf{f}_{ms}^g = \mathbf{T}_m \cdot \mathbf{f}_{ms} \qquad \mathbf{v}_{ms}^g = \mathbf{T}_m \cdot \mathbf{v}_{ms}, \tag{2.23b}$$

$$\mathbf{f}_{mr}^g = \mathbf{T}_m \cdot \mathbf{f}_{mr} \qquad \mathbf{v}_{mr}^g = \mathbf{T}_m \cdot \mathbf{v}_{mr}, \tag{2.23c}$$

$$\mathbf{f}_r^g = \mathbf{T}_r \cdot \mathbf{f}_r \qquad \mathbf{v}_r^g = \mathbf{T}_r \cdot \mathbf{v}_r, \tag{2.23d}$$

where superscript $(.)^g$ indicates the forces and velocities with respect to the global coordinate system and $\mathbf{T}_s$, $\mathbf{T}_m$ and $\mathbf{T}_r$ are the transformation matrices from the local coordinate system of respectively the source, mounts and receiver to the global coordinate system. The components are coupled with each other by demanding continuity for the velocity vectors and equilibrium for the force vectors at the junctions:

$$\mathbf{f}_{ms}^g = -\mathbf{f}_s^g \qquad \mathbf{v}_{ms}^g = \mathbf{v}_s^g, \tag{2.24a}$$

$$\mathbf{f}_{mr}^g = -\mathbf{f}_r^g \qquad \mathbf{v}_{mr}^g = \mathbf{v}_r^g. \tag{2.24b}$$

Using equations (2.20) till (2.24), a total system of equations can be composed to solve the velocities and forces at all junctions for each frequency according to:

$$\begin{bmatrix} \mathbf{I} & \mathbf{0} & -\mathbf{T}_s \cdot \mathbf{Y}_{ss} \cdot \mathbf{T}_s^{-1} & \mathbf{0} \\ \mathbf{0} & \mathbf{I} & \mathbf{0} & -\mathbf{T}_r \cdot \mathbf{Y}_r \cdot \mathbf{T}_r^{-1} \\ \mathbf{T}_m \cdot \mathbf{Z}_{ss} \cdot \mathbf{T}_m^{-1} & \mathbf{T}_m \cdot \mathbf{Z}_{sr} \cdot \mathbf{T}_m^{-1} & \mathbf{I} & \mathbf{0} \\ \mathbf{T}_m \cdot \mathbf{Z}_{rs} \cdot \mathbf{T}_m^{-1} & \mathbf{T}_m \cdot \mathbf{Z}_{rr} \cdot \mathbf{T}_m^{-1} & \mathbf{0} & \mathbf{I} \end{bmatrix} \cdot \begin{Bmatrix} \mathbf{v}_s^g \\ \mathbf{v}_r^g \\ \mathbf{f}_s^g \\ \mathbf{f}_r^g \end{Bmatrix} = \begin{bmatrix} \mathbf{T}_s \cdot \mathbf{Y}_{sd} \\ \mathbf{0} \\ \mathbf{0} \\ \mathbf{0} \end{bmatrix} \cdot \mathbf{f}_d + \begin{bmatrix} \mathbf{0} \\ \mathbf{0} \\ -\mathbf{T}_m \cdot \mathbf{T}_{as} \\ -\mathbf{T}_m \cdot \mathbf{T}_{ar} \end{bmatrix} \cdot \mathbf{f}_a. \tag{2.25}$$

Solving this equation by inversion of the left-hand side matrix results in:

$$\begin{Bmatrix} \mathbf{v}_s^g \\ \mathbf{v}_r^g \\ \mathbf{f}_s^g \\ \mathbf{f}_r^g \end{Bmatrix} = \mathbf{H}_p^{fv} \cdot \mathbf{f}_d + \mathbf{H}_s^{fv} \cdot \mathbf{f}_a, \tag{2.26}$$

where $\mathbf{H}_p^{fv}$ is the primary transfer matrix which represents the frequency response functions of the disturbance force to the velocities and forces at the junctions of the source and receiver structure and $\mathbf{H}_s^{fv}$ is the secondary transfer matrix which represents the frequency response functions of the actuator forces to the velocities and forces at the junctions. From this point the superscript $(.)^g$ will be omitted and the velocity and force vectors are considered in the global coordinate system only. The results of equation (2.26) can be split into:

$$\mathbf{f}_r = \mathbf{H}_p^{fr} \cdot \mathbf{f}_d + \mathbf{H}_s^{fr} \cdot \mathbf{f}_a, \tag{2.27a}$$

$$\mathbf{f}_s = \mathbf{H}_p^{fs} \cdot \mathbf{f}_d + \mathbf{H}_s^{fs} \cdot \mathbf{f}_a, \tag{2.27b}$$

$$\mathbf{v}_r = \mathbf{H}_p^{vr} \cdot \mathbf{f}_d + \mathbf{H}_s^{vr} \cdot \mathbf{f}_a, \tag{2.27c}$$

$$\mathbf{v}_s = \mathbf{H}_p^{vs} \cdot \mathbf{f}_d + \mathbf{H}_s^{vs} \cdot \mathbf{f}_a. \tag{2.27d}$$

This model description is used in chapter 3 to analyze a simple analytical model of a complete hybrid isolation system.

2.4.3 Reduced model: receiver structure

A disadvantage of the hybrid isolation model considered in the previous subsection is that a representative model of the source has to be defined. In the literature on this subject, the source is often modeled as a rigid mass (see also Table 2.1). This is certainly not a realistic model for the behavior of for example a ship engine or gearbox. The behavior of that type of source is quite complex, especially in the higher frequency region, due to the behavior of the internal mechanisms and structural resonances. The focus in this work is on the behavior of the receiver structure. The hybrid mounting system must reduce the vibrational or acoustic response of the receiver structure. Different actuator and sensor strategies are investigated for a complex receiver structure and for this purpose the source component in combination with the mounting system can be omitted and a reduced model can be used.

The source is normally mounted on a passive isolation system to reduce the interior noise and vibration levels in the high frequency region. This passive mounting support consists in most cases of relatively soft rubber mounts on a raft or stiff support. The passive isolation mechanism is based on the created impedance mismatch between the source and receiver structure. For this reason, the source in combination with the mounting system behaves as a 'force source' on the relatively stiff raft and receiver combination [135]. This means that the excitation can be described by a force vector acting on the relatively stiff receiver structure and the source and the mounting system is omitted in the further analysis. This is schematically shown in Figure 2.6, where only the receiver structure is shown with a stiff foundation as the part of this receiver structure. The disturbance force vector $\mathbf{f}_d$ is assumed to act on top of the foundation of the receiver structure. The remaining components are similar to the previously described model. The dynamics of the foundation part are again described by the impedance matrix formulation, in a similar way as described by equation (2.22):

$$\begin{Bmatrix} \mathbf{f}_d \\ \mathbf{f}_{mr} \end{Bmatrix} = \begin{bmatrix} \mathbf{Z}_{ss} & \mathbf{Z}_{sr} \\ \mathbf{Z}_{rs} & \mathbf{Z}_{rr} \end{bmatrix} \cdot \begin{Bmatrix} \mathbf{v}_{ms} \\ \mathbf{v}_{mr} \end{Bmatrix} + \begin{bmatrix} \mathbf{T}_{as} \\ \mathbf{T}_{ar} \end{bmatrix} \cdot \mathbf{f}_a. \tag{2.28}$$

The dynamics of the receiver structure at the junction locations are also determined by a local mobility matrix approach:

$$\mathbf{v}_r = \mathbf{Y}_r \cdot \mathbf{f}_r. \tag{2.29}$$

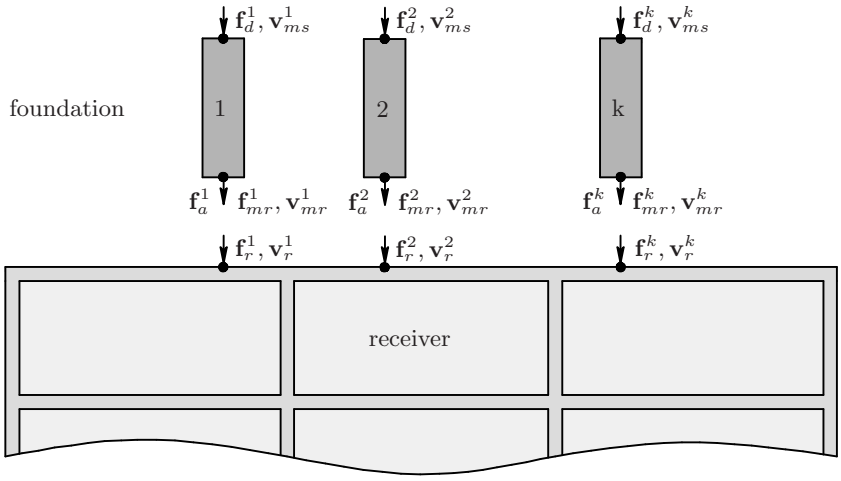

Figure 2.6: Model of a hybrid isolation system consisting of the stiff part of the mounting system and a (complex) receiver structure.

Further, the transformation matrices of the set of equations (2.23) are used to relate the forces and velocities described in the local coordinate system to the global coordinate system. However, the coordinate system used to describe the dynamics of the receiver structure is considered as the global coordinate system. This means that $\mathbf{T}_r$ is equal to the identity matrix and that only a transformation matrix $\mathbf{T}_m$ is needed to transform the variables related with the foundation from its local coordinate system to the global coordinate system. The latter transformation matrix $\mathbf{T}_m$ is now denoted by $\mathbf{T}$. With the use of the continuity and equilibrium conditions shown in equations (2.24a) and (2.24b) the forces and velocities at the junctions can now be calculated according to:

$$\begin{aligned}\mathbf{v}_{ms} = &\left(\mathbf{Z}_{ss}^{-1} + \mathbf{Z}_{ss}^{-1} \cdot \mathbf{Z}_{sr} \cdot \mathbf{T}^{-1} \cdot \mathbf{Y}_r \cdot \mathbf{T} \cdot \mathbf{H}_1\right) \cdot \mathbf{f}_d \\ &+ \left(\mathbf{Z}_{ss}^{-1} \cdot \mathbf{Z}_{sr} \cdot \mathbf{T}^{-1} \cdot \mathbf{Y}_r \cdot \mathbf{T} \cdot \mathbf{H}_2\right) \cdot \mathbf{f}_a, \qquad (2.30a)\\ \mathbf{v}_{mr} = &-\mathbf{T}^{-1} \cdot \mathbf{Y}_r \cdot \mathbf{T} \cdot \mathbf{H}_1 \cdot \mathbf{f}_d - \mathbf{T}^{-1} \cdot \mathbf{Y}_r \cdot \mathbf{T} \cdot \mathbf{H}_2 \cdot \mathbf{f}_a, \qquad (2.30b)\\ \mathbf{v}_r = &-\mathbf{Y}_r \cdot \mathbf{T} \cdot \mathbf{H}_1 \cdot \mathbf{f}_d - \mathbf{Y}_r \cdot \mathbf{T} \cdot \mathbf{H}_2 \cdot \mathbf{f}_a, \qquad (2.30c)\\ \mathbf{f}_{mr} = &\mathbf{H}_1 \cdot \mathbf{f}_d + \mathbf{H}_2 \cdot \mathbf{f}_a, \qquad (2.30d)\\ \mathbf{f}_r = &-\mathbf{T} \cdot \mathbf{H}_1 \cdot \mathbf{f}_d - \mathbf{T} \cdot \mathbf{H}_2 \cdot \mathbf{f}_a, \qquad (2.30e)\end{aligned}$$

where:

$$\mathbf{H}_1 = \left[\mathbf{I} - \left(\mathbf{Z}_{rs} \cdot \mathbf{Z}_{ss}^{-1} \cdot \mathbf{Z}_{sr} - \mathbf{Z}_{rr}\right) \cdot \mathbf{T}^{-1} \cdot \mathbf{Y}_r \cdot \mathbf{T}\right]^{-1} \cdot \mathbf{Z}_{rs} \cdot \mathbf{Z}_{ss}^{-1}, \tag{2.31a}$$

$$\mathbf{H}_2 = \left[\mathbf{I} - \left(\mathbf{Z}_{rs} \cdot \mathbf{Z}_{ss}^{-1} \cdot \mathbf{Z}_{sr} - \mathbf{Z}_{rr}\right) \cdot \mathbf{T}^{-1} \cdot \mathbf{Y}_r \cdot \mathbf{T}\right]^{-1} \cdot \mathbf{T}_a. \tag{2.31b}$$

These equations can be rewritten in similar terms as for the model description in the previous chapter:

$$\mathbf{f}_r = \mathbf{H}_p^{fr} \cdot \mathbf{f}_d + \mathbf{H}_s^{fr} \cdot \mathbf{f}_a, \tag{2.32a}$$

$$\mathbf{v}_r = \mathbf{H}_p^{vr} \cdot \mathbf{f}_d + \mathbf{H}_s^{vr} \cdot \mathbf{f}_a. \tag{2.32b}$$

The dynamics at the junctions of the isolation system are now described as function of the disturbance forces and actuator forces.

This model is used in chapter 4 to analyze an isolation system with a complex dynamic behavior. The *Finite Element Method* is used to determine the mobility matrix $\mathbf{Y}_r$ as shown in equation (2.29).

2.5 Acoustic models

The structural vibrations of the receiver structure are in many cases not the real problem. The vibrations are transmitted to the acoustic medium surrounding the receiver structure in the form of pressure perturbations which are finally experienced as noise. For the considered applications of hybrid isolation, the acoustic noise is finally required to be reduced in a hybrid way. For this reason, models are introduced to determine the acoustic response with the structural response of the receiver structure. These models will be used to investigate acoustic error sensor criteria for hybrid isolation. In this section two types of simplified acoustic models are considered: sound radiation into the free field and sound radiation into an enclosure as a simplified representation of an accommodation. The interaction between the structure and the surrounding environment is assumed to be small. For this reason the influence of the medium on the structure can be neglected and a one-way coupling of the structure with the surrounding medium is justified.

The acoustic wave propagation through a homogeneous fluid such as air is described by the wave equation [34, 35, 89]:

$$\nabla^2 p(\vec{r}) - \frac{1}{c_0^2} \frac{\partial^2 p(\vec{r})}{\partial t^2} = -\frac{\partial^2 m}{\partial t^2}, \tag{2.33}$$

where p is the acoustic pressure at location $\vec{r}$ (the pressure perturbation upon the steady state pressure e.g. the atmospheric pressure) and c_0 is the velocity

of sound in the medium. The $\vec{(.)}$ symbol indicates a geometric vector. The term on the right-hand side can be considered as a source term: m is the mass per unit volume. The term $\frac{\partial^2 m}{\partial t^2}$ can be written as $\rho_0 \frac{\partial q}{\partial t}$ where q is the volume velocity per unit volume and the total term is known as the 'monopole source strength'. In the case of a harmonic time dependence, this equation reduces to the inhomogeneous Helmholtz differential equation:

$$\nabla^2 p(\vec{r}) + k^2 p(\vec{r}) = -\mathrm{j}\rho_0 \omega q(\vec{r}_0), \tag{2.34}$$

where $k = \omega/c_0$ is the acoustic wave number, ρ_0 is the density of the medium and $\vec{r}_0$ is the location of the monopole source. When the Helmholtz differential equation is solved for a pulsating point source radiating into free space (a so-called monopole), the solution can be written as:

$$p(\vec{r}) = \mathrm{j}\rho_0 \omega q(\vec{r}_0) \frac{\mathrm{e}^{-\mathrm{j}kR}}{4\pi R}, \tag{2.35}$$

where $R = |\vec{r} - \vec{r}_0|$ is the distance between the pressure at location $\vec{r}$ and the source at location $\vec{r}_0$. Two terms are distinguished in the solution for the pressure: the monopole source strength and the so-called free space Green's function, which is defined as:

$$g(\vec{r}|\vec{r}_0) = \frac{\mathrm{e}^{-\mathrm{j}kR}}{4\pi R}. \tag{2.36}$$

The Green's function is thus in fact the solution of the Helmholtz equation for a unit harmonic point source at $\vec{r}_0$:

$$\nabla^2 g(\vec{r}|\vec{r}_0) + k^2 g(\vec{r}|\vec{r}_0) = -\delta(\vec{r} - \vec{r}_0). \tag{2.37}$$

With the help of the Helmholtz differential equation and the expression for the free-space Green's function, a formulation of the pressure as a consequence of volume sources in the considered volume and as a consequence of a normal velocity distribution $v_n(\vec{r}_0)$ on the closed surface of a vibrating structure can be derived [35, 89]:

$$p(\vec{r}) = \int_V \mathrm{j}\omega\rho_0 q(\vec{r}_0)\, g(\vec{r}|\vec{r}_0)\, \mathrm{d}V + \int_S \left[\mathrm{j}\omega\rho_0 v_n(\vec{r}_0)\, g(\vec{r}|\vec{r}_0) + p(\vec{r}_0) \frac{\partial}{\partial n} g(\vec{r}|\vec{r}_0)\right] \mathrm{d}S, \tag{2.38}$$

where $p(\vec{r}_0)$ is the pressure distribution on the boundary surface. This equation is called the Kirchhoff-Helmholtz integral equation and forms the basis for numerical evaluation of sound radiation of structures with the help of the *Boundary Element Method* (BEM) [137]. The volume integrand represents the contribution to the pressure due to the sources that are present in the considered volume of the acoustic medium. Two terms are distinguished in the surface integrand: the first (monopole) term represents the pressure contribution due to the free field radiation caused by the normal velocity distribution. The second (dipole) term represents the influence of the presence of the sound radiating body in obstructing the free passage of sound.

2.5.1 Radiated sound power

The sound pressure is a quantity that depends on the location and distance from the vibrating structure. Another more general measure to quantify the radiated sound is the radiated sound power which is defined as:

$$\bar{W} = \int_S \bar{I}_n(\vec{r}_0)\,\mathrm{d}S, \tag{2.39}$$

where $\bar{W}$ is the time averaged radiated sound power and $\bar{I}_n$ is the time averaged sound intensity in the direction normal to the surface S which is calculated by:

$$\bar{I}_n(\vec{r}_0) = \frac{1}{2}\Re\left(p(\vec{r}_0)\,v_n^*(\vec{r}_0)\right), \tag{2.40}$$

where $p(\vec{r}_0)$ is the pressure distribution at the boundary surface and * denotes the complex conjugate. The sound power radiated by the vibrating surface can now be expressed as:

$$\bar{W} = \frac{1}{2}\,\Re\int_S p(\vec{r}_0)\,v_n^*(\vec{r}_0)\,\mathrm{d}S, \tag{2.41}$$

where $\Re(.)$ denotes the real part. The sound pressure is often specified in decibels because this scale is a better representation of the sensitivity of the human ear. For this reason the *sound power level* is often used, defined as:

$$L_w = 10\log\left(\frac{\bar{W}}{\bar{W}_{\mathrm{ref}}}\right), \tag{2.42}$$

where $\bar{W}_{\mathrm{ref}}$ is the reference quantity equal to 10^{-12} W.

2.5.2 Sound radiation of a baffled flat plate

The Kirchhoff-Helmholtz integral can be simplified considerably when the vibrating structure is a flat plate situated in a baffle. The baffle is an infinite rigid surface around the plate and prevents the sound field on one side of the surface affecting the sound field on the other side of the plate.

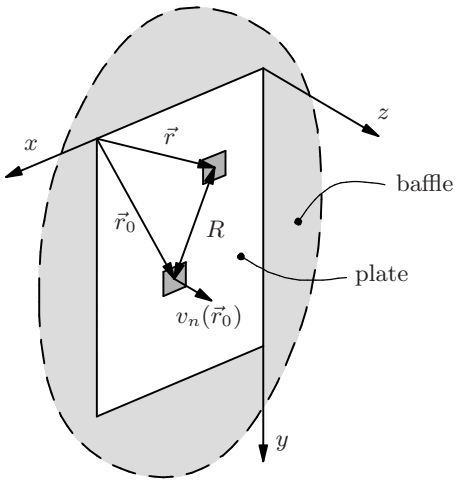

Figure 2.7: Schematic picture with a geometric interpretation used for the evaluation of the Rayleigh integral for free field sound radiation.

Considering the Kirchhoff-Helmholtz integral equation (2.38), only the first term has to be taken into account because only radiation into free space is considered. However, the vibrating sources are now considered to lie on a rigid surface (the surface of the plate is reflective), so the surface Green's function equals twice the free space Green's function. The resulting expression is known as Rayleigh's second integral and relates the pressure to the normal velocity associated with an elementary radiator (monopole) at a point on the surface $\vec{r}_0$ with the pressure at location $\vec{r}$ in the free space as shown in Figure 2.7 according to:

$$p(\vec{r}) = \int_S \mathrm{j}\omega\rho_0 v_n(\vec{r}_0)\frac{\mathrm{e}^{-\mathrm{j}kR}}{2\pi R}\,\mathrm{d}S. \tag{2.43}$$

This equation is numerically implemented by discretization of the considered plate structure into nodes and elements, e.g. by making use of the boundary part of the finite element discretization of (a part of) the structure. When the considered structure is divided into N elements with a constant normal

velocity per element, equation (2.43) can be rewritten as:

$$p(\vec{r}) = \mathrm{j}\omega\rho_0 \sum_{j=1}^{N} \frac{\mathrm{e}^{-\mathrm{j}kR}}{2\pi R} S_j v_{n_j}, \tag{2.44}$$

where S_j is the area of element j and v_{n_j} is the normal velocity of element j. For multiple field points, equation (2.44) is evaluated for each field point for a unit velocity, and can be rewritten in matrix vector terms according to:

$$\mathbf{p}_f = \mathbf{Z}_f \cdot \mathbf{v}_n, \tag{2.45}$$

where $\mathbf{p}_f$ is the vector with pressures evaluated at the field points and $\mathbf{Z}_f$ is the acoustic impedance matrix related with the free field radiation. The radiated sound power is calculated by integration of the sound intensity over the boundary surface of the vibrating object as shown in equation (2.41):

$$\bar{W} = \frac{1}{2}\Re\left(\mathrm{j}\omega\rho_0 \sum_{m=1}^{N} v_{n_m} S_m \sum_{j=1}^{N} \frac{\mathrm{e}^{-\mathrm{j}kR}}{2\pi R} v_{n_j} S_j\right). \tag{2.46}$$

The matrix formulation of this equation is:

$$\bar{W} = \mathbf{v}_n^{\mathrm{H}} \cdot \mathbf{R} \cdot \mathbf{v}_n, \tag{2.47}$$

where $\mathbf{R}$ is the *radiation resistance matrix*:

$$\mathbf{R} = \frac{\omega^2\rho_0}{4\pi c_0} \begin{bmatrix} S_1S_1 & S_1S_2\frac{\sin(kR_{12})}{kR_{12}} & \cdots & S_1S_N\frac{\sin(kR_{1N})}{kR_{1N}} \\ S_2S_1\frac{\sin(kR_{21})}{kR_{21}} & S_2S_2 & & \vdots \\ \vdots & & \ddots & \vdots \\ S_NS_1\frac{\sin(kR_{N1})}{kR_{N1}} & \cdots & \cdots & S_NS_N \end{bmatrix}, \tag{2.48}$$

where R_{jk} is the distance between the elements j and k. The radiation matrix $\mathbf{R}$ is symmetric due to reciprocity and is positive-definite ($\mathbf{v}_n^{\mathrm{H}} \cdot \mathbf{R} \cdot \mathbf{v}_n > 0, \forall\, \mathbf{v}_n \neq \mathbf{0}$) because the radiated sound power is always larger than zero for a nonzero normal velocity vector.

2.5.3 Sound radiation into an enclosure

Besides sound radiation into the free field, the sound radiation into an enclosure is considered as a simplified model of the interior noise response in an accommodation. A schematic picture with a geometrical interpretation to

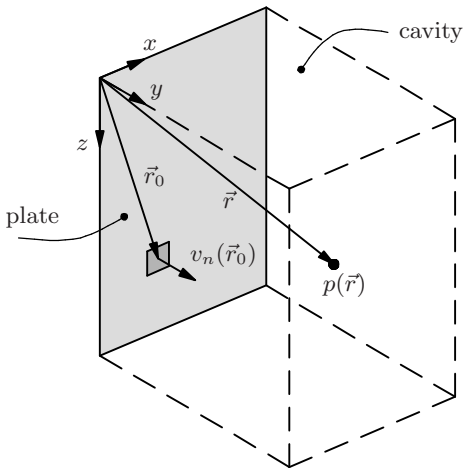

Figure 2.8: Schematic picture with a geometric interpretation for the sound radiation into an enclosure.

determine the sound radiation of a vibrating wall into an enclosure is shown in Figure 2.8. For this type of interior sound modeling, the acoustic response in the enclosure can be determined by a modal expansion of the acoustic modes or eigenfunctions of the enclosure with *rigid walls*. First a Green's function is considered, which by definition satisfies the following inhomogeneous Helmholtz equation:

$$\nabla^2 G(\vec{r}|\vec{r}_0) + k^2 G(\vec{r}|\vec{r}_0) = -\delta(\vec{r} - \vec{r}_0), \tag{2.49}$$

where $G(\vec{r}|\vec{r}_0)$ is a Green's function for a unit harmonic point source in the enclosure. For this reason a solution of the Green's function is sought in the form of an expansion of the rigid-wall eigenfunctions. These eigenfunctions, denoted by $\psi_n(\vec{r})$, satisfy the homogeneous form of the Helmholtz equation (2.34) in the volume V and also satisfy the rigid wall boundary conditions on the surface S [108]:

$$(\nabla^2 + k_n^2)\psi_n(\vec{r}) = 0 \quad \text{in V}, \qquad \nabla\psi_n(\vec{r}) \cdot \vec{n} = 0 \quad \text{on S}, \quad n = 1, 2, ... \tag{2.50}$$

where k_n is the n^{th} eigenvalue and equal to ω_n/c_0, $\psi_n(\vec{r})$ is the corresponding eigenfunction and $\vec{n}$ the outward-pointing normal to the boundary surface S of the enclosure. The Green's function can now be written as a summation of the rigid-wall eigenmodes according to:

$$G(\vec{r}|\vec{r}_0) = \sum_n q_n \psi_n(\vec{r}), \tag{2.51}$$

where q_n is the contribution or participation of each acoustic mode. Substitution of equation (2.51) into equation (2.49), multiplication with the eigenfunction ψ_m and integration over the volume V yields with making use of the principle of orthogonality:

$$q_n = \frac{\psi_n(\vec{r}_0)}{\Lambda_n(k_n^2 - k^2)}, \tag{2.52}$$

where $\Lambda_n = \int_V \psi_n^2(\vec{r})\,\mathrm{d}V$. The Green's function can subsequently be written as:

$$G(\vec{r}|\vec{r}_0) = \sum_n \frac{\psi_n(\vec{r}_0)\psi_n(\vec{r})}{\Lambda_n(k_n^2 - k^2)}. \tag{2.53}$$

The Kirchhoff-Helmholtz equation (2.38) relates the sound pressure at location $\vec{r}$ to the monopole source strength at location $\vec{r}_0$. Substitution of the expression for the Green's function (2.53) into the Kirchoff-Helmholtz equation yields:

$$p(\vec{r}) = j\omega\rho_0 \int_V q(\vec{r_0})G(\vec{r}|\vec{r_0})\,\mathrm{d}V - \int_S G(\vec{r}|\vec{r_0})\frac{\partial}{\partial n}p(\vec{r_0})\,\mathrm{d}S. \tag{2.54}$$

It is possible to prescribe a finite impedance condition at the boundary of the cavity:

$$\frac{\partial p}{\partial n} = \mathrm{j}k\frac{p(\vec{r}_s)}{z_n(\vec{r}_s)}. \tag{2.55}$$

The equation for the pressure response in a rigid-wall cavity with finite impedance boundary condition is:

$$p(\vec{r}) = \mathrm{j}\omega\rho_0 \int_V q(\vec{r}_0)G(\vec{r}|\vec{r}_0)\,\mathrm{d}V - \mathrm{j}k \int_S G(\vec{r}|\vec{r}_0)\frac{p(\vec{r}_s)}{z_n(\vec{r}_s)}\,\mathrm{d}S. \tag{2.56}$$

For a room with rigid walls, the sound pressure waves are completely reflected at the boundaries. For this reason, the influence of the wall-impedance in equation (2.56) can be omitted. With an ad hoc viscous modal damping η_n in the Green's function of equation (2.53) to take account of the dissipation of sound energy, the sound pressure is determined by:

$$p(\vec{r}) = \mathrm{j}\omega\rho_0 \int_V q(\vec{r}_0) \sum_n \frac{\psi_n(\vec{r}_0)\psi_n(\vec{r})}{\Lambda_n(k_n^2 + \mathrm{j}\eta_n k - k^2)}\,\mathrm{d}V. \tag{2.57}$$

When this equation is numerically implemented with the same discretization procedure as for the free field radiation, i.e. by assuming a set of vibrating

pistons to describe the wall vibrations represented by the normal velocity vector $\mathbf{v}_n$, the following impedance relation is derived:

$$\mathbf{p}_e = \mathbf{Z} \cdot \mathbf{v}_n, \tag{2.58}$$

where $\mathbf{p}_e$ is a vector with pressures evaluated at different locations in the enclosure and $\mathbf{Z}$ is the impedance matrix of the enclosure. The terms of the impedance matrix are determined in the following way:

$$Z_{ij} = \mathrm{j}\omega\rho_0 S_j \sum_n \frac{\psi_n(\vec{r}_{s_j})\psi_n(\vec{r}_i)}{\Lambda_n(k_n^2 + \mathrm{j}\eta_n k - k^2)}, \tag{2.59}$$

where S_j is the area of element j, $\psi_n(\vec{r}_{s_j})$ is cavity mode n evaluated at the position of piston j on the boundary of the cavity and $\psi_n(\vec{r}_i)$ is cavity mode n evaluated at field point i in the enclosure.

Numerical determination of the acoustic modes

For rectangular or cylindrical shaped enclosures, the acoustic modes and eigenfrequencies can be determined with the aid of analytical expressions [15]. However, for arbitrarily shaped enclosures the acoustic modes and eigenfrequencies have to be determined in a numerical way. The most suited method for this problem is the Finite Element Method. Another numerical method is the Boundary Element Method (BEM), but this method is more suited for the free field radiation problem. In this work the commercial finite element package Ansys was used to determine the acoustic modes.

Discretizing the homogenous form of equation (2.34) and applying Galerkin's weighted residual finite element procedure leads to the following finite element eigenvalue equation [82]:

$$\left(-\omega_n^2 \mathbf{M}_f + \mathbf{K}_f\right) \cdot \boldsymbol{\psi}_n = 0, \tag{2.60}$$

where $\mathbf{M}_f$ is the equivalent fluid mass matrix, $\mathbf{K}_f$ is the equivalent fluid stiffness matrix and $\boldsymbol{\psi}_n$ and ω_n are the mode shape vector (evaluated at the nodal points) and the natural angular eigenfrequency respectively. In Ansys only linear fluid elements are available to perform an acoustic analysis: a cubic eight-noded fluid element and a tetrahedral four-noded element. The mode shape vectors returned by Ansys can be normalized to the mass matrix or to unity. To determine the Green's function for the sound radiation into an enclosure as shown in equation (2.52), the modal volume Λ_n of each mode

shape must be determined. When the mode shape vectors are normalized to the equivalent fluid mass matrix, the following equation applies:

$$\hat{\boldsymbol{\psi}}_m^{\mathrm{T}} \cdot \mathbf{M}_f \cdot \hat{\boldsymbol{\psi}}_n = \delta_{mn}, \tag{2.61}$$

where $\hat{\boldsymbol{\psi}}_n$ is the n^{th} mode shape vector normalized to the fluid mass matrix. The mass matrix is defined as:

$$\mathbf{M}_f = \frac{1}{c_0^2} \int_V \mathbf{n} \cdot \mathbf{n}^{\mathrm{T}} \, \mathrm{d}V, \tag{2.62}$$

where $\mathbf{n}$ is the vector with linear shape functions for the acoustic element. When the mode shape vectors are normalized to unity ($\boldsymbol{\psi}_n$, meaning that the largest element has a unit magnitude) then by definition:

$$\boldsymbol{\psi}_n^{\mathrm{T}} \cdot \mathbf{M}_f \cdot \boldsymbol{\psi}_n = \frac{\Lambda_n}{c_0^2}, \tag{2.63}$$

where Λ_n is the modal volume of mode shape vector $\boldsymbol{\psi}_n$. Following the approach as presented by Ewins [33], the two mode shape vectors can be expressed as function of each other according to:

$$\hat{\boldsymbol{\psi}}_n = \frac{c_0}{\sqrt{\Lambda_n}} \boldsymbol{\psi}_n. \tag{2.64}$$

Hence, given the fact that the maximum element of $\boldsymbol{\psi}_n$ has magnitude one, the modal volume of the mode shape vector $\boldsymbol{\psi}_n$ becomes [19, 20]:

$$\Lambda_n = \frac{c_0^2}{\left(\max(\hat{\boldsymbol{\psi}}_n)\right)^2}. \tag{2.65}$$

Acoustic response of enclosures

A representative measure of the acoustic response in the cavity is defined by the time averaged acoustic potential energy E_p [123]:

$$E_p = \frac{1}{4\rho_0 c_0^2} \int_V |p(\vec{r})|^2 \, \mathrm{d}V. \tag{2.66}$$

Making use of equations (2.51) and (2.52), the pressure response in the cavity can be written in terms of the acoustic cavity modes and modal participations:

$$E_p = \frac{1}{4\rho_0 c_0^2} \sum_m \sum_n q_{mn}^* \int_V \psi_n(\vec{r})^* \psi_n(\vec{r}) \, \mathrm{d}V q_{mn}, \tag{2.67}$$

where m represents the index of the vibrating piston situated at the vibrating boundary of the enclosure, n is the index indicating the cavity mode number and q_{mn} the participation of mode n due to the source piston m. Making use of the definition for the modal volume and the vector notation results in:

$$E_p = \frac{1}{4\rho_0 c_0^2} \sum_n \mathbf{q}_n^{\mathrm{H}} \cdot \mathbf{q}_n \Lambda_n = \frac{1}{4\rho c_0^2} \mathbf{Q}^{\mathrm{H}} \cdot \mathbf{\Lambda} \cdot \mathbf{Q}, \tag{2.68}$$

where $\mathbf{q}_n$ is a vector with modal participations for all source pistons for mode number n, $\mathbf{Q}$ is a matrix with participations of the acoustic modes for all source pistons and modes and $\mathbf{\Lambda}$ is a diagonal matrix with the modal volumes of each mode.

Another, more straightforward measure is the sum of the squared pressures at the considered field points in the cavity:

$$J_p = \mathbf{p}^{\mathrm{H}} \cdot \mathbf{p}. \tag{2.69}$$

The pressure response in the cavity is often depicted as a sound pressure level (SPL) in dB, which is defined for a harmonic pressure amplitude vector $\mathbf{p}$ as:

$$\mathrm{SPL} = \frac{1}{N} 10 \log \left(\frac{\mathbf{p}_{\mathrm{rms}}^{\mathrm{H}} \cdot \mathbf{p}_{\mathrm{rms}}}{p_{\mathrm{ref}}^2} \right), \tag{2.70}$$

where p_{ref} is the reference pressure level for air with the value of $20 \cdot 10^{-6}$ Pa and $\mathbf{p}_{\mathrm{rms}}$ the root mean square value of the pressure amplitude vector $\mathbf{p}$ and N the number of pressure responses in the vector $\mathbf{p}_{\mathrm{rms}}$. The root mean square value of the pressure is defined as:

$$\mathbf{p}_{\mathrm{rms}} = \frac{\mathbf{p}}{\sqrt{2}}. \tag{2.71}$$

Example: sound radiation into a reverberant rectangular enclosure

The sound radiation into an enclosure is considered as a simplified model of the interior noise in an enclosure. To analyze the acoustic response of such a model in more detail, the derived equations are used to compute the acoustic response in a rectangular reverberant enclosure with one vibrating wall. This example has often been subject of study in the literature, see e.g. [71, 111, 123, 124]. The walls of the rectangular enclosure are assumed to reflect the acoustic waves completely. The rectangular top plate is assumed to be simply supported at its boundaries. In the case of a rectangular enclosure of dimensions $l_x \times l_y \times l_z$,

the eigenfunctions and eigenvalues are given by [15, 35]:

$$\psi_n(\vec{r}) = \cos\left(\frac{n_x \pi x}{l_x}\right) \cos\left(\frac{n_y \pi y}{l_y}\right) \cos\left(\frac{n_z \pi z}{l_z}\right), \tag{2.72a}$$

$$k_n = \left(\frac{\pi n_x}{l_x}\right)^2 + \left(\frac{\pi n_y}{l_y}\right)^2 + \left(\frac{\pi n_z}{l_z}\right)^2, \quad n_x, n_y, n_z = 0, 1, 2, ... \tag{2.72b}$$

Besides a modal expansion with the analytical expressions (2.72), the pressure response in the rectangular enclosure is also determined with a modal expansion of numerically determined cavity modes (FEM) and with a fully coupled harmonic finite element analysis. The main difference between the first two analyses and the third analysis is the coupling between the structure and the fluid domain. The modal expansion analyses assume only a one-way coupling. This means that the structural vibration excites the fluid domain, but not vice versa, i.e. the fluid response exerts no influence on the structural response. The fully coupled harmonic analysis takes this effect into account and thus determines a two-way coupled response. The structural dynamic response of the simply supported plate is determined with the help of an analytical model as will be explained in chapter 3 and appendix D. With the known dynamic response, the pressure response in the cavity can consequently be determined.

More details of this example are shown in Table 2.3. The top plate is excited by a unit force in the z-direction at location $(x, y) = (0.3, 0.4)$. For the modal expansion 1000 acoustic modes were taken into account. The total sound pressure level in the cavity is depicted as a function of the frequency in Figure 2.9 for the three methods. The pressure responses of the three models correspond quite well in the lower frequency range. At frequencies above 350 Hz the deviations in the pressure response become more pronounced because of the high modal density. A lot of system resonances occur and are distinguished by the peaks in the pressure responses. The resonances are caused by both resonances of the vibrating top plate (e.g. the (1,1)-mode[3] at 42 Hz, the (1,2)-mode at 93 Hz) and acoustic resonances in the cavity (e.g. (0,1,0)-mode at 144 Hz and the (0,1,2)-mode at 207 Hz). In Figure 2.10 the structural harmonic response of the top plate and the acoustic harmonic response are depicted at 168, 270 and 462 Hz respectively. The first considered harmonic response is at a frequency situated near the eigenfrequency of the $(2, 2)$ mode of the top plate, see Figure 2.10(a). This can clearly be seen from both the structural and acoustic response. The second considered harmonic response is near the (0,1,2) acoustic mode of the enclosure and is shown in Figure 2.10(b).

[3]The numbers indicate the number of half wavelengths in each direction. The (1,1) plate mode is thus the mode with one half wavelength in the x-direction and y-direction.

The third considered harmonic response is depicted in Figure 2.10(c) and this frequency is situated near the (4,2) mode of the vibrating top plate and the (1,3,0) acoustic mode of the cavity.

Component	Parameter	Value
Top plate	Dimensions ($l_x \times l_y \times h$)	$1.0 \times 1.20 \times 0.01$ m
	Mean density ρ	2700 kg/m^3
	Modulus of elasticity E	$71 \cdot 10^9$ N/m^2
Cavity	Dimensions ($l_x \times l_y \times l_z$)	$1.0 \times 1.20 \times 1.5$ m
	Mean density of air ρ_0	1.2 kg/m^3
	Velocity of sound in air c_0	344 m/s

Table 2.3: Parameters of the rectangular enclosure with vibrating top plate.

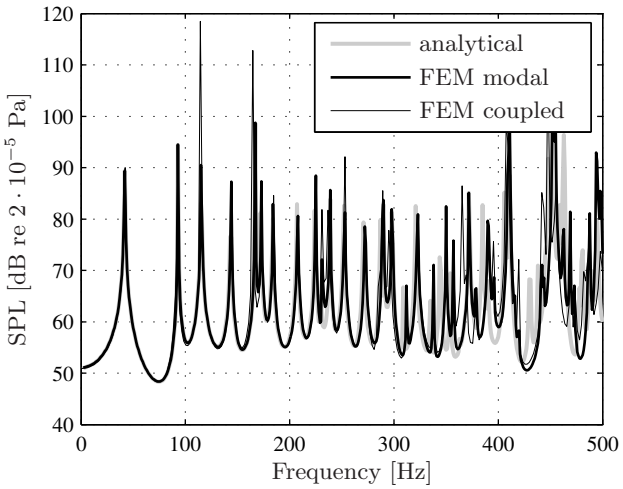

Figure 2.9: Total pressure response in a rectangular cavity with a vibrating simply supported top plate determined for with the uncoupled modal expansion.

2.5.4 Limitations of the acoustic models

The considered acoustic models have some limitations inherent to the modeling approach used. Considering the free field radiation, the assumption of a baffled

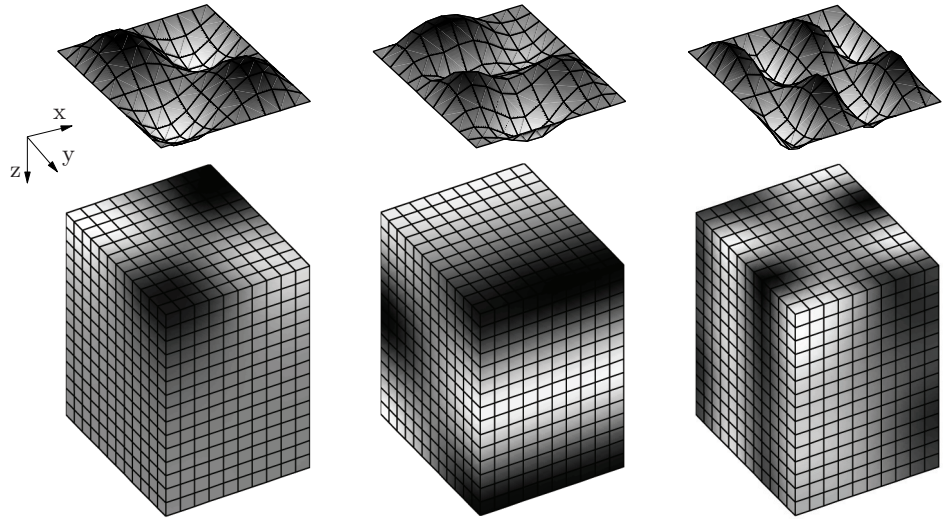

(a) 168 Hz (b) 270 Hz (c) 462 Hz

Figure 2.10: Pressure distribution in a rectangular enclosure due to a vibrating simply supported top plate.

radiation plate is not conform to the real boundary conditions present. The baffle prevents interaction of the sound fields between the considered radiation plate and the surrounding structure, which is also vibrating and radiating sound. Especially at low frequencies, where the acoustic wave lengths are relatively large, this interaction is considerable. Generally speaking, the use of the Rayleigh integral overestimates the radiated sound power into the free field, but the tendencies are predicted quite well [94].

The modal expansion technique used to predict the interior sound levels in an enclosure is only suited for relatively low frequencies. At higher frequencies the modal overlap is too high to model the acoustics with a deterministic approach like the modal expansion theory. The asymptotic density of acoustic modes in a rectangular enclosure is given by [35, 108]:

$$\frac{\mathrm{d}N(\omega)}{\mathrm{d}\omega} \approx \frac{\omega^2 V}{2\pi^2 c_0^3}, \tag{2.73}$$

where $N(\omega)$ is the estimated total number of modes below the radial frequency ω and $\frac{\mathrm{d}N(\omega)}{\mathrm{d}\omega}$ is the average number of modes per unit angular frequency bandwidth or the so-called *modal density*. The asymptotic modal density is pro-

portional to the square of the frequency, meaning that at high frequencies the modal overlap increases rapidly. This implies that the deterministic approach fails at higher frequencies. For these high frequencies another approach can be used like Statistical Energy Analysis (SEA), or the Rayleigh integral method (see equation (2.48)) when the modal density of the structure is not too high.

Another limitation is the uncoupled approach, meaning that the medium surrounding the vibrating structure has no influence on the vibration of the structure itself. The fluid loading effects are assumed to be weak, which is justified in most cases when the surrounding medium is air. When the enclosed fluid has a relatively large density (e.g. water) or the structure is light and unclamped, the fluid loading effects may be considerable and a coupled analysis could be necessary, like with the modal coupling theory [19, 34]. Another condition to justify an uncoupled analysis is that the enclosed volume not be too small. For confined spaces and weak structures (thin plates) the influence of even air on the vibration of the structure is considerable and this concept can even be used for passive noise reduction [1]. When the uncoupled solution is compared with the fully coupled harmonic analysis of the considered example as shown in Figure 2.9, it can be concluded that the influence of the coupling is very small. This can be expected, because the top plate is relatively heavy and stiff and the acoustic cavity relatively large.

It should also be noted that the acoustic modes used for the determination of the acoustic response are the modes of a rigid walled enclosure. This means that the solution based on a modal expansion does not converge to the correct boundary normal velocity and is zero at the boundaries. It does converge correctly to the correct boundary pressure at the vibrating boundaries. This mathematical condition associated with infinite sums is referred to as *Gibb's phenomenon*. However, the pressure prediction at the interior of the cavity is accurate and the deviation in the acoustic potential energy due to the Gibb's phenomenon is negligible according to Jayachandran *et al.* [58].

2.6 Active isolation

In this section a procedure is outlined for the analysis of feedforward active isolation systems. A feedforward control strategy is possible only if information is available about the primary disturbance of the isolation system. When this information is not available, a feedback strategy must be used. In this thesis only feedforward control strategies are considered.

The first application of a feedforward control system was proposed by Lueg [79]. A microphone and an electronically driven loudspeaker were used

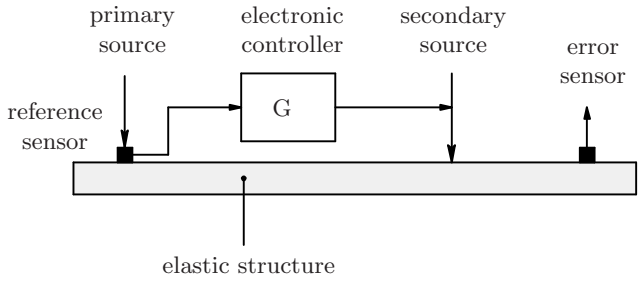

Figure 2.11: General feedforward active control system.

to cancel the sound propagation in a tube. In Figure 2.11 a similar system is depicted for an elastic structure. The structure is excited by a *primary source* (disturbance) resulting in structural waves that travel through the structure. The input from the primary source is measured with the reference sensor, which is fed to the *electronic controller*. The controller drives the *secondary source* (actuator) in such a way that the output from the *error sensor* (objective) is minimized. Generally speaking, the controller is implemented on a digital signal processor (DSP). The DSP causes a delay in the feedforward controller. The feedforward control of random disturbances is only possible when the delay in the path from the reference sensor to the error sensor is smaller than the propagation time of the elastic waves from the disturbance to the error sensor. This is the so-called *causality constraint*. The propagation time of the waves through the structure is very small and it is not possible to attenuate random disturbances when the error sensor is located close to the disturbance. However, when the disturbance is *periodic* e.g. harmonic disturbances, only the fundamental driving frequency of the disturbance has to be known. The causality constraint is of no importance in this situation.

2.6.1 Optimal control

The optimal control theory is used for the analysis of feedforward active isolation systems as shown in Figure 2.12. The primary excitation is a disturbance force, which puts the source in vibration and consequently results in a vibration of the receiver structure that is measured by the error sensor (e.g. an accelerometer). The error sensor produces an error signal that is sent to the controller, which drives the secondary source in such a way that the error signal is minimized. The secondary force is an actuator that produces a force, e.g. an electrodynamic actuator. It is assumed that the whole system (the

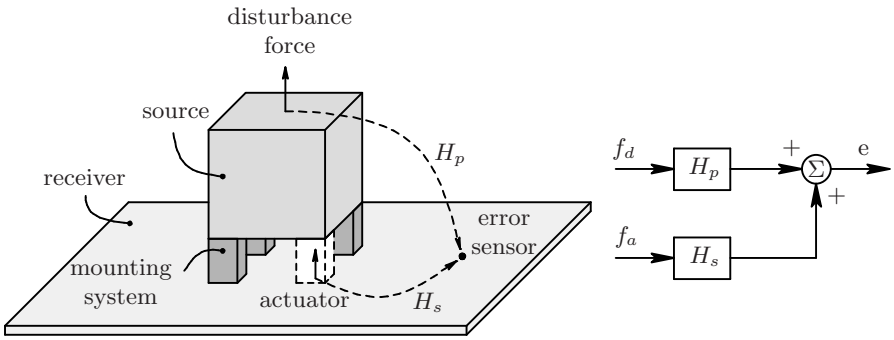

Figure 2.12: A feedforward active isolation system (SISO).

structure, disturbance and actuator forces) behaves *linearly*. Furthermore it is assumed that the signals are *harmonic*, which means that the models can be analyzed for each frequency independently. For these reasons the signals can be superposed as shown by the block diagram in Figure 2.12 and consequently the error signal e is:

$$e = H_p f_d + H_s f_a, \tag{2.74}$$

where H_p is the so-called *primary path* which is a harmonic transfer function from the disturbance force to the error sensor, H_s is the so-called *secondary path* which is a harmonic transfer function from the actuator to the error sensor, f_d is the disturbance force and f_a is the actuator force. In the ideal case considered, the error signal can be reduced to zero with an actuator force of:

$$f_a^{opt} = -\frac{H_p}{H_s} f_d. \tag{2.75}$$

The considered isolation system is a so-called single-input-single-output (SISO) system, which means that only one actuator and one sensor are used for the control system. In practice often multiple sensors and actuators are used, the so-called multiple-input-multiple-output (MIMO) systems. For MIMO systems, equation (2.74) can be written as:

$$\mathbf{e} = \mathbf{H}_p \cdot \mathbf{f}_d + \mathbf{H}_s \cdot \mathbf{f}_a, \tag{2.76}$$

where it is assumed that also multiple independent disturbance forces may be present. For the case that as many sensors as actuators are used for the active isolation, the optimal actuator force can be determined according to:

$$\mathbf{f}_a^{opt} = -\mathbf{H}_s^{-1} \cdot \mathbf{H}_p \cdot \mathbf{f}_d, \tag{2.77}$$

resulting in an error signal equal to zero. Considering equations (2.75) and (2.77) it must be realized that these expressions are only valid for H_s not equal to zero or $\mathbf{H}_s$ not singular. In general the number of sensors is not equal to the number of actuators. In most cases an *overdetermined* system is used, meaning that the number of sensors is larger than the number of actuators and in fact the inverse of $\mathbf{H}_s$ changes into a pseudo-inverse. For this case an error criterion or *cost function* J can be defined consisting of the sum of the squared error signals according to:

$$J = \mathbf{e}^{\mathrm{H}} \cdot \mathbf{e}. \tag{2.78}$$

Substitution of equation (2.76) results in the *Hermitian quadratic* form [92]:

$$J = \mathbf{f}_a^{\mathrm{H}} \cdot \mathbf{A} \cdot \mathbf{f}_a + \mathbf{f}_a^{\mathrm{H}} \cdot \mathbf{b} + \mathbf{b}^{\mathrm{H}} \cdot \mathbf{f}_a + c, \tag{2.79}$$

where the individual terms are defined as:

$$\mathbf{A} = \mathbf{H}_s^{\mathrm{H}} \cdot \mathbf{H}_s, \tag{2.80a}$$

$$\mathbf{b} = \mathbf{H}_s^{\mathrm{H}} \cdot \mathbf{H}_p \cdot \mathbf{f}_d, \tag{2.80b}$$

$$c = \mathbf{f}_d^{\mathrm{H}} \cdot \mathbf{H}_p^{\mathrm{H}} \cdot \mathbf{H}_p \cdot \mathbf{f}_d. \tag{2.80c}$$

The cost function is quadratic in terms of the actuator force vector $\mathbf{f}_a$, and has a unique minimum provided that the matrix $\mathbf{A}$ is positive definite. With this condition the optimal actuator force that minimizes cost function J can be determined according to [92]:

$$\mathbf{f}_a^{opt} = -\mathbf{A}^{-1} \cdot \mathbf{b}, \tag{2.81}$$

with a corresponding minimum value of the cost function:

$$J^{\min} = c - \mathbf{b}^{\mathrm{H}} \cdot \mathbf{A} \cdot \mathbf{b}. \tag{2.82}$$

It is also possible to use less sensors than actuators, the so-called *underdetermined* case. However, this yields an ill-conditioned matrix $\mathbf{A}$ and for this reason problems occur in minimization of the cost function.

2.6.2 Error criteria at the junctions of the receiver structure

Because the structural dynamics of the system are described by a port description, it is possible to define error criteria that minimize the response at

the junctions or the ports directly. Examples of these kinds of error criteria are minimization of the velocity response or force response:

$$J_v = \mathbf{v}_r^{\mathrm{H}} \cdot \mathbf{v}_r, \tag{2.83a}$$

$$J_f = \mathbf{f}_r^{\mathrm{H}} \cdot \mathbf{f}_r, \tag{2.83b}$$

where $\mathbf{v}_r$ and $\mathbf{f}_r$ are the receiver velocities and receiver forces at the locations of the junctions respectively. These cost functions can be rewritten in terms of the disturbance forces and actuator forces by the equations (2.27) or (2.32) according to:

$$\begin{aligned} J_v = {} & \mathbf{f}_a^{\mathrm{H}} \cdot \mathbf{H}_s^{vr^{\mathrm{H}}} \cdot \mathbf{H}_s^{vr} \cdot \mathbf{f}_a + \mathbf{f}_a^{\mathrm{H}} \cdot \mathbf{H}_s^{vr^{\mathrm{H}}} \cdot \mathbf{H}_p^{vr} \cdot \mathbf{f}_d + \\ & \mathbf{f}_d^{\mathrm{H}} \cdot \mathbf{H}_p^{vr^{\mathrm{H}}} \cdot \mathbf{H}_s^{vr} \cdot \mathbf{f}_a + \mathbf{f}_d^{\mathrm{H}} \cdot \mathbf{H}_p^{vr^{\mathrm{H}}} \cdot \mathbf{H}_p^{vr} \cdot \mathbf{f}_d, \end{aligned} \tag{2.84a}$$

$$\begin{aligned} J_f = {} & \mathbf{f}_a^{\mathrm{H}} \cdot \mathbf{H}_s^{fr^{\mathrm{H}}} \cdot \mathbf{H}_s^{fr} \cdot \mathbf{f}_a + \mathbf{f}_a^{\mathrm{H}} \cdot \mathbf{H}_s^{fr^{\mathrm{H}}} \cdot \mathbf{H}_p^{fr} \cdot \mathbf{f}_d + \\ & \mathbf{f}_d^{\mathrm{H}} \cdot \mathbf{H}_p^{fr^{\mathrm{H}}} \cdot \mathbf{H}_s^{fr} \cdot \mathbf{f}_a + \mathbf{f}_d^{\mathrm{H}} \cdot \mathbf{H}_p^{fr^{\mathrm{H}}} \cdot \mathbf{H}_p^{fr} \cdot \mathbf{f}_d. \end{aligned} \tag{2.84b}$$

The actuator force vector that minimizes these error criteria and thus minimizes the forces or the velocities at the junctions of the receiver structure, can consequently be determined with the equations (2.79) and (2.81). The corresponding response is determined by equation (2.82). Furthermore it is possible to define all kinds of error criteria related to the considered forces and velocities, e.g. minimization of the velocities in the axial direction only or another (combination of) DOFs or minimization of a weighted combination of the forces and velocities.

Transmitted power

Another interesting measure is the transmitted power into the receiver structure. As explained before, the source is in general connected with the receiver structure by a multi-directional and multi-point mounting system. The transmission of vibrational energy from the source to the receiver structure occurs along several DOFs. For this reason often the transmitted power is used to determine the isolation performance. The transmitted power is a measure of the power that is dissipated in the receiver structure due to the several damping mechanisms. The total vibrational energy contents of the receiver structure is determined by the summation of the potential and kinetic energy. The total energy is directly related to the difference between the power that is injected and that is dissipated from the structure[4]. In other words, transmitted power

[4] A more detailed analysis of the relation between the transmitted power and the energy levels is described in appendix A for a one-degree-of-freedom oscillator.

is closely connected to the total energy content (the sum of the potential and kinetic energy) of the receiver structure. For this reason it is an interesting measure to define the response and isolation performance of the hybrid isolation system. Besides being used as a measure for the response, it is also an interesting error criterion for active isolation purposes. When the transmitted power is minimized, the sum of the potential and kinetic energy of the receiver structure is minimized as well and a global reduction of the dynamic receiver response is obtained.

The power flow into the receiver structure can be determined by:

$$P_t = \frac{1}{2}\Re\left(\mathbf{f}_r^{\mathrm{H}} \cdot \mathbf{v}_r\right) = \frac{1}{4}\left(\mathbf{f}_r^{\mathrm{H}} \cdot \mathbf{v}_r + \mathbf{v}_r^{\mathrm{H}} \cdot \mathbf{f}_r\right), \tag{2.85}$$

where $\Re(.)$ denotes the real part. The transmitted power P_t can be written in the Hermitian quadratic form using the set of equations (2.27) or (2.32):

$$\begin{aligned} P_t = \frac{1}{4}\mathbf{f}_a^{\mathrm{H}} \cdot \left(\mathbf{H}_s^{fr^{\mathrm{H}}} \cdot \mathbf{H}_s^{vr} + \mathbf{H}_s^{vr^{\mathrm{H}}} \cdot \mathbf{H}_s^{fr}\right) \cdot \mathbf{f}_a + \\ \frac{1}{4}\mathbf{f}_a^{\mathrm{H}} \cdot \left(\mathbf{H}_s^{fr^{\mathrm{H}}} \cdot \mathbf{H}_p^{vr} + \mathbf{H}_s^{vr^{\mathrm{H}}} \cdot \mathbf{H}_p^{fr}\right) \cdot \mathbf{f}_d + \\ \frac{1}{4}\mathbf{f}_d^{\mathrm{H}} \cdot \left(\mathbf{H}_p^{fr^{\mathrm{H}}} \cdot \mathbf{H}_s^{vr} + \mathbf{H}_p^{vr^{\mathrm{H}}} \cdot \mathbf{H}_s^{fr}\right) \cdot \mathbf{f}_a + \\ \frac{1}{4}\mathbf{f}_d^{\mathrm{H}} \cdot \left(\mathbf{H}_p^{fr^{\mathrm{H}}} \cdot \mathbf{H}_p^{vr} + \mathbf{H}_p^{vr^{\mathrm{H}}} \cdot \mathbf{H}_p^{fr}\right) \cdot \mathbf{f}_d. \end{aligned} \tag{2.86}$$

The optimal actuator force that minimizes the transmitted power can consequently be determined by the equations (2.79) and (2.81).

Besides minimization of the net structural power injected into the receiver structure, the models also allow the determination of other power contributions. It is also possible to determine the structural power input by the source or the power exerted by the actuators solely:

$$P_d = \frac{1}{2}\Re\left(\mathbf{f}_d^{\mathrm{H}} \cdot \mathbf{v}_{sd}\right), \tag{2.87a}$$

$$P_a = \frac{1}{2}\Re\left(\mathbf{f}_a^{\mathrm{H}} \cdot \mathbf{v}_{ma}\right), \tag{2.87b}$$

where $\mathbf{v}_{sd}$ is the vector with velocities at the location of the disturbance forces and $\mathbf{v}_{ma}$ is the vector with velocities at the junctions of the mounts in the DOF that are actuated. The expressions for the power input by the source and actuators can also be used as an error criterion for active control because it can be written in the Hermitian quadratic form in terms of the actuator forces, after which the optimal actuator force can be determined.

2.6.3 Error criteria for far-field structural sensors

In the foregoing model presentations, the dynamics of the whole isolation system are described at the junctions only. However, these models can easily be extended to the responses at other locations of the receiver structure, even at a (large) distance from the source, so-called *far-field sensors*. This is necessary to determine the passive and active response at different locations of the receiver structure or for the determination of the acoustic response of (a part of) the receiver structure. Also, global responses such as the kinetic or potential energy or normal velocity distributions of parts of the structure (a first measure of the sound radiation and necessary for performing acoustic analyses) can easily be calculated. This is very useful to judge different error sensor strategies, not only at the response of the error sensors itself, but also by the dynamic responses at other parts of the receiver.

To determine the response at other locations of the hybrid isolation system than the junctions, extra information has to be known. Consider a sensor set of velocities $\mathbf{v}_{sr}$ attached to the receiver structure. The response at this sensor set is determined by the forces acting on the receiver structure according to [6, 7]:

$$\mathbf{v}_{sr} = \mathbf{Y}_{sr} \cdot \mathbf{f}_r, \tag{2.88}$$

where $\mathbf{Y}_{sr}$ is a mobility matrix consisting of the FRFs from the forces at the receiver junctions to the velocity response at the considered sensor set. This mobility matrix must thus be determined by extra measurements or with the help of the numerical model. This equation can be rewritten by substitution of $\mathbf{f}_r$ in equation set (2.27) or (2.32):

$$\begin{aligned} \mathbf{v}_{sr} &= \mathbf{Y}_{sr} \cdot \left(\mathbf{H}_p^{fr} \cdot \mathbf{f}_d + \mathbf{H}_s^{fr} \cdot \mathbf{f}_a \right) \\ &= \left(\mathbf{H}_p^{vsr} \cdot \mathbf{f}_d + \mathbf{H}_s^{vsr} \cdot \mathbf{f}_a \right), \end{aligned} \tag{2.89}$$

where $\mathbf{H}_p^{vsr} = \mathbf{Y}_{sr} \cdot \mathbf{H}_p^{fr}$ is the matrix with primary FRFs from the disturbance forces to the velocity sensor response $\mathbf{v}_{sr}$ at the receiver structure and $\mathbf{H}_s^{vsr} = \mathbf{Y}_{sr} \cdot \mathbf{H}_s^{fr}$ is the matrix with secondary FRFs from the actuator forces to the velocity sensor set $\mathbf{v}_{sr}$ at the receiver structure. This sensor response can again be written in the well-known standard Hermitian quadratic form:

$$\begin{aligned} J = \mathbf{v}_{sr}^{\mathrm{H}} \cdot \mathbf{v}_{sr} = \mathbf{f}_a^{\mathrm{H}} \cdot \mathbf{H}_s^{vsr^{\mathrm{H}}} \cdot \mathbf{H}_s^{vsr} \cdot \mathbf{f}_a + \mathbf{f}_a^{\mathrm{H}} \cdot \mathbf{H}_s^{vsr^{\mathrm{H}}} \cdot \mathbf{H}_p^{vsr} \cdot \mathbf{f}_d + \\ \mathbf{f}_d^{\mathrm{H}} \cdot \mathbf{H}_p^{vsr^{\mathrm{H}}} \cdot \mathbf{H}_s^{vsr} \cdot \mathbf{f}_a + \mathbf{f}_d^{\mathrm{H}} \cdot \mathbf{H}_p^{vsr^{\mathrm{H}}} \cdot \mathbf{H}_p^{vsr} \cdot \mathbf{f}_d. \end{aligned} \tag{2.90}$$

This quadratic cost function can again be minimized by a set of optimal actuator forces.

Minimization of the potential or kinetic energy

Besides the direct minimization of a set of velocity responses, it is also possible to define a more global measure as cost function or to judge the receiver response when numerical models are used. A representative global measure of the receiver response is the potential and kinetic energy of the receiver structure, and for this reason an interesting measure to be considered with the structural isolation models. The maximum kinetic energy is determined by weighting the total velocity response with the mass matrix:

$$E_{kin} = \frac{1}{2}\mathbf{v}_{tot}^{\mathrm{H}} \cdot \mathbf{M} \cdot \mathbf{v}_{tot}, \tag{2.91}$$

where $\mathbf{v}_{tot}$ is the velocity response at all DOFs of the receiver model and $\mathbf{M}$ is the mass matrix composed with the FEM package. In a similar way the maximum potential energy is determined by:

$$E_{pot} = \frac{1}{2}\mathbf{u}_{tot}^{\mathrm{H}} \cdot \mathbf{K} \cdot \mathbf{u}_{tot}, \tag{2.92}$$

where $\mathbf{u}_{tot}$ is the total displacement response of all DOFs of the receiver model and $\mathbf{K}$ is the stiffness matrix that is composed with the FEM package. The evaluation of these error criteria and the calculation of the optimal actuator forces may cost large computational times for models with a large number of DOFs. Fortunately, the calculation of these energies can be reduced considerably by making use of the modal expansion theory. This is explained in more detail in appendix B.

2.6.4 Acoustic error criteria

Once the structural response of the receiver structure is determined, the coupling with the acoustic domain can be made. To investigate the performance of the active control system on the acoustic response of interest, the relation between the vibrational response of a part of the receiver structure to the acoustic response has to be determined in the first place. For the situation that the radiated sound power into the free field is of interest, only a boundary mesh of a part of the receiver structure is needed. This means that the geometrical information of the surface mesh for which the radiated sound power is determined is sufficient to calculate the radiation resistance matrix as described by equation (2.48). When the pressure response at some locations in the free field radiation is used as error criterion, an impedance matrix has to be determined as described by equation (2.44). Besides the surface mesh

information, also the locations of the field points with the error sensors (microphones) must be defined. For the determination of the pressure response of the vibrating surface in an enclosure, the acoustic modes have to be calculated. For arbitrarily shaped enclosures this can be done with a finite element package. The acoustic modes are used for the modal expansion to determine the impedance matrix as described by equation (2.59).

The part of the receiver structure that is coupled to the acoustic analysis is in this study referred to as the radiation plate. The normal velocity response of the radiation plate is consequently determined by:

$$\mathbf{v}_{rp} = \mathbf{Y}_{rp} \cdot \mathbf{f}_r, \tag{2.93}$$

where $\mathbf{v}_{rp}$ is the normal velocity response of the radiation plate and $\mathbf{Y}_{rp}$ is the mobility matrix from the forces at the junctions of the receiver structure to the normal velocity response on the radiation plate. This equation can be rewritten in terms of a primary and secondary frequency response function in a similar way as shown with equation (2.88):

$$\mathbf{v}_{rp} = \mathbf{H}_p^{vrp} \cdot \mathbf{f}_d + \mathbf{H}_s^{vrp} \cdot \mathbf{f}_a. \tag{2.94}$$

First, the free field radiation of the radiation plate is considered:

$$\bar{W} = \mathbf{v}_{rp}^{\mathrm{H}} \cdot \mathbf{R} \cdot \mathbf{v}_{rp}, \tag{2.95}$$

which can be expressed in terms of the primary and secondary frequency response functions as:

$$\begin{aligned}\bar{W} = \mathbf{f}_a^{\mathrm{H}} \cdot \mathbf{H}_s^{vrp\,\mathrm{H}} \cdot \mathbf{R} \cdot \mathbf{H}_s^{vrp} \cdot \mathbf{f}_a + \mathbf{f}_a^{\mathrm{H}} \cdot \mathbf{H}_s^{vrp\,\mathrm{H}} \cdot \mathbf{R} \cdot \mathbf{H}_p^{vrp} \cdot \mathbf{f}_d + \\ \mathbf{f}_d^{\mathrm{H}} \cdot \mathbf{H}_p^{vrp\,\mathrm{H}} \cdot \mathbf{R} \cdot \mathbf{H}_s^{vrp} \cdot \mathbf{f}_a + \mathbf{f}_d^{\mathrm{H}} \cdot \mathbf{H}_p^{vrp\,\mathrm{H}} \cdot \mathbf{R} \cdot \mathbf{H}_p^{vrp} \cdot \mathbf{f}_d.\end{aligned} \tag{2.96}$$

In a similar way the pressure response in a cavity or free field can be written as a quadratic error criterion in terms of the actuator forces according to:

$$\begin{aligned}J = \mathbf{p}_e^{\mathrm{H}} \cdot \mathbf{p}_e = \mathbf{f}_a^{\mathrm{H}} \cdot \mathbf{H}_s^{vrp\,\mathrm{H}} \cdot \mathbf{Z}^{\mathrm{H}} \cdot \mathbf{Z} \cdot \mathbf{H}_s^{vrp} \cdot \mathbf{f}_a + \\ \mathbf{f}_a^{\mathrm{H}} \cdot \mathbf{H}_s^{vrp\,\mathrm{H}} \cdot \mathbf{Z}^{\mathrm{H}} \cdot \mathbf{Z} \cdot \mathbf{H}_p^{vrp} \cdot \mathbf{f}_d + \mathbf{f}_d^{\mathrm{H}} \cdot \mathbf{H}_p^{vrp\,\mathrm{H}} \cdot \mathbf{Z}^{\mathrm{H}} \cdot \mathbf{Z} \cdot \mathbf{H}_s^{vrp} \cdot \mathbf{f}_a + \\ \mathbf{f}_d^{\mathrm{H}} \cdot \mathbf{H}_p^{vrp\,\mathrm{H}} \cdot \mathbf{Z}^{\mathrm{H}} \cdot \mathbf{Z} \cdot \mathbf{H}_p^{vrp} \cdot \mathbf{f}_d,\end{aligned} \tag{2.97}$$

where $\mathbf{p}_e$ is a vector with pressure signals at the field points in the enclosure or free space and $\mathbf{Z}$ is the impedance matrix from the velocity response of the radiation plate to the pressure error sensors in the enclosure or free field. The optimal actuator forces are again determined as shown in section 2.6.1.

2.6.5 Actuator configuration

Apart from the error sensor strategies, also the actuator configuration is an important issue for the success of active vibration control or noise reduction. In other words, the number, locations and directions of the actuators are important on the active performance of the hybrid isolation system.

The influence of the number of actuators on the active isolation performance of a discrete isolation model has been considered in section 2.3.3. It was concluded that for total isolation, meaning that the motion of all the masses are suppressed by the actuators, the number of actuators must be equal to the number of structural transmission paths from the source to the receiver structure. In that case no vibrations are transmitted to the receiver structure at all. For the applications of hybrid isolation systems that are considered here, the number of actuators must be as small as possible for reasons of costs, implementation and the control effort that is needed to drive the actuators. As explained before, hybrid isolation systems in vehicles in general have a multi-point and multi-directional mounting system. This means that a lot of actuators are needed for complete isolation of the source from the receiver structure. This requires many actuators, which is difficult to implement in a practical application and results in too high costs. For this reason, the goal of the applications for hybrid isolation considered in this work is not to obtain complete isolation. Instead, two goals are considered: reduction of the number of actuators and reduction of the needed actuator forces or *actuator effort* to obtain a good active reduction. The actuator effort must be feasible, i.e. the forces exerted by the actuators must not be unrealistically large. Reduction of the actuator effort can also be realized by a modification of the quadratic Hermitian error sensor strategy as shown in equation (2.79). This is done by adding an extra term with the needed actuator inputs [38]:

$$J = \mathbf{f}_a^{\mathrm{H}} \cdot \mathbf{A} \cdot \mathbf{f}_a + \mathbf{f}_a^{\mathrm{H}} \cdot \mathbf{b} + \mathbf{b}^{\mathrm{H}} \cdot \mathbf{f}_a + c + \mathbf{f}_a^{\mathrm{H}} \cdot \mathbf{W}_a \cdot \mathbf{f}_a, \tag{2.98}$$

where $\mathbf{W}_a$ is a diagonal matrix which weights each actuator force component of the total actuator force vector separately. When each actuator force is weighted to the same extent, the matrix $\mathbf{W}_a$ can be replaced by:

$$\mathbf{W}_a = \mu \mathbf{I}, \tag{2.99}$$

where $\mathbf{I}$ is the identity matrix and μ is a coefficient that determines the amount of actuator weighting. The purpose of the actuator weighting term in the cost function is to account for the effort being expended by the control system, so that small reductions in the sensor output are not obtained at the expense of

very high actuator effort levels. The actuator effort weighting term is thus in fact a penalty term: when the value of the error sensor response only becomes very small when applying high actuator forces, the value of the cost function is still considerable. The cost function reaches a minimum of the weighted combination of the error sensor response and the actuator effort. The amount of weighting is determined by the factor μ, which is a factor that has to be determined by trial and error. When μ is zero, the error criterion contains no actuator effort weighting, and no limit is applied to the actuator forces to obtain the minimal sensor response. When μ is very large, hardly any reduction is obtained.

Besides the number, also the location and the direction of the actuators are important because they determine the effectiveness of excitation at the error sensors by the considered actuators. The higher this effectiveness, the better the actuators are able to influence the structure at the location of the error sensors and the better the reductions that can be obtained at the error sensor set. The purpose is in fact to find these locations and directions. In the applications that are considered in the following chapters this is analyzed in more detail. An important consideration with respect to this point is that the information known about the structure is quite limited. For practical applications often not more information is available than the measured FRFs from different excitation or actuator positions to the sensor locations. However, this information can be sufficient to gain some information about the effectiveness of the direction and/or location of actuation.

SVD analysis for actuator configurations

A particularly useful tool for analyzing FRF matrices is the *Singular Value Decomposition* (SVD) [45]. This analytical tool is used in different fields, like the inversion of ill-conditioned matrices and in the field of structural acoustic active control to relate structural sensors to the desired acoustic response with reduction of information. In this work it will be used to analyze different actuator configurations. The SVD decomposition of a mobility matrix $\mathbf{Y}$ is defined as:

$$\mathbf{Y} = \mathbf{U} \cdot \mathbf{S} \cdot \mathbf{V}^{\mathrm{H}} = \sum_i \mathbf{u}_i \, s_i \, \mathbf{v}_i^{\mathrm{H}}, \tag{2.100}$$

where $\mathbf{U}$ is a matrix with in each column the so-called *field shapes*, $\mathbf{S}$ is the diagonal matrix with *singular values* in decreasing order and $\mathbf{V}$ is a matrix with in each column the so-called *source shapes*. The field shapes are in fact response patterns of the sensors and the source shapes are force patterns that effectively excite the structure. The effectiveness of the combination of a

source and field shape is determined by its corresponding singular value. More details concerning the SVD analysis can be found in appendix C. Each combination of a field shape $\mathbf{u}_i$ and a corresponding source shape $\mathbf{v}_i$ contributes independently in the mobility matrix and the efficiency of this contribution is determined by the singular value s_i. The singular values in the matrix $\mathbf{S}$ decrease with increasing number. This means that the contributions of the field shapes and corresponding source shapes also decay with increasing number. This information about the effectiveness of the field shapes and source shapes is important information that can be used to determine the most effective directions of actuation and the number of actuators that are necessary to have an effective active reduction at the error sensor set. The SVD tool is used for the application of hybrid isolation that is considered in chapter 4.

2.7 Concluding remarks

A general model was presented to describe hybrid isolation systems with a source (e.g. an engine), a resilient hybrid mounting system and a receiver structure (e.g. a ship hull). A port description was used to describe the structural dynamics adopted from an existing model presented by Gardonio *et al.* [40, 41]. This model representation, described by the multi-directional force and velocity vectors at each junction, allows modeling of complex receiver structures with a multi-directional and multi-point mounting system. The forces and velocity vectors are related to each other by a mobility matrix (source and receiver) or an impedance matrix (mounts). The mobility matrices can be determined by measurements or by calculation with analytical or numerical models.

The active isolation part is described by the definition of a set of external forces, acting on the receiver structure at the connections of the mounts with the receiver. The actuator forces are determined by minimization of a Hermitian quadratic error function. This is a so-called optimal control procedure that represents a feedforward control strategy with an 'ideal' controller. The optimal actuator force can be determined straightforwardly as function of the different FRFs that describe the combined passive and active responses of the receiver structure. Different kinds of error sensor strategies have been introduced. First of all, error sensor criteria in terms of the forces and velocities at the junctions of the receiver structure are defined, such as minimization of the forces and velocities or the transmitted power. The advantage of numerical models is that the different mobilities and FRFs can be determined rather easily. For this reason all kinds of responses can be determined and all kinds

of error sensor strategies can be analyzed. Error sensor criteria like the minimization of the potential or kinetic energy, are very difficult or even impossible to determine with the help of measurements, but can be determined rather easily with the help of mathematical models.

Besides the description of the structural dynamic behavior of the whole hybrid isolation system, models of the acoustic behavior of (a part of) the receiver structure have been presented. Two types of acoustic models have been treated: the radiation of a baffled flat plate as part of the receiver structure into the free field and the radiation of a part of the receiver structure in an acoustic enclosure. The latter acoustic model is in fact a simplified model of an accommodation. Different acoustic responses have been described and modeled as error sensor strategy.

In the next two chapters two applications of hybrid isolation systems are analyzed with the use of the general hybrid isolation model that has been presented in this chapter. The impedance and mobility matrices are determined with the help of an analytical or a numerical analysis. This allows easy investigation of different kinds of error sensor strategies and even the use of receiver responses that are impossible to measure. In chapter 3 a relatively simple model is analyzed. The mobility and impedance matrices are determined in an analytical way. In chapter 4, a more complex receiver structure is analyzed. The reduced model is used because most attention is paid to the dynamic and acoustic behavior of the receiver structure.

Chapter 3

Analytical study of a simple hybrid isolation system

3.1 Introduction

The discrete analytical models considered in the previous chapter have severe limitations in modeling realistic isolation systems in the considered applications. The mounting system has in practice several structural vibration transmission paths from the source to the receiver structure; i.e. the mounting system is a multi-directional and multi-point supporting structure of the source. Also, the dynamic behavior of the separate subsystems is much more complicated and cannot be accurately described with oscillator models. For this reason, more complicated isolation models are considered consisting of a multi-directional and multi-point mounting system. In this chapter a first introduction is presented in the analytical modeling of such combined passive and active isolation systems in an analytical way. The physical aspects of hybrid isolation systems will be considered in more detail.

The described analytical model is similar to the model introduced by Gardonio *et al.* [40, 41]. The general theory of the port-description as described in the previous chapter, is used to connect the subsystems with each other and to determine the passive and active responses of the receiver structure. The isolation system consists of a rigid source connected with four isolation mounts on a simply supported plate as receiver structure, see Figure 3.1. The dynamic behavior of the separate components is relatively simple, and for this reason analytical models can be used to determine the dynamic behavior of the subsystems and the entire isolation system. The dynamics of the separate components are described in section 3.2. The passive behavior of the com-

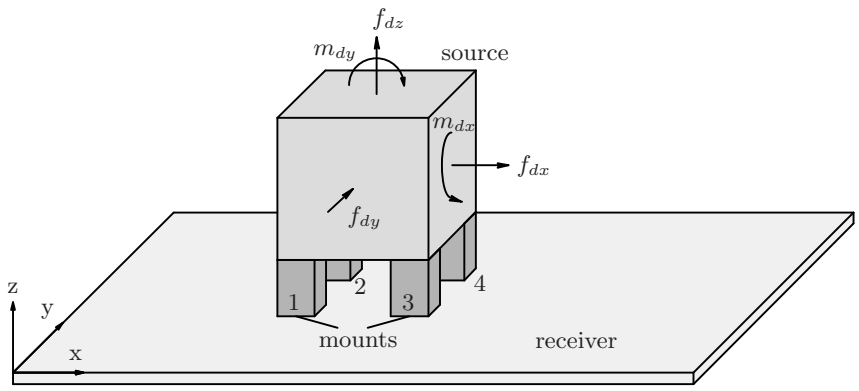

Figure 3.1: Schematic picture of the analytical hybrid isolation system.

posed system is analyzed in section 3.3. Subsequently, the active isolation performance for various control strategies is investigated in section 3.4. The considered isolation system is an idealized structure with an idealized control system model, but it is effective to describe the physical aspects of hybrid isolation systems and some general tendencies can be derived. In section 3.5 conclusions and shortcomings of the presented analytical model are presented.

3.2 Description of the analytical model

The example problem as shown in Figure 3.1 consists of a rigid body source, a mounting system with four mounts and a simply supported plate as receiver structure. The properties of the different components of the studied example problem are shown in Table 3.1.

3.2.1 Dynamics of the source

The dynamic behavior of the source is described with the mobility approach of section 2.4.2. The source is modeled as a rigid body and the disturbance or excitation of the isolation system as a force vector acting in the center of gravity of the source. The theory to determine the mobility matrix of a rigid source mass is described in appendix D.1.

Component	Parameter	Value
Source	Dimensions ($L_x \times L_y \times L_z$)	$0.20 \times 0.20 \times 0.40$ m
(rigid mass)	Density ρ	2700 kg/m^3
Mount	Dimensions cross-section	0.06×0.06 m
(Timoshenko beam)	Length L	0.1 m
	Density ρ	1000 kg/m^3
	Modulus of elasticity E	2.5×10^7 N/m^2
	Poisson's ratio ν	0.33
	Shear number k_s	0.833
	Structural loss factor η	0.1
Receiver	Dimensions ($L_x \times L_y$)	1.2×1 m
(simply supp. plate)	Thickness h	0.025 m
	Density ρ	2700 kg/m^3
	Modulus of elasticity E	70×10^9 N/m^2
	Poisson's ratio ν	0.33
	Structural loss factor η	0.01

Table 3.1: Parameters for the analytical model of the hybrid isolation system.

3.2.2 Dynamics of the mounting system

The dynamic behavior of each mount is described with the impedance approach of section 2.4.2. The impedance matrices are derived with a method known as the *dynamic stiffness matrix* (DSM) *formulation* or *spectral element method* [75]. This method resembles the finite element method because the structure is also divided into a number of elements and junctions (nodes). The displacements and rotations at the nodes (nodal degrees of freedom) are related to the forces and moments at the nodes (nodal loads) by means of a *dynamic stiffness matrix*. The difference with the finite element method lies in the shape functions that are used to describe the spatial dependence of a variable. In the finite element method linear or higher order polynomial shape functions are used, whereas in the DSM method the exact solution is used. The advantage is that for the DSM method a minimum number of elements per wavelength is not required. A disadvantage is that an exact solution must be available. Each mount is modeled with one spectral beam element

and the mount is coupled with the dynamic models of the source and the receiver at the junctions. The mounts are relatively short in comparison to their cross-sectional dimensions. For this reason, the shear effect has a considerable influence on the bending vibration and has been included in the analysis. Also, the influence of the rotary inertia has been taken into account. This influence can be considerable for higher frequencies. More details concerning the modeling of the beams can be found in appendix D.2.

3.2.3 Dynamics of the receiver structure

The dynamic behavior of the receiver structure is described with a mobility approach as shown in equation (2.21). However, no exact solution exists for the equation of motion of a plate. For this reason an approximate method is used: the *modal superposition technique*.

A general two-dimensional harmonic equation of motion (e.g. a plate) can be written as [23]:

$$B(1+\mathrm{j}\eta)L\left[w(x,y)\right]-\rho h\omega^2 w(x,y)=f_z(x,y), \tag{3.1}$$

where B is a stiffness parameter, η is a structural loss factor, L is a differential operator, ω is the circular frequency, h is the height in the z-direction, $w(x,y)$ is the displacement and $f_z(x,y)$ is the distributed force. The eigenfrequencies and mode shapes are calculated by solving the homogeneous form of equation (3.1):

$$B(1+\mathrm{j}\eta)L\left[\varphi_n(x,y)\right]-\rho h\underline{\omega}_n^2\varphi_n(x,y)=0, \tag{3.2}$$

where $\varphi_n(x,y)$ is the n^{th} eigenmode that satisfies the boundary conditions. The n^{th} damped complex eigenfrequency $\underline{\omega}_n$ is defined as:

$$\underline{\omega}_n=\omega_n\sqrt{1+\mathrm{j}\eta}, \tag{3.3}$$

where ω_n is the undamped eigenfrequency. The solution of the inhomogeneous equation (3.1) can be written as a modal superposition of the eigenmodes according to:

$$w(x,y)=\sum_{n=1}^{\infty}W_n\varphi_n(x,y), \tag{3.4}$$

where W_n is the modal participation of the n^{th} mode. Substitution of the modal expansion in equation (3.1) yields with abstraction of equation (3.2):

$$\sum_{n=1}^{\infty}W_n\rho h(\omega_n^2(1+\mathrm{j}\eta)-\omega^2)\varphi_n(x,y)=f_z(x,y). \tag{3.5}$$

Multiplication with $\varphi_m(x,y)$, integration over the surface area of the plate S and using the orthogonality principle results in:

$$W_n(\omega_n^2(1+\mathrm{j}\eta)-\omega^2)\iint \rho h\,\varphi_n^2(x,y)\,\mathrm{d}x\mathrm{d}y = \iint f_z(x,y)\varphi_n(x,y)\,\mathrm{d}x\mathrm{d}y. \quad (3.6)$$

The modal participations are then determined by:

$$W_n = \frac{1}{\Lambda_n(\omega_n^2(1+\mathrm{j}\eta)-\omega^2)}\iint f_z(x,y)\varphi_n(x,y)\,\mathrm{d}x\mathrm{d}y, \quad (3.7)$$

where Λ_n is the so-called modal mass of mode n:

$$\Lambda_n = \iint \rho h\,\varphi_n^2(x,y)\,\mathrm{d}x\mathrm{d}y, \quad (3.8)$$

Furthermore, the term f_z^g is introduced, the generalized force, which is defined as:

$$f_z^g = \iint f_z(x,y)\varphi_n(x,y)\,\mathrm{d}x\mathrm{d}y. \quad (3.9)$$

The displacement is consequently determined by substitution of the modal participations into equation (3.4):

$$w(x,y) = \sum_{n=1}^{\infty}\frac{\varphi_n(x,y)\,f_z^g}{\Lambda_n(\omega_n^2(1+\mathrm{j}\eta)-\omega^2)}. \quad (3.10)$$

Each structure has an infinite number of eigenmodes with corresponding eigenfrequencies. For the calculation of the response, a good estimation can be obtained by taking into account a reduced set of eigenmodes. In practice the modes that have eigenfrequencies lower and somewhat higher than the excitation frequency of the structure are taken into account for the modal superposition.

However, in some cases the truncation of the modal expansion may result in large errors. This is shown in appendix D.3.3. The error of the response due to the modal truncation can be reduced with the concept of *residual flexibility* [22]. This concept can be explained using the derived formulas for the modal expansion. Assume that an accurate prediction of the dynamics of the harmonically excited system is desired in the frequency range from 0 up to ω_e. The total modal expansion is written as:

$$\begin{aligned} w(x,y) = &\sum_{n=1}^{m}\frac{\varphi_n(x,y)\,f_z^g}{\Lambda_n(\omega_n^2(1+\mathrm{j}\eta)-\omega^2)} \\ &+ \sum_{n=m+1}^{\infty}\frac{\varphi_n(x,y)\,f_z^g}{\Lambda_n(\omega_n^2(1+\mathrm{j}\eta)-\omega^2)}, \end{aligned} \quad (3.11)$$

where the second term on the right-hand side represents the error when m modes are taken into account for the modal superposition. In general the eigenfrequencies for the modes $n > m$ are much higher than the maximum frequency of the considered frequency band ω_e. Therefore, the response is estimated by:

$$w(x,y) \approx \sum_{n=1}^{m} \frac{\varphi_n(x,y)\, f_z^g}{\Lambda_n(\omega_n^2(1+\mathrm{j}\eta)-\omega^2)} + \sum_{n=m+1}^{\infty} \frac{\varphi_n(x,y)\, f_z^g}{\Lambda_n(\omega_n^2(1+\mathrm{j}\eta))}. \tag{3.12}$$

The modal terms for $n \gg m$ therefore contribute statically to the response and are the so-called *residual modes*. The static response $w_0(x,y)$ can also be written as a modal expansion by substitution of $\omega = 0$ in equation (3.11):

$$w_0(x,y) = \sum_{n=1}^{m} \frac{\varphi_n(x,y)\, f_z^g}{\Lambda_n \omega_n^2} + \sum_{n=m+1}^{\infty} \frac{\varphi_n(x,y)\, f_z^g}{\Lambda_n \omega_n^2}. \tag{3.13}$$

Notice that the structural damping plays no role in the case of static deformation. Combination of equations (3.12) and (3.13) yields:

$$w(x,y) \approx \sum_{n=1}^{m} \frac{\varphi_n(x,y)\, f_z^g}{\Lambda_n(\omega_n^2(1+\mathrm{j}\eta)-\omega^2)} + \frac{w_0(x,y)}{(1+\mathrm{j}\eta)} - \sum_{n=1}^{m} \frac{\varphi_n(x,y)\, f_z^g}{\Lambda_n(\omega_n^2(1+\mathrm{j}\eta))}. \tag{3.14}$$

The harmonic response is written as a modal superposition of m modes and a residual term consisting of the static response due to the excitation $f_z(x,y)$. The disadvantage of this method is that, besides a modal analysis, also an extra static analysis is needed that depends on the excitation $f_z(x,y)$. Unfortunately, the static response is not exactly known when the equation of motion is analyzed in an analytical way. However, an accurate prediction of the static deformation is obtained by evaluating equation (3.13) with a large number of dynamic modes. The computational effort is in general not so high, because this calculation is independent of the frequency and hence needs only to be evaluated once.

The influence of the residual modes is large for the so-called driving point FRFs, like for example the driving point mobilities. The driving point FRFs describe the transfer between the response and excitation at the same location and with respect to the same degree of freedom. The local deformation is relatively large for this type of FRF, which means that a large number of modes must be taken into account for a correct prediction of the dynamic behavior. The additional contribution of the residual mode results in a considerable improvement in the accuracy of the response for a simply supported plate, which is shown in appendix D.3.3.

In appendix D.3 the dynamic behavior of a simply supported receiver plate is described. The dynamics of the plate consist of flexural or bending deformation and in-plane motions, each described with an equation of motion in the form of equation (3.1).

3.3 Passive response

In the first instance, the passive response of the isolation system is considered. The influence of the damping and the stiffness of the mounting system is studied. As stated in the previous chapter, the mounting system consists of four mounts with five degrees of freedom each to transmit the structural power from the source to the receiver structure. The torsional degree of freedom of the receiver structure is not considered for the structural power transmission. This is discussed in more detail in appendix D.3. The results of the simulations presented in this chapter are for a set of unit excitation forces (in the x-direction, y-direction and z-direction) and unit moments (around the x-axis and y-axis) in the center of gravity of the source as shown in Figure 3.1.

3.3.1 Passive response: transmitted power

The vibrational energy generated by the source excitation flows through the mounting system to the receiver structure. The mounting system absorbs energy due to damping and isolates the source due to the impedance or stiffness mismatch. The influence of reduction of the mount stiffness and the increase of the damping on the transmitted power are shown in Figure 3.2. Increasing the structural damping of the mounts reduces the peaks in the transmitted power, which is especially visible at the low-frequency rigid body modes. The rigid body modes indicate the modes where the rigid mass moves on the mounting support only, without large deformation of the receiver plate, see also appendix D.4. The roll-off remains unchanged due to the structural damping mechanism. Reduction of the mounting stiffness reduces the transmitted

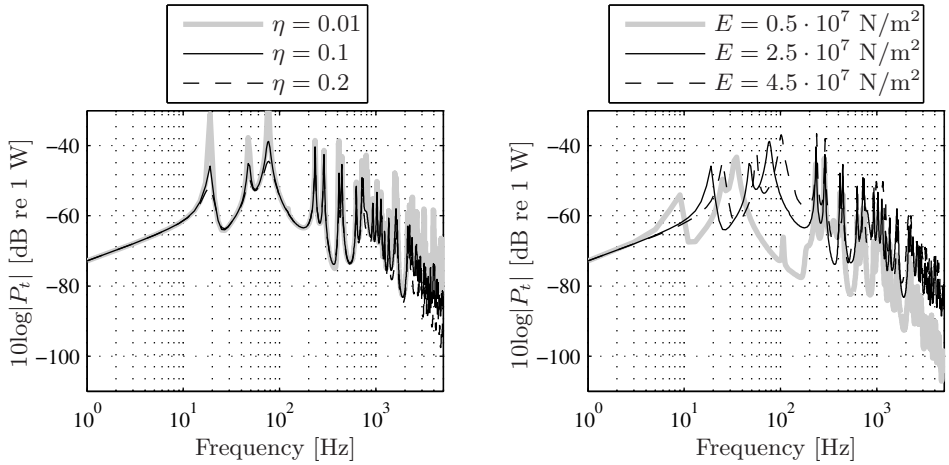

(a) $E = 2.5 \cdot 10^7$ N/m^2 (b) $\eta = 0.1$

Figure 3.2: Influence of the structural damping (a), and the stiffness (b) of the mounting system on the transmitted power.

power, but also causes a shift of the frequencies of the rigid body modes towards a lower frequency. It is also shown that the introduction of a larger impedance mismatch between the source and the supporting plate, created by a reduction of the stiffness of the mounting system, results in a decrease of the transmitted power in the whole frequency range.

3.3.2 Passive response: receiver response

Besides the mobility matrices related to the junctions of the receiver structure, also mobility matrices at other points of the receiver structure can be determined. When a grid of points on the receiver plate is considered, an indication of the global response can be obtained. In Figure 3.3 the passive harmonic response of the receiver structure is visualized at six frequencies near eigenfrequencies of the isolation system, by calculating the responses at the points indicated by the depicted grid on the plate. Figures 3.3(a) - 3.3(d) display the harmonic deformation shapes which strongly resemble the (1,1), (2,1), (1,2) and (2,2) bending modes of the plate. At higher frequencies also in-plane modes of the plate occur, and the first and second in-plane modes can be observed in the harmonic shapes depicted in Figure 3.3(e) and Figure 3.3(f) respectively.

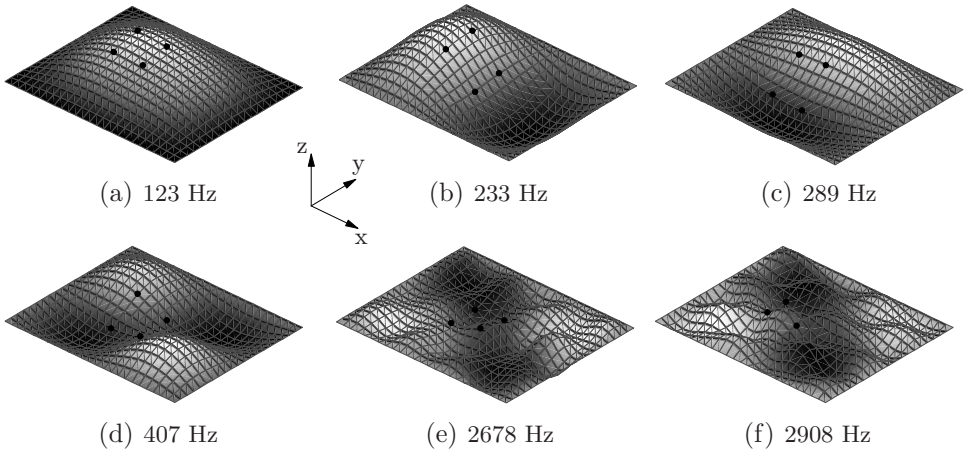

(a) 123 Hz (b) 233 Hz (c) 289 Hz

(d) 407 Hz (e) 2678 Hz (f) 2908 Hz

Figure 3.3: Deformation shapes of the receiver plate for the passive situation, the colors represent the displacement in the z-direction (a-d), y-direction (e) or x-direction (f). The dots indicate the position of the mounts.

3.4 Active isolation

As stated in the previous section, the passive mounting system is in an ideal situation designed to be as flexible as possible with some damping to attenuate the response of the rigid body modes of the source on the mounting system. In general there is a lower bound to the stiffness of the passive mounting system because the static movement of the source must be restricted. Furthermore, some care must be taken to avoid internal resonance frequencies of the mounting system around the excitation frequency and multiple harmonics of this frequency. To gain more reduction, active isolation techniques can be used. In this section a procedure is outlined for the analysis of feedforward active isolation systems.

The configuration of the model for the determination of the active isolation performance is again that of Figure 3.1. The disturbance force is the same as that used for the simulations of the passive system: a unit force in the three translational directions and two unit moments acting at the center of the rigid source. The hybrid mounting system consists of four hybrid mounts. Each hybrid mount consists of a passive isolator (the same as that used in section 3.3 with the properties shown in Table 3.1) in combination with one actuator for each mount which only exerts a force in the out-of-plane direction of the receiver plate (thus the axial z- direction of the mounts).

3.4.1 Error criteria at the junctions of the receiver

The transmitted power is an overall measure for the vibration response of the receiver structure and for this reason an interesting error criterion for active control. However, many different cost functions can be defined to evaluate the active response of the isolation system. For now, the responses at the junctions of the receiver structure are considered for the error criteria. These types of error criteria have also been analyzed by Gardonio *et al.* [40, 41], but here the disturbance force excites five instead of three DOFs. In this subsection results of the active minimization of the following error criteria are shown: the transmitted power, the velocities at the junctions, the forces at the junctions and a combination of the latter two. The effectiveness of these control strategies is compared by considering the influence of these strategies on the transmitted power to the receiver structure. The transmitted power is thus considered as the performance response. The equations to determine the optimal actuator forces for error criteria at the junctions of the receiver structure were derived in section 2.6.2.

The best possible reduction of the transmitted power is by definition obtained by minimization of the transmitted power itself, see Figure 3.4(a). The actuators are able to reduce the transmitted power considerably over the entire considered frequency region. It is remarkable that less reduction is obtained in the frequency range from 2500 till 3000 Hz. This is caused by a relatively large transmitted power contribution in the in-plane directions of the receiver plate. The excitation frequency is close to two in-plane resonances of the receiver. The actuators cannot actuate in these directions and for this reason the transmitted power is hardly reduced at these frequencies.

Besides the minimization of the transmitted power, it is also possible to minimize just the forces ($J = \mathbf{f}_r^{\mathrm{H}} \cdot \mathbf{f}_r$) or the velocities ($J = \mathbf{v}_r^{\mathrm{H}} \cdot \mathbf{v}_r$) at the junctions of the receiver structure (thus at the locations where the mounting system is connected to the receiver structure). The results for these two error criteria are shown in Figure 3.4(b). A good reduction can be achieved with minimization of the forces or velocities at high frequencies. However, minimization of these cost functions results in less reduction of the transmitted power in the frequency region from 100 till 1000 Hz compared to minimization of the transmitted power itself. This effect is most pronounced for minimization of the forces, because the resonance frequencies of the actively controlled receiver structure remain unchanged. When the velocities are minimized also less reduction in transmitted power is obtained, but this is not so clearly visible because the resonance frequencies of the actively controlled receiver are shifted towards higher frequencies. The reason for this is that the minimiza-

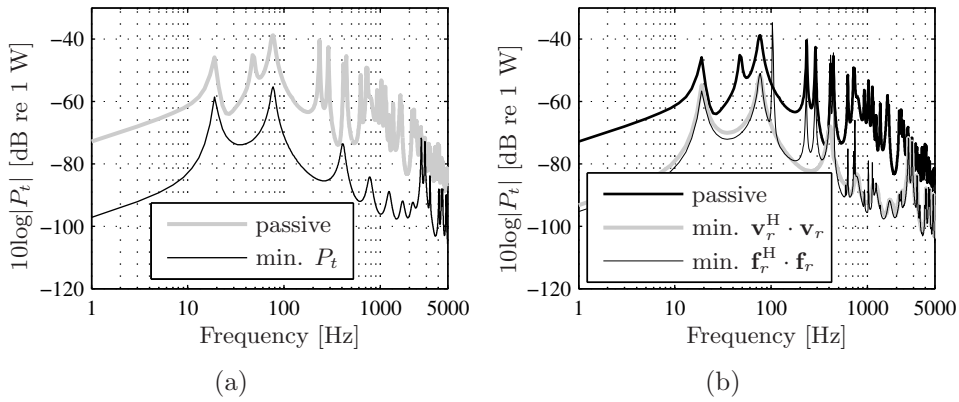

Figure 3.4: Active response of the analytical model of the hybrid isolation system for minimization of the transmitted power (a) and for minimization of the velocities and forces at the receiver junctions (b).

tion of velocities introduces an extra boundary condition at the connection points of the mounts, i.e. the movement of the receiver plate is restricted locally by the actuator influence and a pinned condition is introduced when only the velocities in the out-of-plane direction are considered in the cost function. For frequencies higher than the first few resonance frequencies of the receiver structure, the performance of minimization of velocities and forces is comparable to minimization of the transmitted power.

The active responses shown in Figure 3.4 are determined with error criteria that take into account the response in all the degrees of freedom at the connection points of the mounts with the receiver structure. These control strategies are difficult to implement in practical applications. The measurement of the moments is for example difficult. It has been shown that for this isolation system the transmitted power is dominated by the transfer in the axial direction of the mounts (the out-of-plane direction of the plate). For this reason, also error criteria are considered which minimize the transmitted power, velocities and forces in the axial direction of the mounts only (indicated by P_t^{ax}, $\mathbf{v}_r^{ax}$ and $\mathbf{f}_r^{ax}$ respectively). In Figure 3.5(a) the response is shown when the transmitted power is minimized in the axial direction only. The considerable increase in the transmitted power at low frequencies is remarkable. This is caused by the so-called *power circulation* [41]. The axial transmitted power is reduced in such a way that it even becomes negative. This means that power absorption in the axial direction is achieved, by introducing a lot of power

in especially the angular directions. In other words, power is injected in the angular directions and is absorbed in the axial direction. The result is that in the active situation a larger power transmission is obtained in comparison with the passive situation.

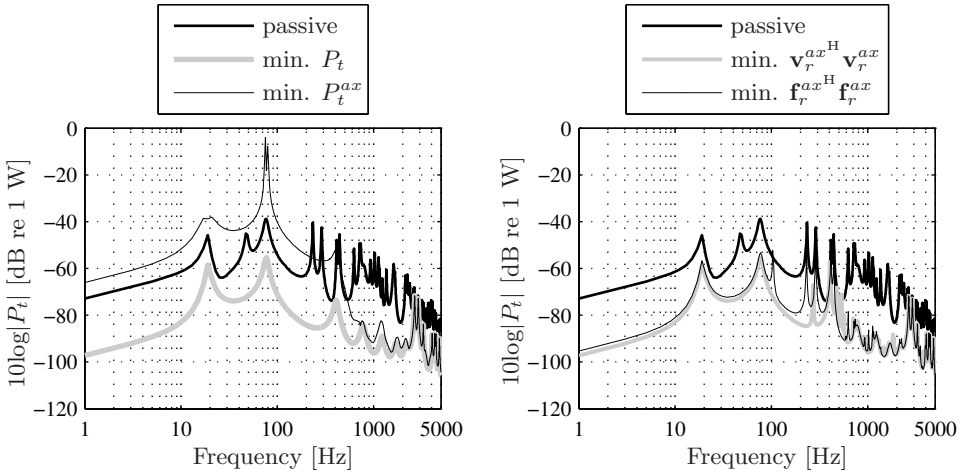

Figure 3.5: Active response of the analytical model of the hybrid isolation system with minimization of the axial transmitted power (a) and with minimization of the axial forces or velocities at the junctions on the receiver structure (b).

In Figure 3.5(b) the transmitted power is plotted for minimization of the axial forces or axial velocities. The same tendencies are observed as for minimization of all the force or velocity components at the connection points. The reduction at the first eigenfrequencies of the receiver is not so large, and for velocity minimization the eigenfrequencies of the actively controlled receiver plate are shifted upwards in the frequency range. To improve the performance of these cost functions it was suggested by Gardonio *et al.* [41] to implement a weighted combination as cost function: $J = \mathbf{v}_r^{ax\mathrm{H}}\mathbf{v}_r^{ax} + \mu\mathbf{f}_r^{ax\mathrm{H}}\mathbf{f}_r^{ax}$. It can be seen in Figure 3.6 that the minimization of this cost function results in a similar reduction compared to the minimization of the total transmitted power. Gardonio determined the factor μ by taking the square of the point mobility of an infinite receiving plate with the same thickness. The simulations presented here were performed for different values of μ, after which the best result was chosen (which was a value of $3.3 \cdot 10^{-8}$ s^2/kg^2). It can also be observed that no increase of the vibration occurs for this cost function.

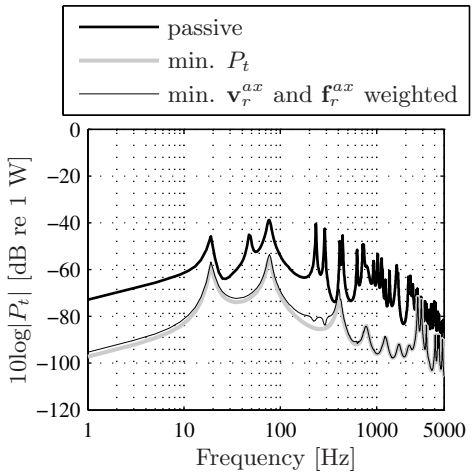

Figure 3.6: Active response in terms of the transmitted power for minimization of a weighted combination of the axial forces and velocities at the receiver junctions compared to minimization of the transmitted power itself.

3.4.2 Actuator effort

The actuators are modeled as an external force acting on the receiver only. It is also possible to design a mount with a reaction force against the source. The first concept, is e.g. a shaker that is attached to the receiver structure and supplies a force by reaction against its own mass. The second concept is the same shaker, but placed between the source and the receiver structure. These two actuator concepts are compared with each other in Figure 3.7(a) for minimization of total transmitted power. No difference can be distinguished in the performance for frequencies above the frequencies of the rigid body modes of the isolation system, but at lower frequencies no reduction is achieved with the actuator concept with reaction against the source. The performance of the second concept has a better performance in the lower frequency range where the rigid body modes occur. In Figure 3.7(b) the actuator effort is depicted for the two actuator principles. Typical of concept 2 is a high actuator force at frequencies below the eigenfrequencies of the rigid body modes [38]. Concept 1 has relatively high actuator forces at frequencies around the eigenfrequencies of the rigid body modes. The control effort at high frequencies is the same for both concepts.

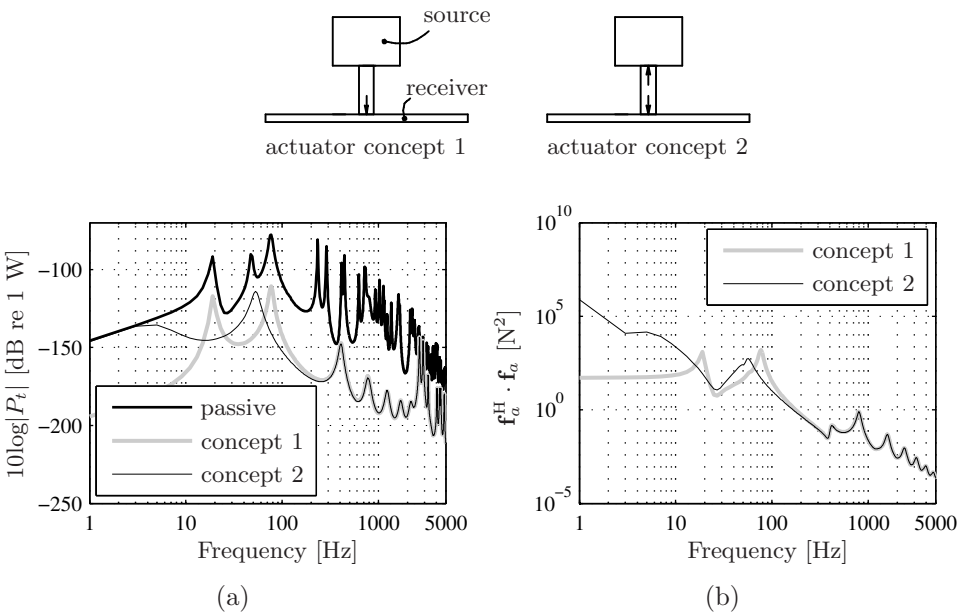

Figure 3.7: Active response with minimization of the transmitted power for the two actuator concepts in combination with the passive isolators (a) and the corresponding control effort (b).

3.4.3 Error criteria at the receiver

So far, error criteria have been considered that only take account of the responses at the connection points of the mounts with the receiver structure. The performance of the hybrid isolation system has been determined in terms of the transmitted power. However, with the used model description it is also possible to examine other error criteria consisting of more sensors attached to the receiver structure. In this subsection cost functions are analyzed that represent a measure for the response of the simply supported receiver plate. The performance of the hybrid isolation system is determined by the velocity distribution of the entire receiver plate.

The cost function related with the response of the receiver plate can in general be written as:

$$J = \mathbf{v}_{rec}^{\mathrm{H}} \cdot \mathbf{T}^{\mathrm{H}} \cdot \mathbf{W} \cdot \mathbf{T} \cdot \mathbf{v}_{rec}, \tag{3.15}$$

where $\mathbf{v}_{rec}$ is the velocity response vector at different points of the receiver structure, $\mathbf{T}$ is a matrix to filter or combine velocity components with dif-

ferent degrees of freedom and $\mathbf{W}$ is a matrix for weighting of the (filtered) velocity response. The matrix $\mathbf{T}$ is for example a matrix that filters the receiver response in such a way that only the velocities in the normal direction are considered. Examples of weighting matrices $\mathbf{W}$ are the mass matrix or the acoustic radiation matrix to analyze the kinetic energy or acoustic radiated power of (a part of) the receiver, respectively. More details about such error criteria and the determination of the optimal actuator forces are given in section 2.6.3. Important for the calculation of the response is the mobility matrix $\mathbf{Y}_{sr}$, which is the mobility matrix from the forces on the receiver structure at the junction points to receiver locations where the velocities are determined (see also equation (2.88)).

An example of a more global error criterion at the receiver structure is the total quadratic normal velocity response. Following the notation used in equation (3.15), this cost function can be written as:

$$J = \mathbf{v}_{rec}^{\mathrm{H}} \cdot \mathbf{T}^{n^{\mathrm{H}}} \cdot \mathbf{T}^{n} \cdot \mathbf{v}_{rec} = \mathbf{v}_{rec}^{n^{\mathrm{H}}} \cdot \mathbf{v}_{rec}^{n}, \tag{3.16}$$

where $\mathbf{v}_{rec}$ is the total velocity vector at the points of the considered grid, $\mathbf{T}^n$ is a matrix to filter the normal velocity vector out of the total velocity vector and $\mathbf{v}_{rec}^n = \mathbf{T}^n \cdot \mathbf{v}_{rec}$ is the resulting normal velocity vector. The normal velocity vector is determined at the same grid of points as shown in Figure 3.3. This cost function is interesting because the normal velocity gives a first indication of the sound field radiated by the receiver plate. The receiver plate behaves more stiffly in the in-plane direction than in the out-of-plane direction. This can be observed by the fact that the eigenfrequencies of the in-plane modes are much higher than the eigenfrequencies of the out-of-plane modes (see also Figure 3.3). For this reason the out-of-plane motion is mostly pronounced. The total kinetic energy of the receiver is dominated by the normal velocity response of the receiver structure. In Figure 3.8(a) the total quadratic normal velocity response is depicted when the transmitted power is minimized, and in Figure 3.8(b) the total quadratic normal velocity response is shown when only the axial velocity vector or axial force vector is minimized. Minimization of the transmitted power yields similar results as minimization of the sum of the potential and kinetic energy of the receiver structure (see appendix A). At higher frequencies (above the eigenfrequencies of the modes where the rigid source moves on the weak mounts without large deformation of the receiver structure), the kinetic energy dominates and has a much larger value than the potential energy. The normal velocity response has the largest contribution to the total kinetic energy. This property in combination with the equal mass distribution of the plate, explains the fact that minimization of the transmitted power results in a good reduction of the normal velocity response at the

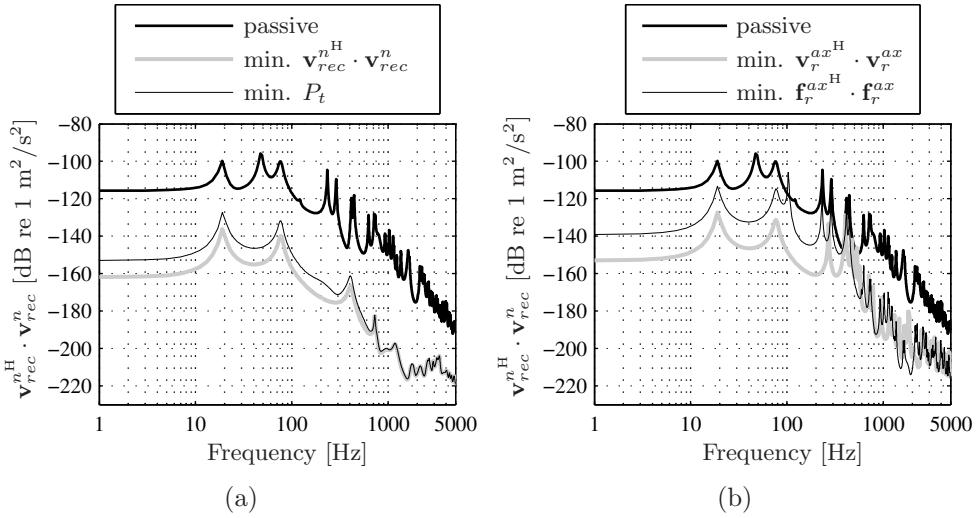

Figure 3.8: Active response in terms of the normal velocity distribution at a grid of points on the receiver plate for different error criteria.

considered grid points. Minimization of the axial velocities or forces at the junction points of the receiver results in less reduction of the normal velocity distribution compared to minimization of the transmitted power, especially in the lower frequency region till 1000 Hz.

It was seen in Figure 3.6 that the cost function consisting of a weighted combination of the axial junction velocities and forces at the receiver structure resulted in a very good reduction of the transmitted power. The reduction is almost as large as for the minimization of the transmitted power itself. For this reason, the influence of minimization of the weighted combination of the axial junction velocities and forces on the considered normal velocity response is considered. The result is shown in Figure 3.9 for the same weighting of the axial force as used in section 3.4.1 (μ is $3.3 \cdot 10^{-8}$ s^2/kg^2). The reduction for the weighted velocity and force combination is considerably less than for minimization of the transmitted power. Although the considered cost function reduces the transmitted power almost maximally (almost the same reduction is obtained as by minimization of the transmitted power itself), the velocity response of the receiver is much larger than when the transmitted power is minimized. Apparently, a small deviation in the actively transmitted power causes a relatively large deviation in the normal velocity response.

To give an impression of the influence of the actuators on the receiver

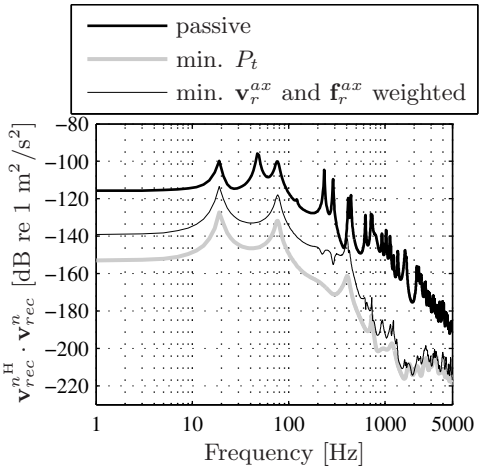

Figure 3.9: Active response in terms of the normal velocity distribution at a grid of points on the receiver plate for minimization of a weighted combination of the axial forces and velocities at the junctions compared to minimization of the transmitted power.

response for the different error criteria, the harmonic responses of the actively controlled receiver plate are shown in Figure 3.10. The harmonic deformation shapes are shown for the frequency of 75 Hz, because the deviations in the active response for the different error criteria are large for this frequency. The source makes a combined rigid body rotation around the x-axis and y-axis in the passive situation, as can be seen by the passive harmonic response of the receiver plate in Figure 3.10(a). A good reduction of the displacement is shown when the transmitted power is minimized. The velocities at the junctions of the receiver structure are reduced considerably which can be seen clearly from the deformed shape in Figure 3.10(b). A similar deformed shape is obtained by minimization of the axial velocities at the mount junctions, see Figure 3.10(d). Minimization of the axial forces yields a reduction of the velocity response, but the deformation shape does not change very much in comparison to the passive deformation as can be seen in Figure 3.10(e). When the transmitted power in the axial direction is minimized, the receiver response has a higher level because of the power circulation phenomenon (see Figure 3.10(c)). Most reduction in terms of the normal velocity response is obtained by definition by minimization of the normal velocities themselves. The deformed shape of the active response of the receiver plate with minimization of this error criterion is shown in Figure 3.10(f).

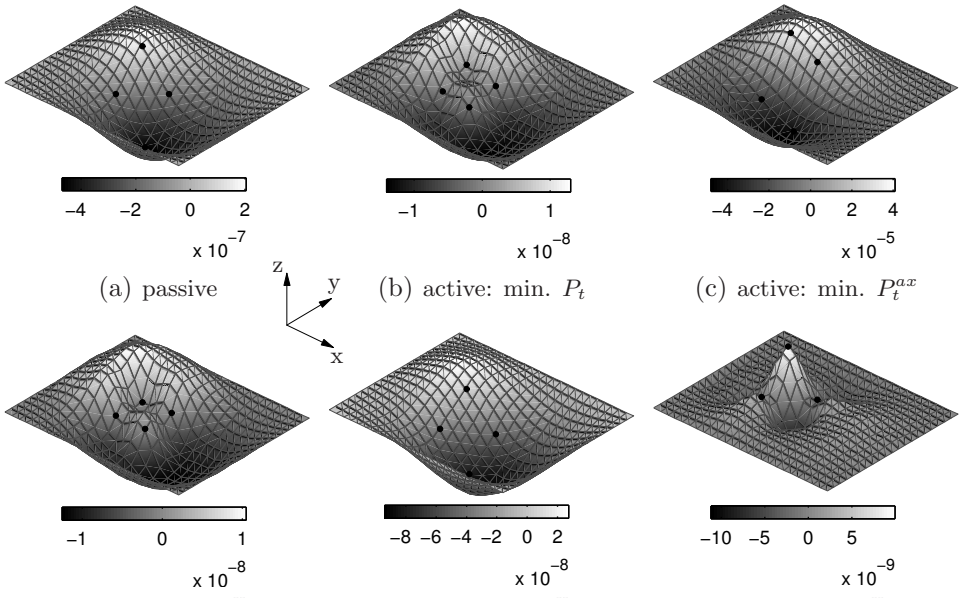

(a) passive (b) active: min. P_t (c) active: min. P_t^{ax}

(d) active: min. $\mathbf{v}_r^{ax^{\mathrm{H}}} \cdot \mathbf{v}_r^{ax}$ (e) active: min. $\mathbf{f}_r^{ax^{\mathrm{H}}} \cdot \mathbf{f}_r^{ax}$ (f) active: min. $\mathbf{v}_{rec}^{n^{\mathrm{H}}} \cdot \mathbf{v}_{rec}^{n}$

Figure 3.10: Active deformation shapes of the receiver plate at 75 Hz. The gray-scale represents the amplitude of the displacement in the z-direction.

3.4.4 Sound radiation and acoustic error criteria

Only structurally related error criteria have been considered so far. These error criteria are referred to as active vibration control (AVC) strategies or in this case active vibration isolation strategies. For this type of isolation, only the structural response of the structure is considered. Another control strategy is to change or reduce the vibration with the objective to minimize the sound radiation of (a part of) the receiver structure, a so-called active structural acoustic control (ASAC) approach. This ASAC approach is considered in this subsection, by considering the performance of the isolation system in terms of the radiated sound power.

In section 2.5.2 it was explained how the radiated sound power L_w of a baffled plate can be determined. With the assumption that the receiver plate is placed in a baffle, the acoustic radiation matrix $\mathbf{R}$ is given by equation (2.48) and the radiated sound power can consequently be written as:

$$J = L_w = \mathbf{v}_{rec}^{n^{\mathrm{H}}} \cdot \mathbf{R} \cdot \mathbf{v}_{rec}^{n}, \tag{3.17}$$

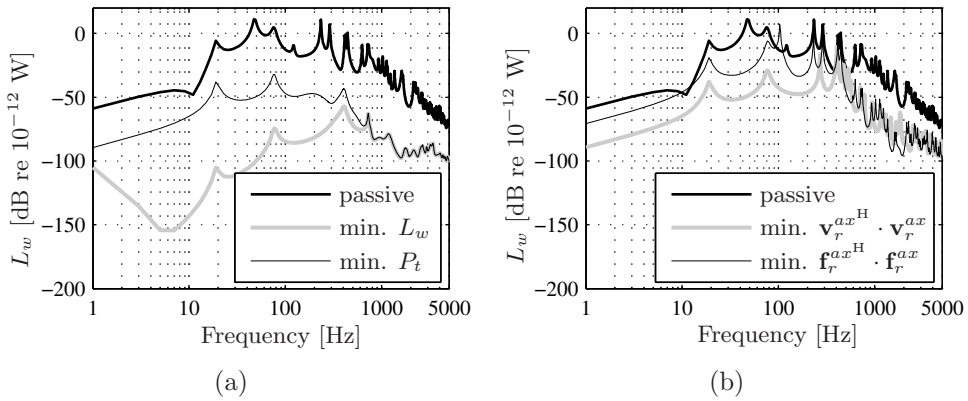

Figure 3.11: Active response in terms of the radiated sound power of the receiver plate when the transmitted power is minimized (a) and when the axial velocities or forces at the junctions are minimized.

where $\mathbf{v}_{rec}^{n\mathrm{H}}$ is the normal velocity vector of the receiver plate at the same grid of points as considered in the previous subsection. This equation can be written in the Hermitian quadratic form in terms of the actuator forces, after which the optimal actuator force can be determined as explained in section 2.6.4.

The active response in terms of the radiated sound power is depicted for minimization of the transmitted power and for minimization of the radiated sound power itself in Figure 3.11(a). The reductions obtained by minimization of the transmitted power are much less than the maximum reduction that is obtained by minimization of the radiated sound power up to a frequency of 1000 Hz. At higher frequencies minimization of the transmitted power results in similar reductions as minimization of the radiated sound power itself.

Also the influence of the error criteria that minimize the axial velocities and forces at the junctions of the receiver structure on the radiated sound power is depicted in Figure 3.11(b). The same tendencies in terms of the radiated sound power can be observed as for the response in terms of the normal velocity distribution. Minimization of the axial velocities has a better performance for the frequency range up to 400 Hz. For higher frequencies, the performance of both error sensor strategies are similar, but slightly less than minimization of the transmitted power. The influence of the error criterion consisting of a weighted combination of the axial velocities and forces on the radiated sound power is depicted in Figure 3.12(a). For the considered weighting factor (μ is $3.3 \cdot 10^{-8}$ s^2/kg^2 as shown in section 3.4.1), this error criterion

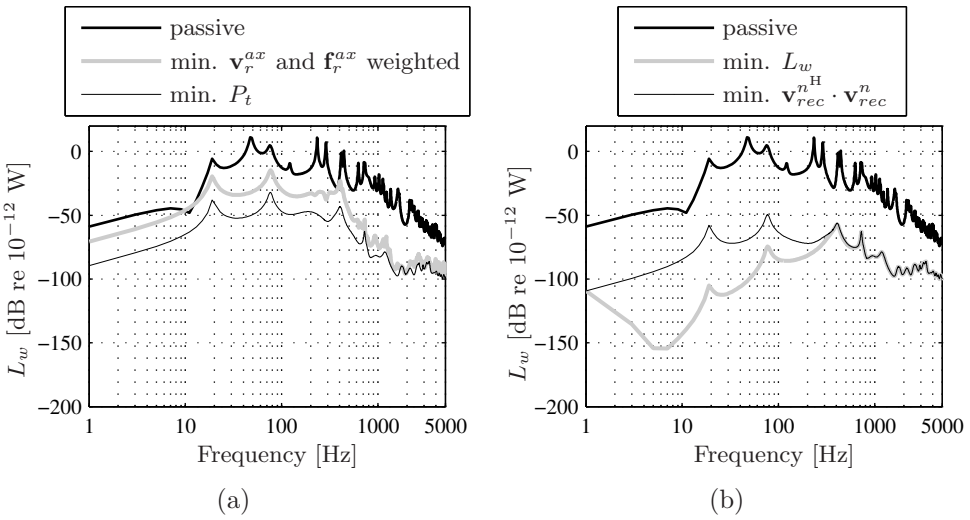

Figure 3.12: Active response in terms of the radiated sound power when the transmitted power and a weighted combination of the axial forces and velocities are minimized (a) and when the normal velocity distribution is minimized (b).

results in the same reductions as minimization of the axial forces only up to a frequency of around 100 Hz. At higher frequencies the results are better compared to minimization of the axial forces and velocities only, and equal to the reductions obtained with minimization of the transmitted power. The reduction of the radiated sound power for minimization of the (unweighted) normal velocity distribution is shown in Figure 3.12(b). This is an example of the fact that active vibration control approach (AVC) differs from the active acoustic vibration isolation approach (ASAC). In the frequency range up to 400 Hz, the weighting with the radiation matrix results in considerable extra reduction. However, for frequencies larger than 500 Hz, the followed approach has no influence and both error sensor strategies result in similar reductions.

3.5 Concluding remarks

In this chapter an analytical model of a hybrid isolation system was presented with a mobility and impedance matrix approach. The general model described in chapter 2 was used as a basis for the presented analytical model. The analytical model itself is based on an existing model presented by Gardonio *et al.* [40, 41], but extended to a three-dimensional excitation of the source. The

general model uses a port description to connect the isolation system components with each other. Therefore also point mobilities of the receiver structure have to be determined. When a modal superposition is used to describe the dynamics of the receiver structure, it was seen that the contribution of the modes with high eigenfrequencies that are omitted in the modal superposition, may be large on the considered mobility. The error due to this effect can be reduced quite effectively by taking into account so-called *residual modes*.

In chapter 2 it was shown that it is preferable to design the mounting system as flexible as possible. However, in practical applications other restrictions play a role that limit the flexibility of the mounting system. Using active isolation is a good option, considering the results of the described analytical model. A large reduction of the transmitted power over the whole frequency range is obtained, even when only the forces or the velocities in the normal direction at the junctions of the receiver plate are considered. Minimization of the transmitted power with respect to one degree of freedom (for each mount) is not preferable because of the *power circulation* phenomenon in the low frequency range. Also control strategies have been analyzed that take account of a more global measure of the whole receiver response. The considered control strategies that only take account of the response at the junctions of the receiver structure have a good performance in terms of the global receiver response at high frequencies. Besides active vibration isolation strategies also an active structural acoustic isolation control strategy is analyzed by considering the radiated sound power of the receiver plate.

The analytical model described in this chapter is a more realistic representation of real-life isolation systems than the oscillator models described in chapter 2. The mounting system is more realistic and has multi-point and multi-directional vibration transmission paths to the receiver structure. Also quite complex dynamic behavior with characteristic deformation patterns occurs like in real-life isolation systems. However, the receiver structure is still a very simple structure and has some typical properties. The structural power transmission occurs especially in the normal direction of the mounts. When other directions play an important role in the power transmission, for example at frequencies where in-plane resonances of the plate occur, it was seen that the actuators were not able to reduce the transmitted power. In realistic isolation systems the vibration transmission is not so pronounced in one direction. For this reason, a more complicated receiver structure will be analyzed in the next chapter.

Chapter 4

Numerical studies on a laboratory setup of a hybrid isolation system

4.1 Introduction

In the previous chapter an analytical model of a hybrid isolation system was studied. This model is useful for understanding the underlying physics of isolation systems, but is in general not suitable for the representation of 'real-life' and complex hybrid isolation systems like resilient mounting systems for heavy machinery in ships. In this chapter a more advanced modeling technique is presented that can be used as a basis for the investigation and design of more complex hybrid isolation systems. The general theory of chapter 2 is again used to determine the passive and active responses of the whole system. The receiver structure is quite complex and for this reason modeled with the numerical Finite Element Method. One of the promising applications of hybrid isolation systems is the isolation of heavy machinery in vehicles. To investigate this kind of applications for applying hybrid isolation techniques in more detail, TNO built a small-scale laboratory arrangement that, as a vibratory system, has sufficient complexity to offer some difficulties representative for a hybrid isolation system in a ship (see section 4.2). In this chapter a numerical model of a laboratory setup is described. This numerical model is used to investigate different actuator and sensor configurations for hybrid isolation.

As stated earlier, the goal of the numerical models is not to have an exact representation of real-life systems. The numerical models are used as models with representative complexity for the considered applications for hybrid

isolation. These models enable the development and testing of general active isolation concepts. More details about the laboratory setup are given in section 4.2.

The procedure to determine the dynamic response of the hybrid isolation system consists of several steps. The first step is to determine the structural behavior of the receiver structure due to the excitation mechanisms of the source. In the next step, a similar procedure is followed to obtain the influence of the actuators on the structural behavior of the receiver structure. The Finite Element Method is used to describe the dynamics of the receiver structure and this is explained in more detail in section 4.3. The numerical model of the laboratory setup is described in section 4.4. In combination with the model of the mounting system, the passive and active structural responses of the whole isolation system can be determined as described in section 2.4.3. For the determination of the active response, the *optimal control* procedure is used again, implying that an ideal feedforward controller is used to tackle the controller problem.

The numerical model of the laboratory setup is used to investigate different actuator and sensor configurations for hybrid isolation. First, attention is paid to the actuator configuration in section 4.5. For cost-effective hybrid isolation, it is important to reduce the number of actuators and to reduce the actuator effort needed to obtain active reduction. For this reason attention is paid how to determine the most effective number of actuators and actuator directions. Both the obtained active reduction and required actuator effort are consequently considered to determine effective actuator configurations.

Also attention is paid to the sensor configuration used for active isolation. First some vibration sensor strategies (AVC approach) are considered in section 4.6. Results of different sensor strategies are considered with variation of the location of the error sensors, i.e. locating the vibration sensors near the source or at some distance from the source where the reduction is desired. Also global error sensor strategies are investigated like the minimization of the kinetic energy of the receiver structure. Attention is paid to the reduction of the error sensor response itself, but also the influence of local vibration control on the global response of the receiver structure ia analyzed. When the vibrational response of the receiver structure is known, it is possible to determine the acoustic sound field of a part of the receiver structure. In this work, the free field radiation of a baffled part of the receiver structure and the acoustic radiation of a part of the receiver structure into an acoustic enclosure is considered. This enables consideration of acoustic error sensor criteria and responses (ASAC approach) as presented in section 4.7.

Finally some conclusions are drawn from the analysis of the different actuator and sensor configurations and presented in section 4.8.

4.2 Laboratory setup used for the numerical simulations

The laboratory setup built by TNO as a representative application for hybrid isolation is shown in Figure 4.1. More detailed information about the laboratory setup can be found in the diagram in Figure 4.2 and Table 4.1. The different components of the isolation system are indicated in the figure: the source, a mounting system consisting of passive vibration isolator, mounts and actuators and a receiver structure. Notice that the whole system is supported by soft supports to dynamically decouple the whole system from its environment. The mounting system is attached via the stiffeners on the foundation plate. This test setup was designed to develop and test different active isolation strategies and was used as a demonstration setup for an operational hybrid isolation system. The test setup is simple enough to be modeled using numerical techniques like the finite element method. These numerical simulations are useful to analyze the influence of different actuator configurations and sensor positions and other physical properties on the performance of the hybrid isolation system in a relatively easy way. Besides that, responses of

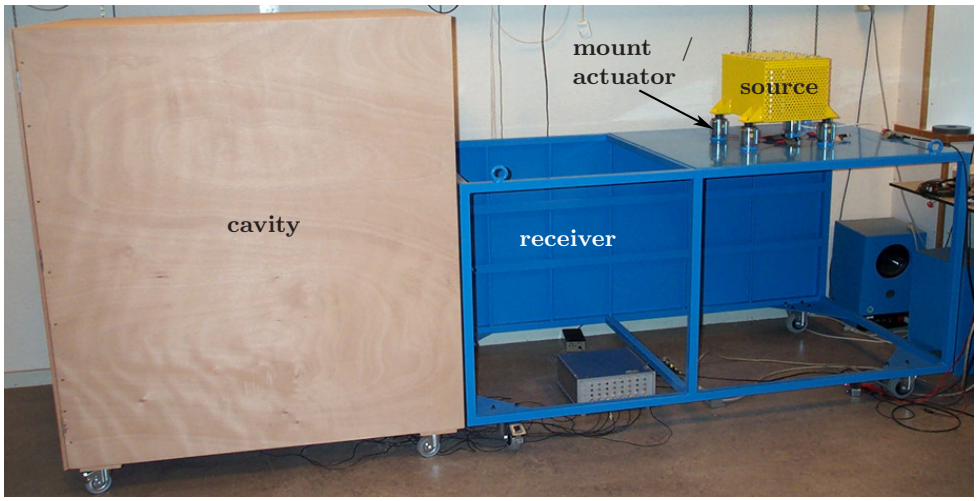

Figure 4.1: Photo of the laboratory setup at TNO.

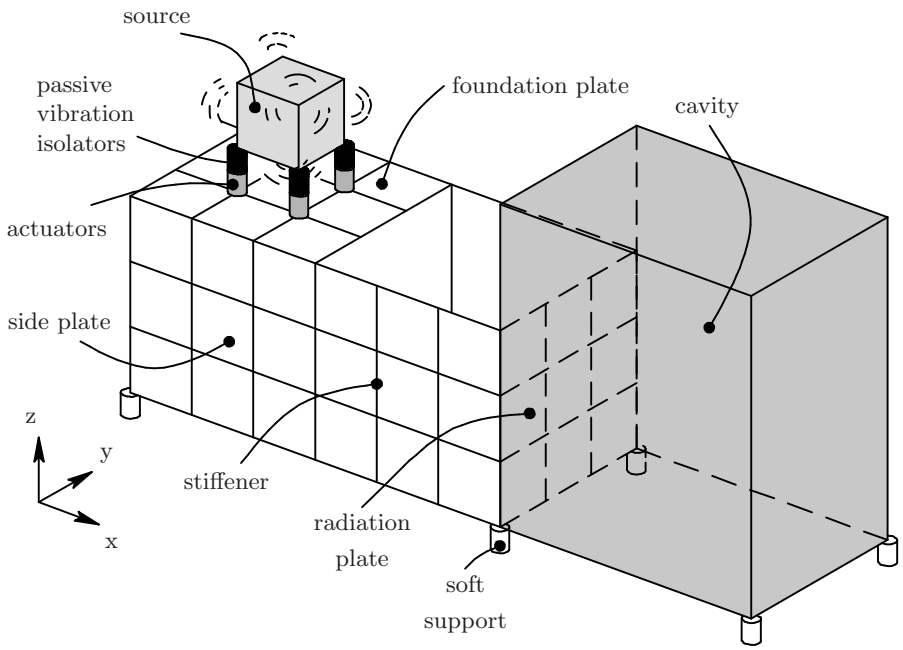

Figure 4.2: Schematic picture of the laboratory setup at TNO.

the isolation system can be considered that are hard or impossible to measure at the setup, like the kinetic energy contents of the receiver structure. Earlier work on this laboratory arrangement concerning actuator and sensor positions was published by Basten and Verheij [2]. The experiences and results obtained with this numerical model provide insight into the use of the hybrid isolation concept for the demonstrator and other complex applications of resilient mounting systems.

4.3 Structural model

The hybrid isolation model is again considered to be composed of three components: a source of vibration, a passive resilient mounting system and a receiver structure. The three components are coupled with each other at the junctions as described in chapter 2. However, the source is not modeled as a rigid mass. Generally speaking, the dynamic behavior of the source is quite complicated, resulting in a frequency dependent multi-directional vibration transmission to the receiver structure. The dynamic behavior of a rigid mass is too simple for

such complex excitations and for this reason the source is modeled by a force excitation vector underneath the passive vibration isolators. The complete model for this case is described by the equations presented in section 2.4.3.

4.3.1 Dynamics of the pedestals

The dynamics of the source is represented by a disturbance force vector acting on top of the actuators as shown in Figure 4.2. The actuators are part of the hybrid mounting system and are modeled as rigid pedestals. The dynamics of the pedestals are represented using the field representation at the junctions (a port at the top and at the bottom-side) of each mount of the mounting system, as described in chapter 2. The frequency dependent forces and velocities at each junction are represented by a vector with three translational and three rotational components. This kind of representation is only valid for linear systems [121, 122] and connections at the top and bottom of the pedestals are modeled as point contacts. The resulting equations that relate the velocities and forces at the junctions of the pedestals with each other can be written in the same way as shown in section 2.4.3 as:

$$\mathbf{f}_d = \mathbf{Z}_{ss} \cdot \mathbf{v}_{ms} + \mathbf{Z}_{sr} \cdot \mathbf{v}_{mr}, \tag{4.1}$$

$$\mathbf{f}_{mr} = \mathbf{Z}_{rs} \cdot \mathbf{v}_{ms} + \mathbf{Z}_{rr} \cdot \mathbf{v}_{mr} + \mathbf{T}_a \cdot \mathbf{f}_a, \tag{4.2}$$

where $\mathbf{f}_d$ is the disturbance force vector acting at the top of the pedestals, $\mathbf{Z}_{ss}$ and $\mathbf{Z}_{rr}$ are the blocked dynamic driving point impedance matrices at the top (source side) and bottom side (receiver side) of the pedestals respectively, $\mathbf{Z}_{sr}$ and $\mathbf{Z}_{rs}$ are the blocked dynamic transfer impedance matrices of the mounting support, $\mathbf{T}_a$ is a transformation matrix to define the degrees of freedom which are actuated and $\mathbf{f}_a$ is the vector containing the actuator forces. The pedestals in this chapter are considered as beams and the impedance matrices are calculated by harmonic analyses with the FEM package Ansys. In chapter 5 attention is focused on the modeling of the rubber part of the mounting system.

4.3.2 Dynamics of the receiver structure

Isolation systems used for heavy machinery such as in ships in general have complex receiver structures. Numerical methods like FEM can be used to obtain a dynamic model of this type of structure. However, in the literature in most cases relatively simple isolation systems are considered which can be described with an analytical formulation as shown in chapter 3. Jenkins *et al.* [59] used a finite element approach to model a raft-isolator-receiver system,

where the receiver was a clamped plate. In this chapter a general procedure is presented to model isolation systems with complex receiver structures across a large frequency range.

FEM equations

The finite element equations of motion for a linear dynamic structure are given by:

$$\mathbf{M} \cdot \ddot{\mathbf{u}}(t) + \mathbf{C} \cdot \dot{\mathbf{u}}(t) + \mathbf{K} \cdot \mathbf{u}(t) = \mathbf{f}(t), \tag{4.3}$$

where $\mathbf{u}(t)$ is the vector with the nodal structural displacements, $\mathbf{f}(t)$ is the vector with nodal forces and $\mathbf{M}$, $\mathbf{C}$ and $\mathbf{K}$ are the mass, damping and stiffness matrices, respectively. Generally speaking, a FEM model contains many degrees of freedom (DOFs) for an accurate prediction of the dynamical behavior. This involves large computation times for the evaluation. To reduce the computation time, the number of DOFs is reduced with the mode superposition technique, often used in the field of structural dynamics.

Modal expansion

The modal expansion is used to express the response of the FEM model in terms of the undamped eigenvectors of the problem. The eigenvectors are determined by solving the equations of motion for the undamped free vibration problem ($\mathbf{C} = \mathbf{0}$ and $\mathbf{f} = \mathbf{0}$). When the excitation varies harmonically with respect to the time ($\mathbf{u}(t) = \mathbf{u}\,\mathrm{e}^{\mathrm{j}\omega t}$), the equation of motion reduces to:

$$\left(-\omega^2\mathbf{M} + \mathbf{K}\right) \cdot \mathbf{u} = \mathbf{0}. \tag{4.4}$$

The solution of this eigenvalue problem yields n eigenfrequencies ω_i and corresponding eigenmodes $\boldsymbol{\phi}_i$ where n is the number of DOFs. The matrices with the eigenfrequencies $\boldsymbol{\Omega}$ and eigenmodes $\boldsymbol{\Phi}$ are defined as:

$$\boldsymbol{\Omega} = \begin{bmatrix} \omega_1 & 0 & \cdots & 0 \\ 0 & \omega_2 & & 0 \\ \vdots & \vdots & \ddots & \vdots \\ 0 & 0 & \cdots & \omega_n \end{bmatrix} \qquad \boldsymbol{\Phi} = \begin{bmatrix} \boldsymbol{\phi}_1 & \boldsymbol{\phi}_2 & \cdots & \boldsymbol{\phi}_n \end{bmatrix}. \tag{4.5}$$

The eigenmodes are normalized with respect to the mass matrix, resulting in:

$$\boldsymbol{\Phi}^{\mathrm{T}} \cdot \mathbf{M} \cdot \boldsymbol{\Phi} = \mathbf{I}, \tag{4.6a}$$

$$\boldsymbol{\Phi}^{\mathrm{T}} \cdot \mathbf{K} \cdot \boldsymbol{\Phi} = \boldsymbol{\Omega}^2, \tag{4.6b}$$

where $\mathbf{I}$ is the identity matrix. The solution of $\mathbf{u}$ for each frequency can now be written in the form of a modal expansion according to:

$$\mathbf{u} = \mathbf{\Phi} \cdot \mathbf{q}\,, \tag{4.7}$$

where $\mathbf{q}$ is the vector with modal participations. Substituting equation (4.7) in equation (4.3) and pre-multiplying with $\mathbf{\Phi}^{\mathrm{T}}$ yields:

$$-\omega^2 \mathbf{I} \cdot \mathbf{q} + \mathrm{j}\omega\, \mathbf{\Phi}^{\mathrm{T}} \cdot \mathbf{C} \cdot \mathbf{\Phi} \cdot \mathbf{q} + \mathbf{\Omega}^2 \cdot \mathbf{q} = \mathbf{\Phi}^{\mathrm{T}} \cdot \mathbf{f}\,. \tag{4.8}$$

If the term $\mathbf{\Phi}^{\mathrm{T}} \cdot \mathbf{C} \cdot \mathbf{\Phi}$ is a diagonal matrix, the equations of motion are uncoupled. Often a diagonal matrix with a damping ratio for each mode i is composed (or determined with measurements) according to:

$$\mathbf{\Phi}^{\mathrm{T}} \cdot \mathbf{C} \cdot \mathbf{\Phi} = \mathrm{diag}(2\zeta_i\, \omega_i) = 2\, \mathbf{\Xi}_m \cdot \mathbf{\Omega}, \tag{4.9}$$

where ζ_i is the damping ratio of mode i and $\mathbf{\Xi}_m$ is the so-called modal damping matrix. Another damping mechanism that results in a diagonal damping matrix is the so-called proportional damping or Rayleigh damping, where the damping matrix is a linear combination of the mass and stiffness matrices:

$$\mathbf{C} = \alpha\, \mathbf{M} + \beta\, \mathbf{K}, \tag{4.10}$$

resulting in:

$$\mathbf{\Phi}^{\mathrm{T}} \cdot \mathbf{C} \cdot \mathbf{\Phi} = \mathrm{diag}(2\, \zeta_i \omega_i) = 2\, \mathbf{\Xi}_p \cdot \mathbf{\Omega}, \tag{4.11}$$

where ζ_i is the damping ratio of mode i and $\mathbf{\Xi}_p$ is the modal damping matrix for the proportional damping mechanism. It can be shown that the damping ratio of each mode is related to the factors α and β of equation (4.10) according to:

$$\zeta_i = \frac{1}{2}\left(\frac{\alpha}{\omega_i} + \beta\, \omega_i\right). \tag{4.12}$$

In the case of these two damping mechanisms, the modal participations for each mode are determined by:

$$q_i = \frac{\boldsymbol{\phi}_i \cdot \mathbf{f}}{\left(-\omega^2 + 2\mathrm{j}\omega\zeta_i\omega_i + \omega_i^2\right)}, \qquad i = 1 \ldots n. \tag{4.13}$$

Another way to model damping is by means of the implementation of a complex stiffness matrix, which is referred to as structural damping. The equations of motion for this damping model and for a construction with isotropic material become:

$$-\omega^2 \mathbf{q} + (1 + \mathrm{j}\eta)\, \mathbf{\Omega}^2 \cdot \mathbf{q} = \mathbf{\Phi}^{\mathrm{T}} \cdot \mathbf{f}\,, \tag{4.14}$$

where η is the structural loss factor. The modal participations are then determined by:

$$q_i = \frac{\boldsymbol{\phi}_i \cdot \mathbf{f}}{\left((1+\mathrm{j}\eta)\,\omega_i^2 - \omega^2\right)}, \qquad i = 1 \ldots n. \tag{4.15}$$

Truncated modal superposition and residual flexibility

In a similar way as in section 3.2.3, the model is reduced by truncation of the modal expansion, depending on the frequency range of interest. When only m modes instead of the total number of modes n are taken into account, the expansion for proportional or modal damping can be written as:

$$\mathbf{u} = \sum_{i=1}^{m} \boldsymbol{\phi}_i q_i + \sum_{i=m+1}^{n} \boldsymbol{\phi}_i q_i, \qquad q_i = \frac{\boldsymbol{\phi}_i \cdot \mathbf{f}}{\left(-\omega^2 + 2\mathrm{j}\omega\zeta_i\omega_i + \omega_i^2\right)}. \tag{4.16}$$

The term that is omitted in the truncated modal superposition can again be estimated in terms of a static response:

$$\mathbf{u} \approx \sum_{i=1}^{m} \frac{\boldsymbol{\phi}_i \cdot \boldsymbol{\phi}_i^{\mathrm{T}} \cdot \mathbf{f}}{\left(-\omega^2 + 2\mathrm{j}\omega\zeta_i\omega_i + \omega_i^2\right)} + \mathbf{u}_0 - \sum_{i=1}^{m} \frac{\boldsymbol{\phi}_i \cdot \boldsymbol{\phi}_i^{\mathrm{T}} \cdot \mathbf{f}}{\omega_i^2}. \tag{4.17}$$

For structural damping, the truncated modal expansion becomes:

$$\mathbf{u} = \sum_{i=1}^{m} \boldsymbol{\phi}_i q_i + \sum_{i=m+1}^{n} \boldsymbol{\phi}_i q_i, \qquad q_i = \frac{\boldsymbol{\phi}_i^{\mathrm{T}} \cdot \mathbf{f}}{(1+\mathrm{j}\eta)\,\omega_i^2 - \omega^2}. \tag{4.18}$$

The truncated modal expansion with residual flexibility is consequently determined by:

$$\mathbf{u} \approx \sum_{i=1}^{m} \frac{\boldsymbol{\phi}_i \cdot \boldsymbol{\phi}_i^{\mathrm{T}} \cdot \mathbf{f}}{(1+\mathrm{j}\eta)\,\omega_i^2 - \omega^2} + \frac{\mathbf{u}_0}{(1+\mathrm{j}\eta)} - \sum_{i=1}^{m} \frac{\boldsymbol{\phi}_i \cdot \boldsymbol{\phi}_i^{\mathrm{T}} \cdot \mathbf{f}}{(1+\mathrm{j}\eta)\,\omega_i^2}. \tag{4.19}$$

The response in terms of velocities is determined in the same way, by multiplication with a $\mathrm{j}\omega$ term because of the harmonic time dependence. Using equation (4.17) or (4.19), the response at different points of the receiver structure can be determined for different excitations of the receiver structure. With a prescribed excitation at each junction of the receiver structure in each degree of freedom the velocity response at all degrees of freedom at the junction points can be determined, resulting in the following mobility matrix as discussed in section 2.4:

$$\mathbf{v}_r = \mathbf{Y}_r \cdot \mathbf{f}_r. \tag{4.20}$$

4.4 Total model

In this section a numerical model of the laboratory setup is introduced and analyzed in more detail. The theory presented earlier in this chapter is applied to this numerical model and passive and active results for structural and acoustic error criteria are presented. First, the passive behavior of the model is analyzed. After that, attention is paid to the actuator configuration and results are presented for different error sensor strategies.

4.4.1 Laboratory arrangement

In Figure 4.2 a schematic picture of the laboratory setup is presented. The receiver consists of a carrier structure and an enclosure into which sound is radiated by a part of the carrier structure, the so-called radiation plate. Furthermore, a foundation plate and a side plate are distinguished as part of the carrier structure. The carrier structure is built from stiffened plates and beams and the overall dimensions are approximately 1.75m $\times$ 0.9m $\times$ 0.85m. The enclosure is a wooden box with approximate dimensions 1.2m $\times$ 0.9m $\times$ 1.4m. More information about the dimensions of the laboratory setup are shown in Table 4.1.

Component	**Parameter**	**Value**
Foundation plate	Dimensions ($L_x \times L_y \times h$)	$950 \times 850 \times 3$ mm
Side plate	Dimensions ($L_x \times L_z \times h$)	$1700 \times 800 \times 3$ mm
Radiation plate	Dimensions ($L_y \times L_z \times h$)	$850 \times 800 \times 3$ mm
Mounts (4)	Dimensions (diameter $\times$ height)	50×100 mm
Cavity	Dimensions ($L_x \times L_y \times L_z$)	$1200 \times 900 \times 1400$ mm

Table 4.1: Most important dimensions of the laboratory setup.

4.4.2 Finite Element Model of the laboratory setup

For an easy investigation of different active isolation concepts, a numerical FEM model is made of the laboratory setup [90]. The main goal is to have a numerical model that is representative for realistic applications. For this reason the demonstrator has relatively large dimensions and is composed of plates and beams and beam-stiffened plates. The structure must have a 'complex' behavior in a dynamic perspective, meaning that a variety of dynamic

deformation shapes occur in the considered frequency range. Another typical property of complex structures is a high number of modes and corresponding high modal density. Furthermore, it is necessary that the machinery excite the structure at different locations (multi-point) and in different directions (multi-directional). First, it is examined whether the numerical model is representative with respect to its dynamical behavior. The finite element model of

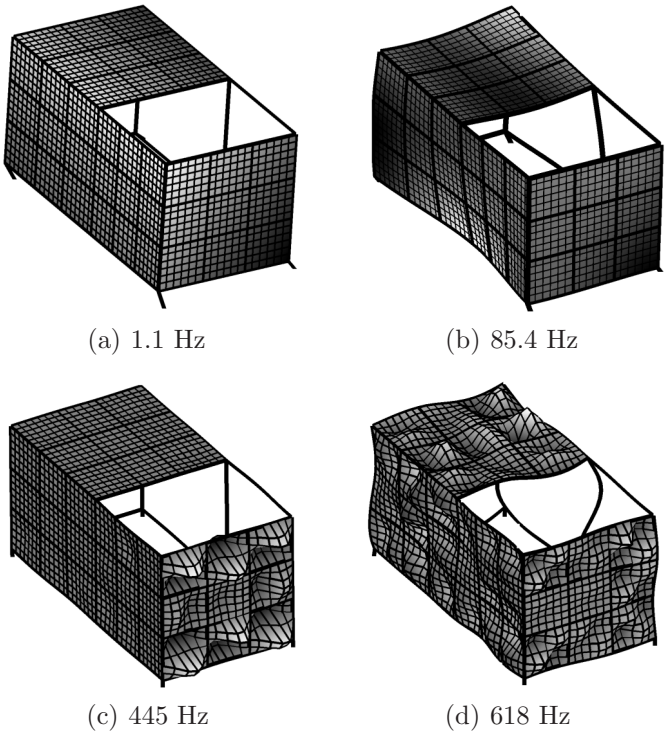

(a) 1.1 Hz (b) 85.4 Hz

(c) 445 Hz (d) 618 Hz

Figure 4.3: Different structural modes of the receiver structure.

the demonstrator is composed in ANSYS and consists of linear shell elements (four-node SHELL63 elements) and three-dimensional beam elements (two-node BEAM4 elements) [82]. The material properties used for the numerical analysis of the structure are shown in Table 4.2.

Four of the eigenmodes resulting from the modal analysis are depicted in Figure 4.3. The mode shown in Figure 4.3(a) has an eigenfrequency of 1.1 Hz and is one of the 'rigid body' modes, clearly distinguished by the rigid motion of the whole structure on the soft mounts. Six of these modes are present because the whole structure moves as a rigid body on the relatively

Component	Parameter	Value
Young's modulus	E	210 GPa
Poisson's ration	ν	0.3 [-]
Structural loss factor	η	0.01 [-]
Density	ρ	7800 [kg/m^3]

Table 4.2: Material properties used for the numerical model of the laboratory setup.

soft supports. These modes have very low eigenfrequencies and are the first modes in the series of the calculated eigenmodes. The second mode which is shown in Figure 4.3(b) is an example of a 'global mode', meaning that the structure deforms in a global sense. This kind of mode occurs especially in the lower frequency range. At higher frequencies the eigenmodes are quite complex and may have very local deformations as shown in Figure 4.3(c) or may have a combination of global and local deformation as for example the mode shown in Figure 4.3(d). Besides the variety of the type of modes, a high number of modes and a high modal overlap are representative for vehicle structures in general. For the considered laboratory model, around 250 modes are found with an eigenfrequency below 1000 Hz. An indication of the modal overlap can be obtained using the natural frequencies of the structure by definition of the half-value bandwidth [23]:

$$b = \eta f_n, \tag{4.21}$$

where b is the half-value bandwidth, η is the structural loss factor and f_n is the n^{th} natural frequency of the structure. The half-value bandwidth is defined as the frequency band around the natural frequency where the response is larger than half of the value of the peak response. With the assumption that each mode is excited equally, an indication of the modal overlap can be calculated as shown in Figure 4.4. The modal overlap is determined with a structural loss factor of $\eta = 0.01$ (see Table 4.2) and for a frequency resolution of 2 Hz (500 frequency steps). For each frequency it is checked whether this frequency is situated in the half-value bandwidth of a natural frequency. The natural frequencies that fulfill this condition are subsequently summed, and in this way an indication of the modal overlap is obtained at the considered frequency. The modal overlap is quite high, especially at high frequencies, meaning that the total response at a single frequency is dominated by several modes, which is representative for many large structures in practice.

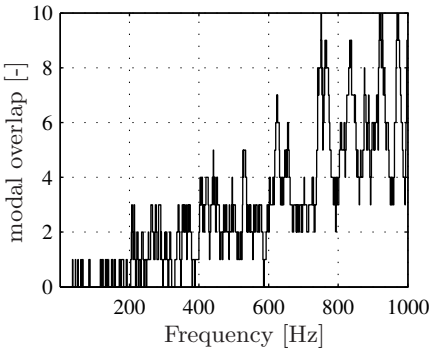

Figure 4.4: Modal overlap of receiver structure.

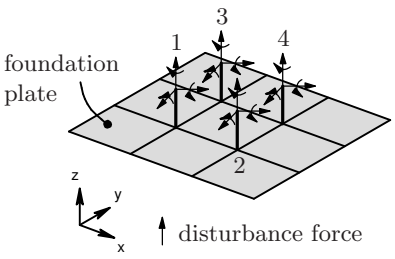

mount	Comp.	Value
1	f_x, f_y, f_z	1 N
	m_x, m_y, m_z	1 Nm
2	f_x, f_y, f_z	1 N
	m_x, m_y, m_z	1 Nm
3	f_x, f_y, f_z	1 N
	m_x, m_y, m_z	1 Nm
4	f_x, f_y, f_z	1 N
	m_x, m_y, m_z	1 Nm

Figure 4.5: Disturbance force configuration used for the simulations.

Although the analytical model of the isolation system described in chapter 3 showed some insight concerning the modeling of isolation systems, it appeared that the model was too simple to describe a real multi-directional structural power transfer from the source to the receiver. The structural power transmission was dominated by the normal direction of the receiver plate. To investigate the power transfer of the numerical model of the laboratory setup, four mounts are attached to the foundation plate and the source is represented by a harmonic unit force in all translational and rotational directions at the top of the mounts. The mounts are modeled as rigid pedestals, and are the parts of the receiver structure underneath the passive vibration isolators as shown in Figure 4.2. The disturbance configuration is shown in Figure 4.5. The disturbance force configuration and the mount properties are used for the

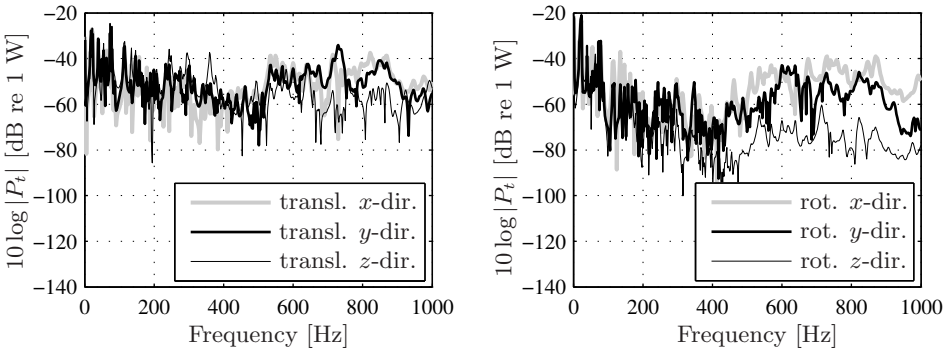

(a) Translational DOFs (b) Rotational DOFs

Figure 4.6: The total injected structural power by the four mounts into the receiver structure in the translational directions (a) and rotational directions (b).

simulations throughout this chapter. To investigate the injected structural power into the receiver structure, the structural power components of each DOF are summed over the mounts; i.e. the total injected power in the x-direction is determined by summation of the injected power in the x-direction of each mount. This is repeated for each DOF, i.e. the translational x, y and z-directions and the rotational x, y and z-directions. The injected structural power into the receiver structure at the junction locations is thus considered. The total injected power in the x-, y- and z-directions is shown in Figure 4.6(a). In the low frequency range the transmitted power is not dominated by one of the translational directions, but at frequencies above the 600 Hz the power transmission in the x- and y-directions dominates over the power transmission in the z-direction, which is the direction normal to the foundation plate. Considering the injected power by the rotational DOFs into the receiver structure in Figure 4.6(b), it can be seen that in the frequency range up to 500 Hz the injected power in the translational directions is a little larger than in the rotational directions. In the frequency range above 500 Hz the power transmission in the rotational degrees of freedom is of the same order of magnitude as the power transmission in the translational directions. The contribution of the power transmission in the torsional direction (rotational direction around the z-axis) to the total injected power is small for frequencies above 300 Hz. It can be concluded that all directions are important for the vibrational power transmission.

To reduce computation times, the complete mobility matrices of the re-

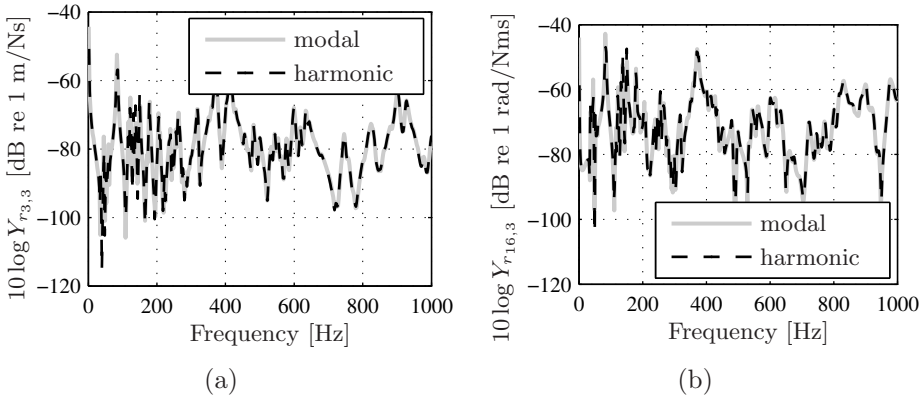

Figure 4.7: Two mobility components of the receiver structure determined with the modal expansion theory and the full harmonic analysis.

ceiver structure are determined by a modal expansion and residual modes as shown in equations (4.17) and (4.20). Besides using a modal expansion, the FRF components can also be determined with a full harmonic analysis. For this purpose the FEM package ANSYS is also used. To investigate the accuracy of the modal expansion, two mobility components are determined in both ways and compared to each other. The two components are part of the mobility matrix $\mathbf{Y}_r$, which relates the force and velocity components with each other at the junction points of the receiver structure. The driving point mobility of the receiver structure at the position of mount 1 in z-direction is depicted in Figure 4.7(a) (indicated by $Y_{r_{3,3}}$) and a transfer mobility between a force excitation in the z-direction at the position of mount 1 and the rotational velocity response in the x-direction of mount 3 is depicted in Figure 4.7(b) (indicated by $Y_{r_{16,3}}$). Both FRFs determined with the modal expansion theory correspond very well with the full harmonic responses, meaning that the implementation of the modal expansion and coupling with the mounting system is correct.

4.5 Active isolation: actuator configuration

The actuator configuration of the laboratory model is considered in more detail in this subsection. For the considered model, many possible actuator configurations exist and can be investigated, but this analysis is restricted to the following three issues:

- Active isolation for actuator configurations with a different number of

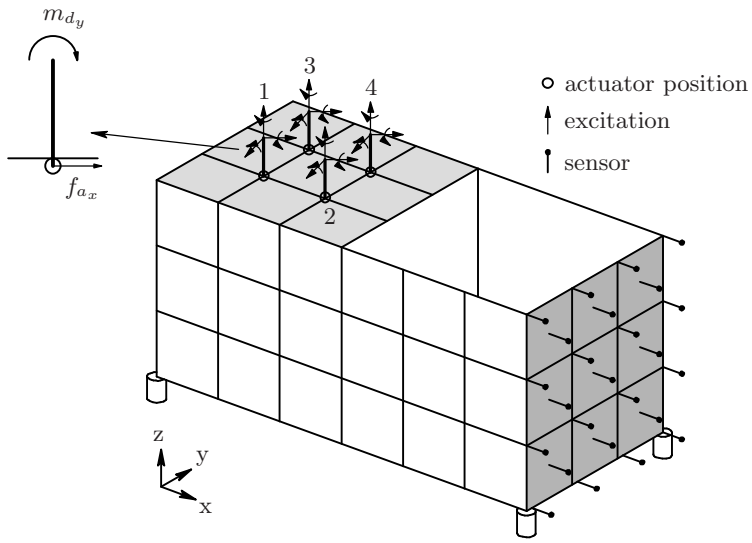

Figure 4.8: Schematic picture of the numerical model of the laboratory setup with the disturbance force configuration, actuator configuration and performance sensor set on the radiation plate.

actuators for a single direction.

- The influence of actuator weighting on the active response.

- Active isolation for a fixed number of actuators but with variation in the directions or DOFs of actuation.

Variation in the position of the actuators is not analyzed and the actuators are modeled as external forces acting on the receiver structure at the junction locations (the bottom side of the mounts) as shown in Figure 4.8. Also a schematic detailed plot of a mount (pedestal) is shown with one disturbance moment around the y-axis and an actuator force component in the x-direction. The performance of the different actuator configurations are examined by the achieved reduction of the error sensor set on the radiation plate in combination with the total actuator effort needed to obtain this reduction. The performance sensor set consists of a set of 25 vibration sensors measuring the velocity in the normal direction to the radiation plate and is shown in Figure 4.8.

4.5.1 The influence of the number of actuators

In section 2.3.3 it was suggested that for total isolation of the source from the receiver structure, the number of actuators must equal the number of structural transmission paths. This means that for the model of the laboratory setup studied here in theory 24 actuators are needed for total isolation (24 DOFs of excitation and 24 DOFs of vibration transmission to the receiver structure). In that case no vibrations are transmitted to the receiver structure at all. However, analysis showed that with far fewer actuators a considerable reduction can still be obtained of the vibrational response of such 'complex' receiver structures [7]. For the applications of hybrid isolation systems considered here, the number of actuators must be as small as possible for reasons of cost, difficult implementation and the control effort that is needed to drive the actuators.

The sensor response can be expressed in terms of the dynamic eigenmodes and corresponding participations as shown in section 4.3.2. In theory, one actuator is able to suppress the contribution of the response of one eigenmode, assuming that the actuator is able to excite the corresponding mode. The discrete isolation model described in section 2.3 showed that, when the number of actuators was less than the number of structural transmission paths, each actuator was able to suppress the vibration of one mass. In the considered applications no direct information is available on the number of dominant modes in the sensor response and this is also very difficult to determine. The available information of the structure only consists of the measured FRFs from the source and actuators to the sensor response. Basten and Verheij [2, 91] showed that with these measured FRFs an estimation of the number of dominant 'modes' can be obtained by means of Singular Value Decomposition. This technique is elucidated with a decomposition of the primary path, i.e. the matrix of FRFs from the disturbance forces to the sensor response. The SVD decomposition of the primary path can consequently be determined for each frequency:

$$\mathbf{H}_p^{vsr} = \mathbf{U} \cdot \mathbf{S} \cdot \mathbf{V}^{\mathrm{H}} = \sum_i \mathbf{u}_i \, s_i \, \mathbf{v}_i^{\mathrm{H}}, \tag{4.22}$$

where $\mathbf{U}$ is a matrix whose columns contain the field shapes, $\mathbf{S}$ is a diagonal matrix with singular values in decreasing order and $\mathbf{V}$ is a matrix whose columns contain the so-called source shapes. More details concerning the SVD analysis can be found in appendix C. In Figure 4.9 the singular values of $\mathbf{H}_p^{vsr}$ are shown as functions of the frequency. The first singular value is relatively large, meaning that the combination of the first field shape and source shape makes a large contribution to the primary path. This means that

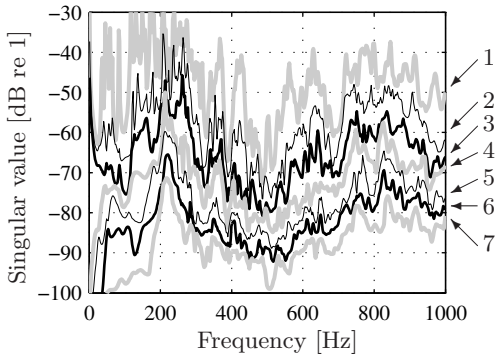

Figure 4.9: The first 7 singular values of the primary path to the error sensor set on the radiation plate.

a good representation of the $\mathbf{H}_p^{vsr}$ can already be obtained when only the first singular value is taken into account. The singular values decay with increasing number, meaning that the contribution of the field shapes and corresponding source shapes also becomes less important with increasing number. When this is translated to the number of actuators that are needed to suppress the vibrations caused by the source and transferred to the error sensor by the primary path, one single actuator already results in considerable reduction. Increasing the number of actuators will result in a decrease of the error sensor response, because the contributions of more field shapes can be reduced.

To investigate the influence of the number of actuators on the active performance of the isolation system, seven different configurations with an increasing number of actuators are analyzed. The SVD analysis of the primary path as shown in equation (4.22) is used to determine the effectiveness of the actuator influence. The different actuator configurations are shown in Table 4.3. The actuators are all located at the junctions with the receiver structure as can seen in Figure 4.8. The disturbance force vectors on top of the mounts are also depicted, and have the same values as shown in Figure 4.5. The response of the receiver structure is evaluated by the sensor set consisting of 25 sensors measuring the normal velocities on the radiation plate. Subsequently, simulations are performed with the described configuration and with minimization of the error sensor set on the radiation plate for the different actuator configurations. The error sensor set and the sensor set to evaluate the performance are thus the same in this situation. The reductions obtained for the different

Actuator set number	Number of act.	Mount number, DOF			
set 1	1	1,z			
set 2	2	1,z	2,z		
set 3	3	1,z	2,z	3,z	
set 4	4	1,z	2,z	3,z	4,z
set 5	5	1,x,z	2,z	3,z	4,z
set 6	6	1,x,z	2,x,z	3,z	4,z
set 7	7	1,x,z	2,x,z	3,x,z	4,z

Table 4.3: Definition of the actuator sets with different number of actuators.

actuator configurations are compared to each other. In Figure 4.10 the active responses are shown for the actuator sets 1 to 4 as well as the passive response. With just one actuator (actuator set 1) the response is already reduced, as was expected from the SVD analysis. When the number of actuators increases, the obtained reduction increases considerably up to the configuration of four actuators. The obtained reductions at the error sensor set when the number of actuators is increased even further is shown in Figure 4.11 for the actuator sets 4 to 7. Actuator set 5 (with 5 actuators) does not result in considerable extra reduction in the response up to 800 Hz. With actuator set 6 and especially actuator set 7 extra reduction of the error sensor response is obtained.

The first point of attention is the reduction at the error sensor set, but another important fact is the actuator effort needed to obtain this reduction. The actuator effort is determined by evaluation of the quadratic sum of the actuator forces. In Figure 4.12(a) the actuator effort is shown for the actuator sets 1 to 4. The first actuator configuration needs less effort compared to the configurations 2 to 4. It can be observed that the actuator effort of the actuator configurations 2 to 4 are of the same order of magnitude. In Figure 4.12(b) the total actuator effort is shown for the actuator sets 4 to 7. For the actuator sets 6 and 7 the actuator effort is considerably larger than for the sets 4 and 5, meaning that a lot of extra actuator force is needed to obtain the extra reduction in the sensor response. This phenomenon is explained in more detail when the actuator effort weighting is explained.

The tendency for each extra actuator to result in extra reduction in the sensor response obtained agrees in general with the conclusions drawn from the SVD analysis of the primary path. The actuators reduce in the first place the most dominant field shapes. This is shown by the amount of reduction which

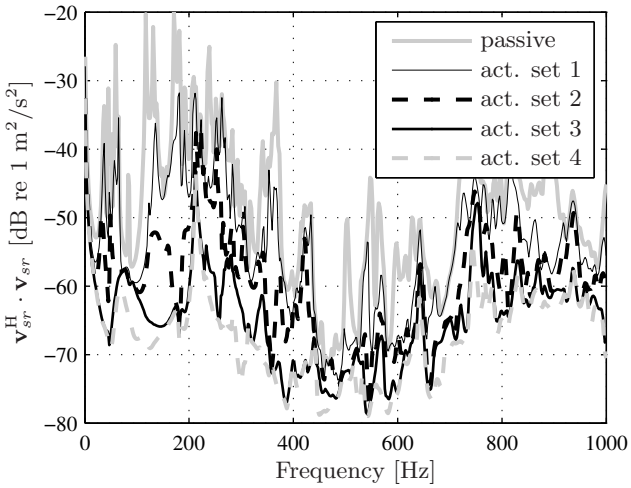

Figure 4.10: Passive response and active response of the sensor set on the radiation plate for actuator sets 1 to 4, obtained by minimization of the same sensor set.

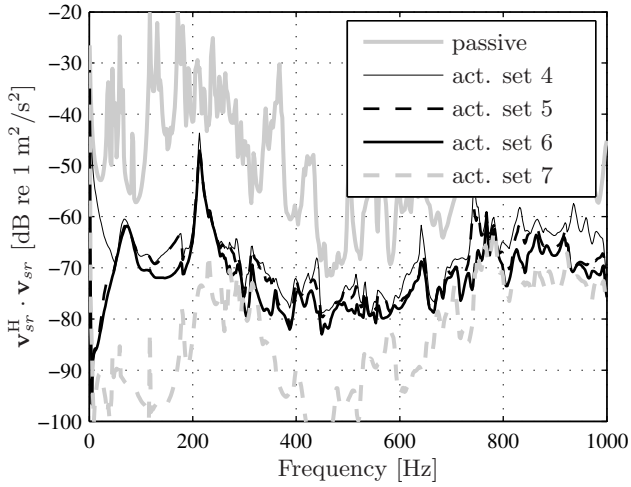

Figure 4.11: Passive response and active response of the sensor set on the radiation plate for actuator sets 4 to 7, obtained by minimization of the same sensor set.

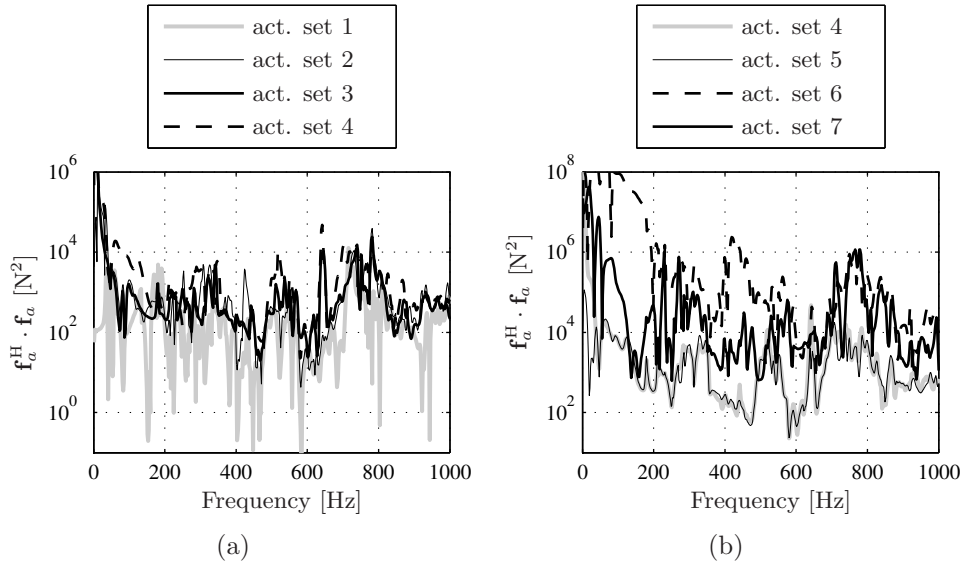

Figure 4.12: Actuator effort for minimization of the sensor set on the radiation plate for the considered actuator sets.

is already obtained with just one or a few actuators. When more actuators are used, the less efficient field shapes are also minimized. This is especially visible for the actuator sets with six or more actuators: the minimization of the less efficient field shapes requires a relatively large actuator effort.

To investigate the effect of the actuators on the field shapes, the participation of the field shapes in the total deformation is considered in more detail. The passive sensor response in terms of the singular vectors can be written as:

$$\mathbf{v}_{sr} = \mathbf{U} \cdot \mathbf{S} \cdot \mathbf{V}^{\mathrm{H}} \cdot \mathbf{f}_d. \tag{4.23}$$

Pre-multiplying this equation by $\mathbf{U}^{\mathrm{H}}$ and taking account the fact that $\mathbf{U}$ is unitary yields:

$$\mathbf{U}^{\mathrm{H}} \cdot \mathbf{v}_{sr} = \mathbf{S} \cdot \mathbf{V}^{\mathrm{H}} \cdot \mathbf{f}_d. \tag{4.24}$$

Because $\mathbf{U}$ and $\mathbf{V}$ are orthonormal, pre-multiplication with the Hermitian of these matrices can be interpreted as a projection of the error sensor response $\mathbf{v}_{sr}$ and disturbance force $\mathbf{f}_d$ onto two linearly independent bases. The participations of each field shape in the sensor response and source shape in the disturbance force are collected in the vectors $\tilde{\mathbf{v}}_{sr}$ and $\tilde{\mathbf{f}}_d$ respectively, defined

as:

$$\tilde{\mathbf{v}}_{sr} = \mathbf{U}^{\mathrm{H}} \cdot \mathbf{v}_{sr}, \tag{4.25a}$$

$$\tilde{\mathbf{f}}_{d} = \mathbf{V}^{\mathrm{H}} \cdot \mathbf{f}_{d}. \tag{4.25b}$$

The participations of each field shape are determined by substitution of the sensor response into equation (4.25a). The influence of the actuators on the participations is determined by substitution of the active sensor response for the term $\mathbf{v}_{sr}$ into this equation. This is done for the actuator configurations 2, 4 and 7. The participations of the first four field shapes in the active sensor response are shown in Figure 4.13. Actuator configuration 2 is only able to reduce the participations of the first two field shapes. The contribution of field shape 1, with the largest contribution in the sensor response, is mostly reduced. Actuator configuration 4 is also able to reduce the contributions of the third and fourth field shapes. Also, a larger reduction of the participations of each field shape is obtained in comparison to the configuration with two actuators. Considering actuator configuration 7, the additional actuators in comparison with configuration 4 are only able to reduce the participations of field shape three and higher and no considerable extra reduction of the participations of the first two field shapes is obtained. This means that the extra active reduction is obtained by excitation of the less efficient field shapes which require high actuator forces to reduce its participations.

4.5.2 Weighting of the actuator effort

It was shown that the actuator effort for the actuator configurations with more than five actuators increased considerably. To investigate this effect in more detail, the quadratic Hermitian cost function can be modified by taking account of a weighted actuator term as explained in section 2.6.5. The purpose of the actuator weighting term in the cost function is to take account of the effort being expended by the control system, so that small reductions in the sensor output are not obtained at the expense of very high actuator effort levels. In Figure 4.14 the active response is depicted for actuator set 7 with different actuator weighting coefficients μ. Weighting of the actuator effort results on the one side in less performance, but on the other side the actuator effort is reduced considerably as shown in Figure 4.16(a). The 20 dB reduction of the sensor response costs in fact about a factor ten more actuator effort for this actuator set. A similar analysis is performed for actuator set 4 and shown in Figure 4.15. The actuator weighting reduces the obtained reduction, but the actuator effort is hardly reduced as can be seen in Figure 4.16(b). The

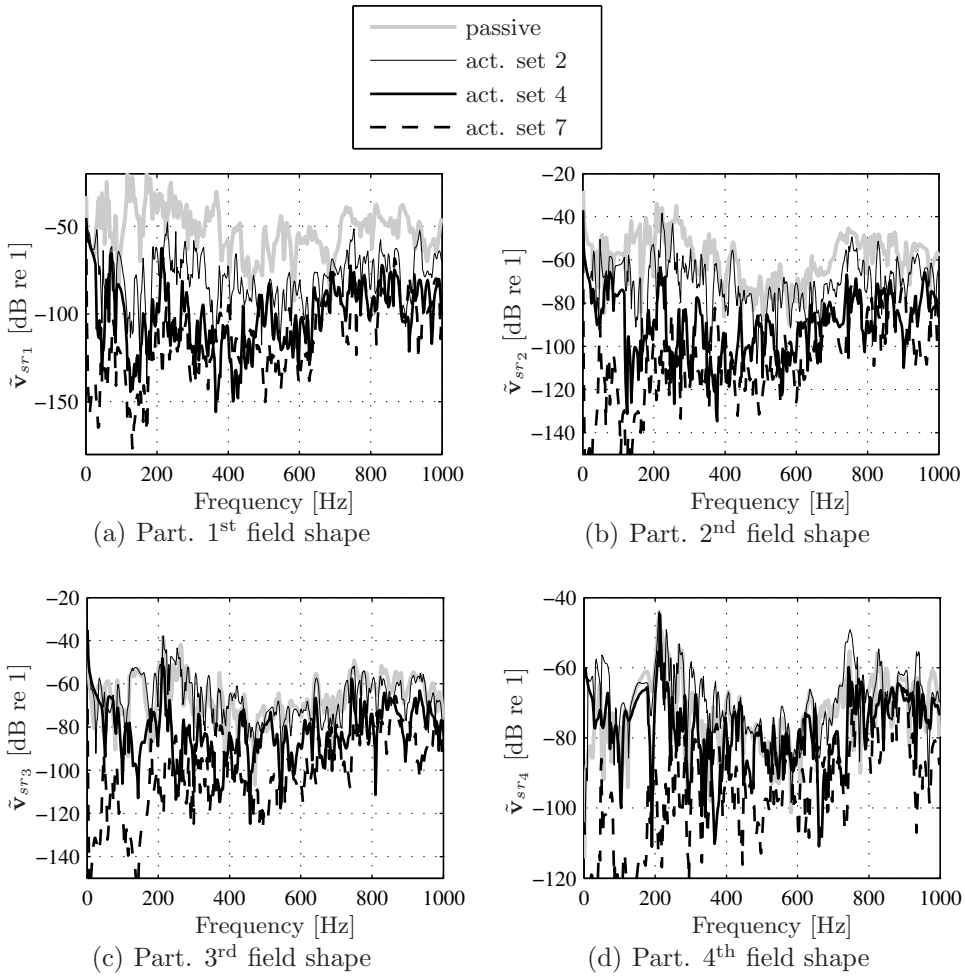

(a) Part. 1st field shape (b) Part. 2nd field shape

(c) Part. 3rd field shape (d) Part. 4th field shape

Figure 4.13: Participations of the first four field shapes for the passive response and the active error sensor responses with actuator configurations 2, 4 and 7.

sets with more than five actuators also put a lot of effort in the suppression of non-efficient deformation modes. In practice this amount of actuator effort is not available, and for the four point mounting system on this laboratory structure, a number of four actuators is a good compromise between the obtained reduction and the actuator effort required.

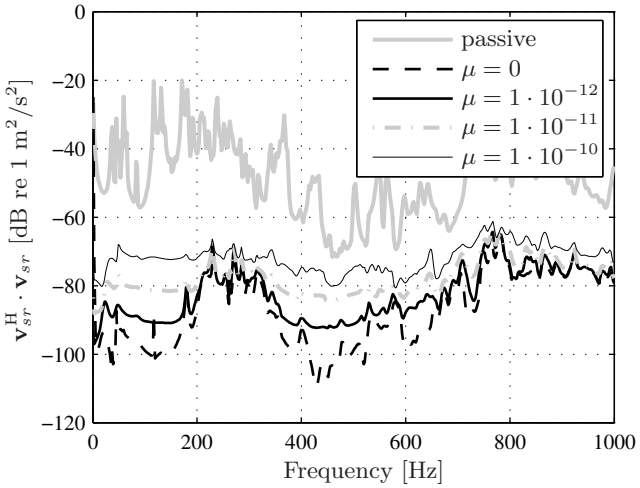

Figure 4.14: Passive response and active response at the sensor set of the radiation plate of the laboratory setup for different weighting factors of the actuator forces for actuator set 7.

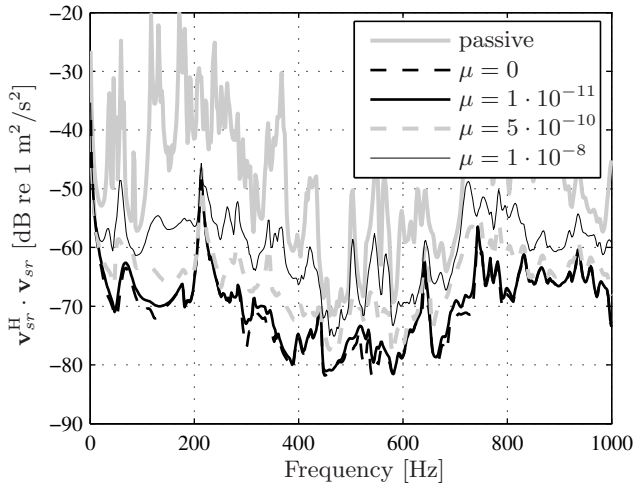

Figure 4.15: Passive response and active response at the sensor set of the radiation plate of the laboratory setup for different weighting factors of the actuator forces for actuator set 4.

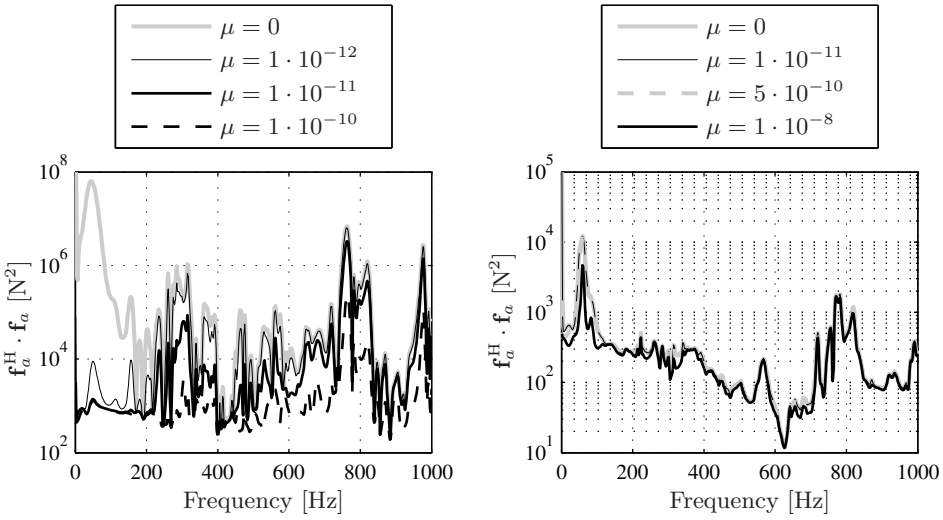

(a) Actuator set 7 (b) Actuator set 4

Figure 4.16: Actuator effort for minimization of the error sensor response on the radiation plate for actuator configurations number 7 (a) and 4 (b).

4.5.3 Active isolation for different actuator directions

Besides the number of actuators, the directions of actuation are also important for active control. For the actuator configuration 4, the actuator forces are exerted in the axial direction of the mounts (in the z-direction), thus normal to the foundation plate. The four actuators can also be configured in such a way that the actuator forces are applied in the x-direction or y-direction (the in-plane directions) of the foundation plate (see also Figure 4.8). The configuration is the same as for the previous simulations presented in this chapter and the same disturbance force vector is used. In Figure 4.17 the reduction of the considered error sensor set on the radiation plate is shown for actuation in the different translational directions. The configuration with the actuator forces in the axial direction of the mounts shows the best performance. Considering the obtained results and practical implementation, it is preferable to situate the four actuators in the axial directions of the mounts.

For real-life applications, most of the time it is difficult to test different actuator configurations because of practical restrictions. To get an indication of the most effective actuator directions, the SVD approach can be used. This technique was demonstrated by Basten and Verheij [2] for frequency re-

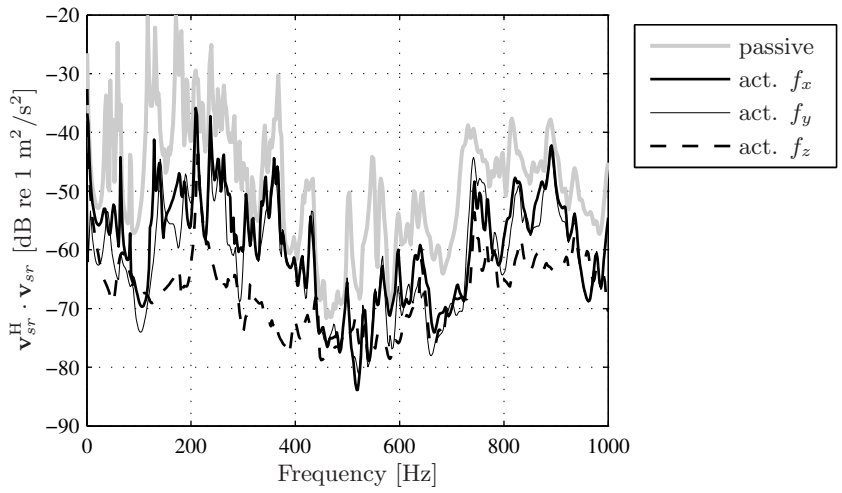

Figure 4.17: Passive response and active responses at the sensor set on the radiation plate for actuation in the translational x-, y- and z-directions with four actuators.

sponse measurements on the laboratory setup. Here, this technique is applied in the same way on the numerically determined FRFs. For this purpose, the secondary path function $\mathbf{H}_s^{vsr}$ as shown in section 2.6.3 (equation (2.90)) is considered. This is the secondary path transfer from all possible actuator positions and directions which are chosen to be interesting for the active isolation to the sensor set (in this case the error sensor set on the radiation plate). In this case the x-direction, y-direction and z-direction at all the junctions of the mounts with the receiver structure are considered, thus in total 12 DOFs for actuation. In a similar way as shown in equation (4.22), the SVD of the secondary path is defined for each frequency as:

$$\mathbf{H}_s^{vsr} = \mathbf{U} \cdot \mathbf{S} \cdot \mathbf{V}^{\mathrm{H}} = \sum_i \mathbf{u}_i s_i \mathbf{v}_i^{\mathrm{H}}, \tag{4.26}$$

where $\mathbf{U}$ is a matrix with the left singular vectors $\mathbf{u}_i$ representing the preferable response patterns of the error sensors on the radiation plate, $\mathbf{S}$ is a diagonal matrix with the singular values in decreasing order and $\mathbf{V}$ is a matrix with the right singular vectors $\mathbf{v}_i$ representing combinations of actuator forces that are able to excite the field shape in an effective way. In Figure 4.18(a) the first four largest singular values are plotted as functions of the frequency. It is shown again that a large part of the response is determined by just one singular value and the corresponding field and source shapes. The information regarding

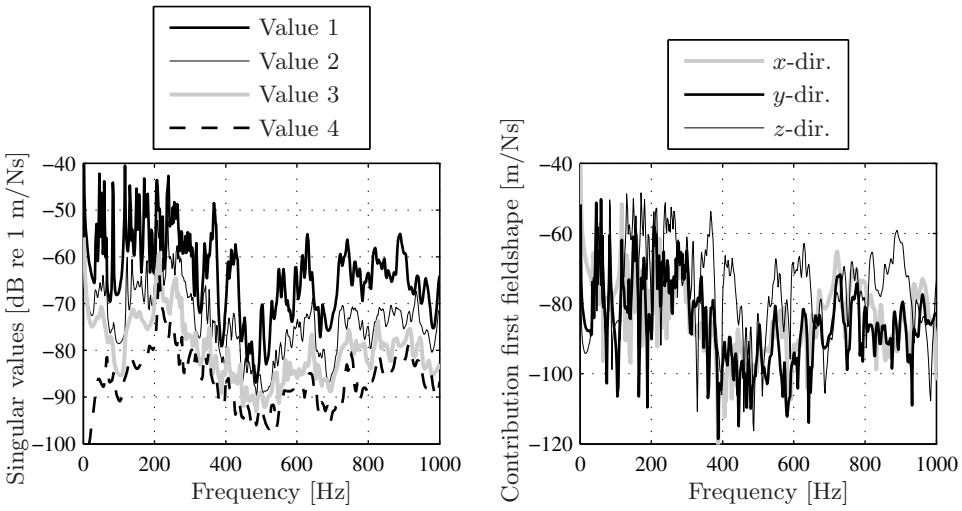

Figure 4.18: The singular values of the secondary path transfer (a) and the contributions to the first field shape for the three actuator directions at mount number 2 (b).

which actuator direction 'couples' best with the field shapes is determined by the singular values and the source shapes, and is determined for the coupling of the i^{th} field shape and the j^{th} actuator direction by $s_i \mathbf{V}_{ij}$. The influence of the actuator directions on the first field shape is the most important one because of the dominance of the first singular value. In Figure 4.18(b) the contributions of the actuators in the x-, y- and z-directions of mount number 2 to the first field shape are shown. The most efficient actuator direction is dependent on the considered frequency range, but in general the z-direction is the most efficient direction for actuation. This is conform to the results presented previously in this section and shown in Figure 4.17. The contributions of the different directions at the other mounts resemble the situation of mount number 2. It must be stressed that it only provides an indication of the effectiveness of the actuator directions, the actual reductions with active control also depends on the disturbance.

4.6 Active isolation: vibration sensor strategies

The influence of different sensor strategies on the structural response of the receiver structure is considered in this section. The configuration of the con-

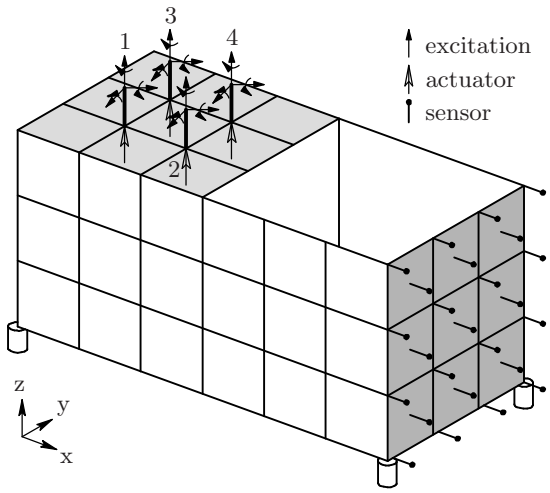

Figure 4.19: Schematic picture of the numerical model of the laboratory setup with the disturbance, actuator and sensor configurations.

sidered isolation system is shown in Figure 4.19. The mounts are assumed to be rigid and the disturbance configuration is the same as that used for the previous simulations and shown in Figure 4.5. The structure is excited at the top side of each mount with a unit force in all translational directions and a unit moment excitation in all rotational directions. The actuators are situated at each connection point between the mounts and the receiver structure and act in the axial direction of each mount. This corresponds with actuator configuration 4 in Table 4.3, which was the best trade-off in terms of achieved reduction and actuator effort. The response of the receiver structure is again judged by the vibrational response of the error sensor set on the radiation plate.

In Figure 4.20(a) the total normal velocity response of the radiation plate is depicted respectively in the passive situation, and for the active situation with minimization of the sensor set response and with minimization of the total normal velocity response of the radiation plate $\mathbf{v}_{rp}$. The total normal velocity response of the radiation plate is the set of normal velocities at all the 361 nodes of the FEM mesh on the radiation plate. It is seen that large reductions compared to the passive situation are obtained and that the difference between the two active responses is very small. Therefore the defined error sensor set with 25 sensors only represents a good measure of the total normal velocity distribution of the radiation plate in the considered frequency range.

When the error criterion of the total injected structural power from the mounting system into the receiver structure is used, reduction of the sensor response is also obtained as shown in Figure 4.20(b). However, the reduction obtained is less compared to minimization of the sensor set response itself. The reason for this is that this cost function tries to minimize a global measure (the sum of the kinetic and potential energy) of the whole receiver structure. The vibrational response of the radiation plate makes just a small contribution to the total kinetic energy of the receiver structure.

Apart from error criteria related to the vibrational response of the radiation plate, error sensors can also be situated near the source or the mounts. This concept resulted in a good active reduction of the vibrational response of the receiver structure considered in chapter 3. This is not the case for the model considered in this chapter. In Figure 4.20(c) and 4.20(d) the response of the error sensor set on the radiation plate is shown for minimization of all the connection velocities and connection forces respectively. These error sensor criteria do not function properly for the laboratory model. The dynamic behavior of the receiver structure is not dominated by only a few excitation directions and the dynamic behavior is much more complex. The minimization of the connection velocities seems to work in the lower frequency range (up to approximately 150 Hz) where reduction is obtained by suppression of the global modes of the receiver structure that are also measured in a certain way by the sensors near the mounts. At higher frequencies, these strategies fail because of the local deformation patterns of the receiver structure, which implies that the chosen cost functions consisting of the near-source velocities or the near-source forces are not a good measure for the structural vibration of the radiation plate.

4.6.1 Global reduction

An important issue for the active control of vibration or sound in general is the influence of the actuator excitation on the response of the system at other locations than the locations of the error sensors. The effort of the actuators is only focused on the reduction of the error sensor response. This can result in an increase of the response at other locations. In the ideal case a global reduction of the response is achieved by choosing a suitable sensor set. In this chapter a sensor set on the radiation plate is considered with the goal of reducing the vibrational response and sound radiation of this part of the receiver structure. To investigate the effect of an increase in the response at other locations on the structure than the error sensors, the performance of these local error criteria is determined in terms of the global response of the

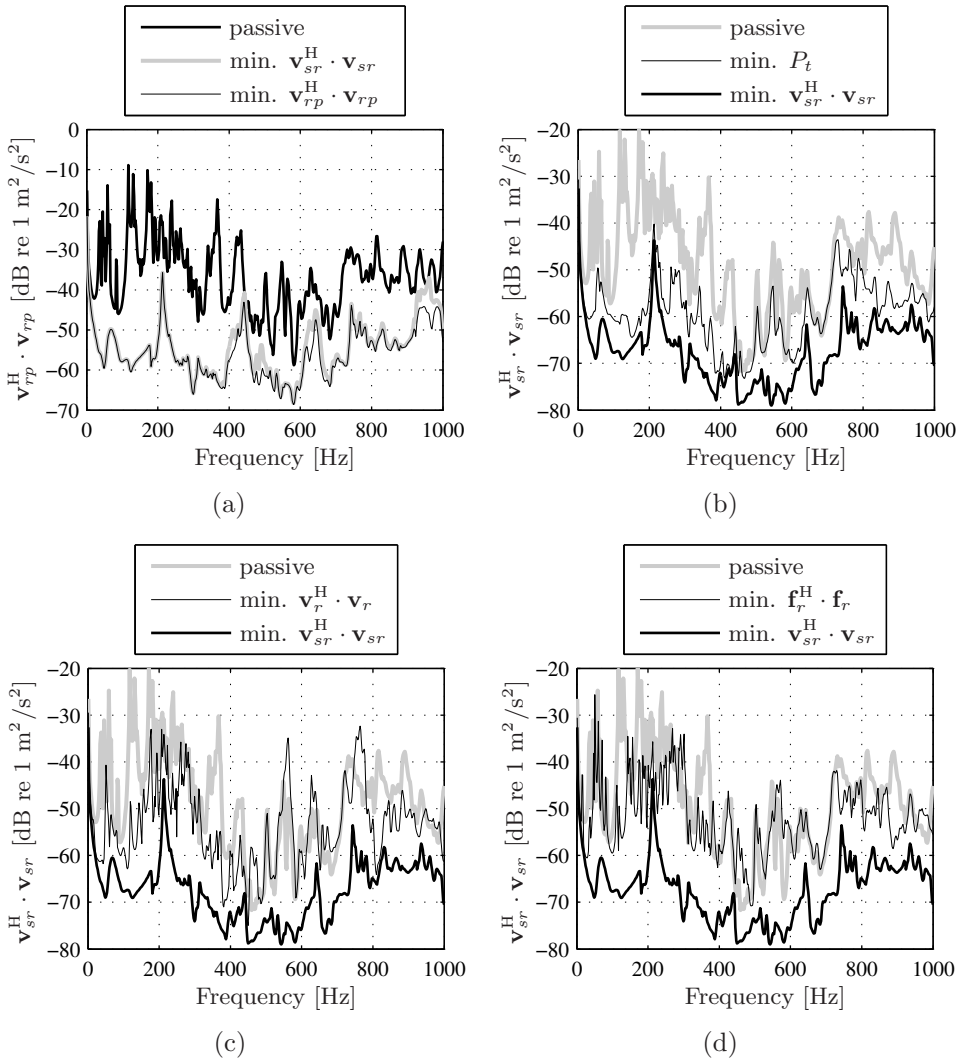

Figure 4.20: Passive and active responses of the radiation plate: active response in terms of all normal nodal velocities on the radiation plate $\mathbf{v}_{rp}$ (a) and the active response at the error sensor set on the radiation plate $\mathbf{v}_{sr}$ for minimization of transmitted power (b), minimization of the junction velocities (c) and minimization of the junctions forces (d) at the receiver structure.

receiver structure.

The influence of different error criteria on the kinetic energy of the receiver structure is considered first, so the kinetic energy is considered as a performance measure. In Figure 4.21 the kinetic energy of the receiver structure is depicted for different error criteria. The calculation of the kinetic energy is explained in more detail in section 2.6.3 and appendix B. It is shown that the performance achieved with minimization of the transmitted power is almost equal to the performance with minimization of the kinetic energy for higher frequencies. In the low frequency range, the potential energy content of the structure is also considerable, which explains the difference in active response between these two error criteria. Active isolation using the error sensor set on the radiation plate yields some reduction in the kinetic energy response in the frequency range up to 500 Hz. In the higher frequency range hardly any reduction in terms of kinetic energy is obtained and in fact an increase in response is observed. This means that, although a reduction of the error sensor response is obtained, the actuator effort causes an increase of vibration at other locations to such an extent that the total kinetic energy of the structure increases. This side effect is not desirable.

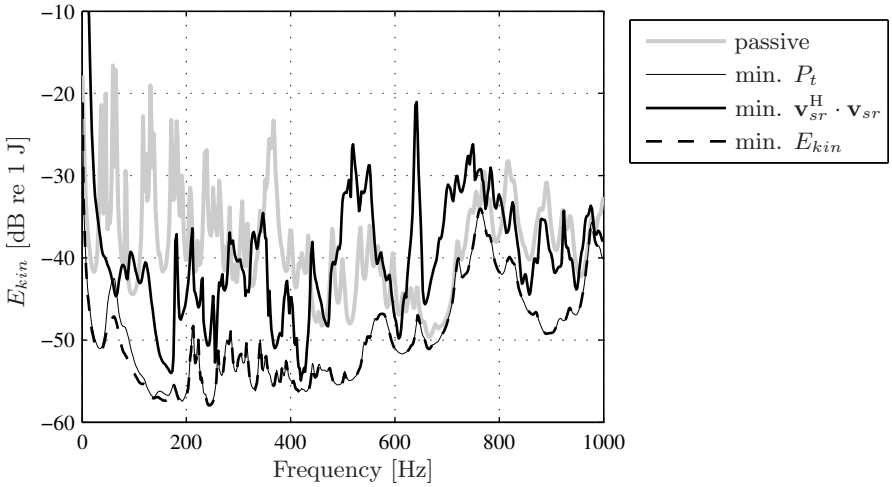

Figure 4.21: Passive response and active responses in terms of the kinetic energy for minimization of the transmitted power and the error sensor response on the radiation plate.

The contribution of the structural response near the source (e.g. the vibrations of the foundation plate) has the largest contribution in the total kinetic energy

of the receiver structure [6]. This can be misleading, because in practical applications it may not be necessary to actively suppress the response near the source but a 'global' suppression may be desirable at some distance away from the source (in this case the response on the radiation plate). To take this effect into account, another global sensor set is considered which consists of the combined normal velocity response at the side plate and the radiation plate. This velocity sensor response is indicated by $\mathbf{v}_{gl}$. In Figure 4.22 the global velocity response is shown for some of the error criteria as considered for the kinetic energy response. Minimization of the injected structural power results in a reduction of the global velocity response. Active isolation using the sensor set on the radiation plate results in a better reduction in terms of global velocity response than in terms of reduction of the kinetic energy. This means that both the choice of the error criterion and the response to judge the performance of the error criterion have to correspond with the goals to be achieved with active isolation. It can be concluded that a global error criterion has to be chosen in order to obtain a global reduction.

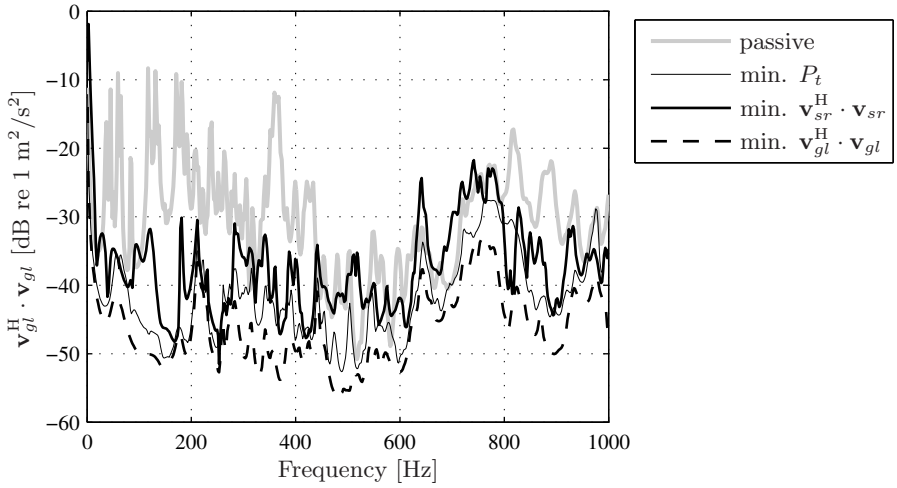

Figure 4.22: Passive response and active responses of the receiver structure in terms of the global far field response (the normal velocity response at the side and radiation plate of the receiver structure) for minimization of the transmitted power and error sensor set response on the radiation plate.

4.7 Active isolation: acoustic sensor strategies

In the previous sections, only error sensor criteria were considered related to the structural response of the receiver structure. Instead of using vibration error sensors (acceleration pick-ups), acoustic error sensors (microphones) can be used for the purpose of active isolation. The advantage of the latter type of error criteria is that the desired goal, namely reduction of noise, is directly minimized. In this section, the performance of the receiver structure is considered in terms of acoustic quantities. The influence of different error criteria on two types of acoustic responses is determined: the free field acoustic radiation of the baffled radiation plate and the acoustic radiation of the radiation plate into an enclosure. Besides determining the acoustic performance responses, different acoustic error criteria can also be investigated like the minimization of pressure responses in the enclosure (measured by microphones). More details concerning the calculation of the acoustic response and the implementation of acoustic error criteria were described in sections 2.5 and 2.6.4 respectively.

4.7.1 Active isolation of free field radiation

The sound power radiated into a free field can be approximated by weighting of the total normal velocity response of the radiation plate with the radiation matrix for a plate in a baffle. This was explained in more detail in section 2.5.2. The radiated sound power can consequently be written as a Hermitian quadratic error criterion (see also equation (2.96)) according to:

$$\bar{W} = \mathbf{v}_{rp}^{\mathrm{H}} \cdot \mathbf{R} \cdot \mathbf{v}_{rp}. \tag{4.27}$$

In Figure 4.23 the radiated sound power of the radiation plate is presented for the passive situation as well as the active responses with minimization of the structural transmitted power and with minimization of the error sensor response. Minimization of the injected structural power does not result in a large reduction of the radiated sound power of the radiation plate for frequencies above 300 Hz. Minimization of the error sensor response on the radiation plate, indicated by $\mathbf{v}_{sr}$ and shown in Figure 4.19, reduces the radiated sound power to almost the same extent as minimization of the radiated power itself. For frequencies lower than 300 Hz, reductions with minimization of the radiated sound power are considerably larger than just minimization of the normal velocity response. The error sensor criteria that minimize the radiated sound power, also changes the shape of the vibration of the radiation plate in such a way that the sound radiation is not efficient ((like the (1,2) mode of a plate where one part of the plate absorbs the acoustic radiation of the

other part). However, this only works in the lower frequency range where the radiation plate is deformed in a global sense.

In practice it is not straightforward to use radiated sound power as an error criterion for the controller. A method is to weight the structural error sensors (measuring the normal velocity response) in such a way that the resulting error criterion is a measure of the radiated sound power. Of course the radiation matrix can be used, but to save computational effort which is an important issue for active control, it is possible to introduce normal velocity distributions that contribute independently to the radiated sound power. These normal velocity distributions are called *radiation modes* and were first introduced by Borgiotti [16]. More details about radiation modes can be found in appendix C.1.

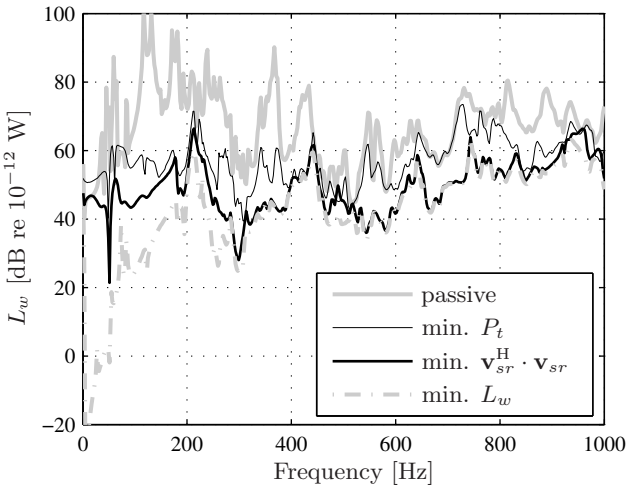

Figure 4.23: The radiated sound power of the radiation plate for the passive situation and with active control with minimization of the injected structural power (P_t), minimization of the error sensor set response on the radiation plate ($\mathbf{v}_{sr}$) and for minimization of the radiated sound power itself.

4.7.2 Active isolation of sound radiation into an enclosure

A part of the laboratory setup consists of an acoustic enclosure attached to the radiation plate. This is a simplified representation of an interior space like a ship cabin. The source causes vibrations in the whole receiver structure. In this section some error criteria are investigated that minimize the pressure

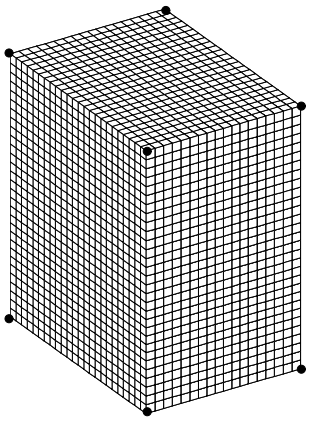

Figure 4.24: Acoustic mesh of the enclosure.

levels in the enclosure by active isolation of the source. Three different error criteria in terms of the enclosure response are considered: the acoustic potential energy in the enclosure E_p (a), the total pressure response in the enclosure $\mathbf{p}_e$ (b) and the pressure response at the corners of the enclosure $\mathbf{p}_c$ (c). The quadratic error criteria are defined respectively (see also section 2.5.3) as:

$$E_p = \frac{1}{4\rho c_0^2}\mathbf{Q}^{\mathrm{H}} \cdot \mathbf{\Lambda} \cdot \mathbf{Q}, \tag{4.28a}$$

$$J_p = \mathbf{p}_e^{\mathrm{H}} \cdot \mathbf{p}_e = \mathbf{v}_{rp}^{\mathrm{H}} \cdot \mathbf{Z}_e^{\mathrm{H}} \cdot \mathbf{Z}_e \cdot \mathbf{v}_{rp}, \tag{4.28b}$$

$$J_{cp} = \mathbf{p}_c^{\mathrm{H}} \cdot \mathbf{p}_c = \mathbf{v}_{rp}^{\mathrm{H}} \cdot \mathbf{Z}_c^{\mathrm{H}} \cdot \mathbf{Z}_c \cdot \mathbf{v}_{rp}, \tag{4.28c}$$

where $\mathbf{p}_c$ is the vector with pressures at the corners of the cavity (see Figure 4.24). $\mathbf{Q}$ is the vector with modal participations of the acoustic modes determined by the normal velocity distribution (see also equation (2.69)), $\mathbf{\Lambda}$ is a matrix with the modal volumes (shown in equation (2.52)) of the acoustic modes, $\mathbf{Z}_e$ is the impedance matrix from the normal velocity field on the radiation plate $\mathbf{v}_{rp}$ to the pressure at all the nodes of the enclosure and $\mathbf{Z}_c$ is the impedance matrix from the normal velocity field on the radiation plate $\mathbf{v}_{rp}$ to the pressure at the corner nodes of the enclosure. In Figure 4.25 the acoustic potential energy response of the enclosure is depicted with minimization of the three considered error criteria. The reduction obtained with minimization of the total pressure response of the cavity is the same as with minimization of the acoustic potential energy. This is expected because of the equidistant mesh of the enclosure that is used for the FEM simulations. The reduction

obtained when only the pressure response at the corners of the enclosure is used also yields very good reductions. The pressure response at the rigid walls is maximal due to the absence of damping at the walls. This means that the pressure response at the corners is a maximum signal because all modes have pressure maxima in the corners and at the boundaries. For this reason a good reduction of the acoustic potential energy is obtained with minimization of the pressure response at the corners only. Active isolation using actuators near the source and error sensors in the enclosure works very well for the reduction of the interior noise.

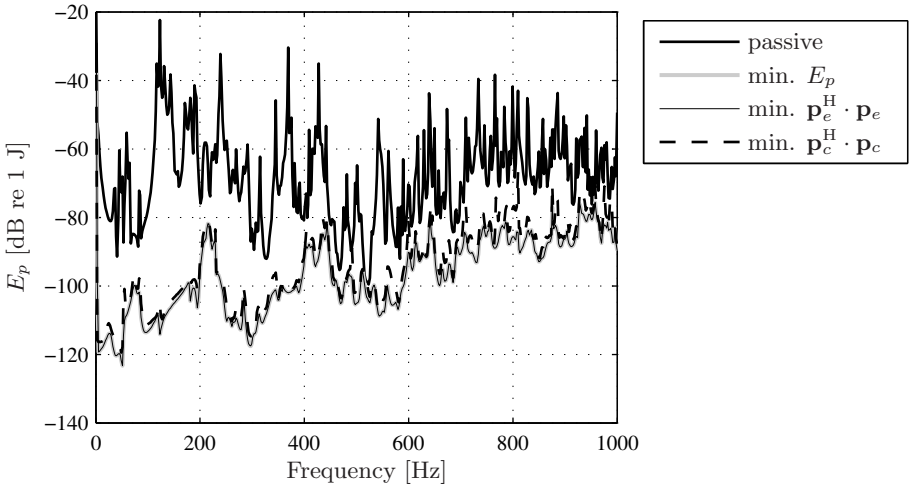

Figure 4.25: Passive response and active responses in terms of the acoustic potential energy in the enclosure for minimization of all the pressures and the pressures at the corners of the enclosure.

The influence of structural error criteria on the pressure response of the enclosure is now investigated. In Figure 4.26 the acoustic potential energy is depicted when the transmitted power and the error sensor set response on the radiation plate are minimized for the described actuator and disturbance configuration. The difference between vibration control and acoustic control can clearly be observed. The structural error criteria result in less reduction of the acoustic potential energy in the enclosure than the considered acoustic error criteria. However, reductions are obtained, which are considerable for frequencies up to around 500 Hz. This can more clearly be observed when the responses are depicted in one-third octave bands, as shown in Figure 4.26(b). Minimization of the vibrational response at the error sensor set on the radia-

tion plate results in a better reduction of the acoustic potential energy than minimization of the transmitted power. It must be noted that minimization of the transmitted power also results in a global reduction (minimizes the kinetic energy of the whole receiver structure) which is not the case for the minimization of the error sensor set as was shown in section 4.6.1.

Active control of vibration differs from the reduction of the acoustic response, and reduction of vibrational response does not necessarily imply a reduction in the acoustic response. In the same way as noted for free field radiation, it is also possible for the case of sound radiation into an enclosure to weight the structural vibration sensors in such a way that a good estimate of the pressure response of the cavity is obtained. More information on this topic can be found in the literature, e.g. [19, 20, 21].

4.8 Concluding remarks

In this chapter an application of a hybrid isolation system was analyzed by numerical studies on a laboratory setup. This laboratory setup was designed to have certain properties similar to those of ships or large vehicles. A numerical model of this laboratory setup was developed to investigate different actuator and sensor configurations. Two types of error sensor criteria were considered: error criteria related to the structural response of (a part of) the receiver structure (AVC) and error criteria related to the acoustic response radiated by a part of the receiver structure (ASAC). In contrast to the application considered in chapter 2, it was demonstrated that the vibration transmission from the source to the receiver structure has a multi-directional character and that the dynamic response of the receiver structure was considered to be realistic and consisting of a variety of modes ('global' and 'local' modes) and a high modal density. The actuator and error sensor configurations were considered in more detail.

First some concluding remarks concerning actuator configurations are presented:

- With a reduced set of actuators a good reduction of the receiver response can be obtained. This can be explained using SVD analysis, which shows that, although the disturbance is modeled as a multi-directional force, just a few field shapes (preferable response patterns of the error sensors) with corresponding source shapes (excitation patterns that couple well with the corresponding field shapes) make a large contribution in the response of the error sensor set.

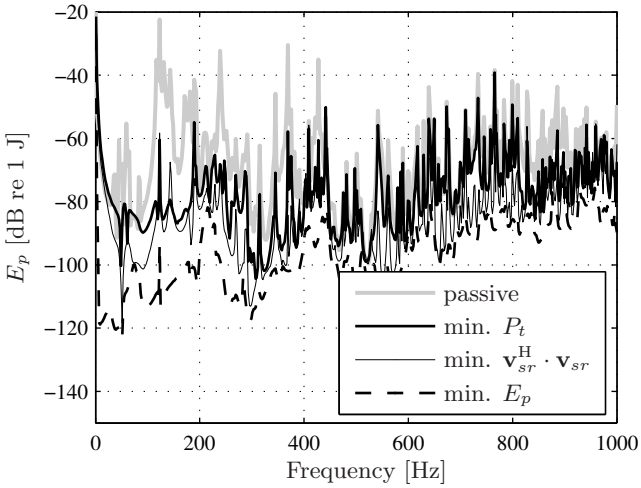

(a)

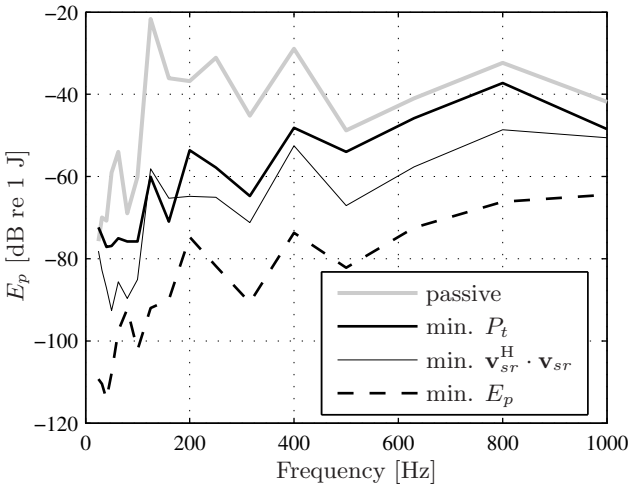

(b) 1/3-octave bands

Figure 4.26: Acoustic potential energy in the enclosure for the passive situation and with active control for minimization of the injected structural power, minimization of the error sensor response on the radiation plate and minimization of the potential energy (a) and the same response in terms of one-third octave bands (b).

- The actuators try to minimize the most efficient field shapes first. Increasing the number of actuators results in extra reduction of the error

sensor response. The SVD analysis of the primary path showed that the number of actuators is an indication of the number of participations of field shapes that can be reduced. Increasing the number of actuators, to a certain limit, also reduce the contributions of the first efficient field shapes.

- An important consideration when designing hybrid isolation systems is, besides the obtained reduction of the error sensor response, the actuator effort needed to obtain reduction. The SVD analysis provides no direct information about this topic. Increasing the number of actuators above a certain number may still provide extra reduction of the error sensor response, but may also result in a disproportional increase of the actuator effort. This is caused by the fact that the 'extra' actuators try to minimize the less efficient field shapes with low corresponding singular values, and high actuator forces are needed to excite these field shapes.
- When a relatively large number of actuators is applied, weighting of the actuator forces can be used as part of the control strategy to prevent the actuator forces becoming disproportionally large to obtain reduction. The actuators also try to minimize less efficient field shape contributions which require relatively large actuator forces. This problem can be circumvented by weighting of the actuator effort. Although the weighting procedure results in a decrease of the actuator effort, the reduction also decreases and is comparable with the reduction obtained with a reduced set of actuators. The optimum number of actuators is therefore a trade-off between the obtained reduction and the actuator effort. To get an indication of the number of actuators that form this best trade-off, the information obtained with an SVD analysis is not sufficient. The active sensor response has to be calculated for the chosen actuator configurations with the different number of actuators and after that the actuator effort or the reduction of the field shape contributions of the primary transfer has to be considered. For the latter type of analysis, it can be observed that increasing the number of actuators results in an increase of the actuator effort whereas no extra reduction is obtained in the most efficient field shapes.
- The SVD analysis of the secondary path provides information on the most efficient actuator directions if no information on the source disturbance is available. This information is obtained by studying the contribution of each actuator direction to the most dominant field shapes.

Next some concluding remarks concerning sensor configurations are presented:

- Sensor responses (both acoustic and vibrational) at a distance from the source can be reduced effectively with actuators near the source.
- The use of a global measure of the receiver response as error sensor strategy for active isolation, like minimization of the kinetic energy or the transmitted power, has the advantage that a global reduction of the receiver response is obtained. This means that the largest reductions are not obtained at certain parts of the receiver structure, but the active response at other parts of the structure does not increase either. A disadvantage is that this type of error criterion tries to minimize the largest responses, which occur near the source of excitation. This is often not desirable, because the largest reduction may be desired at some distance away from the source, e.g. in the accommodations in a ship rather than in the engine room. Another disadvantage of this type of error criterion is the difficult implementation (in case of minimization of the kinetic energy) or the large sensitivity to errors in the sensor signals (in case of minimization of the transmitted power) [41]. This is also shown in chapter 6 of this thesis. Although the minimization of the error sensor set response results in a good reduction of this response, the active response at other locations of the receiver structure may increase.
- Good reductions of acoustic cost functions can be established with active isolation techniques. The structural error criteria perform less well in terms of the active acoustic response (like the radiated sound power of a part of the receiver structure or the acoustic potential energy). However, reductions can still be obtained with the structural error criteria like the minimization of the normal velocity response of the radiation plate. The minimization of the transmitted power also results in a decrease of the acoustic response at low frequencies.
- The performance achieved for active isolation with minimization of the forces or velocities at the connection points of the mounting system with the receiver structure is very poor. This is clearly different in comparison to the active performance of the same error criteria on the more simple isolation system considered in the previous chapter. The multi-directional vibration transmission from the source to the receiver structure in combination with a dynamically complex behavior of the receiver structure makes the straightforward use of this kind of error criteria not suited to obtain reductions away from the source.

The last remark, namely that straightforward minimization of the forces or velocities at the junction of the receiver structure does not result in reductions

at a distance from the source, has some negative implications. These kinds of error criteria are much easier to implement, especially in the considered applications. Besides that, it may also be possible to define error criteria near the source that represent a global measure of the vibrational response, like minimization of the transmitted power to the receiver structure. However, it is known from the literature that this error criterion is ill-conditioned, meaning that it is very sensitive to small errors in the measured sensor response. In chapter 6 it is investigated if it is possible to improve the robustness of the error criterion based on the minimization of the transmitted power. Also an alternative concept of near-source error sensor strategies is presented and investigated in more detail.

Chapter 5

Numerical modeling of rubber isolators

5.1 Introduction

The hybrid isolation model presented in chapter 3 consisted of simplified representation of hybrid mounts; namely a beam model to represent the passive isolator in combination with an external force as a model for the actuator. To apply hybrid isolation in practice, a hybrid module or mount has to be designed. This component consists of an integration of passive vibration isolators, actuators and, when near-source sensors are used, sensors. An important issue for the design of such hybrid mounts is the number of actuators and the actuator effort required to obtain reduction. The number of actuators must be as small as possible for reasons of cost and robustness. Also, the actuator effort needed to obtain a good active reduction must be as small as possible, so relatively small and cheap actuators can be used. Besides that, the forces that can be produced by commercial actuators are quite limited. Also the generation of heat is a problem with large actuators and has to be minimized to guarantee a stable and long-lasting functioning.

As explained in section 1.3, passive isolation is based on two attenuation principles. The first and most important principle is isolation by creating a stiffness or impedance mismatch between the source and the receiver. However, some minimum stiffness is required to restrict the static deformation and low-frequency motion. These conflicting design requirements in combination with the dynamic behavior of the isolators makes it necessary to consider the behavior of the mounting system in more detail, e.g. by means of numerical models. The second attenuation principle is based on the dissipation of energy.

Structure-borne sound is dissipated in the mount by the internal damping of the material. This is especially beneficial for the rigid body resonances of the source on the mounting system. The vibration amplitudes at these resonance frequencies can be quite large but can be subsequently damped by material damping of the mounting system. This is important, because the rigid body resonances occur in the lower frequency region and are often excited, e.g. with the start-up and increase of the rotational speed of the rotating machinery.

The actuator effort and the number of actuators is inherently dependent on the design of the passive part of the hybrid resilient mounting system. This means that a passive isolation characterization is needed to design the active isolation part of the hybrid mount. An important aspect is the identification of the transfer paths which make the largest contribution to the structure-borne sound transmission. These transfer paths will usually correspond with stiff isolator directions and have a smaller dynamic impedance or stiffness mismatch resulting in a worse isolation effect. However, for the concept of hybrid isolation, the impedance mismatch can be enlarged in an active way by locating the actuators in the dominant transfer paths. In order to obtain a minimum number of actuators, the passive mounting system must also have a minimum number of these dominant transfer paths. It was shown in chapter 4 that all directions may play an important role in structure-borne sound transmission. In the considered applications interesting for the application of hybrid isolation, normally rubber vibration isolators are used.

This chapter deals with the modeling of rubber vibration isolators in order to obtain a multi-directional characterization of the passive isolation behavior as a part of the tool for the design of hybrid isolators. It will also be shown that for obtaining reliable numerical results the material model of rubber is very important. Rubber is a complex material and its material behavior is often unknown. For this reason, attention is also paid to obtaining material parameters for the numerical model with the use of measurement data of an entire isolator.

5.1.1 Isolation characterization with numerical models

Although different kinds of materials can be used for the resilient isolators, rubber is most popular. Natural rubber is very suited for isolation purposes, because it can undergo large elastic deformations. Other advantages are the high strength and abrasion resistance. In situations where high resistance to oils, high temperatures, aging and ozone is needed, synthetic rubbers are used. In most cases natural rubber is compounded with non-rubber ingredients to improve its strength, aging resistance and behavior during manufacture

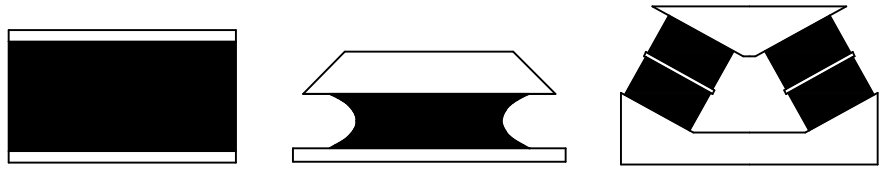

Figure 5.1: Examples of vibration isolators: the black parts are rubber, the white parts indicate the metal components.

of the product [97]. The rubber isolators consist of vulcanized rubber with firmly bonded metal parts. These metal parts facilitate the installation of the isolator between the source and the receiver and distribute the load across the rubber surfaces. In Figure 5.1 examples of rubber vibration isolators are depicted. A consequence of the fact that rubber can undergo large elastic deformations is that the weight of the source causes a large (pre-)deformation of the isolator. The shape of the mount changes considerably, which may have a large influence on the (dynamic) behavior of the isolator. Models to determine the isolation characteristics of rubber vibration isolators have been subject of study in the literature. Dickens [30, 31] described a model based on a relationship between the phase velocity in the rubber and the compression ratio due to the static load. The results were compared with experiments and a satisfactory agreement was obtained for the isolation behavior in the axial direction of the isolators. Kim and Singh [70] studied the vibration transmission through an elastomeric isolator with the Timoshenko beam theory. Besides the vibration transmission due to flexural motion, the longitudinal motion was also considered in [70]. The pre-deformation was not taken into account. Kari [66] presented a linear waveguide model to model the axial dynamic stiffness in the audible frequency range. The results agreed very well with experiments on a rubber isolator, but the influence of the pre-deformation was not taken into account.

As explained in chapter 1, the vibration transmission is a multi-directional phenomenon and for this reason the isolation characteristics in all directions of the vibration transmission of the isolator have to be taken into account. The finite element method is suited for obtaining a multi-directional isolation characterization [43, 44]. Other advantages are the ability to model complex geometries, including pre-deformation, and that complex constitutive equations can be handled. Kari investigated the dynamic stiffness of preloaded vibration isolators with the FEM method [67], but only in the axial direction.

In the present work this analysis is extended to the dynamic stiffness components in the other directions. The isolation characteristics are dependent on many effects like the pre-deformation due to the weight of the source, the excitation frequency, the temperature and aging. Only the dependence on the pre-deformation and the frequency dependent dynamic effects are considered here, because these effects have the largest influence.

First, the procedure is explained to determine the multi-directional isolation characterization with numerical FEM models in section 5.2. After that, the basics of the FEM theory are briefly described in section 5.3. Attention is focused on the theory to model the material behavior of rubber. In section 5.4 an isolator that has been described extensively in the literature is studied as a test case. The literature model only considers the isolation behavior in one direction (i.e. the axial direction). The numerical model presented in this chapter is also used to obtain the isolation characteristics in other directions.

5.1.2 Identification of material properties

The most influential factor for obtaining reliable numerical results is the material definition used to describe rubber material. The material behavior of rubber compounds is not easy to determine and often unknown. In practice, the static material parameters are determined using simple standardized deformation experiments on samples of the rubber material. A commonly used test for this purpose is the tensile test, where a standardized sample of the rubber material is stretched until it breaks. The stress is measured as a function of the strain for several tensile experiments. The static material parameters are subsequently determined by a curve fit of the strain-energy function on the measured stress-strain curve. This curve fit procedure is implemented in some commercial FEM programs [52, 82]. The dynamic material behavior is described by a frequency dependent complex shear modulus. The shear modulus is measured in practice with a DMA or DMTA tester (Dynamic Mechanical (Thermal) Analyzer) [83].

However, there are some difficulties in obtaining a good rubber material characterization. The material properties of most rubber materials, in terms that can be used for numerical analyses, are often not known or difficult to obtain from rubber manufacturers. The material properties are also strongly dependent on the conditions during the vulcanization process. In most practical situations only a finished product is available, which makes it difficult to get test samples from the material without destroying the product. Another restricting factor is that the frequency range of the DMA is limited (most DMA instruments have a frequency limit of 200 Hz) which is in most cases too low for

a characterization in the frequency range important for structure-borne sound. The frequency range for the material specification can be increased with the *time-temperature superposition* principle (TTS) as explained in section 5.3.2, but this principle is not always valid for rubber compounds with a large filler content. For this reason a procedure is described in section 5.5 to determine the rubber material parameters by using measurements of an entire isolator. Static deformation measurements are used to determine the rubber material parameters related with the static behavior. Furthermore, dynamic measurements are performed to determine the dynamic isolation characteristics in one or some directions of the isolator. The material parameters of a numerical model of the isolator are consequently updated in such a way that the difference between the measured and the calculated responses is minimized. With the obtained static and dynamic material parameters, a complete description of the isolation behavior (in all directions) of the isolator can be obtained with the numerical model. First the procedure is described and tested with the analyzed cylindrical vibration isolator studied extensively by Kari. After that, the procedure is used to determine the unknown material properties with real measurement data of a manufactured mount. The mount contains a silica-reinforced rubber compound, which is a representative compound for engine mounts.

Finally, some conclusions are drawn with respect to the numerical modeling of rubber vibration isolators and identification of rubber material parameters in section 5.6.

5.2 Isolation characterization and analysis

The procedure to determine the dynamic behavior of isolators can be split into two parts as illustrated in Figure 5.2. First, the rubber isolator is preloaded statically due to the weight of the source (step 1). This pre-deformation generally involves large deformations of the rubber material and it is assumed that this load is applied for a sufficiently long time so that no viscous effects are present. The effect of the pre-deformation is two-fold: the shape of the isolator changes due to the large elastic deformations and the material behavior changes due to the nonlinear behavior of the rubber material (the rubber material behavior depends on the deformation of the material) [52]. Subsequently, the dynamic viscoelastic response around the pre-deformed elastic state is determined with a harmonic analysis (step 2). A condition for this approach is that the vibration amplitude is sufficiently small such that both the kinematic and material response can be treated as linear perturbations

around the pre-deformed state. This is normally the case for vibrations in the frequency region of interest, i.e. structure-borne sound [104].

Figure 5.2: Analysis procedure for rubber vibration isolators: the first step is the calculation of the static pre-deformation (1) and the second step is the superposed harmonic analysis (2).

The dynamic behavior of the mount is described by a field representation at the junction at the top ① (connection with the source) and the bottom ② (connection with the receiver) of the mount, as depicted in Figure 5.3. This type of description resembles the four-pole or two-port network description [32, 87, 121], but is extended for the multi-directional vibration transmission with six degrees of freedom at each junction. The single mounting is thus characterized with a linear 12-port (six ports for all directions at each junction). The dynamics of the vibration isolator is consequently described in terms of the forces and velocities or displacements at the junctions:

$$\mathbf{f}|_1 = \mathbf{k}_{11} \cdot \mathbf{u}|_1 + \mathbf{k}_{12} \cdot \mathbf{u}|_2, \tag{5.1}$$

$$\mathbf{f}|_2 = \mathbf{k}_{21} \cdot \mathbf{u}|_1 + \mathbf{k}_{22} \cdot \mathbf{u}|_2, \tag{5.2}$$

where $\mathbf{k}_{11}$ and $\mathbf{k}_{22}$ are the blocked dynamic driving point stiffness matrices at junctions 1 and 2, respectively, $\mathbf{k}_{12}$ and $\mathbf{k}_{21}$ are the blocked dynamic transfer stiffness matrices at junctions 1 and 2, respectively, $\mathbf{f}|_1$ and $\mathbf{f}|_2$ are the 6-DOFs force vectors at the junctions and $\mathbf{u}|_1$ and $\mathbf{u}|_2$ are the 6-DOFs displacement vectors at the junctions. The term 'blocked' means that the corresponding stiffness is valid when the harmonic displacement at one port is prescribed, whereas the harmonic displacements at all other ports are constrained to zero (i.e. blocked). The forces, displacements and stiffness matrices all depend on the frequency. This type of representation is only valid for linear systems and it is assumed that the attached plates at the top and bottom (firmly bonded with the vulcanized rubber) behave as rigidly moving flanges. For multi-mounting systems, the total structure-borne sound transfer is calculated by a superposition of the single mounting contributions.

The measurement of the dynamic impedance or stiffness components of vibration isolators is extensively studied in the literature. The components

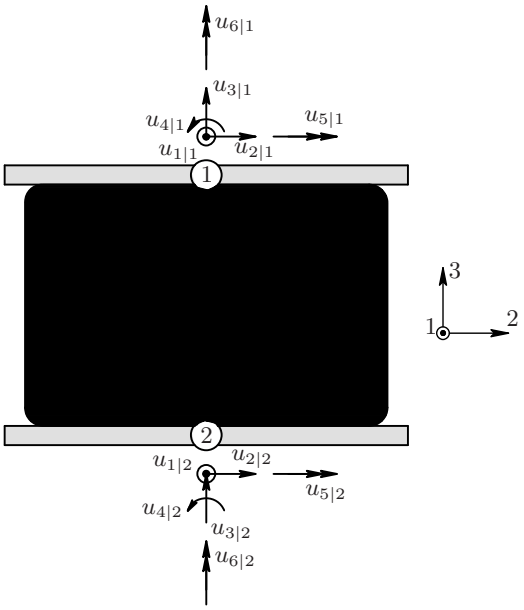

Figure 5.3: Vibration isolator with a field representation at top ① and bottom ② with the displacement vector in positive directions. The same convention is applied for the force components.

of the stiffness matrices are measured by clamping all degrees of freedom at one junction (e.g. by a blocking mass), whereas one degree of freedom is prescribed at the other junction [122, 134]. The same strategy must be used for the numerical model of the vibration isolator, by prescribing the harmonic displacements at the flanges of the model. When for example the dynamic displacement component $u_1|_1$ is prescribed (the displacement u_1 at junction ①), the six force components at the top junction and bottom junction can be determined. In this way the first columns of the blocked dynamic stiffness matrices $\mathbf{k}_{11}$ and $\mathbf{k}_{21}$ are determined. This process is repeated by prescribing the frequency dependent displacement components at all 12 ports, and in this way the complete dynamic stiffness matrix is obtained. Each dynamic stiffness matrix contains 36 components, but some of the components are zero or equal to each other when the isolator has some degree of symmetry. An overview of independent stiffness components for common cases of symmetry applied to typical mount shapes is presented by Verheij [134]. With the principle of reciprocity it can be derived that $\mathbf{k}_{12}$ is equal to $\mathbf{k}_{21}^{\mathrm{T}}$.

As explained before, the objective of a resilient mounting system is to

introduce a large impedance or stiffness mismatch for an effective isolation of the source from the receiver structure. If this is realized, then the driving point stiffness of the receiver structure is much larger than the mount stiffness, resulting in [134]:

$$\mathbf{f}|_2 \approx \mathbf{k}_{21} \cdot \mathbf{u}|_1. \tag{5.3}$$

This means that the force vector at the bottom side of the mount, which is equal and opposite to the force vector acting on the receiver structure, is solely determined by the blocked transfer stiffness of the isolator.

5.3 Numerical model of rubber isolators

5.3.1 Finite element modeling

To apply the FEM method for the passive characterization of rubber mounts, more information is needed about the theory of the FEM method and the material characterization. More detailed information about the theory behind the modeling of rubber material with the help of FEM can be found in appendix E, where the kinematics and strain deformation definitions are briefly described for rubbers. Subsequently, attention is paid to the material modeling of the rubber. The elastic behavior of isotropic hyperelastic materials is normally described by means of a strain energy function [5, 24, 97]. The strain energy function determines the strain energy stored in the material per unit of reference volume. For filled rubbers often the *Yeoh* model [143] is used, which is a four-term polynomial fit of the strain energy function. This strain energy function is given by:

$$U = C_{10}(\bar{I}_1 - 3) + C_{20}(\bar{I}_1 - 3)^2 + C_{30}(\bar{I}_1 - 3)^3 + \sum_{p=1}^{3} \frac{1}{D_1} (J-1)^{2p}, \tag{5.4}$$

where the coefficients C_{10}, C_{20}, C_{30} and D_1 are used to fit the material behavior on the standardized experiments on samples of the rubber materials. More information can be found in appendix E. Rubber behaves nearly incompressibly (i.e. the volume does not change much during deformation) and one of the four terms is the bulk modulus to take account of this compressibility. With the strain energy function and the strain definitions, a formulation of the virtual work can be derived. A discretized form (in terms of finite elements) of this virtual work formulation is solved in an iterative way. The virtual work formulation describes briefly the theory behind the FEM code needed to calculate the pre-deformation of the rubber vibration isolator.

After the calculation of the pre-deformation, a frequency domain (or harmonic) analysis is superimposed on the deformed state as explained in section 5.2. The theory behind the harmonic analysis using FEM is described in appendix E.4. The FEM formulation assumes that the frequency dependence of the shear (deviatoric) and volumetric behaviors are independent. For the harmonic analysis extra material parameters are required by the FEM package, namely a dynamic shear storage modulus, a dynamic shear loss modulus and a dynamic bulk modulus. In this work, the dynamic shear modulus is considered to be dependent on the frequency only (see section 5.3.2) in the considered frequency range relevant for structure-borne sound. The dynamic bulk modulus is assumed to be frequency independent in the considered frequency range. More details concerning the dynamic material behavior of rubber are given in the next subsection.

5.3.2 Dynamic material behavior

Rubber has a visco-elastic material behavior and thus combines the viscous properties of a liquid with the elastic properties of a solid material. The dynamic behavior is described by frequency dependent shear and loss moduli. The modulus depends on many different factors such as the frequency, temperature and vibration amplitude [78, 120]. The dynamic properties are altered substantially by the addition of a filler, such as carbon black or silica. The addition of the filler has a positive effect on the strength and other mechanical properties, but also introduces nonlinear effects. Medalia [84] gives a good overview of the influence of the frequency, amplitude and temperature effects on the dynamic material properties of carbon black filled rubber vulcanizates. A short overview of the nonlinear effects is given in this subsection.

Frequency dependence

The dynamic shear modulus of rubber exhibits strong frequency dependent behavior and three regions are distinguished with increasing frequency: a rubber region, a transition region and a glassy region. A schematic characterization of this frequency dependence with the three regions is shown in Figure 5.4. The frequency regions for unfilled natural rubber at room temperature are approximately 0 till 5000 Hz for the rubber region, 5000 till 10^9 Hz for the transition region and 10^9 Hz and larger for the glassy region. The magnitude of the shear modulus increases with frequency and with the greatest rate of change in the transition region. For frequencies larger than 10^9 Hz, the rubber material behaves in a very brittle way. The loss factor increases with

frequency in the rubber region, reaches a maximum in the transition region and decreases in the glassy region.

In practice it is nearly impossible to measure the dynamic shear modulus at such high frequencies. However, it is possible to determine the dynamic characteristics at high frequencies by making use of the temperature-frequency shift. This principle is based on the fact that the influence of the temperature and frequency on the dynamic characteristic of rubber material are equivalent. This is the so-called time-temperature superposition principle (TTS) and means that the shear modulus of rubber at a certain reference temperature and excitation frequency is similar to that for the same rubber at lower temperatures and with a lower excitation frequency. The relation between the frequency and temperature dependence is described by an empirical shift function, such as the William-Landel-Ferry (WLF) equation [37]. This relation is valid for so-called thermo-rheologically simple materials, behaving in a linear way. For natural rubber with a large filler content, the behavior may become strongly nonlinear, and the time-temperature superposition principle may become invalid.

The frequency range for the structure-borne sound considered in this study on hybrid isolation is low enough for the rubber to stay in the rubber region. Sjöberg has studied the influence of the frequency on the dynamic characteristics of vibration isolators with models and measurements [117]. A typical phenomenon mentioned in his paper is that there is a jump in the dynamic stiffness from the point of quasi-static behavior in the frequency region of 0.05 Hz to 1 Hz, followed by an increase of the dynamic stiffness with increasing frequency. This effect is more pronounced when more filler is present in the rubber compound and for low amplitude vibrations. This effect was observed earlier, e.g. by Payne and Whittaker [104].

Temperature dependence

The dynamic shear modulus and loss factor also depend on the temperature of the material. The temperature dependence of rubber is similar to the effect of changing the vibration frequency and a schematic characterization is shown in Figure 5.5. The material behavior can again be divided into three regions: a glassy region at low temperatures with a relatively high magnitude of the shear modulus, a transition region with a decreasing magnitude of the shear modulus and a rubber region at high temperatures with a low shear modulus magnitude. The shear modulus and loss factor only change slightly in the rubber region. The transition region, denoted by the increase in stiffness or shear modulus, starts at around -20 °C and at a temperature of -60 °C the

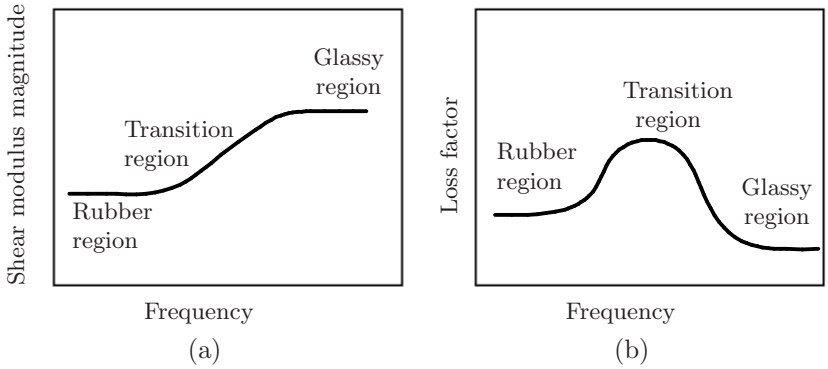

Figure 5.4: Schematic representation of the frequency dependent behavior of rubber material.

rubber is glass-like and brittle [78]. Kari and Sjöberg studied the effect of the temperature on the dynamic stiffness of a rubber isolator with the help of theoretical models [68].

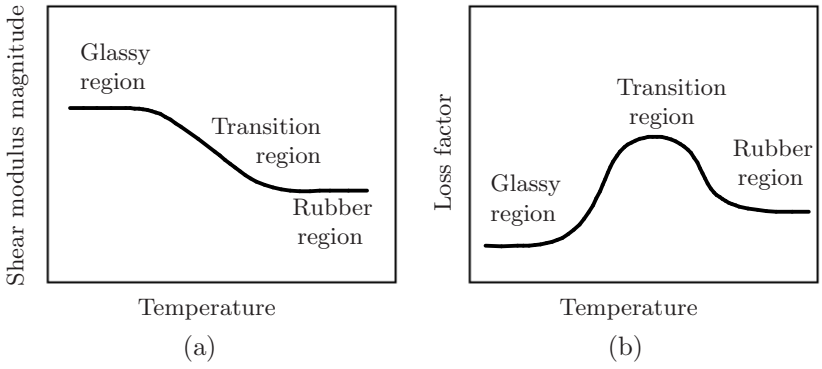

Figure 5.5: Schematic characteristics of rubber material temperature dependence.

Amplitude dependence

In contrast to unfilled rubbers, the dynamic shear modulus and loss factor of filled rubbers depend on the vibration amplitude [122]. The filler particles, consisting for example of particles carbon black or silica, are strongly bonded to other primary particles and form so-called aggregates [97]. The aggregates are weakly bonded to other aggregates and form agglomerates. These interac-

tions between the different kinds of particles can be considered as friction-like behavior and cause the complex nonlinear behavior of the filled rubber. There are two well-known stress-softening effects that occur in filled vulcanized rubber material, known as the Mullins effect and the Payne effect. The first effect is seen when a previously unstrained rubber material is subjected to strain cycles with a constant amplitude. The first few cycles show a decrease in peak stress values. This is thought to be due to the rearrangement of the molecular networks in the rubber itself and not due to filler interactions. This is the reason why rubber isolators, before starting the measurements of the dynamic properties, are 'mechanically conditioned' by subjecting the isolator to a few large deformation cycles to eliminate the influence of this effect. The Payne effect displays a larger shear modulus at small strain amplitudes than at larger strain amplitudes. This effect is more pronounced when more filler is added to the rubber compound. For small amplitudes, the filler structure remains intact and the dynamic shear modulus is relatively large. When the amplitude of the vibration increases, the filler structure breaks and the dynamic modulus decreases. Also, the energy dissipation decreases, resulting in a lower loss factor. Sjöberg and Kari have also studied the effect of the amplitude of the vibration on the dynamic stiffness of rubber isolators with experiments and models [117, 118, 119, 120].

Constitutive assumptions

The rubber material for passive vibration isolators in this work is assumed to be isotropic, homogeneous, nearly incompressible and time invariant. The material behavior of the rubber is confined to the isothermal rubber region and the influence of glass hardening and low-temperature crystallization is not considered. The influence of aging and dynamic amplitude dependence is also ignored. The dynamic amplitude dependence can be ignored for filled rubbers when the strain amplitudes are smaller than 0.1, as was shown by Payne [104]. For the analysis of the structure-borne sound transmission, the amplitudes are in general sufficiently small, especially at higher frequencies.

5.4 Application: model of a cylindrical vibration isolator

The modeling described in the previous section is applied to investigate the dynamic behavior of a rubber mount. A rubber cylindrical mount, which has been studied extensively in the literature by Kari [63], both with models (a

waveguide model [66] and a FEM model [64, 67]) and experiments [65, 66, 67], is studied numerically. The numerical results of the axial dynamic stiffness are compared with the experimental results from the references as a check for the developed procedure. In addition, the other directions are considered with respect to the isolation behavior and structure-borne sound transmission [8, 98]. As stated before, the passive mounting system has multiple directions in which structure-borne sound is transmitted to the receiver structure. For a good characterization of the passive isolation behavior, all these directions have to be taken into account.

5.4.1 Test object

The considered test object is a solid cylindrical compression molded rubber isolator with a height of 50.0 mm and a radius of 50.0 mm. At the top and bottom of the mount, cylindrical plates are bonded to the rubber part (the flanges). The steel plates have a thickness of 2.6 mm. The principal ingredients of the vulcanized natural rubber are given in Table 5.1. The ground-state density of the rubber is 1050 kg/m^3 and has a nominal hardness of 40° IRHD (International Rubber Hardness Degree, which is an alternative to the Shore A hardness measure). The material properties of the rubber compound used for the simulations are shown in Table 5.2.

Material properties of the rubber

The rubber compound consists of natural rubber with a small amount of carbon black (10 parts per hundred rubber (phr)). For this kind of rubber, the Yeoh model as given in equation (5.4) is suited to fit the strain-energy function for the FEM calculation. The values of the Yeoh constants fitted on the measured static behavior of the rubber material are shown in Table 5.2. The dynamic material properties, described by the frequency dependent magnitude and loss factor of the shear modulus, are depicted in Figure 5.6(a) and 5.6(b) respectively, and show the for natural rubber characteristic behavior of a slightly increasing loss factor and magnitude of the shear modulus with the frequency. Kari measured the dynamic modulus with a DMA analyzer [67].

5.4.2 Procedure and simulations

The considered test object is a cylindrical isolator, and due to symmetry the number of independent dynamic stiffness components can be reduced considerably. With the sign convention displayed in Figure 5.3, the cylindrical mount

Category	Ingredient	Type	Concentration (phr)
Polymer	Natural rubber	SMR CV50	100
Filler system	Carbon black	N772	10
Stabilizer system	Anti-degradant system	Anti-ozonant	1
		Anti-oxidant	1
		Waxe	1
Vulcanization system	Activators	Stearic acid	1
		Zinc oxide	5
	Vulcanizing agent	Sulphur	3
	Accelerator	CBS	2
Special materials	Processing oils	Paraffinic	1
		Aromatic	5

Table 5.1: Principal ingredients of the natural rubber compound of the studied mount [67].

Parameter	Value
Density ρ_0	$1050\ \mathrm{kg/m^3}$
Yeoh model:	
C_{10}	$G_\infty/2 = 2.97 \cdot 10^5\ \mathrm{N/m^2}$
C_{20}	$-4.5 \cdot 10^4\ \mathrm{N/m^2}$
C_{30}	$1.5 \cdot 10^4\ \mathrm{N/m^2}$
D_1	$2/k_0 = 1.515 \cdot 10^{-9}\ \mathrm{N/m^2}$
Shear mod. :	
G_∞	$5.94 \cdot 10^5\ \mathrm{m^2/N}$

Table 5.2: Material parameters used for the FEM model [67].

has a mirror plane perpendicular to the 3-axis and is axisymmetric around the 3-axis. The dynamic stiffness matrices (both the driving point and transfer

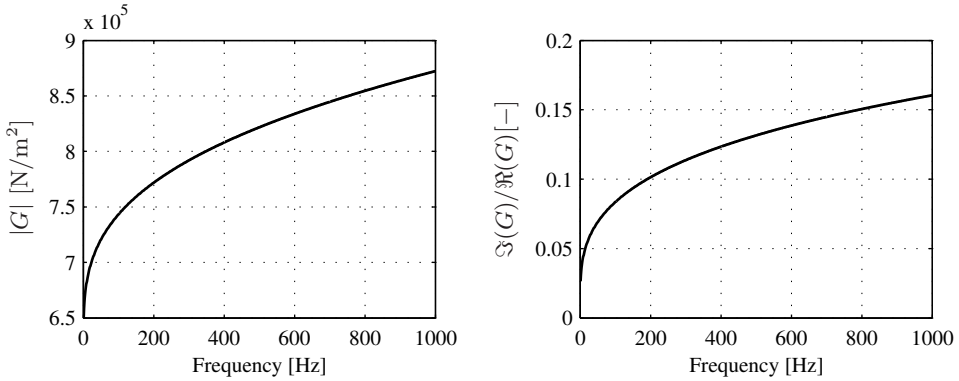

Figure 5.6: Magnitude and loss factor of the shear modulus as a function of the frequency [67].

stiffness matrices) have the following components:

$$\mathbf{k}_{ij} = \begin{bmatrix} k_{ij}(1,1) & 0 & 0 & 0 & k_{ij}(1,5) & 0 \\ 0 & k_{ij}(2,2) & 0 & k_{ij}(2,4) & 0 & 0 \\ 0 & 0 & k_{ij}(3,3) & 0 & 0 & 0 \\ 0 & k_{ij}(4,2) & 0 & k_{ij}(4,4) & 0 & 0 \\ k_{ij}(5,1) & 0 & 0 & 0 & k_{ij}(5,5) & 0 \\ 0 & 0 & 0 & 0 & 0 & k_{ij}(6,6) \end{bmatrix} \qquad i,j = 1,2. \tag{5.5}$$

Furthermore, some components within each stiffness matrix can be related to each other due to symmetry. Some of the components for the blocked dynamic driving point stiffness matrices $\mathbf{k}_{11}$ and $\mathbf{k}_{22}$ are related to each other according to:

$$\begin{aligned} k_{11}(1,1) &= k_{11}(2,2) = k_{22}(1,1) = k_{22}(2,2), \\ &\quad k_{11}(3,3) = k_{22}(3,3), \\ k_{11}(4,4) &= k_{11}(5,5) = k_{22}(4,4) = k_{22}(5,5), \\ &\quad k_{11}(6,6) = k_{22}(6,6), \\ k_{11}(2,4) &= k_{11}(4,2) = -k_{11}(1,5) = -k_{11}(5,1) = \\ &\qquad - k_{22}(2,4) = -k_{22}(4,2) = k_{22}(1,5) = k_{22}(5,1). \end{aligned} \tag{5.6}$$

In a similar way, some components of the two blocked dynamic transfer stiffness matrices $\mathbf{k}_{21}$ and $\mathbf{k}_{12}$ are related to each other according to:

$$\begin{aligned} k_{21}(1,1) = k_{21}(2,2) = k_{12}(1,1) = k_{12}(2,2), \\ k_{21}(3,3) = k_{12}(3,3), \\ k_{21}(4,4) = k_{21}(5,5) = k_{12}(4,4) = k_{12}(5,5), \\ k_{21}(6,6) = k_{12}(6,6), \\ k_{21}(2,4) = -k_{21}(4,2) = -k_{21}(1,5) = k_{21}(5,1) = \\ - k_{12}(2,4) = k_{12}(4,2) = k_{12}(1,5) = -k_{12}(5,1). \end{aligned} \tag{5.7}$$

Due to the symmetry properties of the cylindrical mount, only four simulations have to be performed for each pre-deformation as a function of frequency. The four simulations needed for a complete dynamic description of the considered isolator are shown schematically in Figure 5.7. The displacement component $u_{3|1}$ is prescribed to determine the axial dynamic stiffness components ($k_{11}(3,3)$ and $k_{21}(3,3)$, see Figure 5.7(a)), $u_{1|1}$ is prescribed to determine the transverse dynamic stiffness components and the cross-coupling between the transverse and rotational directions ($k_{11}(1,1)$, $k_{21}(1,1)$, $k_{11}(5,1)$ and $k_{21}(5,1)$, see Figure 5.7(b)), $u_{4|1}$ is prescribed to determine the rotational dynamic stiffness components and the cross-coupling with the translational direction ($k_{11}(4,4)$, $k_{21}(4,4)$, $k_{11}(2,4)$ and $k_{21}(2,4)$, see Figure 5.7(c)) and $u_{6|1}$ is prescribed to determine the torsional dynamic stiffness components ($k_{11}(6,6)$ and $k_{21}(6,6)$, see Figure 5.7(d)).

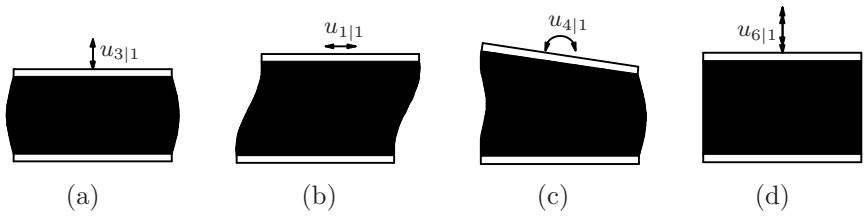

Figure 5.7: Schematic pictures of the load cases for the harmonic FEM simulations to determine the independent dynamic stiffness components.

Numerical FEM model

The simulations were performed with the commercial finite element package ABAQUS. The mesh of the undeformed cylindrical vibration isolator is

shown in Figure 5.8(a) and the mesh after a static pre-deformation is shown in Figure 5.8(b). The bulging behavior is typical and due to the almost incompressible behavior of the rubber. The rubber material is meshed with solid quadratic 20-node brick elements (type C3D20H). These elements use a hybrid formulation to circumvent numerical problems due to the almost incompressible behavior of the material [24]. The plates, bonded to the vulcanized rubber at the top and the bottom side of the mounts are modeled with quadratic 8-node shell elements (type S8R). It must be noted that, in case of the determination of the axial dynamic transfer stiffness ($k_{ij}(3,3)$), a two-dimensional axisymmetric model can be used. However, for the determination of the stiffness components in the other directions, a three-dimensional model is necessary.

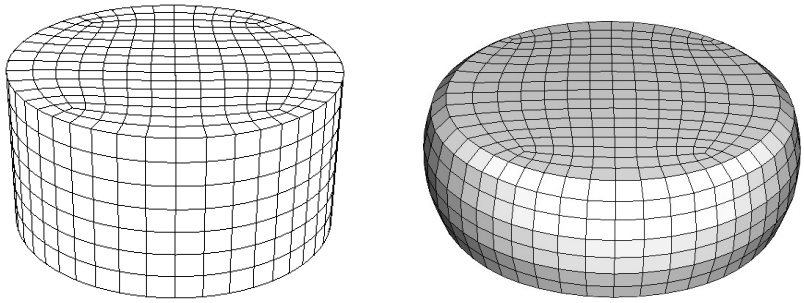

(a) (b)

Figure 5.8: Mesh of the studied cylindrical vibration isolator in the undeformed situation (a) and after pre-deformation (b).

5.4.3 Results

Static behavior

The first step in the analysis procedure is the static pre-deformation due to the weight of the source. The pre-deformation is determined with a nonlinear analysis in ABAQUS because of the large elastic deformations. The static stiffness is quite important because the mounting system has to support the source and transmit the torque (in the case of an engine). The force-displacement curve in the axial direction is depicted in Figure 5.9, and shows the force that is needed to obtain the axial pre-deformation (indicated by u_{pr}). Further, it is shown that the slope of the curve, which presents the compression stiffness of the mount, increases gradually as a function of the pre-deformation. This is

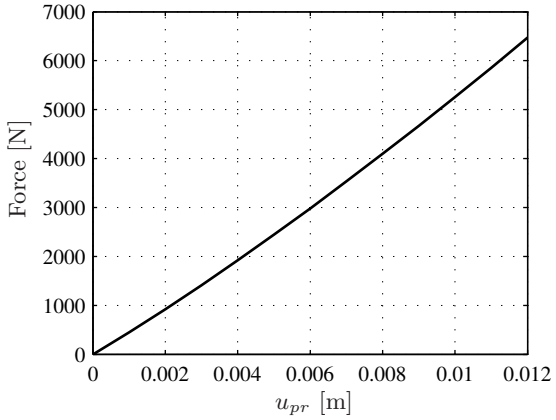

Figure 5.9: Force-displacement curve for the axial or longitudinal directions of the cylindrical isolator.

due to the change of material characteristics and due to the change of shape of the mounts, which is taken into account in the nonlinear calculation. The results agree very well with the static measurements in the literature [67].

Dynamic results

After the determination of the static pre-deformation, the dynamic stiffness components are calculated. This is done for four different pre-deformations: $u_{pr} = 0, 3, 6$ and 9 mm, corresponding with preloads of $0, 1410, 2980$ and 4670 N respectively. The dynamic transfer stiffness components are determined with the simulations as shown schematically in Figure 5.7. The transverse, axial, moment and torsional dynamic transfer stiffness are shown in Figures 5.10(a) - 5.10(d). The cross-coupling terms $k_{21}(5,1)$ and $k_{21}(2,4)$, which should be equal to each other as shown in equation (5.7), are both given in Figures 5.11(a) and 5.11(b). The dynamic transfer stiffness is depicted as a magnitude response (the graph at the top side of each subfigure) and a phase plot (the graph at the bottom side of each subfigure).

Considering the dynamic transfer stiffness components in general, it can be seen that the isolator behaves quasi-statically at low frequencies (for frequencies $<$ 200 Hz). The dynamic stiffness at low frequencies is equal to the static stiffness. The tendency for the static stiffness to increase with increasing pre-deformation can also be seen in Figure 5.10(b): the axial dynamic stiffness at low frequencies is higher for a larger pre-deformation. The influence

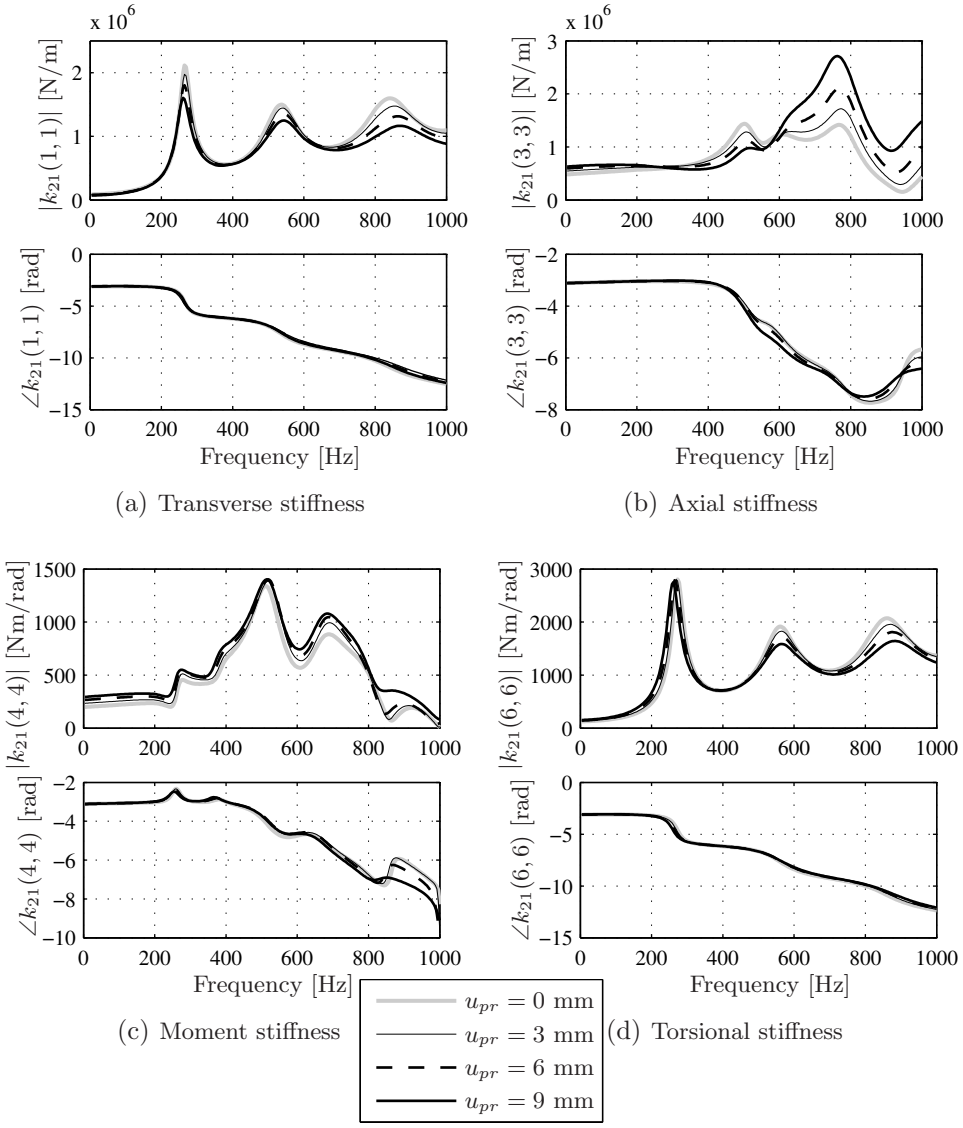

Figure 5.10: Blocked dynamic transfer stiffness components as a function of frequency and pre-deformation.

of the pre-deformation is especially considerable for the axial dynamic transfer stiffness, and for the transverse stiffness at higher frequencies. When the excitation frequency is increased, the inertial properties of the mount start to play a role and wave effects occur in the rubber material. This dynamic be-

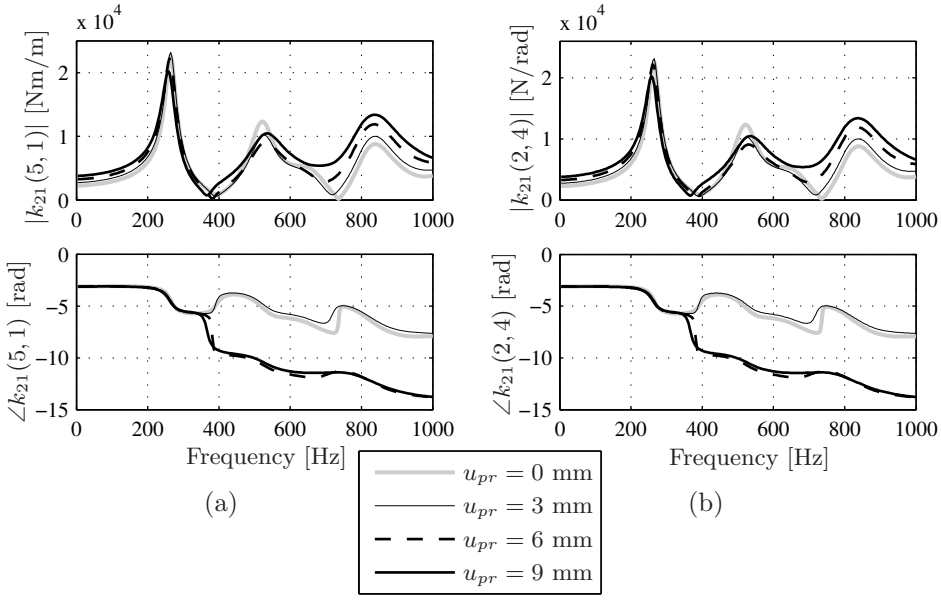

Figure 5.11: Cross-coupling components of the blocked dynamic transfer stiffness as a function of frequency and pre-deformation.

havior has a large influence on the dynamic stiffness and thus on the isolation characteristics of the mount. Considering the transverse, axial and torsional stiffnesses, the quasi-static behavior at low frequency is followed by a strong increase in dynamic stiffness as the frequency increases. This is due to the occurrence of a wave and is also characterized by a phase shift of $-\pi$ radians. The wave effects start in the transverse and torsional directions at a frequency of about 270 Hz. The increase is very pronounced, resulting in a dynamic stiffness that is 20 times the static stiffness for the transverse and torsional directions. Wave effects in the axial direction are observed at around 500 Hz and decrease with increasing pre-deformation. After the first increase in the dynamic stiffness, the curve drops, after which it starts to rise again. As the frequency increases, the wavelengths of the waves formed in the rubber material become smaller. However, the introduction of wave effects cannot be so clearly distinguished at higher frequencies. This is caused by the large amount of damping, which also increases as a function of the frequency. The large amount of damping is denoted by a flattening of the magnitude peaks and a smoothing of the phase transitions. Considering the moment transfer stiffness in Figure 5.10(c), a first rise of the stiffness occurs at around 270 Hz, corresponding with the frequency where wave effects occur in transverse di-

rection of the mount. The curve shows two more rises at 500 and 680 Hz. The cross-coupling terms depicted in Figure 5.11 show a similar behavior as the dynamic transverse stiffness, except for the influence of the pre-deformation. The cross-coupling terms act as a good check of the procedure, and fulfill the condition shown in equation (5.7): $k_{21}(2,4) = k_{21}(5,1)$. The results for the axial dynamic transfer stiffness agrees very well with the experimental results found by Kari [67].

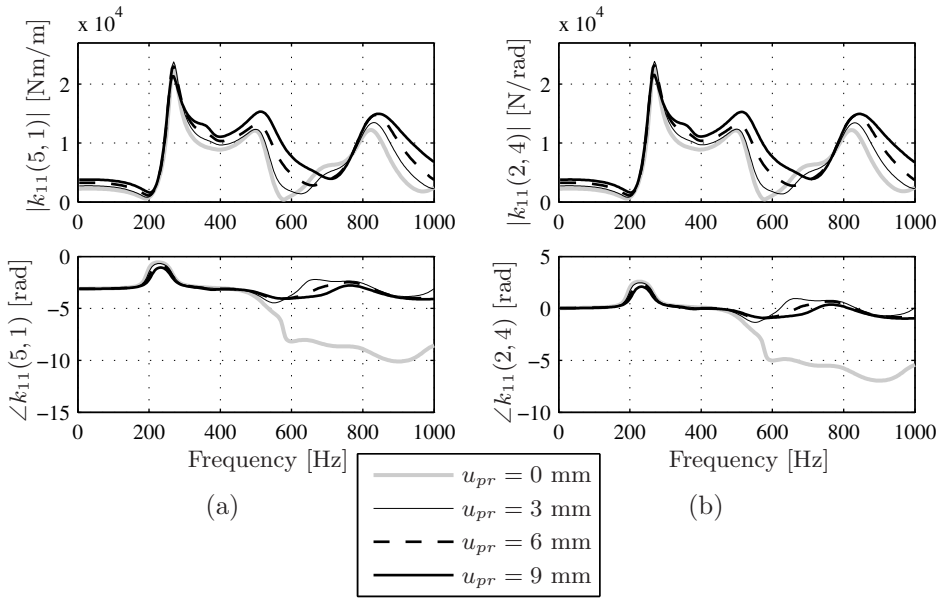

Figure 5.12: Cross-coupling components of the blocked dynamic driving point stiffness as a function of frequency and pre-deformation.

In Figures 5.12(a) and 5.12(b) both dynamic cross-coupling coefficients are shown. Because of symmetry, these components should be equal to each other, which is indeed observed. The other dynamic driving point stiffnesses, namely the transverse, axial, moment and torsional driving point stiffness components, are depicted in Figures 5.13(a) - 5.13(d). Except for the cross-coupling components, the driving point responses are dominated by the plate mass contributions in the largest part of the frequency range.

With the derived dynamic stiffness components, a complete characterization of the passive isolation behavior of the isolator is obtained. This is important for the design of a hybrid mount, because an indication is obtained of the contribution of the different structural transmission paths of the isolator to the total injected structural power into the receiver structure. For the

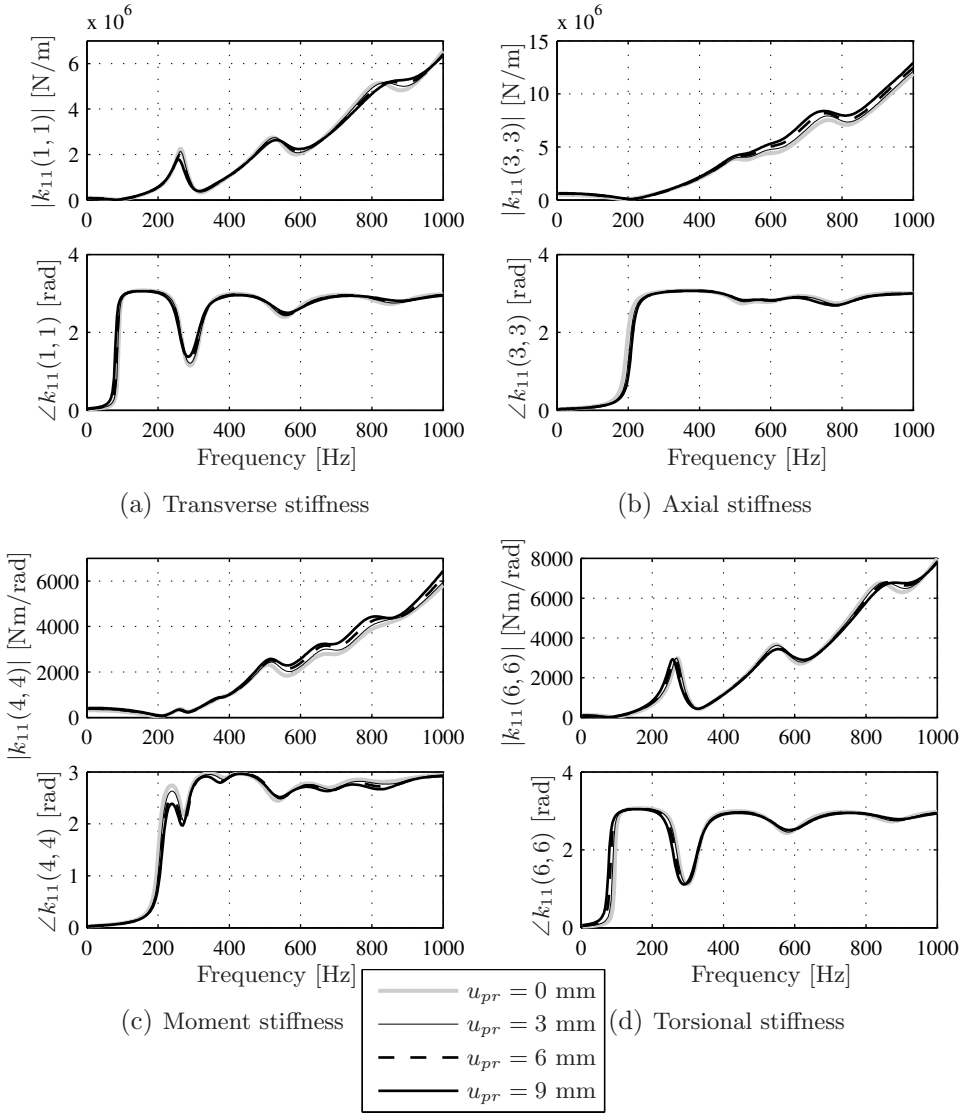

Figure 5.13: Blocked dynamic driving point stiffness components as a function of frequency and pre-deformation.

isolator analyzed, it can be seen for example that the transverse dynamic stiffness is dominant in comparison to the axial dynamic stiffness in the frequency region from 230 till 300 Hz. This means that the transverse direction may have the largest contribution of the transmitted power and for this reason the

most dominant sound path. So, for an effective reduction of the structure-borne sound transmission, it may be favorable to position the actuator in the transverse direction in cases where the isolation needs to be improved in the corresponding frequency range.

Wave effects

The wave effects have a considerable influence on the dynamic stiffness of the isolators. Hence, the isolation characteristics vary considerably with respect to the excitation frequency. To give an idea of what is actually happening in the rubber material itself, several harmonic deformation shapes of an axisymmetrical section of the rubber mount are shown in Figure 5.14. The pictures show the real and imaginary contour plots of the longitudinal displacements for simulations at different frequencies. The harmonic displacement at the top of the isolator is prescribed as a linear perturbation around its static shape. In this case the isolator has no pre-deformation. It is shown that at 100 Hz the deformed shape resembles a static deformed shape. At 400 Hz the mass behavior starts to play a role and a wave is introduced into the material, which can be observed at the outside of the isolator (b). The influence of the mass behavior is also observed by an increase of the dynamic stiffness as a result of the wave effect. When the excitation frequency is increased even further, the first wave is introduced at around 500 Hz (d). It can also be seen, that the increase of the excitation frequency results in a decrease of the wavelength. The reduction of the wavelength is clearly noticeable at the outside of the isolator. Furthermore it can be seen that the waves are not synchronous and the nodal lines (lines with zero longitudinal displacement) travel through the material during one period.

5.5 Determination of the rubber material parameters

The most important factor for a reliable numerical model is a good description of the material behavior. As stated before, rubber behaves in a quite complex way and it is not easy to obtain a good description of the material behavior. For this reason a procedure is described to determine the rubber material parameters using measurements from an entire isolator. This is done by updating the material parameters of a numerical model in such a way that the difference between the measured and the calculated responses is minimized. First, the procedure is described and tested with the analyzed cylindrical vibration

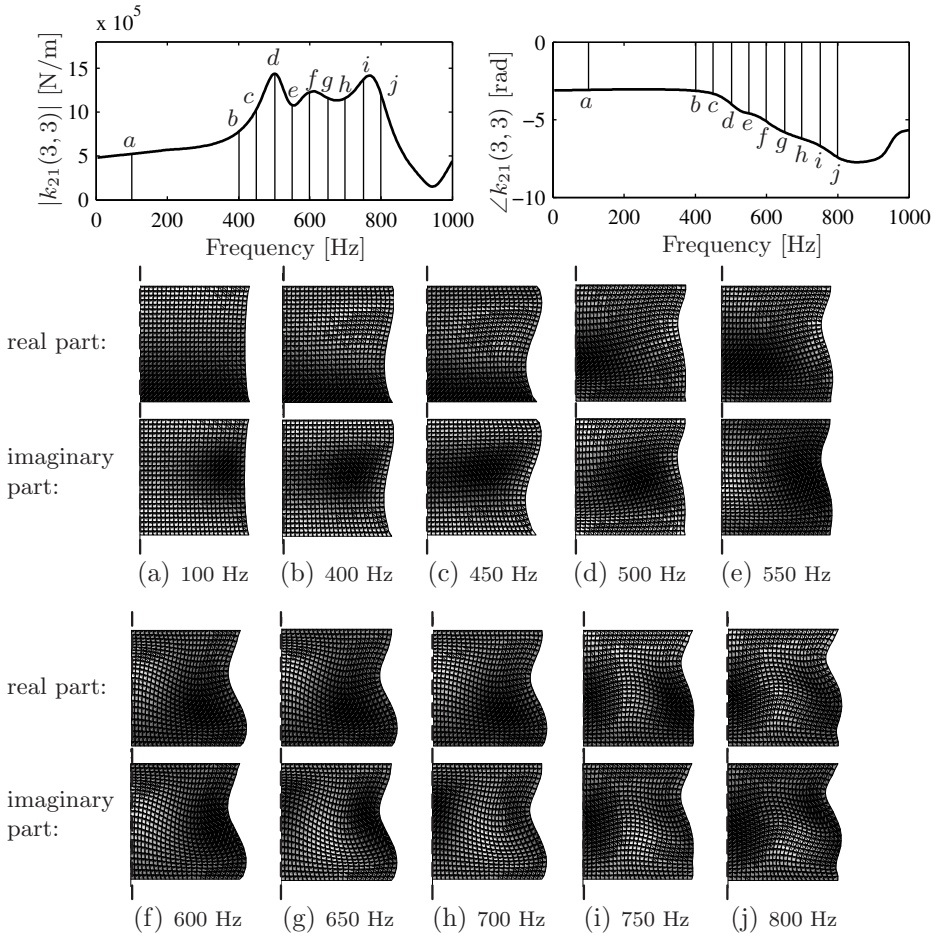

Figure 5.14: Contour plots of the longitudinal displacement on the deformed shape of an axisymmetric part of the isolator without pre-deformation.

isolator that was studied extensively by Kari. After that, the procedure is used to determine the unknown material properties of a manufactured mount with a silica-reinforced rubber compound representative for engine mounts.

5.5.1 Procedure

The procedure to obtain rubber material parameters with updating numerical models is similar to the procedure described by Willes *et al.* [138, 139] and De

Boer [29]. The procedure is subdivided into two stages: in the first stage the material parameters to describe the static pre-deformation of the isolator are determined and in the second stage, the dynamic material properties related to the dynamic behavior of the isolator are determined [9]. An overview of the procedure is given in appendix F.

The static material parameters, in the form of three Yeoh parameters (when fully incompressible behavior is assumed: $J = 1$) which describe the strain-energy function as shown in equation (5.4), are determined by means of a static force-displacement measurement. This measurement can be carried out with a uni-axial test setup. The isolator is loaded with different pre-deformations at the top, after which the reaction force is measured. In this way a force-displacement curve can be determined and the forces are assembled in the vector $\mathbf{f}_m$. A numerical model is then composed of the considered vibration isolator, and the reaction forces are calculated for the same set of pre-deformations as used for the measurements. The static forces determined with this numerical model are gathered in the vector $\mathbf{f}_u$, where the subscript u indicates that this force vector is updated in the optimization procedure. The Yeoh parameters are now determined with an iterative optimization procedure, where the numerical results are fitted on the experimental results by minimizing the following quadratic objective function:

$$J_s = (\mathbf{f}_m - \mathbf{f}_u)^{\mathrm{T}} \cdot (\mathbf{f}_m - \mathbf{f}_u). \tag{5.8}$$

When the updated force $\mathbf{f}_u$ converges towards the measured force vector, a minimum of the objective function is found and the obtained Yeoh parameters describe the static force-displacement curve quite well.

After the determination of the Yeoh parameters, the dynamic material properties are determined in the second stage. For the determination of these material parameters, a dynamic transfer stiffness measurement for the rubber isolator is needed as a function of frequency. In a similar way as was shown in the first stage, the dynamic shear storage and loss modulus of a numerical model are updated such that the difference between the updated numerically determined dynamic stiffness and the experimentally measured dynamic stiffness is minimized. This procedure is repeated for each frequency minimizing the following quadratic objective function:

$$J_d = (\Re(k_m) - \Re(k_u))^2 + (\Im(k_m) - \Im(k_u))^2\,, \tag{5.9}$$

where k_m is the complex measured dynamic transfer stiffness and k_u is the complex numerical dynamic transfer stiffness that is updated. After convergence for one frequency, an initial guess value of the dynamic shear modulus

for the next frequency can be obtained by extrapolation of the values at the current and previously determined frequencies. After determination of the shear modulus for all frequencies, a complete material description is obtained consisting of the Yeoh parameters and the complex frequency dependent dynamic modulus.

For the numerical simulations the finite element package ABAQUS was used. The optimization procedure was implemented in MATLAB, where ABAQUS was invoked within each iteration. The optimization procedure used was a standard unconstrained nonlinear optimization procedure based on the simplex method [49].

5.5.2 Validation

The identification method for the material parameters is validated for the numerically determined static force-displacement graph and dynamic stiffness for the cylindrical vibration isolator studied in section 5.4. The numerical exercise is considered as a simulated 'measurement' to identify the material properties of the rubber material used. The reconstructed material parameters are required to reproduce the static material properties shown in Table 5.2 and the dynamic shear modulus shown in Figure 5.6. The numerical model updated to determine the material properties, is a two-dimensional axisymmetric model that can be used for this case because only the axial dynamic stiffness is considered. This is in fact the same model as used to visualize the wave effects in the axial direction as shown in Figure 5.14.

In Figure 5.15(a) the numerically determined force-displacement curve is shown (used as reference solution and 'measurement') together with the force-displacement curve that corresponds to the material parameters identified. For the update procedure, the rubber is considered to be incompressible and only three Yeoh parameters have to be determined. The reconstructed force-displacement results reproduce the reference solution very well. The Yeoh parameters obtained corresponding with the updated result are shown in Table 5.15(b). The coefficient C_{10} is estimated quite well, but some deviations are present in the second and third coefficients C_{20} and C_{30}. However, the influence of the second and third coefficients on the total static response is quite small.

After the determination of the static material parameters, the dynamic shear modulus of the material can be obtained. In Figure 5.16(a) the reference axial dynamic stiffness and the axial stiffness obtained after the optimization procedure are shown. Again, a good agreement is obtained between the updated solution and the reference solution. In Figure 5.16(b) the dynamic

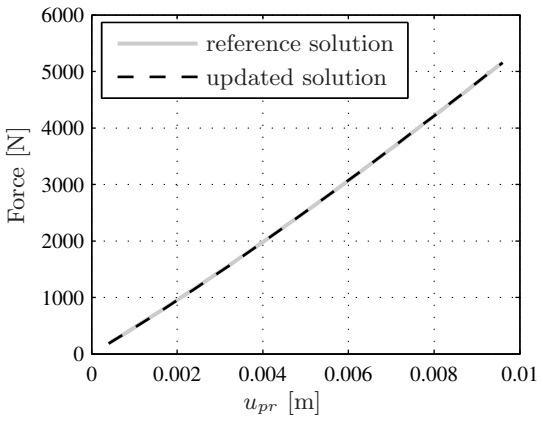

(a)

Yeoh param.	Reference value	Updated value
C_{10}	$2.98 \cdot 10^5$	$2.96 \cdot 10^5$
C_{20}	$-4.5 \cdot 10^4$	$-3.8 \cdot 10^4$
C_{30}	$1.5 \cdot 10^4$	$6.33 \cdot 10^3$

(b)

Figure 5.15: Static force-displacement response and identified Yeoh material parameters of the considered test case.

shear storage modulus obtained G_s and the dynamic shear loss modulus G_l are shown as a function of frequency, together with the reference solution. A good agreement is seen and therefore good material properties of the rubber material are obtained.

5.5.3 Example: silica-reinforced isolator

The procedure is now applied on measured data for the rubber isolator shown in Figure 5.17. The goal of this exercise is to demonstrate how the described procedure works on actually measured data to determine the unknown material properties. The rubber compound is a compound typically used in engine mounts and has a much larger filler content than the cylindrical mount considered so far [28]. Instead of black carbon, silica is used as filler and due to the relatively large filler content (50 phr), the isolator has a hardness of approximately 65 Shore A. This means that the rubber material itself is much stiffer (a higher shear modulus) than the rubber of the mount analyzed by Kari and described in the previous section. The ingredients of the rubber compound are shown in Table 5.3. The mount was manufactured[1] with a compression moulding process and has a diameter of 62 mm and a height of 30 mm. The

[1]The mount was manufactured in the laboratory of the Rubber Technology group at the University of Twente.

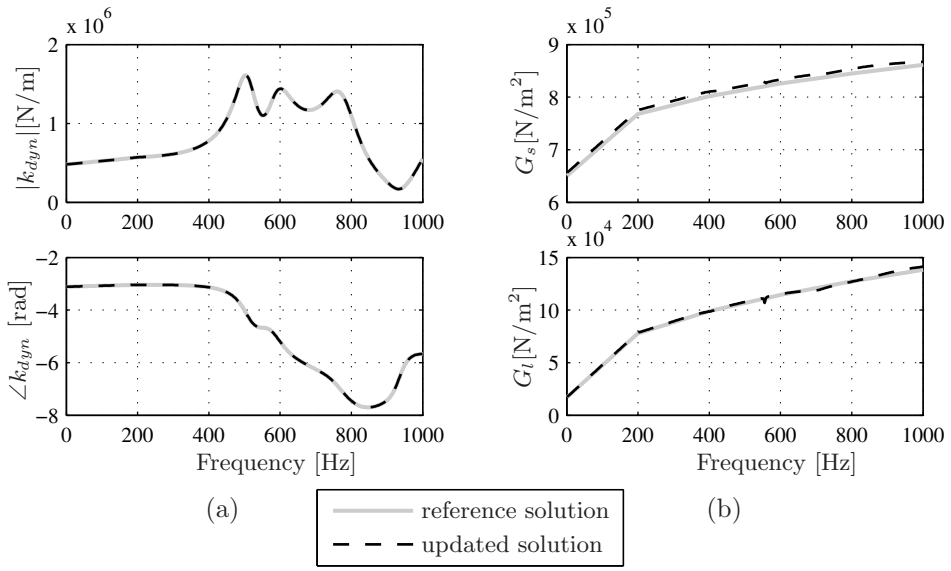

Figure 5.16: The dynamic response (a) and dynamic material properties (b) as a function of the frequency.

flanges at the top and bottom consist of two aluminium plates which are vulcanized with the rubber and with a thickness of 2 mm. The density of the rubber is 1200 kg/m^3. More details about the isolator and its manufacture can be found in [98].

Determination of the static material parameters

The force-displacement curve was measured with a uni-axial tester for different pre-deformations. The uni-axial tester is shown in Figure 5.18 with the preloaded isolator that can be recognized by its bulge shape. The measurement results are shown in Figure 5.19(a), together with the force-displacement curve obtained by the determination of the Yeoh parameters. As can be seen a good fit of the measured curve is obtained with the material parameters shown in Table 5.19(b). Although the isolator with the silica-reinforced rubber has almost the same static stiffness as the rubber isolator considered by Kari, the silica-reinforced rubber material itself behaves more stiffly than the rubber of the mount of Kari. Again it can be seen that the mount behaves slightly more stiffly for increasing pre-deformation.

Figure 5.17: The analyzed rubber mount.

Category	Ingredient	Type	Concentration (phr)
Polymer	Natural rubber	SIR	100
Filler system	Silica	Zeosil 1165MP	50
Coupling agent	Silane	Si-69 (TESPT)	5
Stabilizer system	Anti-degradant system	6-PPD	1
		TMQ	0.5
Vulcanization system	Activators	Stearic acid	1
		Zinc oxide	3
	Vulcanizing agent	Sulphur	0.3
	Accelerator	CBS	3
	Accelerator	DPG	1.5
	Accelerator	TMTD	0.5
Special materials	Processing oils	Aromatic	5

Table 5.3: Principal ingredients of the silica-reinforced natural rubber compound.

Determination of the dynamic material parameters

The transfer stiffness can be measured in two ways: a direct or indirect method. The first uses a force transducer on the output side of the isolator, while the latter uses a blocking mass. The measurement setup at TNO is based on the indirect method [65, 134] and shown in Figure 5.20. The upper block is excited in a certain direction, while the vibrations of other degrees of freedom are suppressed. The lower block (the so-called blocking mass) restricts the

movement of the bottom-side of the isolator and is placed on auxiliary mounts to decouple the test object from the test rig frame. The blocking mass only blocks the movements well for frequencies above the natural frequency of the mass-spring system consisting of the blocking mass, the test isolator and the auxiliary mounts. The motion of the upper mass is measured with acceleration pickups. The blocking force is determined with the mass and the measured

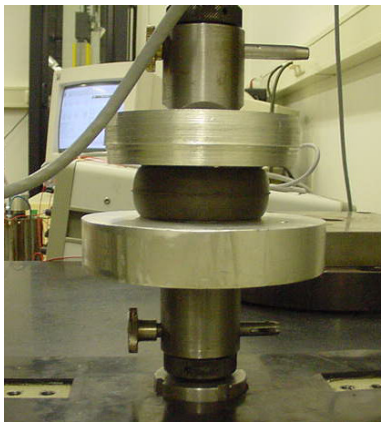

Figure 5.18: The uni-axial tester with the preloaded silica-reinforced isolator.

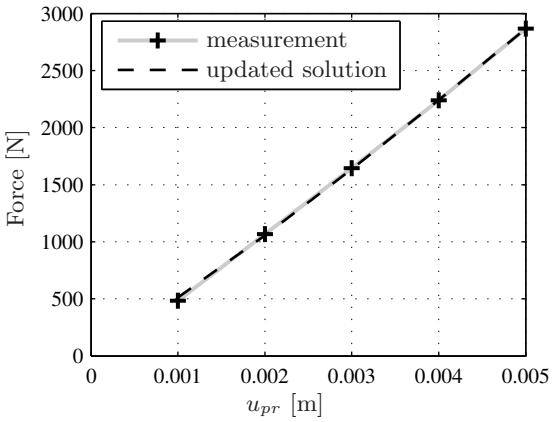

(a)

Yeoh param.	**Updated value**
C_{10}	$5.11 \cdot 10^5$
C_{20}	$-6.38 \cdot 10^4$
C_{30}	$1.16 \cdot 10^4$

(b)

Figure 5.19: Static force-displacement response and identified Yeoh material parameters of the considered silica-reinforced isolator.

accelerations of the lower mass. In Figure 5.20 a photo and a diagram of the measurement setup is shown, in the configuration for measuring the dynamic transverse stiffness. This configuration uses two shakers: a primary shaker to excite the top mass in the horizontal direction and a secondary shaker to suppress the rotations of the upper mass by an active control system [136]. This control system drives the secondary shaker by minimizing the rotation around the y-axis that is measured with the acceleration pickups 1 and 2.

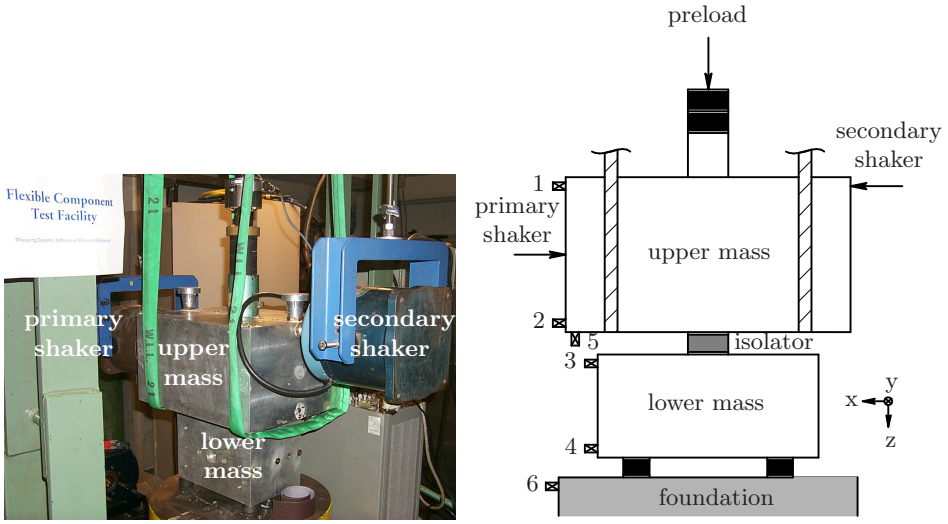

Figure 5.20: Photo and diagram of the measurement setup to determine the dynamic transverse stiffness (laboratory setup at TNO). The acceleration pickups are numbered from 1 to 6.

The magnitude of the measured transverse stiffness of the isolator is shown in Figure 5.21(b). The dynamic shear modulus were determined at seven frequencies in the considered frequency range (200, 400, 600, 800, 1000, 1200 and 1400 Hz). The dynamic shear storage modulus (indicated by the $\circ$) and the dynamic shear loss modulus (indicated by $\times$) found with the iterative procedure are both shown in Figure 5.21(a). A representation of the shear modulus over the whole frequency range is then obtained by a parabolic least-squares curve fit through all these points. The calculated dynamic transverse stiffness determined with the curve fit of the shear modulus is also plotted in Figure 5.21(b). A good agreement between the measured and the simulated results is found up to a frequency of 1000 Hz. At higher frequencies significant

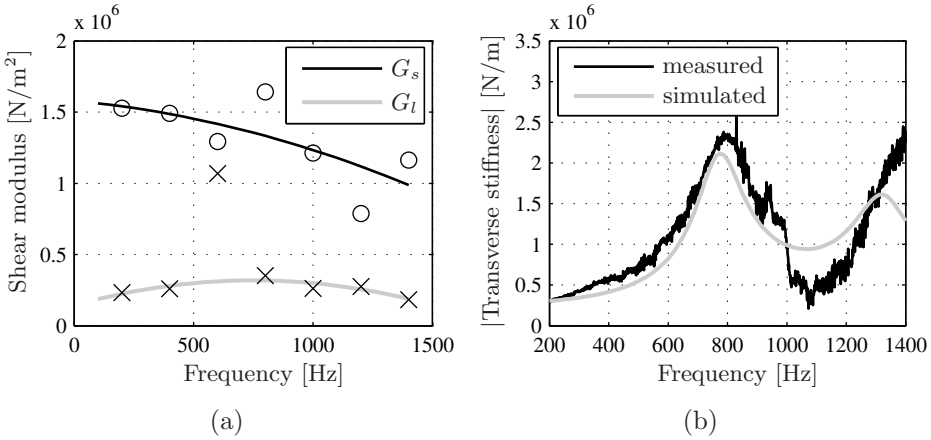

Figure 5.21: Determined dynamic storage modulus G_s (indicated by $\circ$) and loss modulus G_l (indicated by $\times$) with the curve fits (a) and the measured and simulated dynamic transverse stiffness (b) of the silica-reinforced vibration isolator.

deviations occur. The source of these high-frequency errors has not been investigated.

The applied strain amplitudes in the measurements were very small, so the influence of nonlinear effects due to interaction between the filler content and the rubber molecules are assumed to be small. When the strain amplitudes are large, these nonlinear effects play an important role. The physical way to describe these interaction effects is by using friction models [68, 117, 118, 119, 120].

It can be concluded that the static material parameters can be estimated in a robust way by fitting the Yeoh coefficients onto a static force-displacement measurement. The procedure to determine the dynamic material parameters, by fitting the dynamic shear modulus on a measured dynamic stiffness component, seems to work. However, a good measurement of at least one dynamic stiffness component is necessary.

5.6 Conclusions

Two procedures concerning the modeling of rubber vibration isolators have been described in this chapter. First, a numerical method was presented to determine the multi-directional dynamic stiffness matrix of rubber vibration isolators. An important condition to obtain reliable numerical results is a

correct material description of the rubber. This material description is often unknown. For this reason, a procedure was also presented to determine the rubber material properties by updating the numerically determined response for a single direction with actual measurements of the complete isolator.

Numerical modeling of rubber vibration isolators to determine the passive isolation behavior:
In practice, the actuators and the passive isolators are integrated, resulting in a hybrid module. An important goal to be reached with the design of the hybrid component is the use of a minimum number of actuators. The actuators are in general placed in the dominant transfer paths (or stiff directions) of the passive isolators. To reduce the number of actuators, the passive isolator must also have a minimum number of dominant transfer paths. The directions of the passive isolator that have the largest dynamic stiffness in certain frequency ranges is likely to be the most dominant structural transmission for the structure-borne sound transmission. To determine the dominant transfer paths with the goal of designing an integrated hybrid module, design analyses of the passive isolators are needed and the passive isolation behavior must be determined. For this reason, a procedure has been described to obtain the multi-directional isolation characteristics of the passive isolator.

The passive isolation behavior depends on many factors, but in this work only two effects were considered: the influence of a pre-deformation due to the weight of the source and the influence of dynamic excitation. A nonlinear calculation of the pre-deformation is performed first. The pre-deformation causes a large elastic deformation of the isolator. After that, a linear harmonic analysis is superimposed on the pre-deformed isolator, hereby assuming that the dynamic amplitudes are sufficiently small to allow such a linear approach. From the simulation results in terms of the dynamic stiffness it can be concluded that the isolation behavior depends on both the frequency and the pre-deformation. It was seen that the influence of the dynamic excitation is more pronounced than the influence of the pre-deformation: the dynamic stiffness may increase to up to 20 times the static stiffness for certain frequencies and stiffness components. This implies that the isolation of structure-borne sound for certain directions and at certain frequencies is much less than expected from the static stiffness. The dynamic excitation causes wave effects in the isolator above a certain frequency because the inertial properties of the rubber start to play an important role. This is observed as an increase in the amplitude and a change of the phase of the dynamic stiffness.

The method presented in this work to determine the dynamic stiffness matrices works well and provides sufficient information about the passive iso-

lators. However, the performance of the hybrid isolator also depends on the dynamics of the source, the receiver structure and the excitation. For this reason, additional analyses must be performed. The dynamic stiffness matrices obtained have to be implemented in the general model described in chapter 2. With this kind of model, different hybrid components can be analyzed (like the use of actuators in the stiff directions of the passive mounting system) for several sensor configurations.

Identification of rubber material parameters:
Rubber is a complex material, in particular natural rubber compounds that contain a large amount of filler. A procedure has been presented in this chapter to determine the material parameters with the help of a limited number of measurements at an entire vibration isolator: a static force-displacement measurement to determine the static material parameters and one dynamic transfer stiffness measurement to determine the dynamic material parameters. The method was validated and after that applied on a silica-reinforced vibration isolator to investigate whether the procedure can be applied on actual measured data. The method is robust for the determination of the static material parameters. The procedure also seems to work for the determination of the dynamic material parameters. However, the measurement of the dynamic stiffness needs to be accurate in order to obtain a correct material description. The obtained material parameters can consequently be used to determine a complete isolation characterization of the isolator with the numerical model.

The procedure described works quite well for rubber compounds with a small filler content and with small vibration amplitudes. For natural rubber compounds with a relatively large amount of filler, a material description with frequency dependent shear modulus cannot be used to describe the nonlinear effects (frequency dependence like the ratio between the dynamic stiffness and static stiffness and the amplitude dependence like the Payne effect) that occur in this kind of rubber material. For this reason new material models have to be developed when these nonlinear effects play an important role for the isolation behavior.

Chapter 6

Further study on near-source error sensor strategies

6.1 Introduction

In chapter 4 simulation results were presented of the numerical model of the laboratory setup with error sensors at the locations where active reduction is desired. For the considered applications of these isolation systems, e.g. a ship, this means that the error sensors should be located in or near the accommodations. The response at these sensor sets can be reduced efficiently by a set of actuators as was shown with the numerical simulations. This type of error sensor is referred to as a *far-field* sensor, i.e. a sensor that is situated at locations where the response is desired to be minimized, mostly at some distance from the source. In this chapter it is investigated whether it is possible to position sensors near the source of vibration (the so-called *near-source* sensors) to obtain a global reduction or a far-field reduction. A schematic overview of both the far-field and near-source sensor strategies was shown in Figure 1.3. Some near-source sensor strategies were already investigated in chapter 4, namely minimization of the velocities and the forces at the junctions of the receiver structure. As can be seen in Figures 4.20(c) and 4.20(d), these sensor strategies yield a poor reduction at the far-field sensor set. In this chapter alternative near-source error sensor strategies are presented.

Positioning of the error sensors near the source has some advantages compared to positioning the sensors in the accommodation:

- First of all, it is easier to implement near-source sensors in practical applications. When the sensors are located in the passenger accommodations, the implementation is more difficult due to for example the

wiring from the sensors to the amplifiers and control system. The use of near-source sensors results in a compact configuration; the actuators, sensors and control system can be located close to each other. This implies lower implementation costs.

- It is possible to define a global measure of the vibrational or acoustic responses of the receiver structure. One concept has already been investigated in chapter 3, namely the minimization of the transmitted power. It was also shown in chapter 4 that, when far-field sensors are used, the actuators minimize the response at the sensor locations, but the response at other far-field locations may even increase due to the influence of the actuators. This means that a more global reduction can probably be obtained with the far-field sensor concept by placing many sensors, but at the expense of higher costs. Besides the increased number of sensors, also the data acquisition increases and more amplifiers and a more complex controller are needed. With the near-source error sensor strategy it might be possible to define a global measure using a relatively small number of sensors. It was shown that the number of sensors for the near-source error sensor strategy based on minimization of the transmitted power was determined by the number of DOFs involved in the vibrational energy transmission from the mounting system to the receiver structure.

- Using near-source sensors also has the advantage that the error sensor response itself can be measured accurately. Far-field sensors are located at a large distance from the source, and the error sensor signal may be small due to the transmission attenuation in the receiver structure. This means that noise may make a relatively large contribution to the total error sensor response, which has a negative influence on the performance of the active control system. This effect is smaller when near-source error sensors are used.

- The near-source error sensors also measure some of the influence of flanking paths (like the airborne noise from the engine), but measure in particular the structure-borne sound transmitted by the transfer path from the engine through the passive mounting system to the receiver structure. This implies that other transfer paths may have no large influence on the error response. When far-field sensors are used, it is more probable that these sensors also measure contributions from other transfer paths. It is difficult to reduce these contributions with the actuators and this may even result in an increase of the vibrational or acoustic response

at other locations than the error sensors. This results in a decrease of the active performance.

6.1.1 Investigated near-source sensor strategies

Transmitted power

The first near-source error sensor strategy that is considered in this chapter is the minimization of the transmitted power. This concept was already analyzed in chapters 3 and 4 and it was shown that it has the advantage that it represents a global measure of the receiver response. It is shown in appendix A that minimizing the transmitted power results in a minimization of the sum of the potential and kinetic energy of the receiver structure. However, the near-source sensor concept with minimization of the transmitted power is known to be very sensitive to measurement errors [40, 41], in particular for light-weight and stiff structures. These kinds of structures have low damping, resulting in a low value of the transmitted power. Another disadvantage is that both the forces and velocities at the connection points between the mounting system and the receiver structure have to be measured. Furthermore, the number of sensors is determined by the number of DOFs for the vibration transmission; omitting one DOF in the sensor set will result in an increase of the transmitted power in that direction due to power circulation. This effect was described in section 3.4.1. In the present chapter, the concept of minimization of the transmitted power will be considered in more detail. To circumvent the problem of using two types of sensors (force sensors and acceleration pickups), a new concept is studied with sensors that measure the connection velocities or forces only. The error sensor response is consequently weighted in such a way that a measure for the transmitted power is obtained. The transmitted power is an error sensor criterion that is known to be sensitive to measurement errors. For this reason, attention is also paid to the robustness of this strategy and the influence of regularization of the weighting matrix on the robustness. The simulations are again performed on the numerical model of the laboratory setup, the same model as used in chapter 4.

Near-source error sensor weighting

The error sensitivity of the transmitted power has stimulated the investigation of alternative near-source error sensor strategies. It was shown in chapter 4 with the numerical model of the hybrid isolation setup, that good reductions can be obtained with only four actuators. This was explained by the fact that the major part of the sensor response was dominated by just four so-called

field shapes. The four actuators are able to reduce the contributions of these four field shapes effectively, resulting in a considerable decrease of the sensor response. This indicates that a relatively small number of characteristic deformation patterns, the field shapes or field modes, contribute to the dynamic response of the receiver structure. In chapter 4 it was also shown with simulations on the numerical model of the laboratory setup, that sensor strategies that minimize only the velocities or only the forces at the connection points of the resilient mounting system with the receiver structure, result in a poor reduction at the far-field sensor set. Because of these two observations, weighting of a near-source error sensor set could be a good strategy. This *weighting procedure* is based on a chosen far-field response, i.e. the response that is desired to be minimized and for this reason called the performance response. After determination of the weighting matrix, which relates the actual near-source error sensor response to the far-field response, the far-field sensors are no longer needed and only the near-source error sensors with their weighting are implemented for the real-time control. The weighting matrix needs thus to be determined with *off-line* experiments. This concept is similar to the use of *radiation modes* in the field of ASAC. In that method the structural response of a structure is measured and weighted with radiation modes in such a way that a measure for the radiated sound power is obtained, and the controller minimizes an acoustic quantity based on measured structural responses (see e.g. [3, 11, 12, 42, 94]). The radiation modes are velocity patterns (or field shapes) of the used structural sensor set that contribute independently to the radiated sound power. In the low frequency region, only a small number of these radiation modes is needed to obtain a good measure for the radiated sound power. More details about this concept are given in appendix C.1. The idea is to use a similar concept for hybrid isolation systems: weighting of a near-source sensor set in such a way that a far-field sensor response (e.g. the structural velocities or acoustic pressure responses near the location where sound or vibration reduction is wanted, the accommodation for example) is minimized.

Overview

Summarizing, in this chapter two near-source error sensor strategies are investigated:

- Minimizing the structural injected power into the receiver structure. The concept of the use of a weighting matrix to reduce the type and number of sensors is investigated for reasons of practical applicability.

- Minimizing a weighted near-source error sensor set to obtain a reduction at a far-field performance sensor set.

The near-source error sensor strategies are investigated on the numerical model of the laboratory setup. It was shown in chapter 4, that this numerical model has a dynamic behavior that is representative for the considered applications of hybrid isolation. For this reason, the conclusions drawn from this case study are also assumed to be valid for the considered type of application.

In this chapter first the transmitted power is analyzed in section 6.2. The theory is presented to determine a measure for the transmitted power by weighting of the measured forces or velocities at the junctions of the receiver structure. Also the robustness of this weighted error criterion is investigated. The influence of regularization of the weighting matrix on the robustness is investigated. The alternative near-source sensor strategy based on the weighting of the near-source error sensor response with a far-field sensor response, is presented in section 6.3. Also, an error analysis is performed to investigate the robustness of this near-source sensor strategy. It will be shown that the latter near-source sensor strategy is more robust for measurement errors in the weighting matrix than the error criterion of the transmitted power. For this reason, the near-source sensor strategy with a weighting matrix based on a chosen far-field sensor response is analyzed in section 6.4 with measured FRFs on the actual laboratory setup. This is done to check the applicability of the derived near-source error sensor strategy on an actual representative setup. Finally, conclusions are drawn in section 6.5.

6.2 Near-source error sensor weighting based on transmitted power

6.2.1 Transmitted power determined with a weighting matrix

The power P through a general multi-point interface between the mounting system and receiver is given by (frequency domain notation):

$$P = \frac{1}{2}\mathbf{f}_r^{\mathrm{H}} \cdot \mathbf{v}_r, \tag{6.1}$$

where $\mathbf{f}_r$ is the multi-point and multi-directional force vector acting on the receiver structure and $\mathbf{v}_r$ is the vector with velocities at the same DOFs. The real part of the power is considered here and represents the dissipated, active or transmitted power:

$$P_t = \frac{1}{2}\Re\left(\mathbf{f}_r^{\mathrm{H}} \cdot \mathbf{v}_r\right). \tag{6.2}$$

The imaginary part of P represents the reactive power. The relation between the forces and velocities at the junction points between the mounting system and the receiver structure can be written in terms of a mobility matrix or an impedance matrix (see also equation (2.21)) according to:

$$\mathbf{v}_r = \mathbf{Y}_r \cdot \mathbf{f}_r, \tag{6.3a}$$

$$\mathbf{f}_r = \mathbf{Z}_r \cdot \mathbf{v}_r. \tag{6.3b}$$

With the help of equations (6.3a) and (6.3b) the transmitted power can be expressed in terms of the junction forces or velocities as:

$$P_t = \frac{1}{2}\left(\mathbf{f}_r^{\mathrm{H}} \cdot \Re\left(\mathbf{Y}_r\right) \cdot \mathbf{f}_r\right), \tag{6.4a}$$

$$P_t = \frac{1}{2}\left(\mathbf{v}_r^{\mathrm{H}} \cdot \Re\left(\mathbf{Z}_r\right) \cdot \mathbf{v}_r\right). \tag{6.4b}$$

Using the set of equations (2.32), the transmitted power can be rewritten in the well-known Hermitian quadratic form in terms of the actuator forces. For the transmitted power measured in terms of the connection velocities this quadratic expression can be written as:

$$P_t = \frac{1}{2}\left(\mathbf{v}_r^{\mathrm{H}} \cdot \Re\left(\mathbf{Z}_r\right) \cdot \mathbf{v}_r\right) \tag{6.5}$$

$$= \mathbf{f}_a^{\mathrm{H}} \cdot \mathbf{A} \cdot \mathbf{f}_a + \mathbf{f}_a^{\mathrm{H}} \cdot \mathbf{b} + \mathbf{b}^{\mathrm{H}} \cdot \mathbf{f}_a + c, \tag{6.6}$$

where $\mathbf{A}$, $\mathbf{b}$ and c are defined respectively as:

$$\mathbf{A} = \frac{1}{2}\left(\mathbf{H}_s^{vr^{\mathrm{H}}} \cdot \Re\left(\mathbf{Z}_r\right) \cdot \mathbf{H}_s^{vr}\right), \tag{6.7a}$$

$$\mathbf{b} = \frac{1}{2}\left(\mathbf{H}_s^{vr^{\mathrm{H}}} \cdot \Re\left(\mathbf{Z}_r\right) \cdot \mathbf{H}_p^{vr} \cdot \mathbf{f}_d\right), \tag{6.7b}$$

$$c = \frac{1}{2}\left(\mathbf{f}_d \cdot \mathbf{H}_p^{vr^{\mathrm{H}}} \cdot \Re\left(\mathbf{Z}_r\right) \cdot \mathbf{H}_p^{vr} \cdot \mathbf{f}_d\right). \tag{6.7c}$$

The optimal actuator force to minimize the transmitted power is now calculated by:

$$\mathbf{f}_a^{opt} = -\mathbf{A}^{-1} \cdot \mathbf{b}. \tag{6.8}$$

The optimal actuator force that minimizes the transmitted power with a mobility matrix to weight the forces, as given in equation (6.4a), is determined in a similar way with equation (2.32b).

Using equation (6.4a), the transmitted power can be determined by measuring the connection forces at the junctions and weighting of this error sensor

response with the real part of the local mobility matrix $\mathbf{Y}_r$. Another option is to measure the connection velocities and use the real part of the local impedance matrix $\mathbf{Z}_r$ as weighting matrix (i.e. using equation (6.4b)). The advantage of the first concept is that the weighting matrix is a mobility matrix that can be measured directly. The disadvantage of this concept is that the forces acting on the receiver structure have to be measured, which is difficult to implement in practice. For the second concept, simple acceleration pickups can be used, but the weighting matrix is an impedance matrix. The impedance matrix cannot be measured directly, so the inverse of the local mobility matrix is needed:

$$P_t = \frac{1}{2}\left(\mathbf{v}_r^{\mathrm{H}} \cdot \Re\left(\mathbf{Y}_r^{-1}\right) \cdot \mathbf{v}_r\right). \tag{6.9}$$

This inversion is often ill-conditioned, and as a consequence small measurement errors have a large influence on the active performance.

6.2.2 Power modes

The weighting matrices $\Re(\mathbf{Y}_r)$ and $\Re(\mathbf{Z}_r)$ as shown in equations (6.4a) and (6.4b), respectively, have some characteristic properties. The matrices are square and positive definite. The latter property can easily be verified because the transmitted power is always larger than zero for each source-generated nonzero velocity or force vector for structures with a certain amount of damping. Furthermore, the matrices are symmetric due to reciprocity. The singular value decomposition (SVD) of these matrices also has some characteristic properties: the left singular and right singular vectors are equal to each other and are also equal to the eigenvectors of the matrix. The singular values and the eigenvalues are also equal to each other and are real and nonnegative. The eigenvalue decomposition of the weighting matrices can be written as:

$$\Re(\mathbf{Y}_r) = \mathbf{\Psi}_Y \cdot \mathbf{\Lambda}_Y \cdot \mathbf{\Psi}_Y^{\mathrm{T}}, \tag{6.10a}$$

$$\Re(\mathbf{Z}_r) = \mathbf{\Psi}_Z \cdot \mathbf{\Lambda}_Z \cdot \mathbf{\Psi}_Z^{\mathrm{T}}, \tag{6.10b}$$

where $\mathbf{\Lambda}_Y$ and $\mathbf{\Lambda}_Z$ are the real diagonal matrices with the nonnegative eigenvalues of $\Re(\mathbf{Y}_r)$ and $\Re(\mathbf{Z}_r)$, respectively, $\mathbf{\Psi}_Y$ and $\mathbf{\Psi}_Z$ are the orthogonal matrices composed of the corresponding eigenvectors, so that $\mathbf{\Psi}_Y \cdot \mathbf{\Psi}_Y^{\mathrm{T}} = \mathbf{\Psi}_Y^{\mathrm{T}} \cdot \mathbf{\Psi}_Y = \mathbf{I}$ and $\mathbf{\Psi}_Z \cdot \mathbf{\Psi}_Z^{\mathrm{T}} = \mathbf{\Psi}_Z^{\mathrm{T}} \cdot \mathbf{\Psi}_Z = \mathbf{I}$. The eigenvalues are arranged in

descending order. The transmitted power can now be written as:

$$\begin{aligned} P_t &= \frac{1}{2}\mathbf{f}_r^{\mathrm{H}} \cdot \mathbf{\Psi}_Y \cdot \mathbf{\Lambda}_Y \cdot \mathbf{\Psi}_Y^{\mathrm{T}} \cdot \mathbf{f}_r \\ &= \frac{1}{2}\mathbf{q}^{f^{\mathrm{H}}} \cdot \mathbf{\Lambda}_Y \cdot \mathbf{q}^f \\ &= \frac{1}{2}\sum_{n=1}^{N} \lambda_{Y_n} |q_n^f|^2, \end{aligned} \tag{6.11a}$$

$$\begin{aligned} P_t &= \frac{1}{2}\mathbf{v}_r^{\mathrm{H}} \cdot \mathbf{\Psi}_Z \cdot \mathbf{\Lambda}_Z \cdot \mathbf{\Psi}_Z^{\mathrm{T}} \cdot \mathbf{v}_r \\ &= \frac{1}{2}\mathbf{q}^{v^{\mathrm{H}}} \cdot \mathbf{\Lambda}_Z \cdot \mathbf{q}^v \\ &= \frac{1}{2}\sum_{n=1}^{N} \lambda_{Z_n} |q_n^v|^2, \end{aligned} \tag{6.11b}$$

where $\mathbf{q}^f = \mathbf{\Psi}_Y^{\mathrm{T}} \cdot \mathbf{f}_r$ and $\mathbf{q}_n^v = \mathbf{\Psi}_Z^{\mathrm{T}} \cdot \mathbf{v}_r$. The symbols λ_{Y_n} and λ_{Z_n} represent the n^{th} eigenvalues of $\Re(\mathbf{Y}_r)$ and $\Re(\mathbf{Z}_r)$, respectively. Considering equation (6.11a), the vibrational power transmitted to the receiver by N forces can be regarded as the power transmitted by N independent contributions, where N is the number of DOFs involved in the vibration transmission. These independent contributions are the so-called *power modes*, and $\mathbf{q}^f$ is the so-called *power mode force vector*, by analogy of the radiation modes technique (see also appendix C.1). This concept was first suggested by Moorhouse *et al.* [88] and later extended to the multi-point vibration transmission by Jianxin *et al.* [62]. This technique was also used by Ji *et al.* [60, 61] to predict the vibrational power transmission . The same technique can be applied when the transmitted power is expressed in terms of the junction velocities as shown in equation (6.11b). The first approach in terms of the junction forces will be referred to as the *power force mode* approach and the second approach in terms of the junction velocities will be referred to as the *power velocity mode* approach. The theory of the power modes is used in this work to investigate the possibility of defining a robust error criterion in terms of the transmitted power.

The idea is to first measure the frequency dependent weighting matrix (the real part of the mobility or impedance matrix) off-line, after which it is applied in the control system to obtain a measure for the transmitted power. However, the local mobility or impedance weighting matrix is ill-conditioned. This means that small measurement errors in these weighting matrices result in an unreliable prediction of the transmitted power. There are different regularization techniques to obtain a better conditioned matrix for a more reliable

measure of the transmitted power. One of these techniques is the Truncated Singular Value Decomposition (TSVD) technique, in which one or more of the smaller singular values are put to zero. This is explained in more detail in appendix C.2. The TSVD technique is applied in the following study to the weighting matrices and is the same as regularization in terms of power modes. First it is investigated whether it is possible to reduce the weighting matrix. As shown in equations (6.11a) and (6.11b), it is possible to reduce the amount of information by determining the weighting matrix with a reduced set eigenvectors and eigenvalues. These equations also show that each power force mode or power velocity mode contributes independently in the transmitted vibrational power, and that each mode contribution is positive, meaning that for a reduced weighting matrix an underestimation of the real transmitted power is obtained. The transmitted power can consequently be approximated by:

$$\begin{aligned} P_t &\approx \sum_{n=1}^{k} \lambda_n |q_n^f|^2 \\ &= \frac{1}{2} \mathbf{f}_r^{\mathrm{H}} \cdot \widehat{\mathbf{\Psi}}_Y \cdot \widehat{\mathbf{\Lambda}}_Y \cdot \widehat{\mathbf{\Psi}}_Y^{\mathrm{T}} \cdot \mathbf{f}_r \\ &= \frac{1}{2} \mathbf{f}_r^{\mathrm{H}} \cdot \widehat{\Re(\mathbf{Y}_r)} \cdot \mathbf{f}_r, \end{aligned} \tag{6.12a}$$

$$\begin{aligned} P_t &\approx \sum_{n=1}^{k} \lambda_n |q_n^v|^2 \\ &= \frac{1}{2} \mathbf{v}_r^{\mathrm{H}} \cdot \widehat{\mathbf{\Psi}}_Z \cdot \widehat{\mathbf{\Lambda}}_Z \cdot \widehat{\mathbf{\Psi}}_Z^{\mathrm{T}} \cdot \mathbf{v}_r \\ &= \frac{1}{2} \mathbf{v}_r^{\mathrm{H}} \cdot \widehat{\Re(\mathbf{Z}_r)} \cdot \mathbf{v}_r, \end{aligned} \tag{6.12b}$$

where k is a reduced number of eigenvectors and eigenvalues taken into account ($k < N$) and the symbol $\widehat{(.)}$ indicates that a regularized or reduced formulation is used.

The theory of the power modes is illustrated with simulations on the numerical model of the laboratory setup. This model was extensively described in chapter 4 and the configuration used for the simulations is shown in Figure 4.8. The disturbance force set consists of a set of unit translational forces and moments in each degree of freedom at the top of each mount and that are in phase with each other. The actuator set consists of four actuators that can exert forces in the normal direction of the foundation plate and located at the junctions between the mounting system and the receiver structure.

In Figure 6.1(a) the first four eigenvalues of the weighting matrix $\Re(\mathbf{Y}_r)$ are plotted as a function of frequency. It is shown that the decay in the values is quite large, which implies that a good estimation of the weighting matrix can be obtained when just a few eigenvalues and corresponding eigenvectors are taken into account. This is confirmed by the results presented in Figure 6.1(b); a good representation of the passive transmitted vibrational power is obtained at most frequencies when the weighting matrix is reconstructed by taking account of only four eigenvalues and eigenvectors. When eight eigenvectors are taken into account, a good estimation of the transmitted power is obtained across the whole frequency region.

The same analysis is performed for the power velocity mode approach. The first four eigenvalues of the weighting matrix $\Re(\mathbf{Z}_r)$ are shown in Figure 6.2(a) as a function of the frequency. In contrast to the eigenvalues of the real part of the mobility matrix, the difference between the eigenvalues of the impedance matrix is not so large, especially in the low frequency region. At higher frequencies, the first eigenvalue is clearly the largest, but the difference between the higher eigenvalues is still small. When the passive transmitted power is calculated for eight eigenvalues, large deviations are distinguished as shown in Figure 6.2(b). Even when twenty singular values are taken into account, still relatively large discrepancies are present at some frequencies.

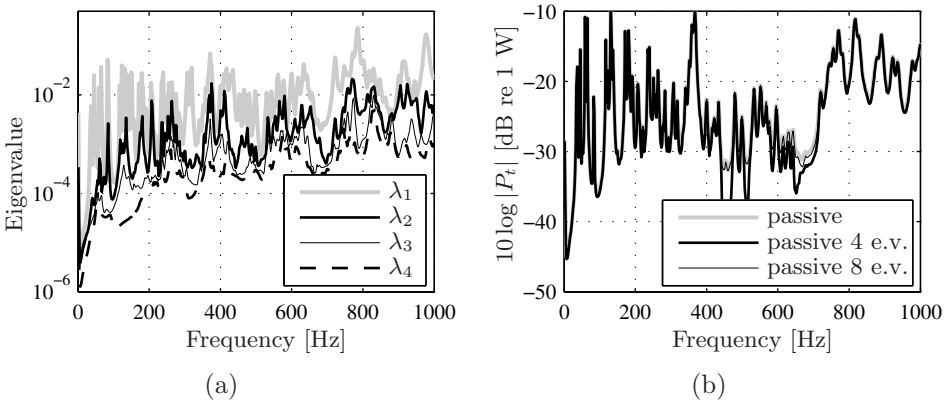

Figure 6.1: The four larger eigenvalues of $\Re(\mathbf{Y}_r)$ (a) and the passive transmitted power when respectively 4 and 8 eigenvalues (e.v.) are taken into account for the weighting matrix (b).

The next step is to investigate whether the reduced formulation of the weighting matrix can also be used as an error criterion for active isolation. The power

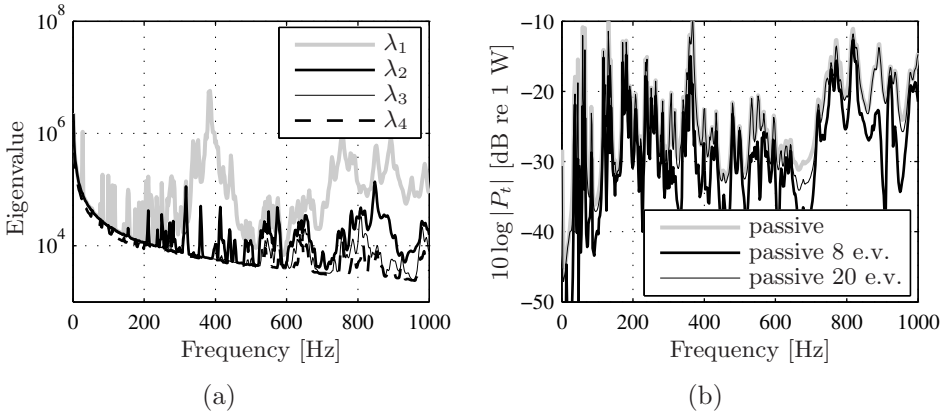

(a) (b)

Figure 6.2: The four larger eigenvalues of $\Re(\mathbf{Z}_r) = \Re\left(\mathbf{Y}_r^{-1}\right)$ (a) and the passive transmitted power when respectively 8 and 20 eigenvalues (e.v.) are taken into account for the weighting matrix (b).

force mode approach is considered first as shown in equation (6.12a). It was seen that a good estimation of the passive transmitted power was obtained with a reduced weighting matrix composed of four eigenvectors. In Figure 6.3 the active response is shown in terms of the reduction of the transmitted power P_t when the force error sensor response is weighted with the reduced weighting mobility matrix. Notice that the reduction is plotted; a negative value means an increase in the transmitted power. When the weighting matrix is reduced by retaining only four eigenvectors, the reductions obtained are very poor, and in fact an increase in the transmitted power is observed at several frequencies. When the weighting mobility matrix is reduced by retaining eight eigenvectors, the reductions obtained are similar to the optimal solution when the transmitted power itself is reduced. This means that the weighting matrix can be reduced considerably when it is used as an error criterion for active isolation. A similar analysis is performed for the power velocity mode approach as described by equation (6.12b). A reduced formulation of the weighting impedance matrix to describe the passive transmitted power was not so effective as for the weighting mobility matrix of the power force mode approach. It was seen that still around twenty eigenvectors are needed for a correct description of the transmitted power. The performance of the error criterion with a reduced formulation of the weighting impedance matrix is also investigated, and the results are shown in Figure 6.4 for eight and for twenty eigenvectors. The performance of the weighting matrix determined with eight eigenvectors

is poor, the reduction obtained by taking into account twenty eigenvectors is similar to the optimal solution. This means that some reduction of the weighting matrix is possible for the power velocity method, but reduction appears not to be as effective as for the power force method because a relatively large number of eigenvalues has to be taken into account for a good description of the transmitted power.

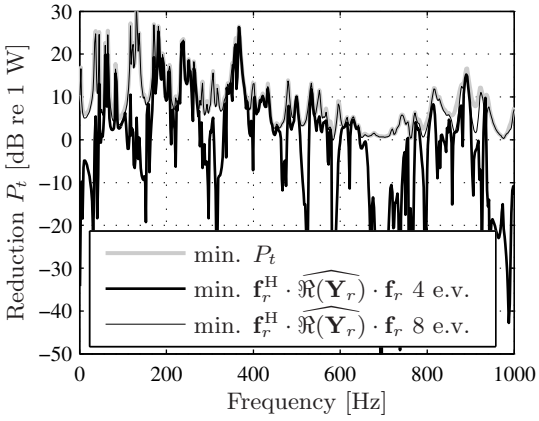

Figure 6.3: Reduction of the active transmitted vibrational power in dB when 4 and 8 eigenvalues (e.v.) and eigenvectors are taken into account to reconstruct the weighting matrix $\Re(\mathbf{Y}_r)$.

6.2.3 Error sensitivity of the power weighting matrices

First the influence of measurement errors on the power force mode approach is considered, after which the robustness of the power velocity mode approach is analyzed. As stated before, the weighting mobility matrices are measured off-line. During these FRF measurements it is inevitable that small errors are introduced on the measured responses. The influence of small errors in the off-line measured weighting matrix on the active isolation performance is investigated by adding errors upon the 'true' numerically determined velocity responses. The off-line measurement procedure is simulated by adding small numerically determined 'measurement' errors on the velocity responses. In practice, errors will also occur at the input sensor (the force sensor), but these are not taken into account here. The introduction of measurement errors on the measured response is described in more detail in appendix G. The amplitude of the error signal is chosen to be 3 % of the frequency averaged

magnitude of the FRF.

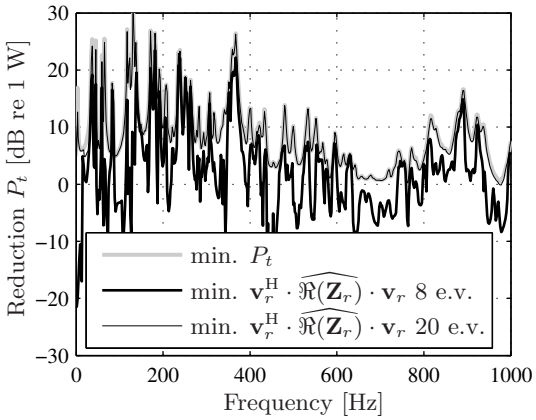

Figure 6.4: Reduction of the active transmitted vibrational power in dB when 8 and 20 eigenvalues (e.v.) and eigenvectors are taken into account to reconstruct the weighting matrix $\Re(\mathbf{Z}_r)$.

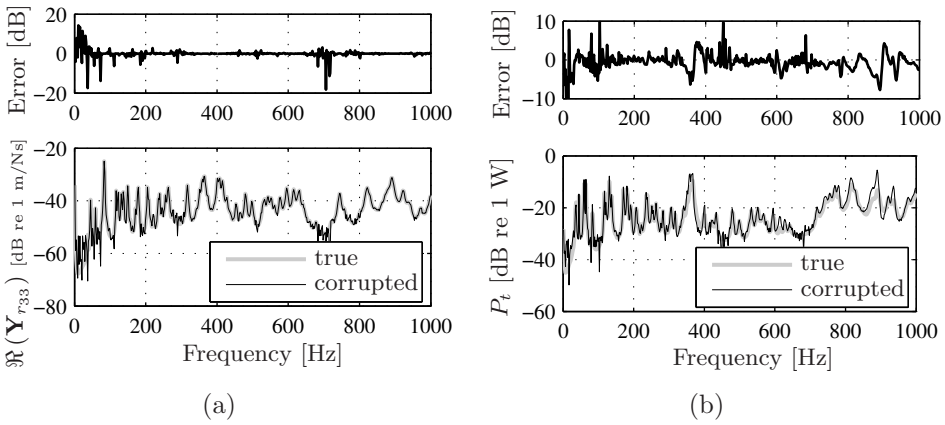

Figure 6.5: Introduction of measurement errors on the mobility matrix used for weighting: corrupted mobility component (a) and the passive transmitted power with the corrupted weighting matrix (b).

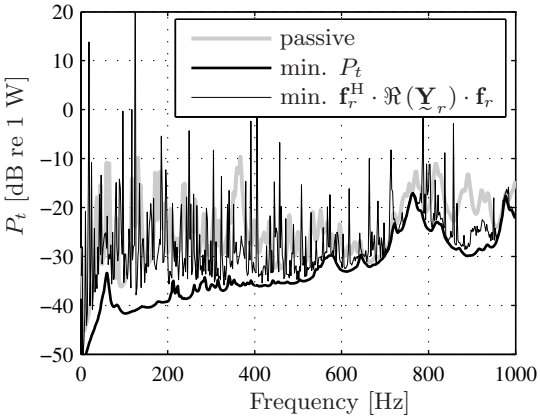

Figure 6.6: The transmitted vibrational power when the transmitted power is minimized for the uncorrupted case and with use of a corrupted weighting mobility matrix.

Robustness of the power force mode approach

The influence of the measurement errors on the real part of one component of the measured mobilities is shown in Figure 6.5(a), where in the upper part the error on the response (the difference in dB between the true and corrupted response) and in the lower part both the true and corrupted mobilities are shown. The mobility considered is the $(3,3)$ component of the mobility matrix $\Re(\mathbf{Y}_r)$ and relates the force in the normal direction to the velocity in the normal direction of the foundation plate at the junction of mount 1 (see also Figure 4.8). It is stressed that the errors are introduced on both the real and imaginary parts of the mobility, after which the real part is taken to determine the structural transmitted power. For most components of the considered weighting matrix, the amplitude of the real part is smaller than the imaginary part, implying that the error on the real part is relatively larger. Especially in the frequency region where the value of the measured mobility is low, the errors introduced are large (e.g. the frequency region from 0 till 100 Hz). In this way, all 24 components of the weighting matrix are corrupted, and the corrupted transmitted power is consequently given by:

$$\underset{\sim}{P}_t = \mathbf{f}_r^{\mathrm{H}} \cdot \underset{\sim}{\mathbf{Y}}_r \cdot \mathbf{f}_r, \tag{6.13}$$

where the symbol $\underset{\sim}{(.)}$ indicates a corrupted FRF matrix. The influence of the corrupted mobility matrix on the passive transmitted power is shown in Figure 6.5(b). The errors in the transmitted power varies from several dB up

to 10 dB at frequencies where the value of the transmitted power is relatively low.

The influence of the corrupted weighting matrix on the active performance of the error criterion is shown in Figure 6.6. The performance of the active isolation is very poor and in fact even increases in the active response are observed in comparison with the passive response. This means that the considered error criterion is very sensitive to errors in the weighting matrix. The considered weighting matrix is especially sensitive to measurement errors because the real part of the mobility matrix has a relatively small contribution to the total magnitude of the response.

It was shown in section 6.2.2 that a good representation of the weighting matrix is obtained when the matrix is reconstructed with a reduced set of singular values and singular vectors. This TSVD technique is also often applied for the regularization of ill-conditioned matrices for the inversion. To determine the optimal actuator force, an inversion is determined and also an inversion of the weighting matrix is needed. This is shown in equation (6.8). The TSVD technique is applied on the weighting matrix $\Re(\underset{\sim}{\mathbf{Y}}_r)$, to obtain the reconstructed matrix:

$$\widehat{\Re(\underset{\sim}{\mathbf{Y}}_r)} = \sum_{i}^{k} \left(\mathbf{u}_i \cdot \mathbf{v}_i^{\mathrm{H}}\right) s_i, \tag{6.14}$$

where $\mathbf{u}_i$, $\mathbf{v}_i$ and s_i are respectively the singular vectors and values of the mobility matrix $\Re(\underset{\sim}{\mathbf{Y}}_r)$. The truncation number k is based on the definition of a threshold, meaning that singular values that are smaller than this threshold are rejected. Simulations have been performed with different thresholds to reject singular values, but the TSVD regularization did not result in a better performance in comparison with the active results obtained with the unregularized weighting matrix.

It can be concluded that the transmitted power can be predicted well by measuring the junction forces and weighting with a mobility matrix. However, this error criterion is still very sensitive to measurement errors in the off-line determined weighting matrix, even after regularization using power force modes.

Robustness of the power velocity mode approach

The power velocity mode approach has the advantage that simple acceleration pickups can be used. These sensors can be much more easily applied in practice than the force sensors that are needed for the power force method. Force transducers must be placed in the transfer path, whereas this is not required

for the accelerometers. However, the error sensor signal has to be weighted with an impedance matrix. The impedance matrix must be determined by an inversion of the measured mobility matrix as was shown in equation (6.9). This inversion is ill-conditioned, meaning that the error criterion is sensitive to small measurement errors. In Figure 6.7(a) the corrupted impedance component is depicted, obtained after inversion of the mobility. It is shown that the inversion enlarges the error on the transfer function. Also the error on the passive transmitted power determined with the corrupted weighting matrix, as shown in Figure 6.7(b), contains larger errors compared to the power force method. The increase in the error is caused by the ill-conditioned behavior of the mobility matrix. The small errors of the components of the mobility matrix are enlarged during inversion. In Figure 6.8 the passive transmitted power is shown when the mobility matrix is regularized before inversion. The TSVD technique is again used for the regularization of the mobility matrix:

$$\Re\left(\hat{\underset{\sim}{\mathbf{Z}}}_r\right) = \Re\left(\hat{\underset{\sim}{\mathbf{Y}}}_r^{-1}\right) = \Re\left(\sum_i^k \frac{\mathbf{v}_i \cdot \mathbf{u}_i^{\mathrm{H}}}{s_i}\right), \tag{6.15}$$

where $\mathbf{u}_i$, $\mathbf{v}_i$ and s_i are the frequency dependent singular vectors and value respectively of the mobility matrix $\underset{\sim}{\mathbf{Y}}_r$. The regularization is analyzed by simulations with different thresholds for which the singular values are discarded. The regularization results in a better prediction of the transmitted power. However, the regularized weighting matrix is not good enough for the purpose of active isolation to obtain reductions in the transmitted power. This can clearly be seen in Figure 6.9. The reductions in transmitted power decrease substantially and at several frequencies even an increase of the transmitted power in comparison with the passive transmitted power is observed.

From the simulation results described in this section, it can be concluded that the transmitted power is very sensitive to measurement errors in the weighting matrices. Regularization of the weighting matrix does not improve the results. This means that the practical application of this near-source error criterion with the use of an off-line determined weighting matrix is very difficult for the considered applications of hybrid isolation.

It can be concluded that the transmitted power can be well predicted by measuring the junction velocities and weighting with an impedance matrix. However, this error criterion is also very sensitive to measurement errors in the off-line determined weighting matrix. Regularization of the measured off-line mobility matrix before inversion improves the results, but the robustness is still poor.

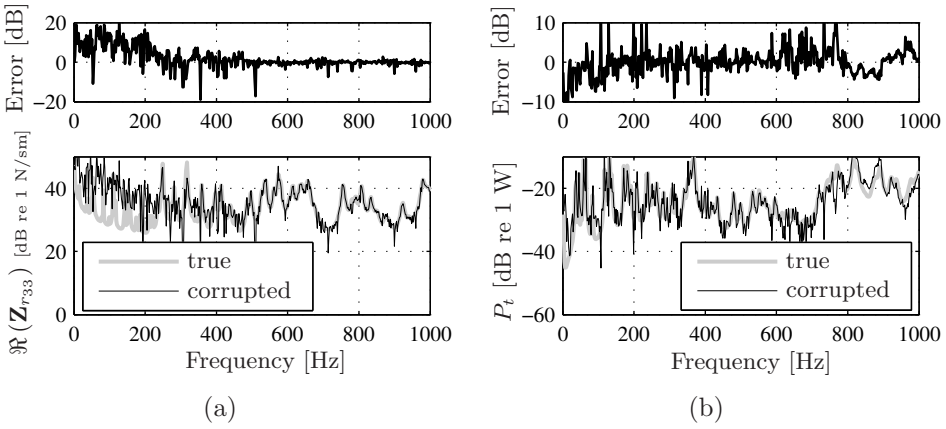

Figure 6.7: Introduction of measurement errors on the impedance matrix used for weighting: corrupted impedance component (a) and the passive transmitted power with the corrupted weighting matrix (b).

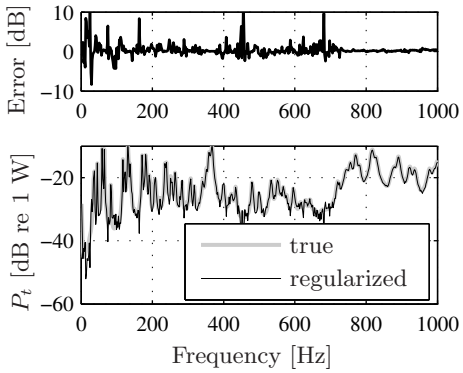

Figure 6.8: Passive transmitted power without corruption (true) and with the corrupted and regularized weighting impedance matrix.

6.3 Near-source error sensor weighting based on a far-field response

Besides the approach based on the minimization of the transmitted power as described in the previous section, an alternative method can also be used. This method is based on the weighting of near-source error sensor signals with the use of sensor responses at locations where reduction is desired [6,

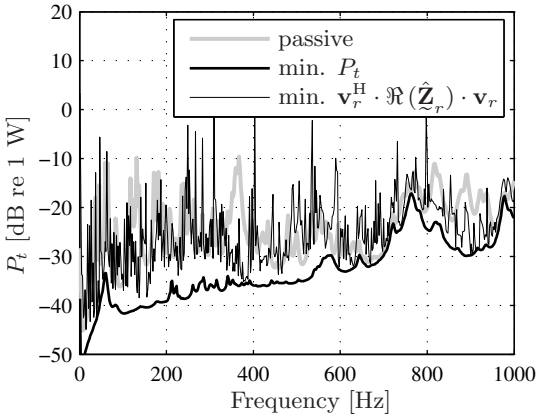

Figure 6.9: The transmitted vibrational power when the transmitted power is minimized for the uncorrupted case and for a corrupted weighting impedance matrix after regularization.

133]. The idea is to locate a set of sensors at a certain distance of the source of vibration for example in the accommodations of the ship: the *far-field* sensor set. This sensor set is considered as the *performance* sensor set and represents the actual response that is desired to be minimized. The far-field sensor set can consist of e.g. pressure microphones or accelerometers in the passenger accommodations. Besides the far-field sensor set, a near-source sensor set is attached to the receiver structure. The near-source sensor set is also used as the error sensor set for the real-time active control. With the help of FRF measurements, a weighting matrix is derived which can be used to weight the near-source error sensor response in such a way that a good measure for the far-field sensor response is obtained. The weighting matrix is determined *off-line* and implemented in the controller to weight the real-time near-source error sensor response. The far-field sensors are only used for the off-line determination of the weighting matrix and are not part of the actual control system. The weighted near-source error sensors in fact 'virtually' measure the far-field sensor response when the near-source error sensors are weighted according to the described procedure.

Considering the numerical model of the laboratory setup, it was shown in section 4.5 that with a relatively small number of actuators a large reduction of the (rather local) far-field sensor response was obtained. This means that only a few field shapes dominate the far-field sensor response and can thus be effectively reduced with a reduced number of actuators. When the contribu-

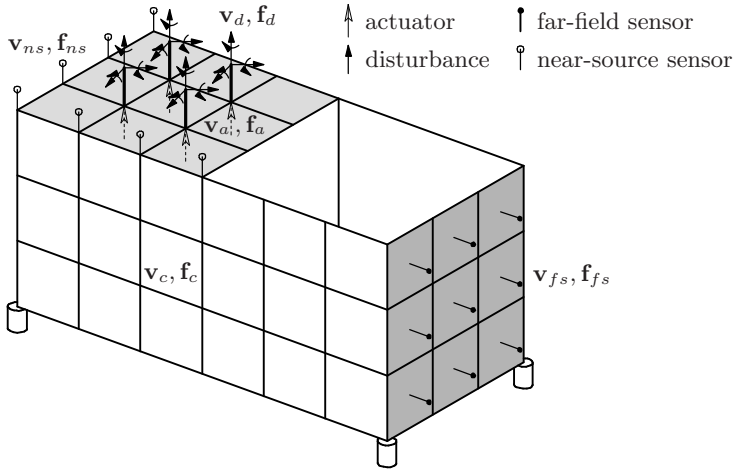

Figure 6.10: Responses at different characteristic parts of the numerical model of the laboratory setup.

tions of these field shapes at the far-field sensor response can be related to a near-source sensor response, it might be possible to obtain a relatively robust near-source measure. In this section a procedure is introduced to determine such a weighting matrix. An important issue is the robustness of this type of near-source sensor strategy, because the power mode approach failed as near-source sensor strategy at this point. The simulations are again performed with the same numerical model of the laboratory setup as used in chapter 4.

6.3.1 Weighting of the near-source error sensors

The first step is to describe a procedure to determine the appropriate weighting matrix for the near-source error sensor set that forms a representative measure for the far-field performance sensor response. The dynamic behavior of the complete hybrid isolation system can be represented in terms of one mobility matrix:

$$\begin{Bmatrix} \mathbf{v}_d \\ \mathbf{v}_a \\ \mathbf{v}_{ns} \\ \mathbf{v}_{fs} \\ \mathbf{v}_c \end{Bmatrix} = \begin{bmatrix} \mathbf{Y}_{dd} & \mathbf{Y}_{da} & \mathbf{Y}_{dns} & \mathbf{Y}_{dfs} & \mathbf{Y}_{dc} \\ \mathbf{Y}_{ad} & \mathbf{Y}_{aa} & \mathbf{Y}_{ans} & \mathbf{Y}_{afs} & \mathbf{Y}_{ac} \\ \mathbf{Y}_{nsd} & \mathbf{Y}_{nsa} & \mathbf{Y}_{nsns} & \mathbf{Y}_{nsfs} & \mathbf{Y}_{nsc} \\ \mathbf{Y}_{fsd} & \mathbf{Y}_{fsa} & \mathbf{Y}_{fsns} & \mathbf{Y}_{fsfs} & \mathbf{Y}_{fsc} \\ \mathbf{Y}_{cd} & \mathbf{Y}_{ca} & \mathbf{Y}_{cns} & \mathbf{Y}_{cfs} & \mathbf{Y}_{cc} \end{bmatrix} \cdot \begin{Bmatrix} \mathbf{f}_d \\ \mathbf{f}_a \\ \mathbf{f}_{ns} \\ \mathbf{f}_{fs} \\ \mathbf{f}_c \end{Bmatrix}, \tag{6.16}$$

where $\mathbf{v}_d$ and $\mathbf{f}_d$ are the velocities and forces at the upper side of the mounts, $\mathbf{v}_a$ and $\mathbf{f}_a$ are the velocities and forces at the actuator positions, $\mathbf{v}_{ns}$ and $\mathbf{f}_{ns}$ are the velocities and forces at the near-source sensor locations, $\mathbf{v}_{fs}$ and $\mathbf{f}_{fs}$ are the velocities and forces at the far-field sensor locations and $\mathbf{v}_c$ and $\mathbf{f}_c$ are the velocities and forces at the remaining locations on the receiver structure. The different velocity responses and force excitations of the laboratory setup are also schematically depicted in Figure 6.10. When it is assumed that only disturbance forces are present at the top of the mounting system and actuator forces at the connection points of the mounts with the receiver structure, the response at the near-source and far-field sensor sets can be written respectively as:

$$\begin{Bmatrix} \mathbf{v}_{ns} \\ \mathbf{v}_{fs} \end{Bmatrix} = \begin{bmatrix} \mathbf{Y}_{nsd} & \mathbf{Y}_{nsa} \\ \mathbf{Y}_{fsd} & \mathbf{Y}_{fsa} \end{bmatrix} \cdot \begin{Bmatrix} \mathbf{f}_d \\ \mathbf{f}_a \end{Bmatrix}. \tag{6.17}$$

The disturbance and actuator force vectors $\mathbf{f}_d$ and $\mathbf{f}_a$ can be combined into one force vector $\mathbf{f}_{da}$:

$$\mathbf{v}_{ns} = \mathbf{Y}_{nsda} \cdot \mathbf{f}_{da}, \tag{6.18a}$$

$$\mathbf{v}_{fs} = \mathbf{Y}_{fsda} \cdot \mathbf{f}_{da}. \tag{6.18b}$$

Method 1

The equations (6.18) can be used to express the far-field sensors in terms of the near-source sensors. The first equation can be rewritten to express the disturbance forces and actuator forces in terms of the near-source error sensor response according to:

$$\mathbf{f}_{da} = \mathbf{Y}^{+}_{nsda} \cdot \mathbf{v}_{ns}, \tag{6.19}$$

where the symbol $(.)^+$ indicates the pseudo-inverse. With this equation and the equation for the far-field response (6.18b), the far-field sensor response can be written as function of the near-source sensor response according to:

$$\mathbf{v}_{fs} = \mathbf{Y}_{fsda} \cdot \mathbf{Y}^{+}_{nsda} \cdot \mathbf{v}_{ns} = \mathbf{W}_v \cdot \mathbf{v}_{ns}, \tag{6.20}$$

where $\mathbf{W}_v$ is the weighting matrix of the near-source error sensor response. Considering the pseudo-inverse of the mobility matrix $\mathbf{Y}_{nsda}$, the number of near-source sensors must be at least equal to the sum of the number of independent excitation forces (or the number of mounts times the number of degrees of freedom per mount) and the number of actuator forces. In the situation that the number of near-source sensors is less than the sum of the

number of disturbance and actuator forces, the pseudo-inverse of an underdetermined matrix $\mathbf{Y}_{nsda}$ is calculated. This means that the weighting matrix is not reliable for weighting the near-source sensors to represent the far-field response due to ill-conditioning. Equation (6.20) can be written as a Hermitian quadratic cost function J according to:

$$\begin{aligned} J = \mathbf{v}_{fs}^{\mathrm{H}} \cdot \mathbf{v}_{fs} &= \mathbf{v}_{ns}^{\mathrm{H}} \cdot \mathbf{W}_v^{\mathrm{H}} \cdot \mathbf{W}_v \cdot \mathbf{v}_{ns} \\ &= \mathbf{v}_{ns}^{\mathrm{H}} \cdot \mathbf{W} \cdot \mathbf{v}_{ns} \\ &= \mathbf{f}_a^{\mathrm{H}} \cdot \mathbf{A} \cdot \mathbf{f}_a + \mathbf{f}_a^{\mathrm{H}} \cdot \mathbf{b} + \mathbf{b}^{\mathrm{H}} \cdot \mathbf{f}_a + c, \end{aligned} \tag{6.21}$$

where $\mathbf{W}$ is the quadratic expression in terms of the weighting matrix $\mathbf{W}_v$. This method is denoted as method 1 to express the far-field sensor response in terms of the near-source error sensor response, to distinguish it from the two alternative methods discussed in section 6.3.2. The expressions for the matrix $\mathbf{A}$, the vector $\mathbf{b}$ and the scalar c are shown in the first column of Table 6.1. The optimal actuator force that minimizes this Hermitian quadratic cost function can be calculated as described by equation (6.8).

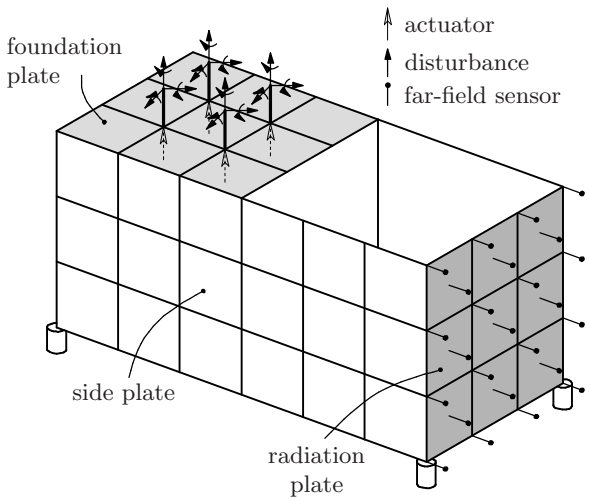

Figure 6.11: Numerical model of the isolation setup with the considered disturbance and actuator configuration and far-field sensor set 1.

The suggested method for the determination of the weighting matrix is applied to the numerical model of the laboratory setup with the disturbance and actuator configuration as shown in Figure 6.11. Two far-field sensor sets are considered: a far-field sensor set with 25 normal velocity sensors on the

radiation plate as shown in Figure 6.11 and a far-field sensor set with 46 normal velocity sensors on the side plate and 25 normal velocity sensors on the radiation plate as shown in Figure 6.12. The latter sensor set with a total of 71 normal velocity sensors, represents a more global measure of the receiver response and is indicated as the second far-field sensor set 2, whereas the far-field sensor set 1 is the same sensor set as used in chapter 4. The weighting matrices for these two considered far-field sensor sets are determined using equation (6.20):

$$\mathbf{W}_1 = \mathbf{W}_v^{1^{\mathrm{H}}} \cdot \mathbf{W}_v^1 = \left(\mathbf{Y}_{fsda}^1 \cdot \mathbf{Y}_{nsda}^+\right)^{\mathrm{H}} \cdot \left(\mathbf{Y}_{fsda}^1 \cdot \mathbf{Y}_{nsda}^+\right), \tag{6.22a}$$

$$\mathbf{W}_2 = \mathbf{W}_v^{2^{\mathrm{H}}} \cdot \mathbf{W}_v^2 = \left(\mathbf{Y}_{fsda}^2 \cdot \mathbf{Y}_{nsda}^+\right)^{\mathrm{H}} \cdot \left(\mathbf{Y}_{fsda}^2 \cdot \mathbf{Y}_{nsda}^+\right), \tag{6.22b}$$

where $\mathbf{Y}_{fsda}^1$ and $\mathbf{Y}_{fsda}^2$ are the combined FRFs of the disturbance and actuator forces to the far-field sensor sets 1 and 2, respectively. In Figure 6.13(a) the far-field response 1 is shown when the weighted near-source error sensor response is minimized, and when the response at the considered far-field sensor set is directly minimized. The near-source sensor set is also shown in this figure and consists of the junction velocities at the connection points of the mounts with the receiver structure (24 sensors) and four additional sensors at the corners of the foundation plate. This means a total number of 28 near-source sensors, implying that the matrix $\mathbf{Y}_{nsda}$ is determined and square. The performance of the near-source weighting strategy is the same as the optimal result, namely minimization of the far-field sensor response itself. The same conclusion can be drawn for far-field sensor set 2 as shown in Figure 6.13(b). This implies that also a rather global measure of the receiver response can be obtained with the weighting of a relatively small near-source sensor set.

6.3.2 Reduction of the number of near-source sensors

For the determination of the weighting matrix described in equation (6.20) and denoted by method 1, both the primary and secondary FRFs are used. The term primary indicates the FRFs from the disturbance forces to the sensors and secondary indicates the FRFs from the actuator forces to the sensors. It is also possible to determine a weighting matrix based on the primary FRFs only [132]. In that case, the number of near-source sensors can be smaller to have a square near-source mobility matrix. An alternative method to determine this weighting matrix is explained below. This weighting matrix is used for two alternative ways of weighted near-source error sensor strategies, denoted by method 2 and method 3 respectively.

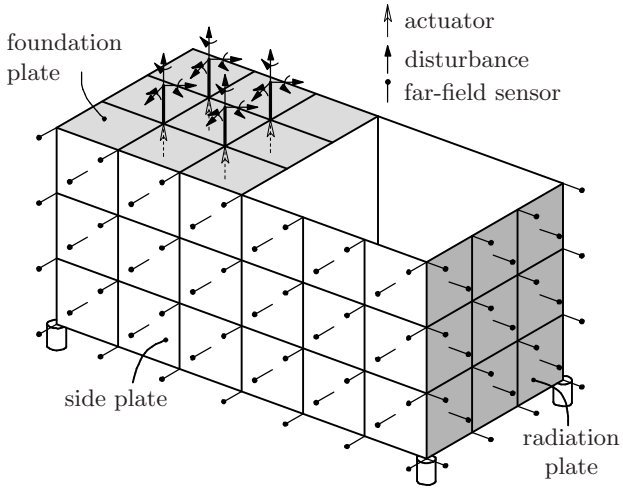

Figure 6.12: Numerical model of the isolation setup with the far-field sensor set 2.

Method 2

The far-field response in equation (6.17) can be expressed as:

$$\mathbf{v}_{fs} = \left(-\mathbf{Y}_{fsd} \cdot \mathbf{Y}_{nsd}^{+} \cdot \mathbf{Y}_{nsa} + \mathbf{Y}_{fsa}\right) \cdot \mathbf{f}_a + \mathbf{Y}_{fsd} \cdot \mathbf{Y}_{nsd}^{+} \cdot \mathbf{v}_{ns}. \tag{6.23}$$

In equation (6.23) the far-field sensor response is expressed in a term depending on the actuator forces and a term containing a weighted near-source velocity vector. The weighting matrix is shown to be:

$$\mathbf{W}_v^d = \mathbf{Y}_{fsd} \cdot \mathbf{Y}_{nsd}^{+}. \tag{6.24}$$

For the SISO case (single input and single output, meaning only one sensor and only one actuator) with just one disturbance force component, it can be seen that the first term at the right-hand side of equation (6.23) reduces to zero. For a MIMO system (multiple sensors and actuators) with multiple independent disturbance excitations this is not so straightforward. Taking a closer look at the influence of the actuator force vector in equation (6.23) results in the following consideration:

$$\underbrace{\underbrace{-\mathbf{Y}_{fsd} \cdot \mathbf{Y}_{nsd}^{+}}_{\mathbf{W}_v^d} \cdot \underbrace{\mathbf{Y}_{nsa} \cdot \mathbf{f}_a}_{\mathbf{v}_{ns}^a} + \underbrace{\mathbf{Y}_{fsa} \cdot \mathbf{f}_a}_{\mathbf{v}_{fs}^a}}_{\approx -\mathbf{v}_{fs}^a \,?}, \tag{6.25}$$

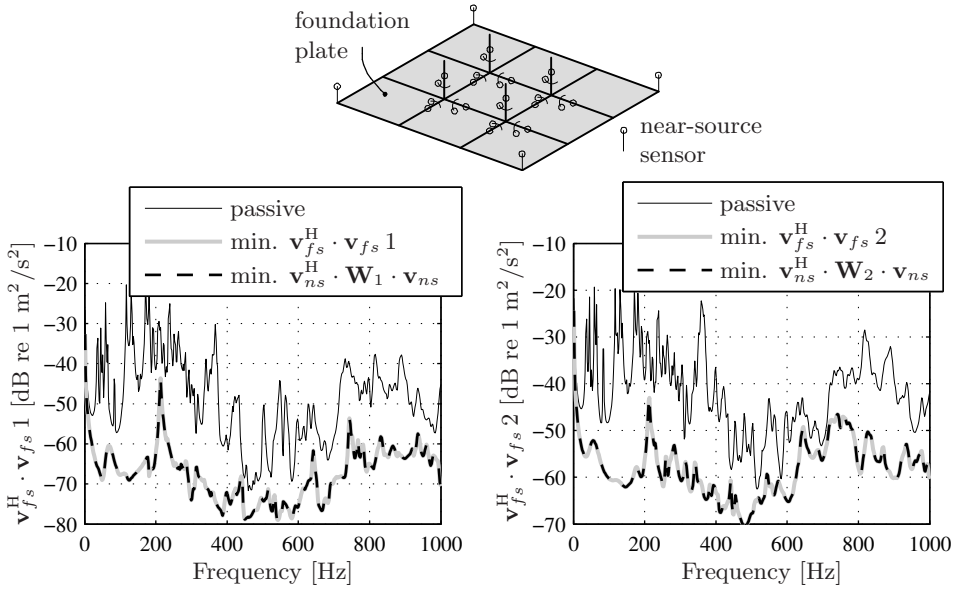

(a) far-field sensor set 1 (b) far-field sensor set 2

Figure 6.13: Active response at the far-field sensor sets 1 and 2 with minimization of the depicted near-source sensor response weighted with the weighting matrices that are determined with both the primary and secondary FRFs (method 1).

where $\mathbf{v}_{ns}^{a}$ denotes the near-source sensor response due to the actuator forces and $\mathbf{v}_{fs}^{a}$ denotes the far-field sensor response due to the actuator forces. The question mark indicates that the far-field response due to the actuator forces is only determined correctly when the inversion of mobility matrix $\mathbf{Y}_{nsd}$ can be determined in a correct way. This means that the mobility matrix must be square or overdetermined and not ill-conditioned for a reliable inversion. Hence, the number of near-source sensors must be at least equal to the number of disturbance forces, or in general at least equal to the number of mounts times 6. When this condition is fulfilled, the first term of equation (6.25) reduces to zero and the far-field sensor response only depends on the near-field response:

$$\mathbf{v}_{fs} = \mathbf{W}_v^d \cdot \mathbf{v}_{ns} = \mathbf{Y}_{fsd} \cdot \mathbf{Y}_{nsd}^{+} \cdot \mathbf{v}_{ns}\ . \tag{6.26}$$

This expression for the active response at the far-field sensor set can be written again in a Hermitian quadratic form in a similar way as shown in equa-

tion (6.21):

$$\begin{aligned} J = \mathbf{v}_{fs}^{\mathrm{H}} \cdot \mathbf{v}_{fs} &= \mathbf{v}_{ns}^{\mathrm{H}} \cdot \mathbf{W}_v^{d^{\mathrm{H}}} \cdot \mathbf{W}_v^d \cdot \mathbf{v}_{ns} \\ &= \mathbf{v}_{ns}^{\mathrm{H}} \cdot \mathbf{W}^d \cdot \mathbf{v}_{ns} \\ &= \mathbf{f}_a^{\mathrm{H}} \cdot \mathbf{A} \cdot \mathbf{f}_a + \mathbf{f}_a^{\mathrm{H}} \cdot \mathbf{b} + \mathbf{b}^{\mathrm{H}} \cdot \mathbf{f}_a + c. \end{aligned} \tag{6.27}$$

The components of the Hermitian quadratic error criterion are shown in the second column of Table 6.1 under method 2. The only difference between this method and method 1 is the weighting matrix: method 2 only uses the primary FRFs for the determination of the weighting matrix. The optimal actuator force that minimizes this quadratic cost function can be determined by equation (6.8). For the numerical model, this means that for a square or overdetermined mobility matrix $\mathbf{Y}_{nsd}$ at least 24 near-source sensors are needed (number of mounts times the size of the disturbance force vector). This means for the considered numerical model of the laboratory setup that 24 error sensors are needed. That is four error sensors less than the near-source error sensor strategy with a weighting matrix based on both the primary and secondary FRFs of method 1. This method to determine the weighting matrix is applied on the numerical model of the laboratory setup. In Figure 6.14 the responses at the two considered far-field sensor sets are shown for the weighted near-source sensor strategy and where the weighting matrix is based on the primary transfers only, as shown in equation (6.24). The four sensors at the corners of the foundation plate are thus omitted to reduce the number of near-source sensors in comparison with the near-source error sensor strategy considered in the previous subsection. The figures show that minimization of the near-source error sensor response weighted with $\mathbf{W}_v^d$ yields the same reductions at both considered far-field sensor sets as minimization of the far-field sensor responses themselves. This concept, with the advantage that the number of near-source error sensors decreases with the number of actuators, works well for the considered near-source sensor configurations. The robustness of method 2 is investigated in the next subsection.

Method 3

An important disadvantage of method 2 is that it only works when the condition in equation (6.25) is fulfilled. This implies that the actuator forces must have no influence on the far-field sensor response after weighting of the near-source error sensor response with the weighting matrix $\mathbf{W}_v^d$. This appears to be the case for the considered laboratory setup. However, this condition is not necessarily fulfilled in other situations. The influence of the actuators on the

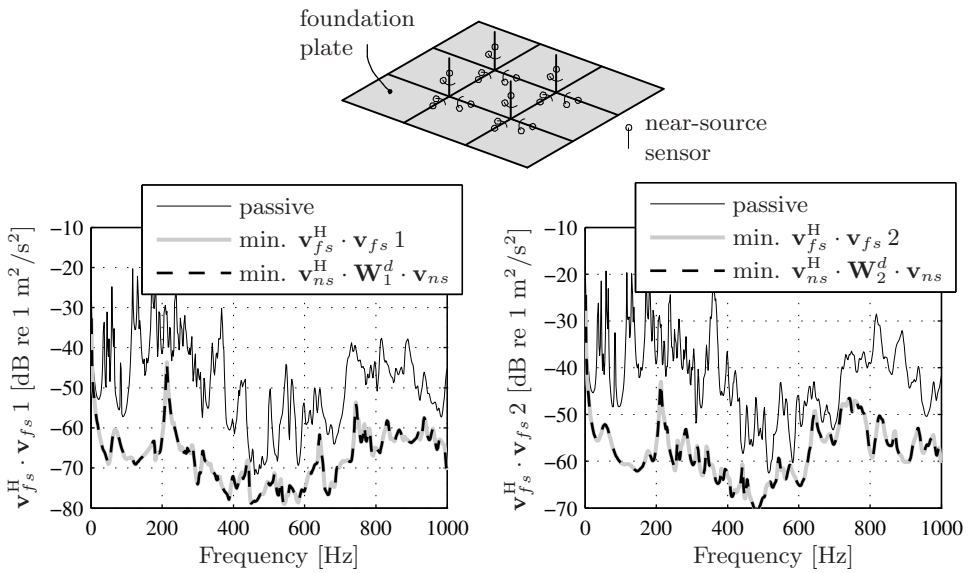

(a) far-field sensor set 1 (b) far-field sensor set 2

Figure 6.14: Active response at the far-field sensor sets 1 and 2 with minimization of the depicted near-source sensor set weighted with the weighting matrices that are determined with the primary FRFs only (method 2).

near-source error response can be reduced by the error sensor strategy introduced by Berkhoff [13]. After that, the weighting matrix determined with the primary FRFs only can be applied as shown in equation (6.24). This leads to a third method for using near-source error sensors. The first step is to determine the near-source error sensor signal:

$$\mathbf{v}_{ns} = \mathbf{Y}_{nsd} \cdot \mathbf{f}_d + \mathbf{Y}_{nsa} \cdot \mathbf{f}_a \,. \tag{6.28}$$

The near-source error sensor response is subsequently corrected for the actuator influence. This is done by subtracting the influence of the actuator with an off-line determined secondary FRF $\mathbf{Y}_{nsa}$ from equation (6.28) resulting in:

$$\mathbf{v}_{ns}^d = \mathbf{v}_{ns} - \mathbf{Y}_{nsa} \cdot \mathbf{f}_a = \mathbf{Y}_{nsd} \cdot \mathbf{f}_d \,. \tag{6.29}$$

The remaining near-source sensor response, indicated by $\mathbf{v}_{ns}^d$, is then only determined by the disturbance forces. This residual near-source sensor response is consequently weighted, resulting in the far-field response determined by the disturbance forces only:

$$\mathbf{v}_{fs}^d = \mathbf{W}_v^d \cdot \mathbf{v}_{ns}^d = \mathbf{W}_v^d \cdot \mathbf{Y}_{nsd} \cdot \mathbf{f}_d \,. \tag{6.30}$$

	Method 1	Method 2	Method 3
$\mathbf{W}_v$	$\mathbf{W}_v = \mathbf{Y}_{fsda} \cdot \mathbf{Y}^{+}_{nsda}$	$\mathbf{W}^d_v = \mathbf{Y}_{fsd} \cdot \mathbf{Y}^{+}_{nsd}$	$\mathbf{W}^d_v = \mathbf{Y}_{fsd} \cdot \mathbf{Y}^{+}_{nsd}$
$\mathbf{A}$	$\mathbf{Y}^{\mathrm{H}}_{nsa} \cdot \mathbf{W} \cdot \mathbf{Y}_{nsa}$	$\mathbf{Y}^{\mathrm{H}}_{nsa} \cdot \mathbf{W}^d \cdot \mathbf{Y}_{nsa}$	$\mathbf{Y}^{\mathrm{H}}_{fsa} \cdot \mathbf{Y}_{fsa}$
$\mathbf{b}$	$\mathbf{Y}^{\mathrm{H}}_{nsa} \cdot \mathbf{W} \cdot \mathbf{Y}_{nsd} \cdot \mathbf{f}_d$	$\mathbf{Y}^{\mathrm{H}}_{nsa} \cdot \mathbf{W}^d \cdot \mathbf{Y}_{nsd} \cdot \mathbf{f}_d$	$\mathbf{Y}^{\mathrm{H}}_{fsa} \cdot \mathbf{W}^d_v \cdot \mathbf{Y}_{nsd} \cdot \mathbf{f}_d$
c	$\mathbf{f}^{\mathrm{H}}_d \cdot \mathbf{Y}^{\mathrm{H}}_{nsd} \cdot \mathbf{W} \cdot \mathbf{Y}_{nsd} \cdot \mathbf{f}_d$	$\mathbf{f}^{\mathrm{H}}_d \cdot \mathbf{Y}^{\mathrm{H}}_{nsd} \cdot \mathbf{W}^d \cdot \mathbf{Y}_{nsd} \cdot \mathbf{f}_d$	$\mathbf{f}^{\mathrm{H}}_d \cdot \mathbf{Y}^{\mathrm{H}}_{nsd} \cdot \mathbf{W}^d \cdot \mathbf{Y}_{nsd} \cdot \mathbf{f}_d$

Table 6.1: The components of the error criterion for the three methods of near-source error sensor weighting based on a far-field sensor response.

The influence of the actuators on the far-field sensor response is taken into account by an off-line determined secondary mobility matrix $\mathbf{Y}_{fsa}$:

$$\mathbf{v}_{fs} = \mathbf{W}^d_v \cdot \mathbf{Y}_{nsd} \cdot \mathbf{f}_d + \mathbf{Y}_{fsa} \cdot \mathbf{f}_a \,. \tag{6.31}$$

This expression can again be written in the standard Hermitian quadratic form according to:

$$\begin{aligned} J = \mathbf{v}^{\mathrm{H}}_{fs} \cdot \mathbf{v}_{fs} &= \left(\mathbf{W}^d_v \cdot \mathbf{Y}_{nsd} \cdot \mathbf{f}_d + \mathbf{Y}_{fsa} \cdot \mathbf{f}_a\right)^{\mathrm{H}} \cdot \left(\mathbf{W}^d_v \cdot \mathbf{Y}_{nsd} \cdot \mathbf{f}_d + \mathbf{Y}_{fsa} \cdot \mathbf{f}_a\right) \\ &= \mathbf{f}^{\mathrm{H}}_a \cdot \mathbf{A} \cdot \mathbf{f}_a + \mathbf{f}^{\mathrm{H}}_a \cdot \mathbf{b} + \mathbf{b}^{\mathrm{H}} \cdot \mathbf{f}_a + c. \end{aligned} \tag{6.32}$$

The components of this Hermitian quadratic error criterion, namely the matrix $\mathbf{A}$, the vector $\mathbf{b}$ and the scalar c are shown in the third column of Table 6.1 under method 3. The disadvantage of this method with respect to method 2 is that extra off-line measurements have to be performed to determine the secondary path mobility matrices $\mathbf{Y}_{fsa}$ and $\mathbf{Y}_{nsa}$. This approach also results in the same reductions for the weighted near-source sensors as minimization of the far-field sensor sets directly.

Three methods are now available to obtain a weighted near-source error sensor strategy in such a way that a measure for the far-field sensor response is obtained.

- Method 1 uses off-line measured FRFs of the disturbance forces and actuator forces to the far-field sensor set and near-source error sensor set.

- Method 2 uses only off-line measured FRFs from the disturbance forces to the far-field and near-source sensor sets.

- Method 3 is a modification of method 2 by making use of off-line measured FRFs from the actuators to both sensor sets in order to determine the near-source error response due to the disturbance forces only.

An overview of the three methods is shown in Table 6.1. All three methods were shown to work well in the error-free numerical model of the laboratory setup. The next step is to investigate the robustness of the three methods when small corruptions are present in the weighting matrices.

6.3.3 Error sensitivity of the near-source error sensor strategies

Method 1

The FRFs needed for the weighting matrices have to be determined by off-line measurements and are inherently corrupted by measurement errors. The robustness of the near-source error sensor strategies considered in this subsection is investigated by applying small 'measurement' errors to these off-line determined FRFs. The numerical model of the laboratory setup is again used to investigate the robustness of the near-source error sensor strategies. The method to corrupt these FRFs is explained in appendix G. A corrupted matrix is denoted by the symbol $\underset{\sim}{(.)}$. The error percentage of the FRFs to determine the weighting matrix is assumed to be 6 % of the magnitude of each FRF for the presented simulation results in this subsection. The weighting matrix can be determined with the corrupted mobility matrices according to:

$$\underset{\sim}{\mathbf{W}}_v = \underset{\sim}{\mathbf{Y}}_{fsda} \cdot \underset{\sim}{\mathbf{Y}}^{+}_{nsda}. \tag{6.33}$$

The weighted passive far-field sensor response at far-field sensor set 1 ($\mathbf{v}_{ns}^{\mathrm{H}} \cdot \underset{\sim}{\mathbf{W}}_1 \cdot \mathbf{v}_{ns}$) and at far-field sensor set 2 ($\mathbf{v}_{ns}^{\mathrm{H}} \cdot \underset{\sim}{\mathbf{W}}_2 \cdot \mathbf{v}_{ns}$) with the corrupted weighting matrices are shown in Figure 6.15. It is shown that the errors in the weighting matrices result in considerable errors in the passive far-field response, especially at frequencies where the far-field response has a low value.

The next step is to consider the active isolation performance. The active far-field sensor response is depicted in Figure 6.16 for both far-field sensor sets with minimization of the error sensor strategy as shown in equation (6.21), but with a corrupted weighting matrix as described by equation (6.33). The components of the Hermitian quadratic error criterion are shown in Table 6.2 (method 1). Considering the active response at far-field sensor set 1, the performance decreases considerably. However, large reductions are still obtained in the far-field response, namely reductions larger than 10 dB at many frequencies. It can also be seen that the active response does not exceed the

passive response. The unstable behavior for small measurement errors in the weighting matrices as was shown for the power mode approach does not occur for this type of near-source error sensor strategy. It must be stressed that the FRFs for determination of the weighting matrices are corrupted twice as much (6 %) as the weighting matrices for the power mode approach (3 %).

The reductions at far-field sensor set 2 are also less than for the optimal solution. However, far-field sensor set 2 represents a more global measure of the dynamic response of the receiver structure, and is more robust for measurement errors. This is concluded from the fact that the difference between the far-field response obtained with the weighting strategy and the optimal reduction of the far-field response is less than for far-field sensor set 1.

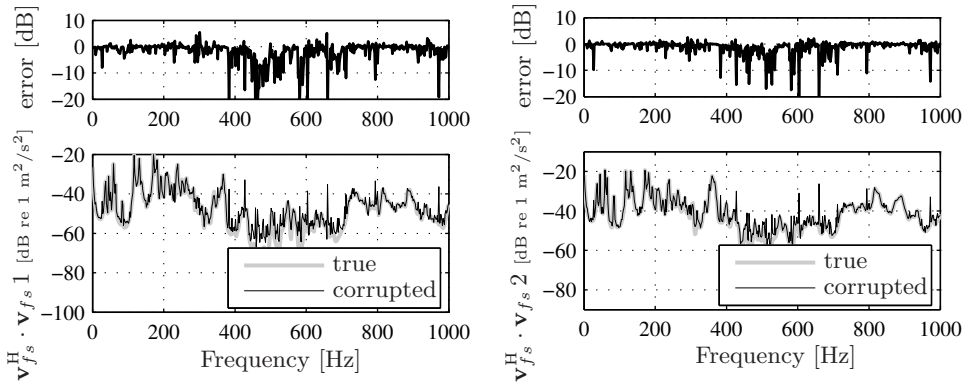

(a) far-field sensor set 1 (b) far-field sensor set 2

Figure 6.15: Passive response and the error of the passive response after weighting the near-source sensor set with the corrupted weighting matrix that is determined with the use of both the primary and secondary FRFs at far-field sensor set 1 (a) and at far-field sensor set 2 (b), respectively.

Method 2

The weighting matrix determined by the primary FRFs only, as shown in equation (6.24), is corrupted in a similar way to investigate the robustness and can be determined by:

$$\underset{\sim}{\mathbf{W}}_v^d = \underset{\sim}{\mathbf{Y}}_{fsd} \cdot \underset{\sim}{\mathbf{Y}}_{nsd}^{+} . \tag{6.34}$$

The passive far-field responses are shown in Figure 6.17, when the passive near-source sensor response is weighted with the corrupted weighting matrices $\underset{\sim}{\mathbf{W}}_1^d$

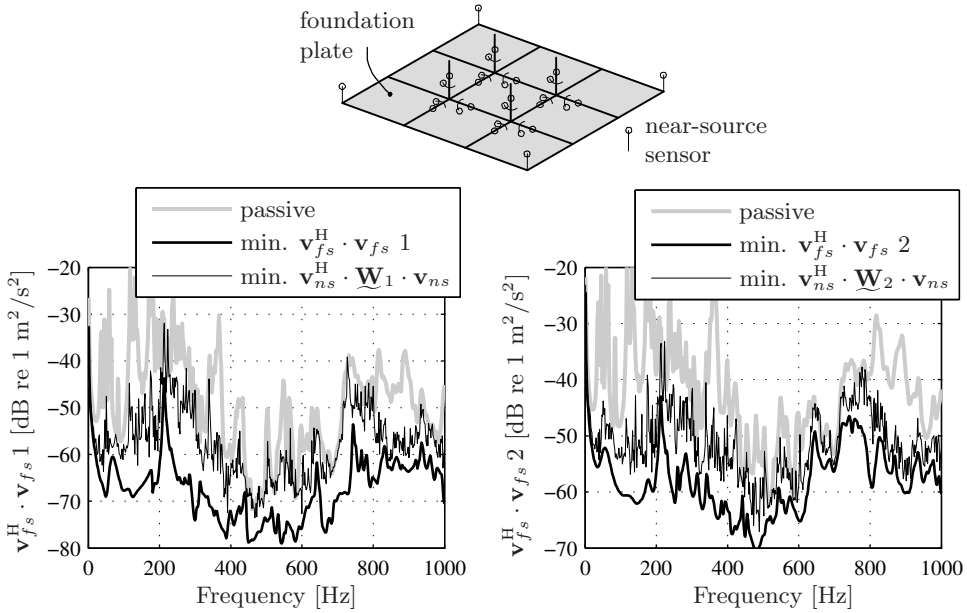

(a) far-field sensor set 1 (b) far-field sensor set 2

Figure 6.16: Active response for the near-source sensor strategy, with the corrupted weighting matrices that are determined using both the primary and secondary FRFs at far-field sensor set 1 (a) and at far-field sensor set 2 (b) respectively (method 1).

and $\underset{\sim}{\mathbf{W}}_2^d$ for far-field sensor set 1 and 2, respectively. The error in dB between the passive weighted near-source response and the true far-field response is shown in the upper part of the figure. The errors introduced are similar to the case where the weighting matrix is determined with a combination of primary and secondary FRFs as shown in Figure 6.15. The weighted error sensor response can again be written in the Hermitian quadratic form with the components shown in Table 6.2 (method 2). The active responses at both far-field sensor sets are depicted in Figure 6.18. The near-source error sensor strategy with a weighting matrix with far-field sensor set 2 as performance sensor set, is a little more robust with respect to errors in the weighting matrix.

Methods 3 en 4

It was shown that another method to implement the weighting matrix $\underset{\sim}{\mathbf{W}}_v^d$ is realized by correcting the near-source error sensor response for the actuator

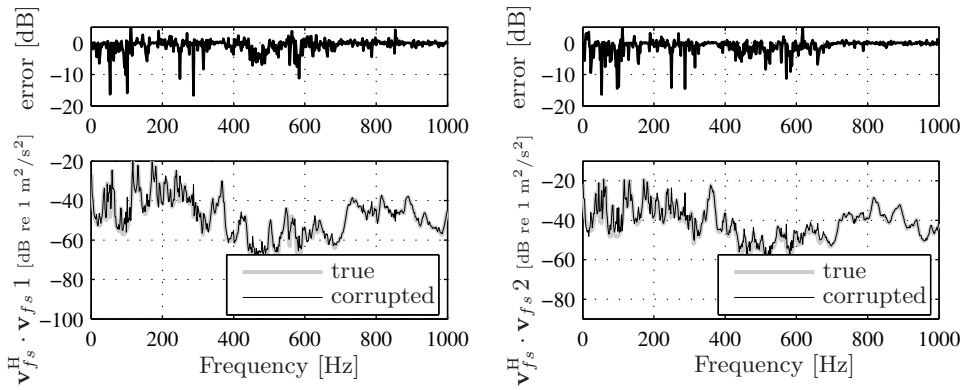

(a) far-field sensor set 1 (b) far-field sensor set 2

Figure 6.17: Passive response after weighting the near-source sensor set with the corrupted weighting matrix that is determined with the use of the primary FRFs only at far-field sensor set 1 (a) and at far-field sensor 2 (b), respectively.

influence, as introduced by Berkhoff. The near-source error sensor response is determined by:

$$\mathbf{v}_{ns} = \mathbf{Y}_{nsd} \cdot \mathbf{f}_d + \mathbf{Y}_{nsa} \cdot \mathbf{f}_a \,. \tag{6.35}$$

The first step is to subtract the actuator influence on the near-source error sensor response:

$$\mathbf{v}_{ns}^{d} = \mathbf{Y}_{nsd} \cdot \mathbf{f}_d + \mathbf{Y}_{nsa} \cdot \mathbf{f}_a - \underset{\sim}{\mathbf{Y}}_{nsa} \cdot \mathbf{f}_a \,, \tag{6.36}$$

where $\underset{\sim}{\mathbf{Y}}_{nsa}$ is the off-line determined secondary mobility matrix describing the transfer from the actuator forces to the near-source error sensors. This matrix contains small measurement errors and is therefore not equal to the true secondary mobility matrix $\mathbf{Y}_{nsa}$. For this reason the actuator influence on the near-source error response is not completely eliminated. The next step is to weight this near-source error response with the off-line determined weighting matrix $\underset{\sim}{\mathbf{W}}_{v}^{d}$ to obtain the far-field response due to the influence of the disturbance only:

$$\mathbf{v}_{fs}^{d} = \underset{\sim}{\mathbf{W}}_{v}^{d} \cdot \mathbf{v}_{ns}^{d} = \underset{\sim}{\mathbf{W}}_{v}^{d} \cdot \left(\mathbf{Y}_{nsd} \cdot \mathbf{f}_d + \left(\mathbf{Y}_{nsa} - \underset{\sim}{\mathbf{Y}}_{nsa} \right) \cdot \mathbf{f}_a \right) . \tag{6.37}$$

The better the off-line measured mobility $\underset{\sim}{\mathbf{Y}}_{nsa}$ matches the true mobility $\mathbf{Y}_{nsa}$, the better the far-field sensor response $\mathbf{v}_{fs}^{d}$ due to the disturbance forces only is determined. The influence of the actuators on the far-field sensor

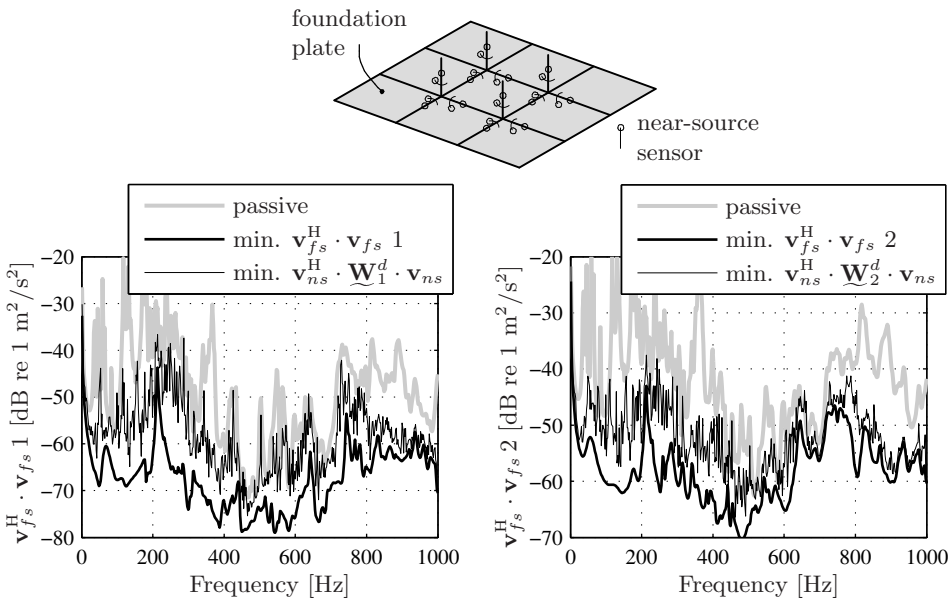

(a) far-field sensor set 1 (b) far-field sensor set 2

Figure 6.18: Active response for the near-source sensor strategy with the corrupted weighting matrices that are determined with the use of the primary FRFs only at far-field sensor set 1 (a) and at far-field sensor set 2 (b), respectively (method 2).

response is taken into account by an off-line determined secondary mobility matrix $\underset{\sim}{\mathbf{Y}}_{fsa}$:

$$\mathbf{v}_{fs} = \underset{\sim}{\mathbf{W}}_v^d \cdot \left(\mathbf{Y}_{nsd} \cdot \mathbf{f}_d + \left(\mathbf{Y}_{nsa} - \underset{\sim}{\mathbf{Y}}_{nsa}\right) \cdot \mathbf{f}_a\right) + \underset{\sim}{\mathbf{Y}}_{fsa} \cdot \mathbf{f}_a. \tag{6.38}$$

This expression can again be written in the standard Hermitian quadratic form with the components shown in Table 6.2 (method 3). The optimal actuator force vector that is determined in this way differs from the actuator force vector that is determined with the uncorrupted FRFs shown in Table 6.1 under method 3. In the ideal case it is thus assumed that the off-line measured FRFs $\underset{\sim}{\mathbf{Y}}_{nsa}$ and $\underset{\sim}{\mathbf{Y}}_{fsa}$ are equal to the true FRFs. In Figure 6.19 the active far-field sensor responses are shown when the actuator forces are determined with the corrupted weighting matrices and corrupted secondary FRFs. It is shown that the reductions obtained in this way are similar in magnitude compared to the reductions obtained with the straightforward use of the weighting matrix $\mathbf{W}^d$ of method 2 as shown in Figure 6.18.

For the results presented in Figure 6.19 it was assumed that all the off-line

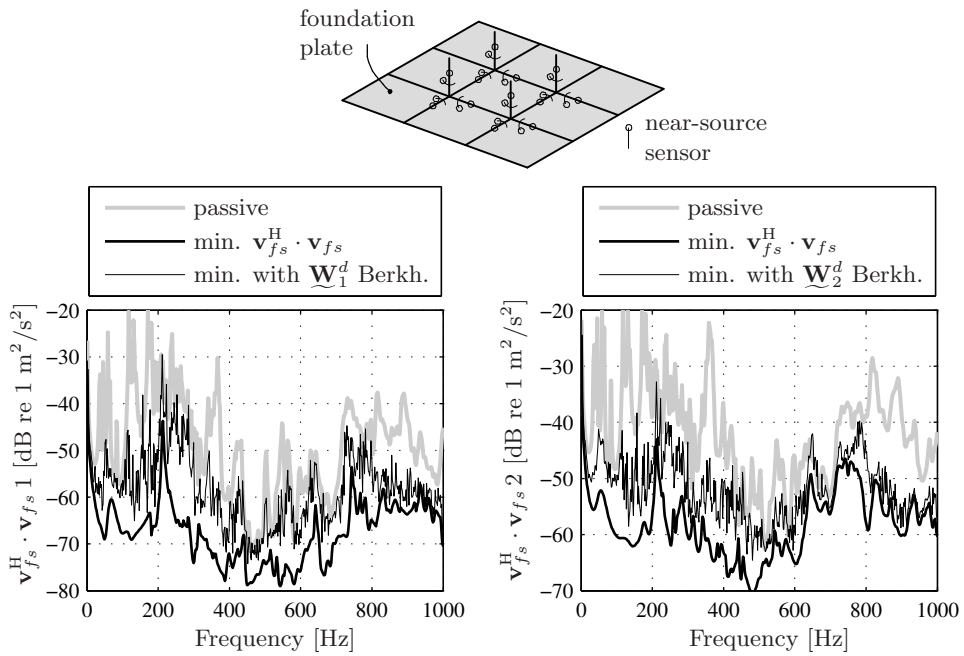

(a) far-field sensor set 1 (b) far-field sensor set 2

Figure 6.19: Active response for the near-source sensor strategy with the corrupted weighting matrices determined with the use of the primary FRFs only at far-field sensor set 1 (a) and at far-field sensor set 2 (b) and with the use of off-line measured secondary FRFs to obtain the far-field response (method 3).

measured FRFs have the same magnitude of corruption. This is realistic for the FRFs from the disturbance and actuator forces to the far-field sensors, because these transfer matrices are measured off-line. However, the near-source error sensors are attached to the structure and used as error sensors for the real-time controller. This allows a frequent update of the measured secondary path, because the actuators and error sensors are part of the real-time controller and for this reason ready to be used. Actually, this measurement must also be performed to implement the filtered-x LMS algorithm that is commonly used for this kind of feedforward active control problems [96]. For this reason simulation results are presented for a perfect estimation of this secondary transfer and therefore it is assumed that $\underset{\sim}{\mathbf{Y}}_{nsa} = \mathbf{Y}_{nsa}$. The coefficients of the actuator forces for the Hermitian quadratic error criterion are shown in Table 6.2 (method 4).

The active far-field sensor responses for this near-source error sensor strat-

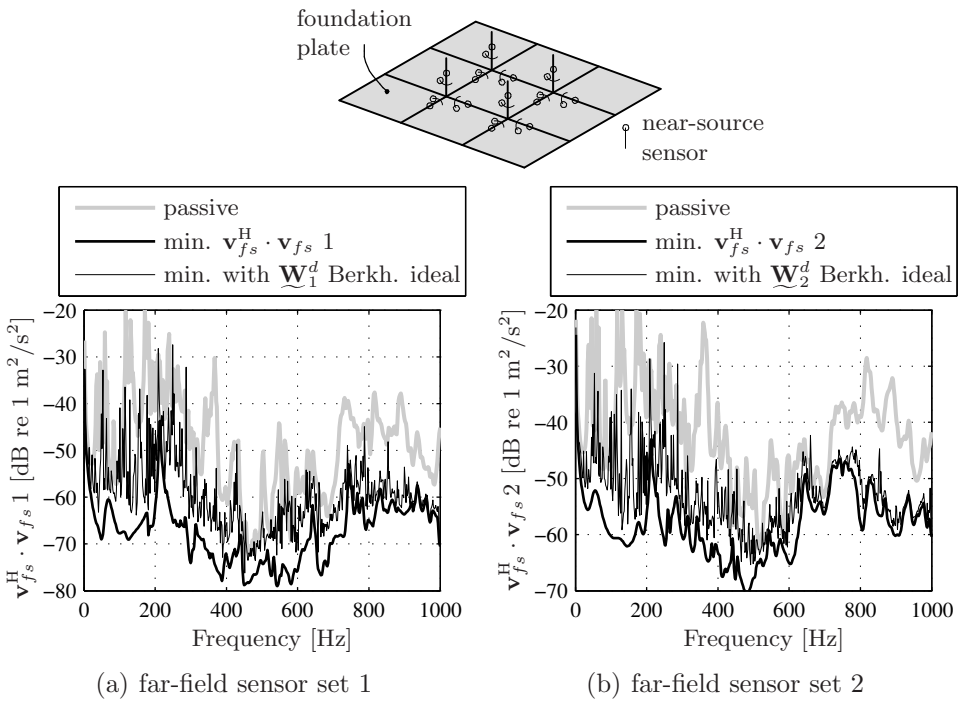

(a) far-field sensor set 1 (b) far-field sensor set 2

Figure 6.20: Active response for the near-source sensor strategy with the corrupted weighting matrices determined with the use of the primary FRFs only at far-field sensor set 1 (a) and at far-field sensor set 2 (b) and with the use of off-line measured secondary FRFs to obtain the far-field response and a perfect estimated FRF $\mathbf{Y}_{nsa}$ (method 4).

egy are shown in Figure 6.20. Two tendencies are observed in the depicted active responses. First of all, the strategy is less robust at lower frequencies compared to the other near-source sensor strategies considered in this subsection. This behavior is observed by the larger peaks in the active response in the frequency range of 0 up to 300 Hz. The second tendency that is observed is that the obtained reductions of the far-field velocities are larger in the higher frequency range of 600 up to 1000 Hz.

6.3.4 Regularization

For the determination of the weighting matrix a (pseudo)-inverse is needed, which can cause problems when the matrix is ill-conditioned. In this subsection two regularization techniques are considered: TSVD and using additional near-source sensors. The regularization techniques are used to obtain a more

	Method 1	**Method 2**
$\underset{\sim}{\mathbf{W}}_v$	$\underset{\sim}{\mathbf{W}}_v = \underset{\sim}{\mathbf{Y}}_{fsda} \cdot \underset{\sim}{\mathbf{Y}}^{+}_{nsda}$	$\underset{\sim}{\mathbf{W}}^{d}_v = \underset{\sim}{\mathbf{Y}}_{fsd} \cdot \underset{\sim}{\mathbf{Y}}^{+}_{nsd}$
$\mathbf{A}$	$\mathbf{Y}^{\mathrm{H}}_{nsa} \cdot \underset{\sim}{\mathbf{W}} \cdot \mathbf{Y}_{nsa}$	$\mathbf{Y}^{\mathrm{H}}_{nsa} \cdot \underset{\sim}{\mathbf{W}}^{d} \cdot \mathbf{Y}_{nsa}$
$\mathbf{b}$	$\mathbf{Y}^{\mathrm{H}}_{nsa} \cdot \underset{\sim}{\mathbf{W}} \cdot \mathbf{Y}_{nsd} \cdot \mathbf{f}_d$	$\mathbf{Y}^{\mathrm{H}}_{nsa} \cdot \underset{\sim}{\mathbf{W}}^{d} \cdot \mathbf{Y}_{nsd} \cdot \mathbf{f}_d$
c	$\mathbf{f}^{\mathrm{H}}_d \cdot \mathbf{Y}^{\mathrm{H}}_{nsd} \cdot \underset{\sim}{\mathbf{W}} \cdot \mathbf{Y}_{nsd} \cdot \mathbf{f}_d$	$\mathbf{f}^{\mathrm{H}}_d \cdot \mathbf{Y}^{\mathrm{H}}_{nsd} \cdot \underset{\sim}{\mathbf{W}}^{d} \cdot \mathbf{Y}_{nsd} \cdot \mathbf{f}_d$
	Method 3	**Method 4**
$\underset{\sim}{\mathbf{W}}_v$	$\underset{\sim}{\mathbf{W}}^{d}_v = \underset{\sim}{\mathbf{Y}}_{fsd} \cdot \underset{\sim}{\mathbf{Y}}^{+}_{nsd}$	$\underset{\sim}{\mathbf{W}}^{d}_v = \underset{\sim}{\mathbf{Y}}_{fsd} \cdot \underset{\sim}{\mathbf{Y}}^{+}_{nsd}$
$\mathbf{A}$	$\left(\underset{\sim}{\mathbf{Y}}^{\mathrm{H}}_{fsa} + \left(\mathbf{Y}_{nsa} - \underset{\sim}{\mathbf{Y}}_{nsa}\right)^{\mathrm{H}} \cdot \underset{\sim}{\mathbf{W}}^{d^{\mathrm{H}}}_v\right) \cdot \left(\underset{\sim}{\mathbf{W}}^{d}_v \cdot \left(\mathbf{Y}_{nsa} - \underset{\sim}{\mathbf{Y}}_{nsa}\right) + \underset{\sim}{\mathbf{Y}}_{fsa}\right)$	$\underset{\sim}{\mathbf{Y}}^{\mathrm{H}}_{fsa} \cdot \underset{\sim}{\mathbf{Y}}_{fsa}$
$\mathbf{b}$	$\left(\underset{\sim}{\mathbf{Y}}^{\mathrm{H}}_{fsa} + \left(\mathbf{Y}_{nsa} - \underset{\sim}{\mathbf{Y}}_{nsa}\right)^{\mathrm{H}} \cdot \underset{\sim}{\mathbf{W}}^{d^{\mathrm{H}}}_v\right) \cdot \underset{\sim}{\mathbf{W}}^{d}_v \cdot \mathbf{Y}_{nsd} \cdot \mathbf{f}_d$	$\underset{\sim}{\mathbf{Y}}^{\mathrm{H}}_{fsa} \cdot \underset{\sim}{\mathbf{W}}^{d}_v \cdot \mathbf{Y}_{nsd} \cdot \mathbf{f}_d$
c	$\mathbf{f}^{\mathrm{H}}_d \cdot \mathbf{Y}^{\mathrm{H}}_{nsd} \cdot \underset{\sim}{\mathbf{W}}^{d} \cdot \mathbf{Y}_{nsd} \cdot \mathbf{f}_d$	$\mathbf{f}^{\mathrm{H}}_d \cdot \mathbf{Y}^{\mathrm{H}}_{nsd} \cdot \underset{\sim}{\mathbf{W}}^{d} \cdot \mathbf{Y}_{nsd} \cdot \mathbf{f}_d$

Table 6.2: The components of the error criterion for the four methods of near-source error sensor weighting based on a far-field sensor response with corrupted weighting matrices. Method 1 is based on the weighting matrix determined with both primary and secondary FRFs and method 2 with a weighting matrix determined with primary FRFs only. Method 3 uses the same weighting matrix as method 2, but has a correction for the actuator influence. Method 4 is the same method as 3, but for and ideal off-line estimation of the secondary mobility matrix from the actuators to the near-source error sensors.

reliable inverse of the mobility matrices in order to improve the performance of the active control system. The regularization techniques are applied on the weighting matrices that are determined with the numerical model of the laboratory setup.

Method 1

The near-source sensor strategy method 1 based on the FRFs from both the disturbance and actuator forces to the near-source error sensor set and the far-field performance sensor set as shown in equation (6.20), is considered first. An inversion of the mobility matrix from the disturbance and actuator forces to the near-source error sensors is needed in order to obtain the weighting matrix:

$$\widehat{\underset{\sim}{\mathbf{W}}}_v = \underset{\sim}{\mathbf{Y}}_{fsda} \cdot \widehat{\underset{\sim}{\mathbf{Y}}}^{+}_{nsda}, \tag{6.39}$$

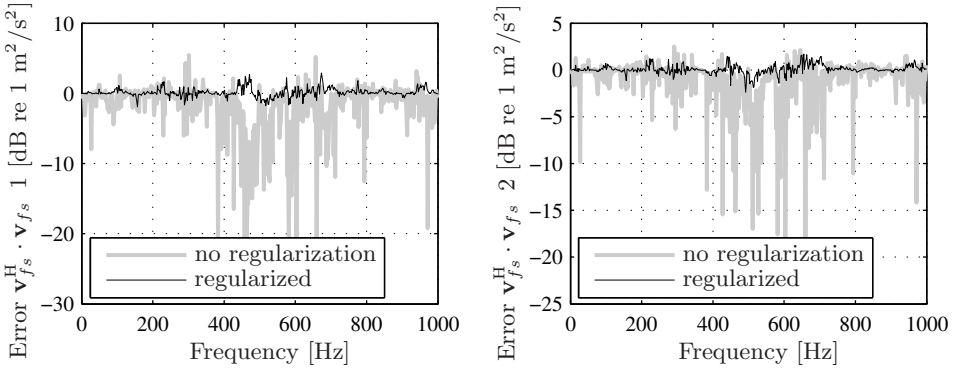

(a) far-field sensor set 1 (b) far-field sensor set 2

Figure 6.21: Error of the passive response at both far-field sensor sets after weighting of the near-source sensor set with the corrupted weighting matrix based on both the primary and secondary FRFs and with regularization of this weighting matrix at far-field sensor set 1 (a) and at far-field sensor set 2 (b).

where $\widehat{(.)}$ denotes a regularized representation. The (pseudo-)inversion in equation (6.39) is ill-conditioned, and therefore the influence of regularization on the performance of the considered near-source error sensor strategy is investigated. The regularized (pseudo-)inverse of the mobility matrix is determined using the TSVD technique (see also appendix C.2):

$$\widehat{\underset{\sim}{\mathbf{Y}}}^{+}_{nsda} = \sum_{i}^{k} \frac{\mathbf{v}_i \cdot \mathbf{u}_i^{\mathrm{H}}}{s_i}, \tag{6.40}$$

where $\mathbf{u}_i$ and $\mathbf{v}_i$ are the left and right singular vectors of $\underset{\sim}{\mathbf{Y}}_{nsda}$, respectively, s_i the i^{th} singular value and k is the number of singular values taken into account for the regularization. This number is determined by definition of a noise floor. The singular values that are smaller than this noise floor are rejected and omitted in the reconstruction. In Figure 6.21 the error in the prediction of the passive response at the two far-field performance sensor sets is shown when the near-source error sensor set is weighted with an unregularized matrix and a regularized weighting matrix. It is clear that the large errors in the response that occur due to the small errors in the FRFs, reduce considerably when the inversion of $\underset{\sim}{\mathbf{Y}}_{nsda}$ is regularized. Regularization has a similar effect on the passive response of both far-field sensor sets.

The regularization of the near-source weighting matrix also influences the active performance at the far-field performance sensor sets. This effect is

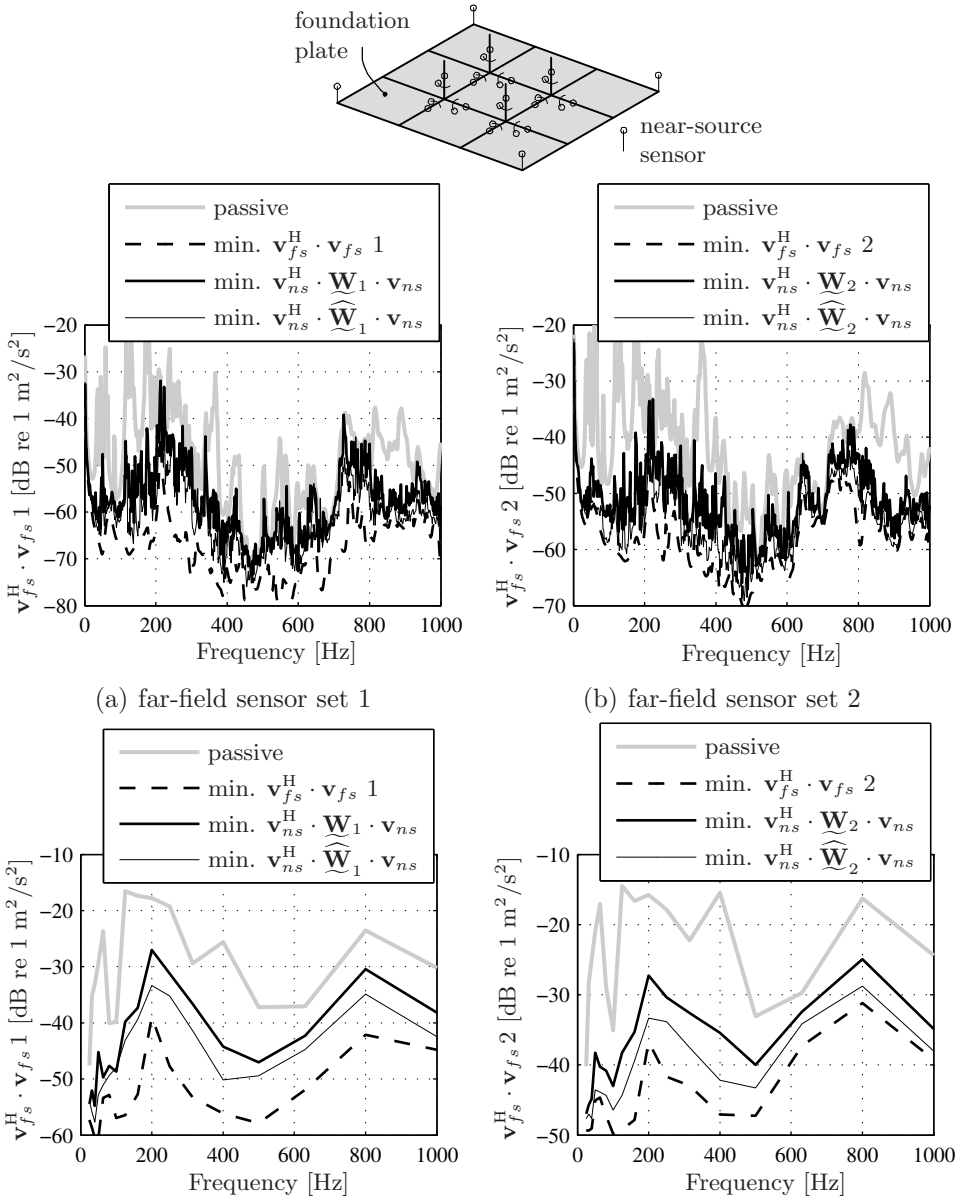

(a) far-field sensor set 1

(b) far-field sensor set 2

(c) far-field sensor set 1 (1/3-octave bands)

(d) far-field sensor set 2 (1/3-octave bands)

Figure 6.22: Active response for the near-source sensor strategy with the regularized and unregularized corrupted weighting matrices based on both the primary and secondary FRFs at far-field sensor set 1 (a,c) and at far-field sensor set 2 (b,d) (method 1).

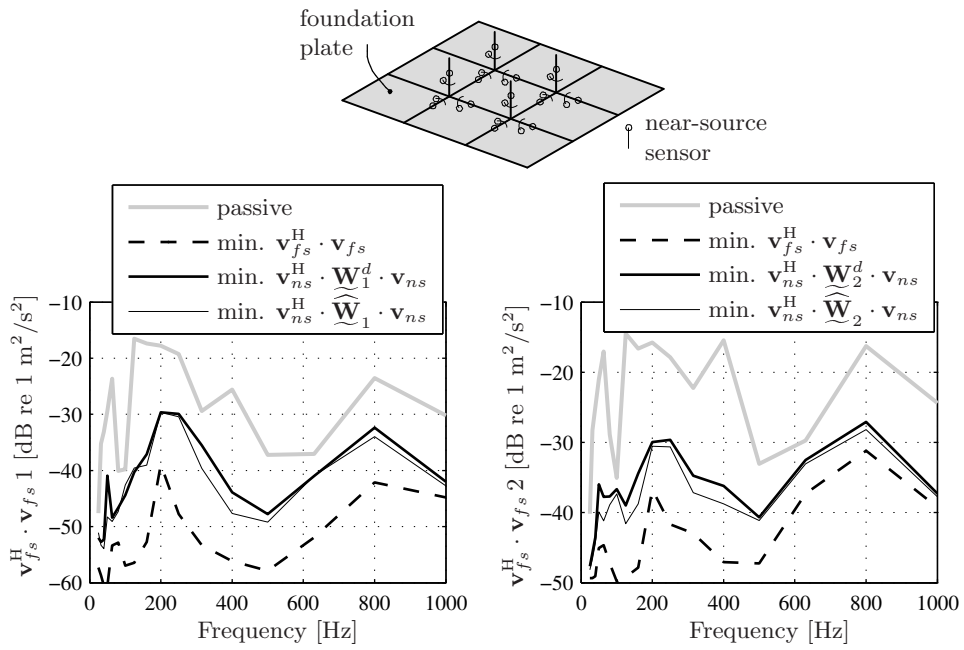

(a) far-field sensor set 1 (1/3-octave bands) (b) far-field sensor set 2 (1/3-octave bands)

Figure 6.23: Active response for the near-source sensor strategy with the regularized and unregularized corrupted weighting matrices based on the primary FRFs only at far-field sensor set 1 (a) and at far-field sensor set 2 (b) (method 2).

shown for the far-field sensor sets 1 and 2 in Figures 6.22(a) and 6.22(b) respectively. For a more clear picture of the obtained reductions, the frequency responses are also shown in one-third octave bands in Figures 6.22(c) and 6.22(d). The regularization results in an extra reduction of about 3 to 4 dB for both far-field sensor sets. The regularized solution of far-field sensor set 2 is a little more robust, because it shows a smaller difference between the optimal active far-field response and the active regularized weighted near-source response.

Method 2

The robustness of the near-source error sensor strategy with the weighting matrix $\mathbf{W}_v^d$ method 2 is analyzed in the same way. The regularized weighting matrix is calculated by:

$$\widehat{\underset{\sim}{\mathbf{W}}}_v^d = \underset{\sim}{\mathbf{Y}}_{fsd} \cdot \widehat{\underset{\sim}{\mathbf{Y}}}_{nsd}^{+}, \tag{6.41}$$

where $\widehat{\underset{\sim}{\mathbf{Y}}}^{+}_{nsd}$ is the regularized inversion of the primary error sensor transfer matrix. The influence of the regularization on the performance of the active isolation system is not large as can be seen in Figure 6.23. The extra reduction obtained at the far-field sensor sets is at maximum merely a few dB.

Methods 3 and 4

Instead of using the weighting matrix $\underset{\sim}{\mathbf{W}}^{d}_{v}$ in a straightforward way, a strategy was described that only weighted the contribution of the disturbance forces to the near-source error sensor response (method 3). The influence of the actuator forces was taken into account by extra off-line measured secondary FRFs to the near-source and far-field sensor sets as shown in equation (6.38). The influence of regularization on this near-source sensor strategy is shown in Figures 6.24(a) and 6.24(b). The improvements are small, a few dB across the whole frequency range. This near-source error sensor strategy can be improved because the off-line measured mobility matrix $\underset{\sim}{\mathbf{Y}}_{nsa}$ can be updated regularly. For this reason the active performance responses at the far-field sensor sets are determined in the ideal situation that the off-line measured mobility $\underset{\sim}{\mathbf{Y}}_{nsa}$ equals the real mobility $\mathbf{Y}_{nsa}$ (method 4). The results are shown in Figures 6.24(c) and 6.24(d). The regularization improves the active performance in the frequency region up to 400 Hz. The effect of the regularization on the active far-field response is smaller for higher frequencies.

To compare the performance of the different regularized near-source error sensor strategies, all responses are plotted in Figure 6.25 for far-field sensor set 1 and in Figure 6.26 for far-field sensor set 2. This means that, besides the passive response and the active response with direct minimization of the far-field sensor response, also the regularized near-source error strategies are depicted in the following order:

- Method 1: a weighting matrix based on both the primary and secondary FRFs (min. $\mathbf{v}^{\mathrm{H}}_{ns} \cdot \widehat{\underset{\sim}{\mathbf{W}}} \cdot \mathbf{v}^{d}_{ns}$).
- Method 2: the weighting procedure based on the near-source error response due to the disturbance forces only (min. $\mathbf{v}^{\mathrm{H}}_{ns} \cdot \widehat{\underset{\sim}{\mathbf{W}}}^{d} \cdot \mathbf{v}_{ns}$).
- Method 3: the weighting procedure based on the near-source error response due to the disturbance forces only but with a correction for the actuator influence (min. with $\widehat{\underset{\sim}{\mathbf{W}}}^{d}$ Berkh.).
- Method 4: same weighting procedure as for method 3, but without errors in the secondary FRF $\underset{\sim}{\mathbf{Y}}_{nsa}$ (min. with $\widehat{\underset{\sim}{\mathbf{W}}}^{d}$ Berkh. ideal).

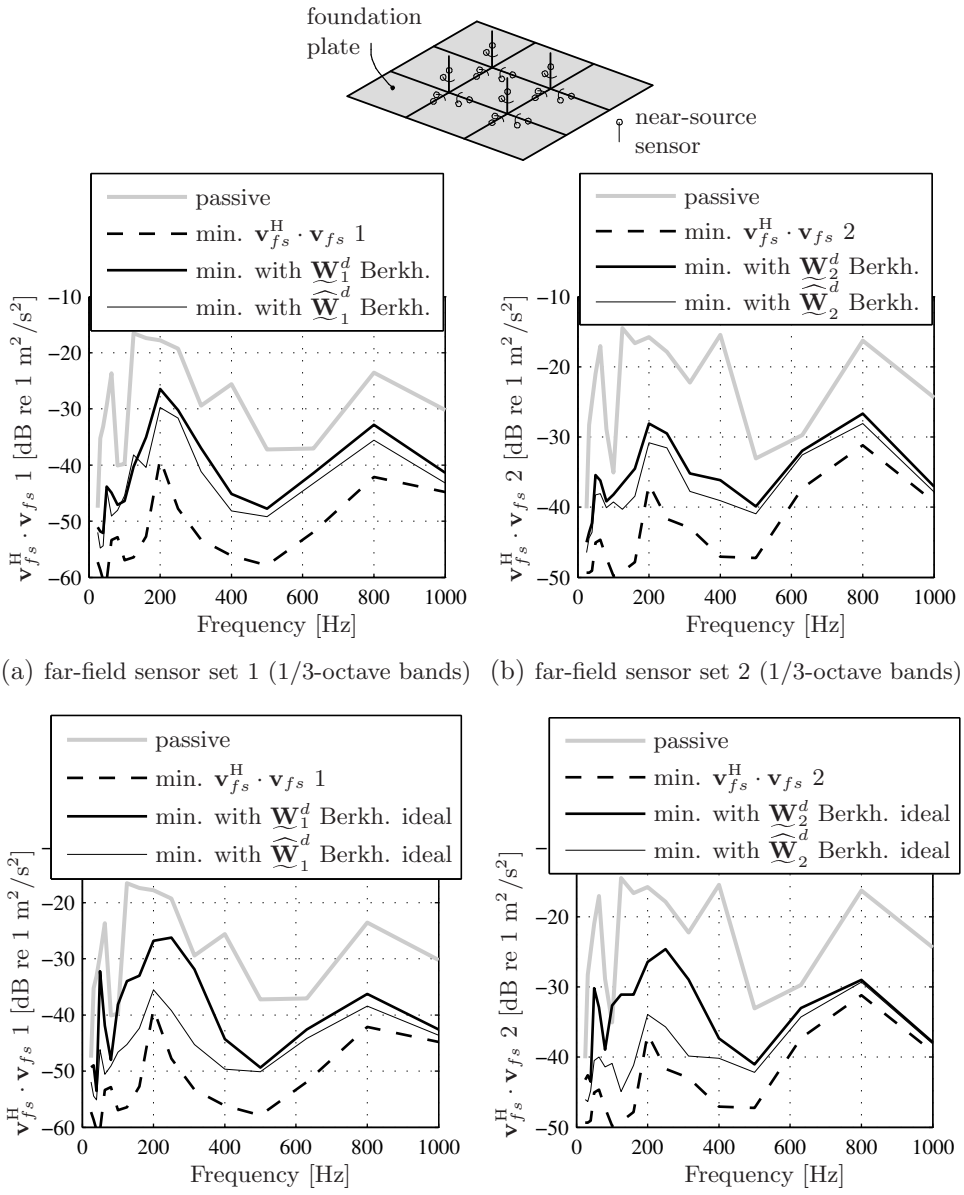

(a) far-field sensor set 1 (1/3-octave bands) (b) far-field sensor set 2 (1/3-octave bands)

(c) far-field sensor set 1 (1/3-octave bands) (d) far-field sensor set 2 (1/3-octave bands)

Figure 6.24: Active response with a weighted (based on primary FRFs only) near-source sensor strategy at far-field sensor set 1 and 2 (a,b) (method 3) and for the ideal situation without errors in $\mathbf{Y}_{nsa}$ (c,d) (method 4).

The least reduction is obtained with the near-source weighting based on the primary FRFs only for both far-field sensor sets (method 2). When a correction is applied on the near-source error sensor response to take account of the response due to the disturbance forces only (method 3), the performance improves only slightly. Taking account of both the primary and the secondary transfers for the determination of the weighting matrix itself (method 1), results in better reductions over the whole frequency range. For far-field sensor set 2, this near-source error sensor strategy has the best results in the frequency region below 100 Hz and from 400 up to 500 Hz. For the other frequencies, the largest reduction is obtained for the 'ideal' near-source error strategy, with a correction of the actuator influence on the near-source error sensor response before the weighting procedure and with the assumption that the secondary path is estimated perfectly (method 4). The latter error sensor strategy clearly has the best performance for far-field sensor set 1.

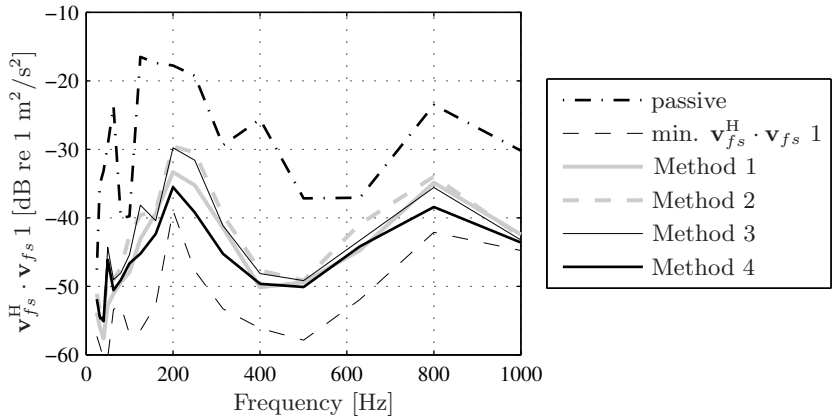

Figure 6.25: Overview of the active responses at far-field sensor set 1 for the considered regularized near-source error sensor strategies in one-third octave bands.

Increasing the number of near-source sensors

The inversion of the primary near-source mobility matrix that is necessary to determine the weighting matrix can also be regularized by increasing the number of near-source sensors. The configurations considered so far were determined systems, meaning that the number of near-source error sensors is equal to the number of applied disturbance forces. The mobility matrix $\mathbf{Y}_{nsd}$ is thus a square matrix. It is known that the behavior for inversion can

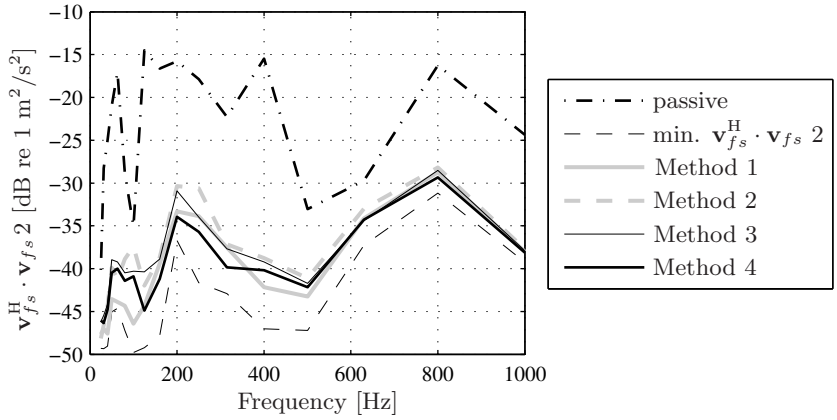

Figure 6.26: Overview of the active responses at far-field sensor set 2 for the considered regularized near-source error sensor strategies in one-third octave bands.

be improved by over-determination, i.e. by increasing the number of near-source sensors a rectangular mobility matrix with more rows than columns is created. To investigate the robustness of this technique, the weighting matrix is determined with the primary FRFs only but with four additional near-source sensors. Besides increasing the number of near-source sensors, regularization is also applied using TSVD. The influence of over-determination is investigated with the near-source error sensor strategy that showed the best results, namely method 4. The weighting matrix for the over-determined near-source error sensor set is derived by:

$$\underset{\sim}{\widehat{\mathbf{W}}}_v^{od} = \underset{\sim}{\mathbf{Y}}_{fsd} \cdot \underset{\sim}{\widehat{\mathbf{Y}}}_{nsd}^{od^+}, \tag{6.42}$$

where $\underset{\sim}{\widehat{\mathbf{Y}}}_{nsd}^{od^+}$ is the over-determined and regularized primary transfer function to the near-source error sensors and $\underset{\sim}{\widehat{\mathbf{W}}}_v^{od}$ is the resulting weighting matrix. The concept of over-determination is investigated with the near-source sensor configuration shown in Figure 6.27. The obtained reductions at far-field sensor set 2 for the over-determined and regularized solution are shown in Figure 6.27. The performance of the over-determined near-source error sensor strategy is slightly better than the determined near-source sensor set. However, these small extra reductions in the performance response is at the expense of four additional sensors. This means that TSVD can be better used for regularization.

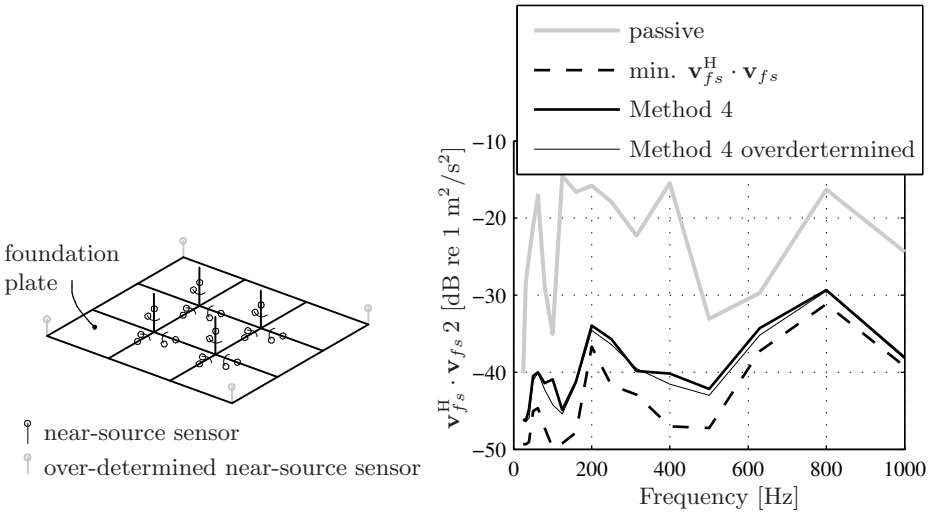

Figure 6.27: Overview of the active performance responses at far-field sensor set 2 for an over-determined near-source error sensor set.

6.3.5 Conclusions

In this section an alternative concept of near-source error sensor strategies was presented. This method, based on a weighting matrix of the near-source error sensors that is determined by the response of a chosen far-field performance sensor set, can be implemented in three different ways. Investigation of the robustness of this alternative concept of near-source error sensor strategies showed that the results are much better and the robustness is much greater compared to the concept of minimization of the transmitted power. For this reason, this alternative concept is investigated with measured FRFs on the laboratory setup in the next section.

6.4 Experiments

So far, the near-source error sensor strategies were studied on the numerical model of the laboratory setup. In this section, the near-source error sensor strategy with the weighting of a near-source sensor set based on a particular far-field sensor response is investigated with experiments on the laboratory setup. This error sensor strategy is more robust than the near-source error sensor strategy based on minimization of the transmitted power.

The procedure followed for the experiments is similar to the procedure used for the numerical simulations. However, instead of the numerically determined FRFs, the FRFs are now measured on the laboratory setup. The FRFs from the disturbance forces to the near-source error sensor set and the far-field performance sensor set are measured. The primary transfer matrices can then be composed for both sensor sets. In the same way, the FRFs from the ac-

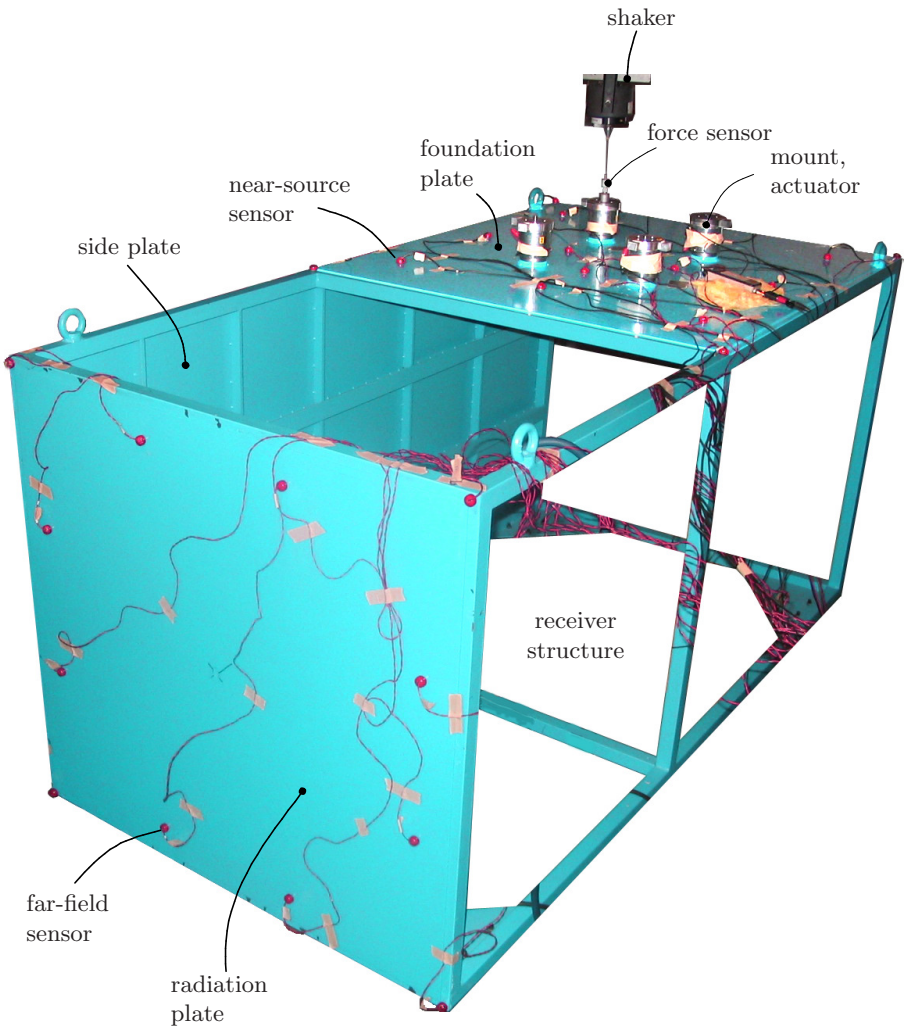

Figure 6.28: Photo of the laboratory setup at TNO.

tuators to both sensor sets are measured, after which the secondary transfer matrices can be composed. The measured transfer matrices are used to determine the active isolation performance off-line with the optimal control theory. This leads thus to the optimal performance that can be obtained theoretically with an ideal controller, as explained in section 2.6.1. The three different near-source error sensor strategies discussed in section 6.3 are applied, and the performance of each of these methods is determined with the measured transfer matrices. The controller is thus not implemented real-time and no real active experiments are performed, but only the primary and secondary transfer matrices are measured.

6.4.1 Experimental setup

The measurements were carried out on the laboratory setup described in chapter 4. The setup is shown in Figure 6.28. The foundation plate, side plate and radiation plate can be distinguished as characteristic components of the receiver structure. Furthermore, the following components are depicted:

- A *shaker* (B&K 4809) to apply the disturbance force in the translational directions at the top of each mount on the foundation plate.

- A *force sensor* (B&K 8200) to measure the force exerted on top of the mounts by the shaker. This sensor signal is used as reference signal to measure the primary transfer functions between the force input and responses at different parts of the receiver structure.

- *Actuators* (Motran IFX 30-100) to apply actuator forces for the determination of the secondary transfer functions (between the actuator forces and the responses at the receiver structure). A total of four actuators are mounted on the foundation plate. Each actuator is able to exert a force in the normal direction to the foundation plate. In contrast with the applied disturbance forces, the actuator forces cannot be measured directly because of the absence of a force sensor between the actuator and the receiver structure. However, the current from the amplifiers to the actuators can be measured and can be related directly to the actuator force by means of the motor constant (which is 10.1 N/A for the considered actuators). The measured current is used as reference signal for the determination of the secondary transfer functions.

- *Near-source sensors* to measure the response near the source. These sensors are accelerometers (Endevco 50) and used as error sensors in

the off-line calculation of the active response. The near-source sensors measure the normal accelerations at different locations of the foundation plate.

- *Far-field sensors* to measure the performance response in the far-field. These sensors are accelerometers (Endevco 50) and located at some distance from the mounts and are used as performance sensors for the off-line determination of the weighting matrix. Two far-field sensor sets have been used: 1) a far-field sensor set with 12 accelerometers on the radiation plate only and 2) a larger far-field sensor set consisting of 28 accelerometers on the radiation plate and the side plate.

The sensor signals were processed by a Bruël & Kjær (B&K) PULSE system with 29 measurement channels. One channel was reserved for the reference signal (the disturbance force or actuator force signal), so a maximum of 28 accelerometers could be used in each measurement simultaneously.

Measurement procedure

Two types of FRFs were measured: the FRFs for the primary transfer matrix (to determine the influence of the source) and the FRFs for the secondary transfer matrix (to determine the actuator influence). The source was represented by a force excitation on the top of the mounts (see Figure 6.28) in the three translational directions. This means that no moment excitations are taken into account, because these are difficult to apply and to measure. Hence, for the determination of the primary transfer matrix, 12 measurements must be performed. The secondary FRFs were determined by measuring the response at the accelerometers for each actuator excitation separately, implying that 4 measurements are needed. The measurements have been performed in two sessions:

- *Session 1*: The FRFs to both sensor sets (near-source and far-field) are measured in one setup for each disturbance force and actuator force separately.

- *Session 2*: Only an extended far-field sensor set is measured for each disturbance force and actuator force. For the determination of the transfer matrix to the near-source sensor sets, the measurement results of session 1 were used.

The advantage of the latter procedure is that a larger far-field sensor set can be measured (maximum 28 channels), and thus a more global measure of the

receiver response can be obtained. The disadvantage is that the 'coherence' between the near-source sensor set and far-field sensor set is less: the responses of each sensor set are determined in separate measurements and thus under different conditions.

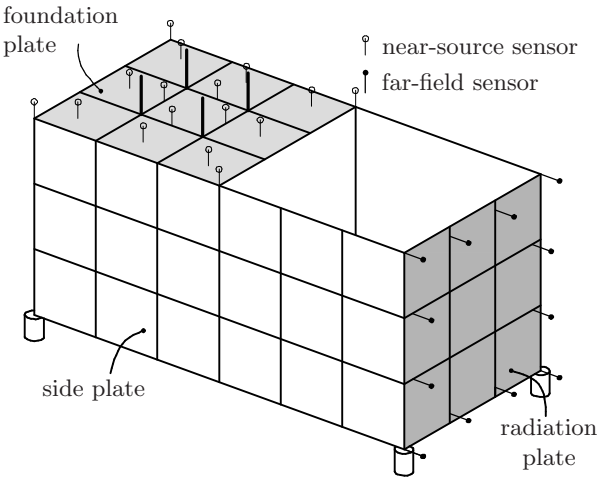

(a) Session 1

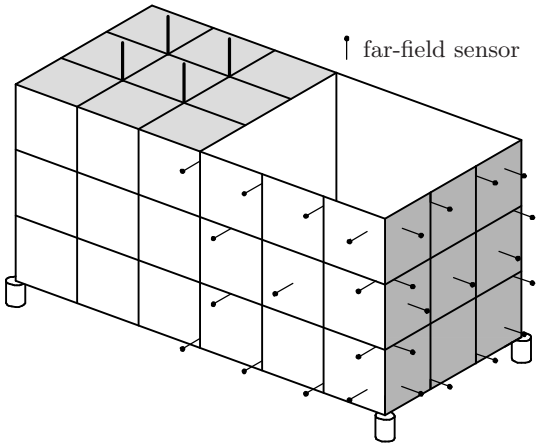

(b) Session 2

Figure 6.29: Schematic picture of the sensor sets of the two measurement sessions.

The sensor set of the first measurement session is shown in Figure 6.29(a). The number of independent disturbance forces is 12 (three in each translational direction at the top of the mounts). This means that at least 12 near-source

sensors have to be used for a reliable determination of the weighting matrix. Also, 4 extra near-source sensors were used for over-determination, resulting in a better conditioning of the FRF matrix from the disturbance forces to the near-source error sensors. This was shown in the previous subsection with the numerical simulations. Consequently, 12 sensors remain for the far-field performance sensor set. These far-field sensors are all located on the radiation plate.

The sensor set for the second measurement session is shown in Figure 6.29(b). During this measurement session only far-field sensors were used. The far-field sensor set consists of a total of 28 sensors: 15 sensors attached to the radiation plate and 13 sensors attached to the side plate. The sensor set on the radiation plate of the second measurement differs from the sensor set of the first measurement. The sensors at the corners of the radiation plate were translated a little the improve the response due to the excitation of the receiver structure.

The measurements were performed with a swept sine from 0 to 800 Hz. The sweep duration was 1 second and for the FRF estimation averaging over 60 signal blocks was used. Apart from the H_1 estimate of the FRF between the reference signal and accelerometers, the cross-spectra, auto-spectra and coherence were also determined. More information about the determination of the H_1 FRF estimate can be found in appendix G.

6.4.2 Measurement results

The measured FRFs are used to determine the optimal active performance off-line at the two considered far-field sensor sets (indicated by 1 and 2) by means of the optimal control theory. First, the performance of the unweighted near-source error sensor strategy is determined. The results are shown in Figure 6.30. Direct minimization of the near-source error sensors results in a poor performance with hardly any reduction at both far-field sensor sets. This tendency was also seen in the simulations. Besides the active performance for direct minimization of the near-source error sensors, also the optimal results are shown. These optimal results are obtained by using the far-field performance sensor sets as error sensor sets, resulting in a theoretical reduction of around 15 dB across the whole frequency range. Similar reductions were also shown in the simulations with the numerical models.

Next, the measured FRFs are used to compose the primary and secondary transfer matrices to the near-source and far-field sensor sets. The weighting matrices can subsequently be determined with these transfer matrices, in the same way as shown for the numerical simulations. First, the weighting procedure is considered taking into account both the primary and secondary FRFs,

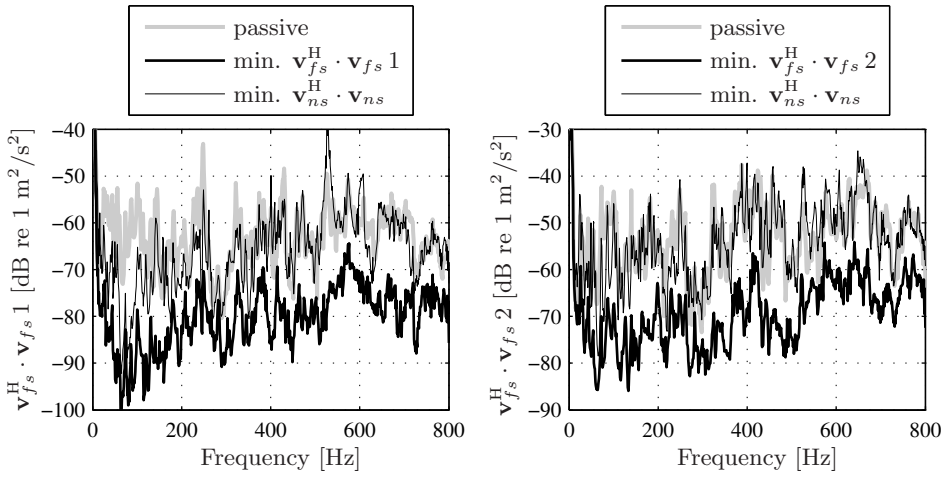

(a) far-field measurement 1 (b) far-field measurement 2

Figure 6.30: Active response with minimization of the unweighted near-source error sensor set at the two far-field sensor sets with the measured FRFs on the laboratory setup.

as was shown in equation (6.33) (method 1). When the weighting matrix is determined in this way, the actuator force vector that minimizes the weighted near-source error sensors can be determined. However, the 'real' FRFs are not known, so the same measured FRFs are used to determine the response at the far-field sensor sets. This means that the primary and secondary FRFs for the determination of the weighting matrix and the actual response are the same. This should give 'perfect' results, i.e. yield the same reduction as direct minimization of the far-field sensor set, because the weighting matrix is determined for the uncorrupted FRFs. This is indeed the case as shown in Figure 6.31.

Another way to determine a weighting matrix can be realized by using the primary transfers only, as shown in equation (6.34) (method 2). The results when the near-source error sensors are weighted with this weighting matrix are shown in Figure 6.32. To reduce the near-source sensor set in order to have a square and determined weighting matrix (12 sensors are needed for 12 disturbance forces), the four sensors at the corners of the foundation plate were omitted in the transfer matrices from the disturbance and actuator forces to the near-source error sensors (see also Figure 6.29(a)). For far-field sensor set 1, this weighting strategy results in considerably less performance than the

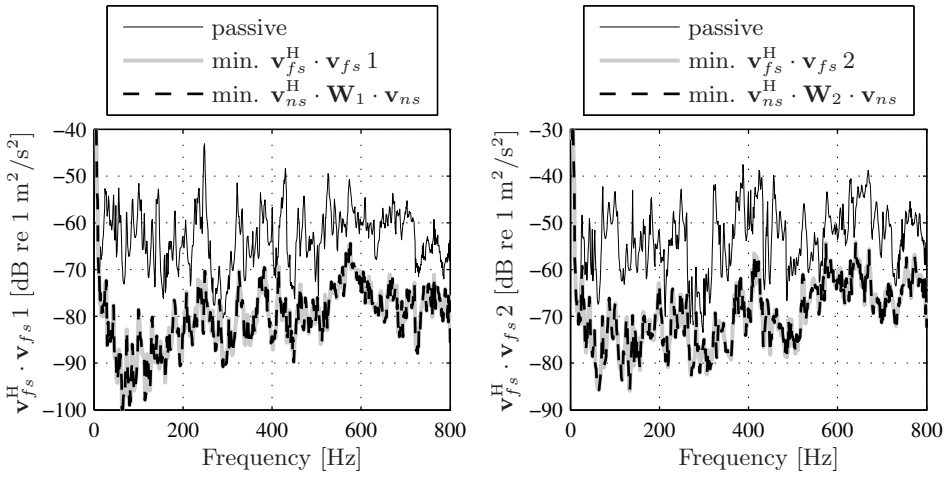

(a) far-field measurement 1 (b) far-field measurement 2

Figure 6.31: Active response at the two far-field sensor sets for the weighted near-source error sensor set determined with the measured FRFs on the laboratory setup. The weighting matrices are determined with a combination of primary and secondary FRFs ($\mathbf{W}_1$ and $\mathbf{W}_2$ respectively).

optimal result. However, reductions are still obtained and the performance is better than for minimization of the unweighted near-source sensors. In Figure 6.32(b) it can be seen that this near-source error strategy does not work for far-field sensor set 2. The performance is not better than for minimization of the unweighted error sensors. At just a few frequencies some reductions are observed, but increases also occur compared to the passive response occur. The reason for this is bad weighting: the weighting matrix $\mathbf{W}_v^d$ applied to the near-source error sensor response is not a good measure for the far-field sensor response. This is elucidated in Figure 6.33 for far-field sensor set 2. In Figure 6.33(a) the passive response of the far-field sensor set is shown as well as the passive near-source error sensor responses (indicated by $\mathbf{v}_{ns}^p$) is weighted with the weighting matrix $\mathbf{W}_2^d$ and with $\mathbf{W}_2$, respectively. It can be seen that the three results agree very well with each other, which means that both the weighting matrices function properly in order to obtain a good measure of the passive performance response in the far-field. So, the weighting matrix determined with the primary FRFs ($\mathbf{W}_2^d$) and determined with both the primary and secondary FRFs ($\mathbf{W}_2$) function well to represent the passive far-field response. Instead of weighting the passive near-source

error sensor response, also the active near-source error sensor response can be weighted. When the far-field sensor response is minimized, the corresponding active near-source sensor response can be determined and is indicated by $\mathbf{v}_{ns}^{a}$. This near-source error sensor response can subsequently be weighted to obtain a measure for the active far-field sensor response. The results are shown in Figure 6.33(b). It can be observed that the weighting matrix based on the primary FRFs only, $\mathbf{W}_2^d$, is not a good measure for the active far-field response, whereas the weighting matrix $\mathbf{W}_2$ also functions for the active situation. It can be concluded that the weighting matrix based on the primary FRFs only is not a good weighting matrix when the actuators influence the receiver structure, despite the fact that it functions well in the passive situation.

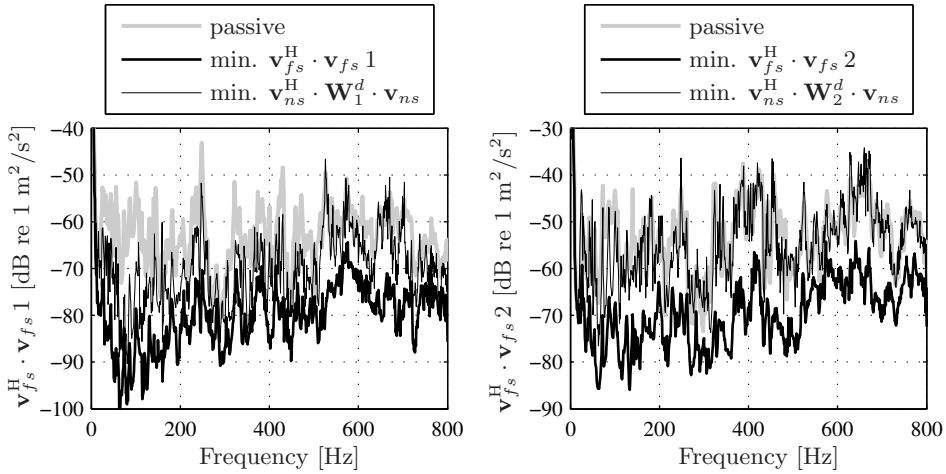

(a) far-field measurement 1 (b) far-field measurement 2

Figure 6.32: Active response at the two far-field sensor sets for the weighted near-source error sensor set determined with the measured FRFs on the laboratory setup. The weighting matrices are determined with the primary FRFs only ($\mathbf{W}_1^d$ and $\mathbf{W}_2^d$, respectively).

The procedure with a weighting matrix based on the primary FRFs can be functional when the near-source error sensor response is corrected for the influence of the actuators (method 3). This concept was described in section 6.3.2. In terms of the measured FRFs, the near-source error sensor response due to the disturbance only can be determined as in equation (6.36). However, in this situation the correction term that is subtracted (the 'off-line' determined secondary FRF) is the same as the real-time secondary FRF. In practice, there will be always a little discrepancy between these two FRFs, but in this situ-

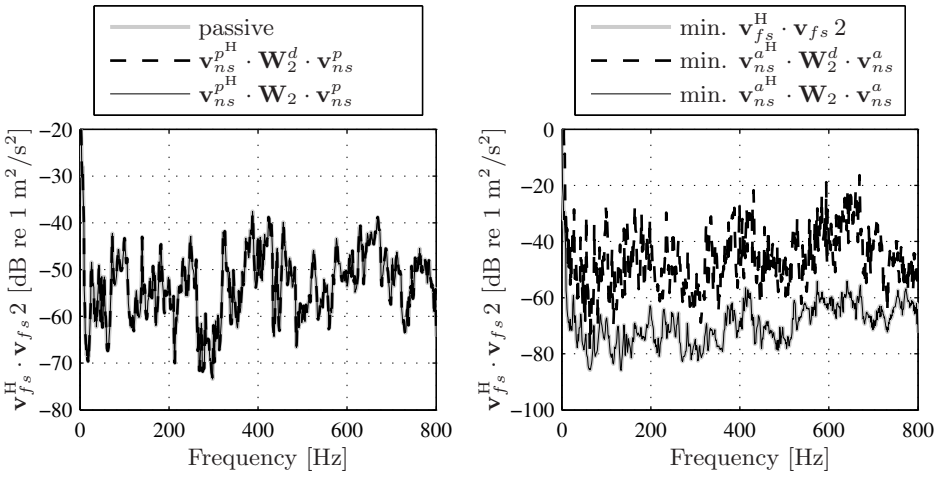

(a) far-field measurement 2 passive (b) far-field measurement 2 active

Figure 6.33: Response at far-field sensor set 2 on the laboratory setup determined by weighting of the passive near-source error sensor response (a) and determined by weighting of the active near-source error sensor response (b). The considered weighting matrices are determined with the primary FRFs only ($\mathbf{W}_2^d$) and with both the primary and secondary FRFs ($\mathbf{W}_2$).

ation only one secondary FRF is measured. The corrected near-source error sensor response is subsequently weighted with a weighting matrix based on the primary FRFs only as shown in equation (6.37). After that, the influence of the actuator forces on the far-field sensor response is taken into account as described by equation (6.38). This procedure is also used to determine the active response with the measured FRFs. When the near-source error sensor response is corrected for the actuator influence before the weighting $\mathbf{W}_v^d$ is applied, the obtained reductions appear to be similar to the reductions obtained with minimization of the far-field response itself.

Error sensitivity

It has been shown that the different near-source error criteria gave optimal results for the near-source error sensor strategies based on a weighting matrix procedure that eliminates the actuator influence. This was to be expected, because the FRFs that are used to determine the weighting matrices are the same FRFs that are used to determine the 'real-time' transfer to the receiver structure. This is never the case in a real application and the off-line measured

FRFs that are used for the weighting procedure will consequently always differ from the actual FRFs. The influence of these (small) differences between the off-line and real-time FRFs on the active performance is now investigated in more detail.

The weighting strategies of the near-source error sensors were applied to the two far-field sensor sets, as shown in Figure 6.29. These two sensor sets have 8 sensors in common, and are the so-called 8 joint sensors located on the radiation plate. The measurements were performed at different times; the time difference between the two measurement sessions was one day. This implies that the measured FRFs differ from each other and this can be seen in Figure 6.34. One mobility component is illustrated in this figure, namely the FRF from the actuator at mount 1 to one of the 8 joint sensors on the radiation plate. In Figure 6.34(a) the magnitude of this mobility component is depicted for the measurement on day 1 and on day 2. The differences in the magnitude are considerable for these two measurements, but the same tendencies can still be observed. The same conclusion can be drawn for the phase of the FRFs, as shown in Figure 6.34(b).

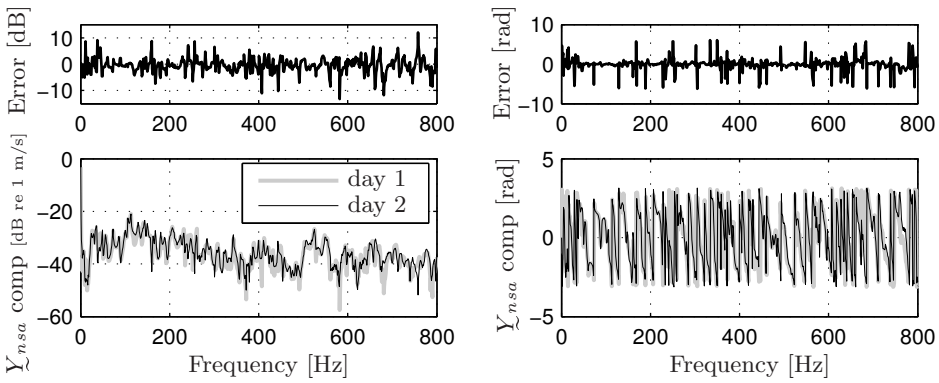

(a) magnitude (b) phase

Figure 6.34: The magnitude and phase of the secondary mobility component from the actuator at mount 1 to one of the far-field sensors on the radiation plate measured on day 1 and 2.

The dynamic properties of the considered laboratory setup apparently change with time. Hence, the weighting procedure must be quite robust to cope with such changes. The weighting matrix is based on off-line measurements and does not adapt to changes in the dynamic behavior of the structure after the off-line measurements. To investigate the robustness of the considered near-

source error sensor strategy, the weighting based on the 8 joint sensors of the far-field response of day 1 is applied as a weighting matrix on the near-source error sensor response of day 2. The weighting matrix is thus determined with the measured FRFs of day 1:

$$\mathbf{W}_v^1 = \underset{\sim}{\mathbf{Y}}_{fjda}^1 \cdot \underset{\sim}{\mathbf{Y}}_{nsda}^{1^+}, \tag{6.43}$$

where $\underset{\sim}{\mathbf{Y}}_{fjda}^1$ is the matrix with FRFs from both the disturbance and actuator forces to the 8 joint sensors on the radiation plate and where the measured FRFs on day 1 are indicated by a superscript $(.)^1$. The far-field sensor response on day 1 can consequently be determined according to:

$$\mathbf{v}_{fj}^1 = \mathbf{W}_v^1 \cdot \mathbf{v}_{ns}^1, \tag{6.44}$$

where $\mathbf{v}_{fj}^1$ is the far-field sensor response at the 8 joint sensors. The same procedure can be applied to the measurements on day 2, and the weighting matrix can be determined according to:

$$\mathbf{W}_v^2 = \underset{\sim}{\mathbf{Y}}_{fjda}^2 \cdot \underset{\sim}{\mathbf{Y}}_{nsda}^{1^+}, \tag{6.45}$$

where $\underset{\sim}{\mathbf{Y}}_{fjda}^2$ is the matrix with FRFs from both the disturbance and actuator forces to the 8 joint sensors on the radiation plate and the measured FRFs on day 2 are indicated by a superscript $(.)^2$. Notice that the secondary FRFs of day 1 are used, because only an extended far-field sensor set was measured on day 2. The weighting matrix $\mathbf{W}_v^1$ will differ from $\mathbf{W}_v^2$, due to the differences between the far-field FRFs $\underset{\sim}{\mathbf{Y}}_{fjda}^1$ and $\underset{\sim}{\mathbf{Y}}_{fjda}^2$. It was shown in the previous subsection that these weighting matrices function very well.

First, assume that the off-line measured weighting matrix is determined with the measurements of day 1, see equation (6.43). The next step is to calculate the optimal actuator force by minimization of the Hermitian quadratic form of equation (6.44). This actuator force vector is indicated by $\mathbf{f}_a^1$. The next step is to apply this actuator force vector on the measured FRFs on day 2 according to:

$$\mathbf{v}_{fj}^2 = \underset{\sim}{\mathbf{Y}}_{fjd}^2 \cdot \mathbf{f}_d + \mathbf{Y}_{fja}^2 \cdot \mathbf{f}_a^1, \tag{6.46}$$

where $\underset{\sim}{\mathbf{Y}}_{fjd}^2$ is the primary transfer to the joint far-field sensors measured on day 2 and $\underset{\sim}{\mathbf{Y}}_{fja}^2$ is the secondary transfer to the joint far-field sensors on day 2. These transfer matrices differ from the corresponding transfer matrices measured on day 1. However, for the considered applications, the near-source error sensor strategy should be robust enough to cope with these variations in the FRFs. The results for the far-field sensor response are shown in Figure 6.35. It can be seen that the weighting matrix $\mathbf{W}_v^1$, that worked perfectly for the

measured FRFs on day 1 as was shown in Figure 6.31 for the whole far-field sensor set, does not work at all when the FRFs differ slightly. In Figure 6.36 the active response at the far-field sensor set of day 2 is shown when the actuator force is determined with minimization of the far-field response with the FRFs measured on day 1. It can be observed that these results are the same as the results obtained with the use of the weighting matrix determined with the FRFs measured on day 1. This implies that the weighting procedure itself works, but the far-field response is sensitive to the actuator forces that are exerted on the receiver structure. The actuator forces that are able to reduce the far-field sensor response on day 1 are not able to reduce the far-field response on day 2.

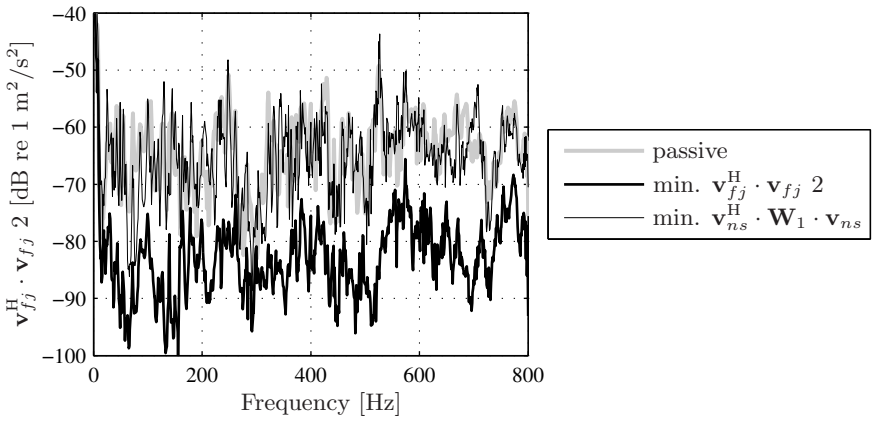

Figure 6.35: Active response with a weighting matrix determined with the FRFs measured on day 1 and applied on the actual FRFs measured on day 2.

6.5 Conclusions

Two basic concepts of near-source error sensor strategies were considered: minimization of the structural power injected into the receiver structure and weighting of a near-source error sensor set based on the off-line measured response of a performance sensor set desired to be minimized.

Concept 1: Minimization of power:
The minimization of the injected structural power was considered with the application of a weighting matrix to reduce the number of error sensors. This

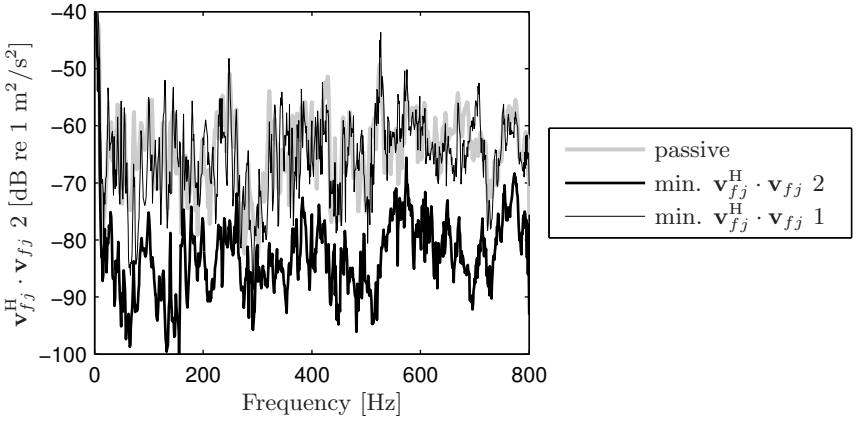

Figure 6.36: Active response with direct minimization of the far-field response of day 1 and applied on the actual FRFs measured on day 2.

means that only the velocities or the forces have to be measured at the connection points of the passive resilient mounting system with the receiver structure. The weighting matrix is a local mobility matrix of the receiver when the junction forces are measured or a local impedance matrix of the receiver when accelerometers are used. The advantage of this error sensor strategy is that with a reduced number of sensors (equal to the number of structural transmission paths of the mounting system) a global measure of the dynamic receiver response is obtained. It was shown that a good measure of the transmitted power is obtained when only a few of the power modes of the weighting matrix are used. The weighting matrix must be determined with off-line measurements, and contain for this reason small measurement errors (corrupted). The concept of power modes can be used to regularize the weighting matrix. However, this regularization is not very effective and no good reductions are obtained for the regularized corrupted weighting matrices when used as an error criterion for active isolation. This sensor strategy is very sensitive to small measurement errors in the responses and small measurement errors in the weighting matrices. In practice it is also not easy to measure the local mobility matrix, because the source has to be removed and accurate multi-directional mobility measurements are extremely demanding. This is a disadvantage for the practical applicability of this weighting procedure. For these reasons, and in particular because of the bad robustness, another approach

was introduced based on weighting of a near-source sensor set with a far-field approach.

Concept 2: weighting of a near-source sensor set based on a far-field response:
To obtain a possibly more robust near-source error sensor strategy, a concept was investigated based on the off-line measurement of a far-field performance sensor set. The response of the performance sensor set was used to determine a weighting matrix for the near-source error sensor strategy. When this weighting procedure is applied on the near-source error sensor response, the far-field response is 'virtually' measured. Two different approaches were studied to derive this weighting matrix: using both the primary and secondary FRFs to the near-source and far-field sensors and using the primary FRFs only. Simulations showed a more robust behavior in comparison with minimization of the injected structural power. The robustness of the concept with a weighting matrix based on the primary FRFs only can be improved by correcting the near-source error sensor response for the actuator influence and has a similar performance as when using a weighting matrix determined with both the primary and secondary transfer matrices. The concept with elimination of the actuator influence is preferred, because less near-source sensors are needed as when the weighting matrix approach based on the primary and secondary FRFs is used.

The main difference between the two concepts is that the concept of minimization of injected structural power results in global reduction of the receiver response. This is not easy to implement using the second concept, because it can only be obtained by a definition of a large performance sensor set. However, with a good choice of the performance sensor set reductions are obtained at locations where reductions are desired. It was shown in chapter 4 that minimization of the transmitted power does not necessarily mean that reduction is obtained at the desired locations. In particular, large reductions are obtained at locations with a large contribution to the kinetic energy, i.e. near the source. This disadvantage and also the expected lack of robustness have led to the decision not to use power minimization in the experimental part of this study. Instead, the second concept of near-source sensor weighting was used for the experiments on the laboratory setup.

To investigate the use of the second concept of near-source error sensor weighting on a real application, measurements have been performed on the laboratory setup. The measured FRFs were used to determine the weighting matrix and to calculate the active response off-line with the optimal control theory. It was shown that the weighting matrix has to be determined with

both the primary and secondary measured FRFs to obtain a good measure for the far-field response. When the weighting matrix was determined with the primary FRFs only, a correction of the near-source error sensor response had to be applied for the actuator influence. It was shown that the measured FRFs can change considerably: the response of some sensors of the far-field sensor set was measured on two different days and showed some difference. These differences are considered quite realistic and are therefore expected to be present in the considered applications for hybrid isolation. It was shown that these realistic variations in the FRFs have a large influence on the actual actuator forces and the reduction obtained. When the receiver structure behaves slightly differently than during the off-line measurements for the determination of the weighting matrix, that weighting matrix is no longer a representative measure of the far-field response. This makes the use of these off-line weighting techniques very doubtful for the considered applications of hybrid isolation. Therefore, the final conclusion of this chapter on near-source sensor strategies is that neither the injected power approach nor the approaches with off-line determined matrices are promising for active (hybrid) vibration isolation in complex vibrating structures.

Chapter 7

Conclusions and discussion

7.1 Conclusions

This thesis describes the development, validation and application of efficient analysis tools for hybrid isolation systems. Essentially, three major topics have been treated:

- A general theoretical concept for modeling hybrid isolation systems. This concept has been illustrated with two applications.
- A numerical modeling tool for rubber vibration isolators.
- The concept of using near-source error sensors.

The analysis tools can be used for many kinds of hybrid isolation applications. The application considered in more detail in this thesis is the hybrid mounting of machinery in vehicles and ships. The conclusions arising from each topic are discussed in more detail below.

7.1.1 Models of hybrid isolation systems

A general model was presented to describe hybrid isolation systems with a source, a resilient multi-point and multi-directional hybrid mounting system and a receiver structure. The model allows the use of all types of representations of linear dynamic behavior. Mobility or impedance matrices can be determined by measurements or can be calculated with analytical or numerical models. The active isolation part is described by a set of external actuator forces, which are obtained with the optimal control theory and act on the receiver structure at the connections of the mounts with the receiver.

The actuator forces are determined with optimal control by minimization of a Hermitian quadratic error function. The resulting numerical tools enable the user to perform simulation studies, for example to investigate different types of error sensor strategies. Besides structural response error criteria, like minimization of forces and velocities of the receiver structure, acoustic error criteria have also been considered, namely the free field radiation and the acoustic radiation of a part of the receiver structure into an enclosure.

The general concept was used to analyze two applications of hybrid isolation. First, a relatively simple isolation system was analyzed, where a rigid source is hybridly isolated from a simply supported receiver plate. The dynamics of the subsystems were described analytically. From the analysis of this model, the following conclusions can be drawn:

- When the mobilities of the receiver structure are determined with a modal expansion technique it is important to take residual modes into account. Otherwise the error caused by the modal truncation will be considerable for the driving point mobilities (see section 3.2.3).

- A good global reduction of the whole receiver response can be obtained with just one actuator per mount, whereas the vibration transmission occurs in several more DOFs. A good reduction of the radiated sound power is also obtained (see section 3.4).

- Minimization of the transmitted power works well and yields a global reduction of the receiver plate vibrations. However, all directions of the vibration transmission into the receiver structure have to be taken into account. When, for example, the transmitted power in only one direction is measured for active control, power circulation via other directions is overlooked. This phenomenon was observed especially in the low frequency region (see section 3.4.1).

- Error sensor strategies that directly minimize the velocities, forces or a weighted combination of these two at the junctions between the mounts and the receiver, also yield a global reduction of the receiver plate response (see section 3.4.1).

The second system that has been considered is a FEM model of a laboratory setup with a dynamic behavior that is quite complex and representative for ship-like structures. This was demonstrated by showing the high number of modes in the frequency range of the simulations, the high modal overlap and the multi-directional nature of the structural power transmission via the mounts. In the first place, the actuator configuration was considered:

- The receiver response can be actively controlled with a reduced number of actuators. SVD analysis shows that only a few field shapes with corresponding source shapes have a large contribution to the response of the error sensor set. The actuators minimize the most efficient field shapes in the first place. With an SVD analysis of the primary path it can be shown that the number of actuators is an indication of the number of field shape participations that can be effectively reduced (see section 4.5.1).

- An important point of attention, besides the obtained reduction of the error sensor response, is the actuator effort that is needed to obtain the reduction. Increasing the number of actuators above a certain number may still provide extra reduction of the error sensor response, but may also result in a disproportional increase of the actuator effort (see section 4.5.1).

- When a large number of actuators is used, weighting of the actuator forces may be used as part of the control strategy to prevent that the actuator forces become disproportionately large. Although the weighting procedure results in a decrease of the actuator effort, the performance also decreases and becomes comparable with the performance obtained with a reduced set of actuators, which is more cost-effective. The optimum number of actuators is therefore a trade-off between the obtained reduction and the actuator effort. The optimal solution to this trade-off can be investigated in two ways. The first way is to make an actuator effort analysis (by investigating the active response for different amount of actuator weighting). Another way is using the SVD analysis and investigating the reduction in terms of participations of the primary field shapes. When increasing the number of actuators gives no extra reduction of the most efficient field shapes contributing to the active response, the influence of the extra actuators is not (cost-)effective (see sections 4.5.1 and 4.5.2).

- The SVD analysis of the secondary path provides information on the most efficient actuator directions by considering the contribution of each actuator direction to the most dominant field shapes (see section 4.5.3).

Subsequently, attention was paid to the sensor configuration, leading to the following conclusions:

- Actuators located near the vibration source are able to reduce the vibrational and acoustic responses well at locations far from the source (see

section 4.6).

- The use of a global measure of the receiver response for active isolation, like minimization of the kinetic energy or the transmitted power, has the advantage that a global reduction of the receiver response is obtained. This prevents the increase of the active response at certain locations of the receiver structure in comparison with the passive response. A disadvantage is that these types of error criteria try to minimize the largest responses, which implies that the largest reduction is obtained near the source of excitation. This is often not desirable, because in some cases reduction is desired at some distance from the source of vibrations, e.g. in the passenger accommodations in a ship rather than in the engine room. Minimization of the response of a structural error sensor set attached to the receiver structure results in a good reduction of the error sensor response itself, but an increase of the response may occur at other locations (see section 4.6.1).

- Good reductions of acoustic cost functions can be established with active isolation techniques. Using cost functions for structural vibrations results, generally speaking, in less reduction of the acoustic response (like the radiated sound power or acoustic potential energy in a receiver enclosure), than using an acoustic cost function. However, the use of such structural cost functions will also result in reduction of the acoustic response. In particular it was shown that minimization of transmitted power results in a decrease of acoustic responses in the low frequency range (see section 4.7).

- The performance achieved for active isolation with minimization of the forces or velocities at the connection points of the mounting system with the receiver structure is, in contrast with the simple and analytically described isolation system in chapter 3, very poor for the considered configuration. The multi-directional vibration transmission from the source to the receiver structure in combination with a dynamically complex behavior of the receiver structure makes the straightforward use of this kind of error criteria not suited to obtain reductions at a distance from the source (see section 4.6).

7.1.2 Numerical models of passive rubber vibration isolators

For the actual implementation of the concept of hybrid isolation, a hybrid mount has to be designed. This mount consists of passive vibration isola-

tor(s), actuator(s) and, when useful, integrated sensors. An important point to consider and the first step with respect to the design, is the isolation characterization of the passive vibration isolator.

The isolation characterization was determined by calculating the dynamic stiffness matrix of the isolator. Finite element models were used to determine the stiffness matrices, taking into account the effect of a pre-deformation. With the developed tool the multi-directional stiffnesses of rubber vibration isolators with complex geometries can be calculated. Two effects were taken into account: the influence of the dynamic excitation and the pre-deformation.

- The dynamic excitation causes wave effects in the rubber material of the isolator. These wave effects cause an increase in the dynamic stiffness, even to such an extent that the stiffness may increase by a factor 20 compared to the static stiffness. This means that the stiffness of the isolator is much larger at certain frequencies than expected from the static stiffness.

- The static pre-deformation of the isolator causes a change of the material behavior and a change of shape of the isolator. The effects of these changes on the dynamic stiffness are less pronounced than those of the wave effects, but may still result in an increase in the dynamic stiffness of about a factor 2 at some frequencies.

The most important requirement for obtaining a reliable numerical model of a rubber isolator is a correct material description of the rubber material. Because proper data are often lacking, a procedure has been presented to determine the material parameters with the help of measurements of the whole vibration isolator. The resulting rubber parameters can be used to determine the isolation characteristics in other directions than the directions that can be measured. Also the isolation behavior of different configurations (like other geometries) and pre-deformations can be determined in a numerical way when the material parameters are known. A static force-displacement measurement is performed to determine the static material parameters and a dynamic transfer stiffness measurement is performed to determine the dynamic material parameters. This procedure was demonstrated for measurements on a silica-reinforced rubber vibration isolator.

7.1.3 Near-source error sensor strategies

The last topic studied in this thesis is the use of near-source error sensor strategies. The positioning of the error sensors near the source has several

advantages with respect to the concept of positioning the sensors far away, e.g. in the receiver enclosures. The advantages are easier implementation for the considered applications of hybrid isolation, the possibility to define a global cost function of the receiver response and less influence of flanking paths and measurement noise on the error sensors. Two approaches were considered: minimization of the injected power into the receiver structure and minimization of a near-source error sensor strategy weighted with an off-line measured 'transmission path matrix' between the near-source error sensors and the far-field performance sensor set response.

A disadvantage of the approach based on the minimization of the injected structural power to the receiver structure is that both the multi-directional velocities and forces have to be measured at the mount connection points. This can be circumvented by introduction of an off-line measured weighting matrix, so that only the forces or velocities have to be taken into account for the error criterion. However, error analyses showed that the robustness of this error sensor strategy is very poor.

For this reason, a second approach was introduced based on a weighting matrix determined with an off-line measured far-field performance sensor set response. This approach worked very well for the ideal situation without errors in the weighting matrix. Two concepts were proposed to determine the weighting matrix. One uses both the primary and secondary FRFs and the other uses only the primary FRFs. The error analyses showed that the first method of determining the weighting matrix, thus with using both the primary and secondary FRFs, is more robust. However, the robustness with a weighting matrix determined with the primary FRFs only can be improved by subtraction of the actuator contribution from the near-source sensor response before the weighting is applied. This correction was performed with the use of the off-line measured secondary FRFs.

The second approach of near-source error sensor weighting with a weighting matrix determined with a far-field performance sensor response, showed a more robust behavior for errors in the weighting matrix in comparison with the approach based on minimization of the transmitted power. For this reason this concept was used to determine a weighting matrix with measured FRFs on the laboratory setup. The results of the measurements show that a correct weighting matrix can only be derived when both the primary and secondary FRFs are taken into account for the determination of the weighting matrix. Otherwise, when only the primary FRFs are taken into account, the near-source error sensor response must be corrected with the actuator influence before the weighting. However, from the measurements it appeared that the

FRFs may change in time, resulting in a poor performance of the weighting matrices. It showed that the active performance is very sensitive to small changes in the actuator forces. For this reason it is not possible to use this kind of off-line weighting techniques for the considered applications.

7.2 Discussion

An important conclusion is that hybrid isolation functions; considerable reductions of the (far-field) error sensor response at the receiver structure can be obtained with hybrid isolation. However, this conclusion is not new and has been shown in earlier model studies (e.g. [40, 41]) and even practical applications have already been shown to work (e.g. [80]).

In contrast with the more academic models in the literature, the model presented in chapter 4 is suitable for and applicable in the hybrid isolation of machinery in vehicles. This model has been used to derive some new rules of thumb with respect to the design of the actuator configuration. It was shown that it is possible to determine the optimal number of actuators by considering both the obtained active reductions and the actuator effort by using models based on mobility matrices only (the only information that can be obtained for most practical applications). It was also shown that information about the effective excitation directions of the actuators can be obtained from the mobility matrices that describe the error sensor response due to the actuators only.

Also the design of sensor configurations and in particular near-source error sensor strategies was an important research objective. The concept of near-source error sensors studied in the literature is based on the minimization of the transmitted power (e.g. [41, 100]). In this thesis a new concept was introduced by measuring the transmitted power using a weighting matrix. However, analyses showed that this concept is not robust enough to be applied in the considered applications. Another new concept of near-source error sensor weighting has been presented that is based on an off-line measured performance response. Simulation results showed a more robust behavior for this near-source error sensor strategy than the minimization of the transmitted power. However, analyses with real measurement data on a representative laboratory setup showed that this concept is also not sufficiently robust.

The practical implementation of the passive part of the hybrid isolation systems is a different subject of study. In this study the numerical modeling of rubber vibration isolators was considered. The concept of using (numerical) models to characterize isolators is not new (see e.g. [67]), but obtaining a

multi-directional isolation characterization with the goal to use it in combination with active isolation is a new concept. It was shown that a good multi-directional characterization of the passive vibration isolator can be obtained. In combination with the method presented to obtain the rubber material properties by updating a numerical model with measurement data of the rubber isolator, the presented tools are very useful and needed in the first step in the design process of a hybrid mounting system.

The use of near-source sensors with off-line determined weighting matrices is not promising for further study. The use of far-field sensors is much more relevant. Furthermore, attention must be paid to the integration of the active isolation and the passive isolation, meaning a good 'hybrid' design of the passive isolation system in combination with the application of actuators. The tools used in chapter 5 can be used for this purpose. The passive isolation system must dynamically decouple the different directions of vibration transmission. Some stiff directions must still be present to meet the static requirements and stability, but the actuators can be located in these directions to obtain the dynamic decoupling in an active way. This kind of hybrid components can be investigated in more detail with the tools described in chapter 2 and chapter 4 to analyze different sensor strategies. In practice it is difficult to obtain a global measure of the receiver response with far-field sensors. For this reason, the sensor configuration is an important point of attention and especially the effect of the local vibration or noise control on the global response of the receiver response must be analyzed. Also, the application of unweighted near-source error sensor might work more effectively when the structure-borne sound transmission is directed by just a few dominant transmission paths when the hybrid mounting is designed as described. When local error sensors are located in the few most stiff directions, the influence of the actuators can be considered as a active stiffness reduction for these dominant directions. A similar approach has been used by Nijsse, Super, van Dijk and Jonker [95] on a six degrees of freedom vibration isolation setup and good active reductions could be obtained. Using such an approach, reduction might be obtained with just a few actuators and local near-source sensors and the concept of hybrid isolation can be applied successfully in practical applications where the interior noise levels are dominated by the source that is to be hybridly isolated.

Nomenclature

General

Roman

$\mathbf{B}$	Left Cauchy Green tensor	
c	Viscous damping coefficient	[Ns/m]
c_0	Mean propagation speed of sound	[m/s]
C_l	Wave speed in longitudinal direction of the plate	[m/s]
C_s	Wave speed in shear direction of the plate	[m/s]
$\mathbf{C}$	Viscous damping matrix	
$\mathbf{C}$	Right Cauchy Green tensor	
e	Error signal	
E	Young's modulus	[N/m^2]
E'	Real part of the Young's modulus	[N/m^2]
E''	Imaginary part of the Young's modulus	[N/m^2]
E_{dis}	Dissipated energy	[J]
E_{in}	Energy input	[J]
E_{kin}	Kinetic energy	[J]
E_p	Acoustic potential energy	[J]
E_{pot}	Potential energy	[J]
$\mathbf{F}$	Deformation gradient tensor	
f_a	Actuator force	[N]
f_a^{opt}	Optimal actuator force	[N]
f_i	Filter factor i	[-]
$\mathbf{f}$	Force vector	[N]
$\mathbf{f}_a$	Actuator force vector	[N]
$\mathbf{f}_d$	Disturbance force vector	[N]
$\mathbf{f}_{da}$	Combined disturbance and actuator force vector	[N]

$\mathbf{f}_m$	Total force vector at junctions of mounts	[N]
$\mathbf{f}_{mr}$	Total force vector of mounts at source junctions	[N]
$\mathbf{f}_{ms}$	Total force vector of mounts at receiver junctions	[N]
$\mathbf{f}_r$	Total force vector at receiver junctions	[N]
$\mathbf{f}_s$	Total force vector at source junctions	[N]
$\mathbf{f}_z^g$	Generalized force	[N]
$g(\vec{r}\|\vec{r}_0)$	Green's free space function	[1/m]
G	Shear modulus	[N/m^2]
G_0	Initial shear modulus	[N/m^2]
$G(\vec{r}\|\vec{r}_0)$	Green's function for radiation into enclosure	[1/m]
h	Height or thickness	[m]
$\mathbf{H}_p$	Primary transfer matrix	
$\mathbf{H}_p^{fr}$	Primary transfer matrix to forces at receiver junctions	
$\mathbf{H}_p^{fs}$	Primary transfer matrix to forces at source junctions	
$\mathbf{H}_p^{fv}$	Primary transfer matrix to source and receiver junctions	
$\mathbf{H}_p^{vr}$	Primary transfer matrix to velocities at receiver junctions	
$\mathbf{H}_p^{vs}$	Primary transfer matrix to velocities at source junctions	
$\mathbf{H}_s$	Secondary transfer matrix	
$\mathbf{H}_s^{fr}$	Secondary transfer matrix to forces at the receiver junctions	
$\mathbf{H}_s^{fs}$	Secondary transfer matrix to forces at the source junctions	
$\mathbf{H}_s^{fv}$	Secondary transfer matrix to source and receiver junctions	
$\mathbf{H}_s^{vr}$	Secondary transfer matrix to velocities at receiver junctions	
$\mathbf{H}_s^{vs}$	Secondary transfer matrix to velocities at source junctions	
I	Area moment of inertia	[m^4]
I_{mp}	mass polar moment of inertia per unit length	[kgm]
$\bar{I}_n$	Time-averaged sound intensity in the normal direction	[W/m^2]
J	Cost function or Hermitian quadratic error criterion	
J	Polar moment of inertia of cross-sectional area	[m^4]
k	Acoustic wave number ($= \omega/c_0$)	[1/m]
k	Spring stiffness	[N/m]
k_0	Initial bulk modulus	[N/m^2]
k_l	Longitudinal wave number	[-]
k_s	Shear form factor	[1/m]
k_t	Torsional wave number	[1/m]
$\mathbf{k}_{11}$	Blocked dynamic driving point stiffness matrix junction 1	
$\mathbf{k}_{12}$	Blocked dynamic transfer stiffness matrix junction 1 and 2	
$\mathbf{k}_{21}$	Blocked dynamic transfer stiffness matrix junction 2 and 1	
$\mathbf{k}_{22}$	Blocked dynamic driving point stiffness matrix junction 2	
$\mathbf{K}$	Structural stiffness matrix	

$\mathbf{K}_f$	Acoustic stiffness matrix	
L_w	Sound Power Level	[dB]
L_x	Length in x-direction	[m]
L_y	Length in y-direction	[m]
L_z	Length in z-direction	[m]
m	Discrete mass	[kg]
m	Moment	[Nm]
$\mathbf{M}$	Structural mass matrix	
$\mathbf{M}_f$	Acoustic mass matrix	
$N(\omega)$	Total number of modes below the radial frequency ω	[-]
p	Acoustic pressure	[Pa]
$\mathbf{p}_f$	Acoustic pressure vector at field points	[Pa]
P_t	Transmitted structural power	[W]
q	Volume velocity	[m^3/s]
q_i	Modal participation of the i^{th} mode	[-]
$\mathbf{q}$	Vector with modal participations	[-]
$\mathbf{Q}$	Matrix with modal participations	
$\vec{r}$	Vector from source point to field point	[m]
R	Distance between the source point and field point	[m]
$\mathbf{R}$	Acoustic radiation resistance matrix	
S	Surface domain	[m^2]
s_i	i^{th} singular value	
$\mathbf{S}$	Diagonal matrix with singular values in decreasing order	
t	Time	[s]
$\mathbf{T}$	General filter or transformation matrix	
$\mathbf{T}_{ar}$	Actuator transformation matrix at the receiver side	
$\mathbf{T}_{as}$	Actuator transformation matrix at the source side	
$\mathbf{T}_m$	Transformation matrix of the mounting system	
$\mathbf{T}_r$	Transformation matrix of the receiver	
$\mathbf{T}_s$	Transformation matrix of the source	
U	Strain energy function	[J]
$\mathbf{u}_i$	i^{th} left singular vector	
$\mathbf{U}$	Matrix with the left singular vectors	
v	Structural velocity	[m/s]
v_n	Structural normal velocity	[m/s]
$\mathbf{v}$	Structural velocity vector	[m/s]
$\mathbf{v}_i$	i^{th} right singular vector	
$\mathbf{v}_{fs}$	Far-field sensor velocity response	[m/s]
$\mathbf{v}_n$	Structural normal velocity vector	[m/s]

$\mathbf{v}_m$	Total velocity vector at the mount junctions	[m/s]
$\mathbf{v}_{mr}$	Total velocity vector of the mounts at the receiver junctions	[m/s]
$\mathbf{v}_{ms}$	Total velocity vector of the mounts at the source junctions	[m/s]
$\mathbf{v}_{ns}$	Near-source sensor velocity response	[m/s]
$\mathbf{v}_r$	Total velocity vector at the receiver junctions	[m/s]
$\mathbf{v}_s$	Total velocity vector at the source junctions	[m/s]
$\mathbf{v}_{sr}$	Velocity vector of a structural sensor set	[m/s]
V	Volume domain	[m^3]
$\mathbf{V}$	Matrix with the right singular vectors	
w	Structural displacement	[m]
$\bar{W}$	Time-averaged radiated sound power	[W]
$\mathbf{W}$	Weighting matrix for quadratic near-source error response	
$\mathbf{W}_a$	Actuator weighting matrix	
$\mathbf{W}^d$	Weighting matrix $\mathbf{W}$ based on primary FRFs only	
$\mathbf{W}_v$	Weighting matrix for near-source error velocity sensors	
$\mathbf{W}_v^d$	Weighting matrix $\mathbf{W}_v$ based on primary FRFs only	
$\mathbf{W}_v^{od}$	Weighting matrix $\mathbf{W}_v$ for over-determined near-source sensor set	
x	Structural displacement	[m]
$\mathbf{x}$	Structural displacement vector	[m]
Y	Mobility	[m/Ns]
$\mathbf{Y}_r$	Mobility matrix of the receiver	
$\mathbf{Y}_{fsa}$	Mobility matrix from $\mathbf{f}_a$ to far-field sensors	
$\mathbf{Y}_{fsd}$	Mobility matrix from $\mathbf{f}_d$ to far-field sensors	
$\mathbf{Y}_{fsda}$	Combined mobility matrix from $\mathbf{f}_d$ and $\mathbf{f}_a$ to far-field sensors	
$\mathbf{Y}_{nsa}$	Mobility matrix from $\mathbf{f}_a$ to near-source sensors	
$\mathbf{Y}_{nsd}$	Mobility matrix from $\mathbf{f}_d$ to near-source sensors	
$\mathbf{Y}_{nsda}$	Combined mobility matrix from $\mathbf{f}_d$ and $\mathbf{f}_a$ to near-source sensors	
$\mathbf{Y}_{sd}$	Mobility matrix of the source related with $\mathbf{f}_d$	
$\mathbf{Y}_{sr}$	Mobility matrix from receiver forces to a structural sensor set	
$\mathbf{Y}_{ss}$	Mobility matrix of the source related with $\mathbf{f}_s$	
z	Impedance	[Ns/m]
$\mathbf{Z}_f$	Acoustic impedance matrix for free field radiation	
$\mathbf{Z}_{rr}$	Driving point impedance matrix of the mounts (receiver side)	
$\mathbf{Z}_{rs}$	Transfer impedance matrix of the mounts	
$\mathbf{Z}_{sr}$	Transfer impedance matrix of the mounts	
$\mathbf{Z}_{ss}$	Driving point impedance matrix of the mounts (source side)	

Greek

β	Shear angle of cross-section during bending beam	[rad]
η	Structural loss factor	[-]
η_n	Ad hoc modal damping coefficient	[-]
θ	Angle of rotation	[rad]
λ	Stretch ratio	[-]
Λ_n	modal volume of n^{th} mode shape	
ν	Poisson's ratio	[-]
$\mathbf{\Xi}_m$	Modal damping matrix	
ρ	Structural density	[kg/m^3]
ρ_0	Mean density of fluid	[kg/m^3]
$\varphi_n(x, y)$	Function of n^{th} structural mode	
$\mathbf{\Phi}$	Matrix with modal vectors	
$\psi_n(\vec{r})$	n^{th} Acoustic eigenfunction	[Pa]
ψ	Slope of the deflection curve of a beam without shear effect	[rad]
$\boldsymbol{\psi}$	n^{th} Acoustic mode shape vector	[Pa]
ω	Angular frequency ($= 2\pi f$)	[rad/s]
ω_n	n^{th} angular eigenfrequency	[rad/s]
$\mathbf{\Omega}$	Diagonal matrix with angular eigenfrequencies	

Mathematical

$\mathcal{B} \rightarrow \mathcal{S}$	Deformation from reference config. $\mathcal{B}$ to current config. $\mathcal{S}$
$\cdot$	Inner product, first order contraction
$\mathbf{A}^{-1}$	Inverse of matrix $\mathbf{A}$
$\mathbf{A}^{+}$	Pseudo-inverse of matrix $\mathbf{A}$
$\mathbf{x}^{\mathrm{H}}$	Hermitian of vector $\mathbf{x}$ (complex conjugated transposed)
$\mathbf{x}^{\mathrm{T}}$	Transpose of vector $\mathbf{x}$
$\mathrm{j} = \sqrt{-1}$	Imaginary unit
$\mathbf{I}$	Identity matrix
$\vec{\nabla}$	Gradient operator
Σ	Summation
∇^2	Differential operator
$\Re(\ )$	Real part
$\Im(\ )$	Imaginary part

x^*	Complex conjugate of x
$\dot{\mathbf{x}}$	Time derivative of $\mathbf{x}$
$\underset{\sim}{\mathbf{x}}$	Measured or disturbed $\mathbf{x}$
$\widehat{\mathbf{X}}$	Regularized or reduced reconstruction of $\mathbf{X}$

Abbreviations

ASAC	Active Structural Acoustic Control
AVC	Active Vibration Control
BEM	Boundary Element Method
DMA	Dynamic Mechanical Analyzer
DMTA	Dynamic Mechanical Thermal Analyzer
IRHD	International Rubber Hardness Degrees
DOF(s)	Degree(s) Of Freedom
DSM	Dynamic Stiffness Matrix
DSP	Digital Signal Processing
FEM	Finite Element Method
MIMO	Multiple Input, Multiple Output
NR	Natural Rubber
phr	Part per hundred rubber
SEA	Statistical Energy Analysis
SISO	Single Input, Single Output
SMR	Standardized Malaysian Rubber
SPL	Sound Pressure Level
SVD	Singular Value Decomposition
TSVD	Truncated Singular Value Decomposition
WLF	William-Landel-Ferry equation

Appendix A

Energy analysis of a one-DOF oscillator

An important error criterion for active isolation is the transmitted power in a structure. The transmitted power represents the energy flow that is caused by the dissipation mechanisms in the receiver structure. These dissipation mechanisms are the structural damping in the receiver and the damping caused by the fluid-structure interaction of the receiver with the surrounding environment. The fluid-structure interaction causes noise, that is quantified as the radiated sound power. To explain the physical meaning of the cost function that minimizes transmitted power, the energy contents of a simple one-degree-of-freedom oscillator will be analyzed in more detail, see Figure A.1(a).

When it is assumed that the oscillator is excited by a harmonic force $f(\cos\omega t + \mathrm{j}\sin\omega t)$ the displacement is given by:

$$x = \frac{f\left(\cos\omega t + \mathrm{j}\sin\omega t\right)}{-m\omega^2 + \mathrm{j}\omega c + k}. \tag{A.1}$$

The considered system is nonconservative, which means that energy is dissipated within the system. In that case the total energy of the system is subdivided into four separate contributions: the kinetic energy E_{kin}, the potential energy E_{pot}, the dissipated energy E_{dis} and the energy input E_{in}. The relation between these energies is determined by [85]:

$$\frac{d}{dt}(E_{kin} + E_{pot}) = f_{nc}\dot{x}, \tag{A.2}$$

which states that the rate of work performed by the nonconservative force f_{nc} is equal to the rate of change of the systems total energy. The energy contents

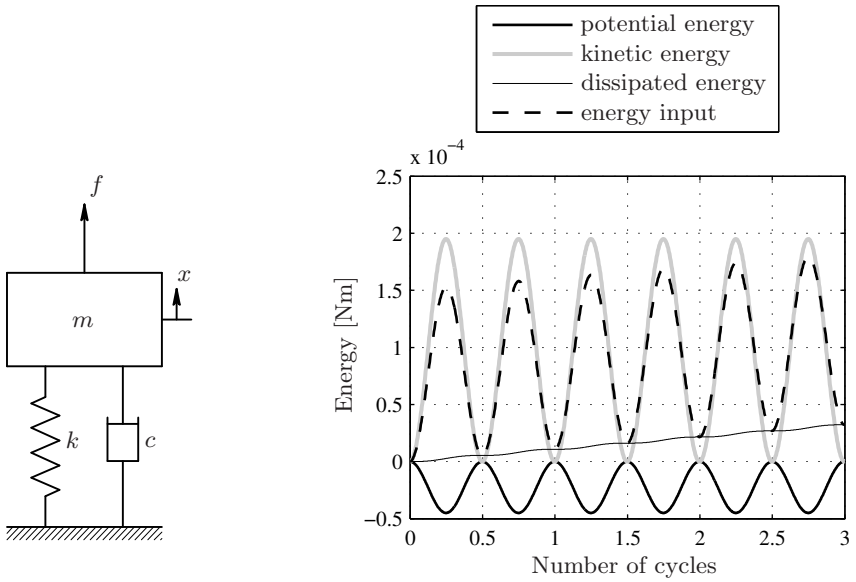

(a) (b)

Figure A.1: Energy contributions as a function of the time for a one-DOF oscillator: the potential energy, the kinetic energy, the dissipated energy and the energy input.

on time t are determined by:

$$E_{kin} = \int_0^t m\,\Re(\ddot{x})\Re(\dot{x})\,\mathrm{d}t \qquad E_{pot} = \int_0^t k\,\Re(x)\Re(\dot{x})\,\mathrm{d}t, \tag{A.3}$$

$$E_{dis} = \int_0^t c\,\Re(\dot{x})\Re(\dot{x})\,\mathrm{d}t \qquad E_{in} = \int_0^t F\cos\omega t\,\Re(\dot{x})\,\mathrm{d}t. \tag{A.4}$$

The energies are depicted in Figure A.1(b) for three vibration cycles, when the oscillator is excited with a frequency equal to twice the eigenfrequency of the undamped system. It is seen that the mean value of conservative energies E_{kin} and E_{pot} does not change, while the mean level of the energy input E_{in} and dissipated energy E_{dis} oscillates with an increasing linear mean value in time. Integration of equation (A.2) for $t = 0$ to $t = t$ yields:

$$E_{kin} + E_{pot} = E_{in} - E_{dis}, \tag{A.5}$$

which states that the total energy on time t is equal to the net energy transport into the system. In Figure A.2 this is shown for the oscillator. From

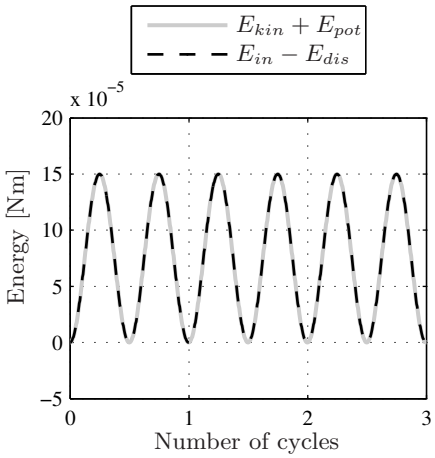

Figure A.2: The total energy $E_{kin} + E_{pot}$ as function of the time and the net energy input for the one-DOF oscillator.

Figure A.1(b) it can be seen that after one period the dissipated energy level is the same as the energy input by the force. The amplitude of the harmonic transmitted power is thus equal to the dissipated energy. This means that minimization of the transmitted power reduces the rate of change of the total energy of the system, which equals to the reduction of the sum of the kinetic and potential energy.

Appendix B

Global response: minimization of energy

The kinetic and potential energies of a structure are measures for the global response of the system. The kinetic energy especially is a useful measure to judge the global vibrational response of a structure and to value the performance of the active isolation system in a global sense. The error criteria that minimize the kinetic and potential energies are explained in this appendix in more detail. A procedure is described to determine the energy content without making use of the mass and stiffness matrix from the FEM analysis.

The amplitude of the kinetic energy E_{kin} in the frequency domain is defined as:

$$E_{kin} = \frac{1}{2}\mathbf{v}_{tot}^{\mathrm{H}} \cdot \mathbf{M} \cdot \mathbf{v}_{tot}, \tag{B.1}$$

where $\mathbf{v}_{tot}$ is a vector with the velocities at all DOFs of the numerical model of the receiver structure and $\mathbf{M}$ is the mass matrix of the finite element model. This mass matrix is square and has a size equal to the number of DOFs of the model. For complex receiver structures like the numerical model of the laboratory setup considered in this thesis, the number of DOF is large which results in large computation times (when the energy contents of the structure has to be determined). The global response is determined by a mobility matrix and the forces at the junctions of the mounts with the receiver structure according to:

$$\mathbf{v}_{tot} = \mathbf{Y}_{rec} \cdot \mathbf{f}_r, \tag{B.2}$$

where $\mathbf{Y}_{rec}$ is the mobility matrix from all the forces at the junctions to all velocity components on the receiver structure. The force vector $\mathbf{f}_r$ is a function

of the disturbance force vector and actuator force vector according to:

$$\mathbf{f}_r = \mathbf{H}_p \cdot \mathbf{f}_d + \mathbf{H}_s \cdot \mathbf{f}_a, \tag{B.3}$$

where $\mathbf{H}_p$ is the primary transfer path and $\mathbf{H}_s$ is the secondary transfer path, as shown in equations (2.30e) and (2.31). Substitution of equations (B.1) and (B.2) into the expression for the kinetic energy (B.3) yields:

$$E_{kin} = \frac{1}{2} \left(\mathbf{H}_p \cdot \mathbf{f}_d + \mathbf{H}_s \cdot \mathbf{f}_a\right)^{\mathrm{H}} \mathbf{Y}_{rec}^{\mathrm{H}} \cdot \mathbf{M} \cdot \mathbf{Y}_{rec} \cdot \left(\mathbf{H}_p \cdot \mathbf{f}_d + \mathbf{H}_s \cdot \mathbf{f}_a\right). \tag{B.4}$$

The mobility matrix $\mathbf{Y}_{rec}$ is determined by a modal expansion of the receiver structure as described in section 4.3.2. When the influence of the residual mode is omitted in the expansion, the mobility matrix can written as:

$$\mathbf{Y}_{rec} = \mathrm{j}\omega \boldsymbol{\Phi} \cdot \mathbf{Q}, \tag{B.5}$$

where $\boldsymbol{\Phi}$ is a matrix with the structural modes and $\mathbf{Q}$ a matrix with modal participations for each connection DOF at the junctions. Substitution of equation (B.5) into the expression for the kinetic energy results in:

$$E_{kin} = -\frac{1}{2}\omega^2 \left(\mathbf{H}_p \cdot \mathbf{f}_d + \mathbf{H}_s \cdot \mathbf{f}_a\right)^{\mathrm{H}} \mathbf{Q}^{\mathrm{H}} \cdot \boldsymbol{\Phi}^{\mathrm{H}} \cdot \mathbf{M} \cdot \boldsymbol{\Phi} \cdot \mathbf{Q} \left(\mathbf{H}_p \cdot \mathbf{f}_d + \mathbf{H}_s \cdot \mathbf{f}_a\right). \tag{B.6}$$

With the eigenmodes being normalized with respect to the mass matrix $\mathbf{M}$ (see equation (4.6)) this equation reduces to:

$$E_{kin} = -\frac{1}{2}\omega^2 \left(\mathbf{H}_p \cdot \mathbf{f}_d + \mathbf{H}_s \cdot \mathbf{f}_a\right)^{\mathrm{H}} \mathbf{Q}^{\mathrm{H}} \cdot \mathbf{I} \cdot \mathbf{Q} \left(\mathbf{H}_p \cdot \mathbf{f}_d + \mathbf{H}_s \cdot \mathbf{f}_a\right), \tag{B.7}$$

where $\mathbf{I}$ an identity matrix. In a similar way, the potential energy can be determined:

$$E_{pot} = \frac{1}{2} \left(\mathbf{H}_p \cdot \mathbf{f}_d + \mathbf{H}_s \cdot \mathbf{f}_a\right)^{\mathrm{H}} \mathbf{Q}^{\mathrm{H}} \cdot \boldsymbol{\Phi}^{\mathrm{H}} \cdot \mathbf{K} \cdot \boldsymbol{\Phi} \cdot \mathbf{Q} \left(\mathbf{H}_p \cdot \mathbf{f}_d + \mathbf{H}_s \cdot \mathbf{f}_a\right), \tag{B.8}$$

which can be rewritten with the help of equation (4.6) in:

$$E_{pot} = \frac{1}{2} \left(\mathbf{H}_p \cdot \mathbf{f}_d + \mathbf{H}_s \cdot \mathbf{f}_a\right)^{\mathrm{H}} \mathbf{Q}^{\mathrm{H}} \cdot \boldsymbol{\Omega}^2 \cdot \mathbf{Q} \left(\mathbf{H}_p \cdot \mathbf{f}_d + \mathbf{H}_s \cdot \mathbf{f}_a\right). \tag{B.9}$$

The kinetic and potential energy are determined with only the modal participations and without the influence of the residual flexibility term. The residual term is only considerable near the points of excitation of the structure, but its contribution to the total response of the structure is negligible.

Appendix C

Singular Value Decomposition

A particular useful tool for analyzing Frequency Response Functions (FRFs) is the *Singular Value Decomposition* (SVD) [45]. This tool is used in different fields, e.g. the inversion of ill-conditioned matrices [50, 137] and in the field of structural active structural acoustic control to relate structural sensors to the desired acoustic response with reduction of information [19, 42].

Considering a transfer matrix $\mathbf{H}$ of size $m \times n$, the SVD of this matrix is written as:

$$\mathbf{H} = \mathbf{U} \cdot \mathbf{S} \cdot \mathbf{V}^{\mathrm{H}} = \sum_i \mathbf{u}_i s_i \mathbf{v}_i^{\mathrm{H}}. \tag{C.1}$$

The matrix $\mathbf{U}$ is of dimensions $(m \times m)$, $\mathbf{S}$ is of size $(m \times n)$ and $\mathbf{V}$ is of size $(n \times n)$. The matrices $\mathbf{U}$ and $\mathbf{V}$ are unitary matrices: $\mathbf{U}^{\mathrm{H}} \cdot \mathbf{U} = \mathbf{I}_m$ and $\mathbf{V}^{\mathrm{H}} \cdot \mathbf{V} = \mathbf{I}_n$. The matrices $\mathbf{U}$ and $\mathbf{V}$ contain the left and right singular vectors $\mathbf{u}_i$ and $\mathbf{v}_i$, respectively:

$$\mathbf{U} = \begin{bmatrix} \mathbf{u}_1 & \mathbf{u}_2 & \cdots & \mathbf{u}_m \end{bmatrix} \qquad \mathbf{V} = \begin{bmatrix} \mathbf{v}_1 & \mathbf{v}_2 & \cdots & \mathbf{v}_n \end{bmatrix}. \tag{C.2}$$

The real and positive singular values s_i are collected on the diagonal of matrix $\mathbf{S}$, for $i = 1, 2, ..., \min(m, n)$ in decreasing order such that $s_1 \geq s_2 \geq \cdots \geq s_{\min(m,n)} \geq 0$.

When the SVD analysis is used for the decomposition of the matrix with FRFs of dynamic or acoustic problems, the left and right singular vectors can be interpreted in a physical way as a sort of 'modal' representation. The left singular vectors represent the so-called *field shapes* or *field modes* and are patterns or modes of preferable responses of the structure. The right singular vectors are the so-called *source shapes* or *source modes* and can be interpreted as patterns of excitations in which the structure responds preferably. The contribution of each field shape and corresponding mode shape to represent

H is uniquely determined by the corresponding singular value. There is only coupling between a field shape $\mathbf{u}_i$ and source shape $\mathbf{v}_j$ for $i = j$ while the most efficient coupling takes place for the case $i = 1$ because of the largest corresponding singular value.

C.1 Radiation modes of a baffled rectangular plate

An example of the use of the SVD analysis can be found in the field of ASAC (Active Structural Acoustic Control). In this field, the goal is reduction of an acoustic response radiated by the structure by influencing the structural vibrations with the help of actuators in combination with a controller. When structural error sensors are used instead of acoustic error sensors (e.g. accelerometers or piezoelectric sensors), the structural sensor response has to be weighted in order to obtain an acoustic measure e.g. the radiated sound power. In this section the SVD analysis is used to investigate the radiated sound power of a baffled plate into the free field [26, 42]. The same configuration is considered as for the described plate-structure in section 2.5.3 with the properties shown in Table 2.3.

The radiated sound power can be written as:

$$\bar{W} = \mathbf{v}_n^{\mathrm{H}} \cdot \mathbf{R} \cdot \mathbf{v}_n, \tag{C.3}$$

where $\mathbf{R}$ is the radiation resistance matrix, which is shown in equation (2.48) for the free field radiation of a baffled plate. The vector $\mathbf{v}_n$ is the velocity response of the plate in the normal direction. The radiation matrix can consequently be decomposed according to:

$$\mathbf{R} = \mathbf{U} \cdot \mathbf{S} \cdot \mathbf{V}^{\mathrm{H}}, \tag{C.4}$$

where $\mathbf{U}$ and $\mathbf{V}$ are the left and right singular vectors respectively and are equal to each other due to the symmetry of the radiation matrix. Substitution of equation (C.4) into equation (C.3) results in:

$$\bar{W} = \mathbf{a} \cdot \mathbf{S} \cdot \mathbf{a}^{\mathrm{H}} = \sum_i s_i |a_i|^2, \tag{C.5}$$

where $\mathbf{a} = \mathbf{v}_n^{\mathrm{H}} \cdot \mathbf{U}$ is the resulting vector when the normal velocity distribution is mapped on the field shapes. This equation shows that the radiation modes contribute independently to the radiated sound power.

The radiation matrix $\mathbf{R}$ is frequency dependent, which means that the radiation modes also depend on the frequency. In Figure C.1 the first six radiation modes are shown for the dimensionless frequency $kL_y = 0.2$. At this

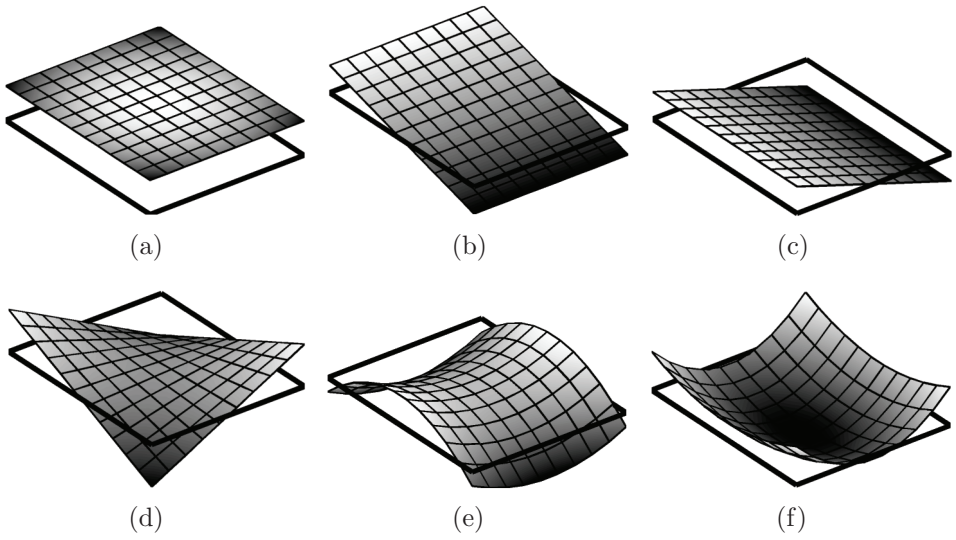

Figure C.1: Radiation modes at $kL_y = 0.2$.

frequency the acoustic wavelength is larger than the largest plate length. In Figure C.2 the first six efficient radiation modes are shown at a dimensionless frequency of $kL_y = 2\pi$, a frequency where the acoustic wavelength is equal to the largest dimension of the plate. The radiation modes change slightly in shape, which is most clearly visible for the first radiation mode. The velocity distribution that radiates the sound most efficiently at low frequencies is the uniform piston movement with a large volume displacement as shown in Figure C.1(a). At higher frequencies, the most efficient radiation mode changes from a uniform piston movement to one with rounded edges ('dome' shaped).

The singular values, a measure for the efficiency of the contributions of the radiation modes to the radiated sound power, are plotted as a function of the frequency in Figure C.3(a). At low frequencies just a few singular values have a large value, meaning that just a few radiation modes contribute significantly to the total radiated sound power. This is also shown in Figure C.3(b), where the radiated sound power is depicted when only four radiation modes are taken into account for the approximation. This approximation works quite well up to a frequency range of $kL_y = \pi$. At higher frequencies, $kL_y \gg \pi$, a large number of modes becomes efficient and it is difficult to distinguish between 'weak' and 'strong' radiation modes. Hence the radiation mode approach has no advantage in terms of data reduction and provides no useful information.

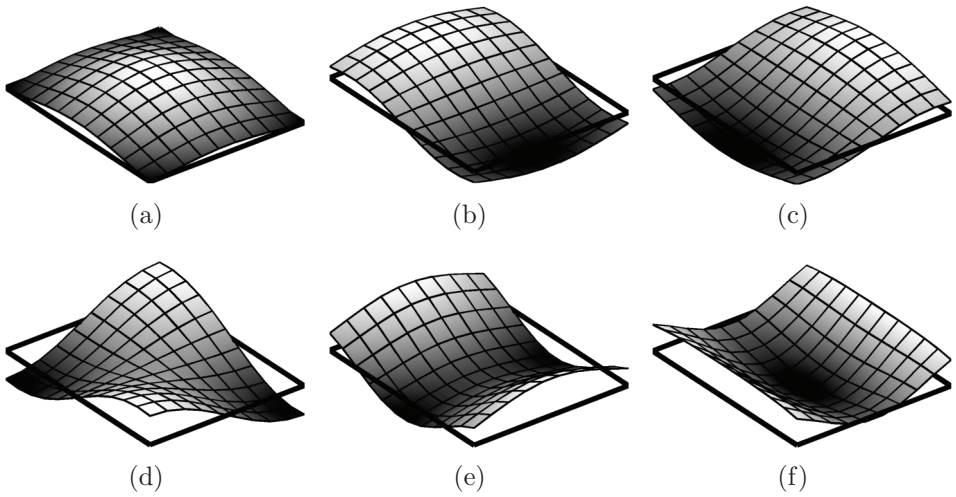

Figure C.2: Radiation modes at $kL_y = 2\pi$.

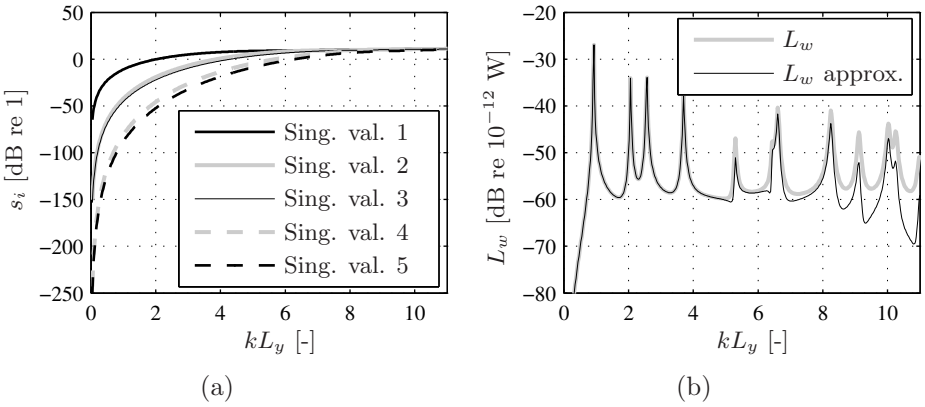

Figure C.3: The singular values of the radiation matrix (a) and the approximated radiated sound power with account of the first four radiation modes (b).

The property that the radiated sound power is dominated by just a few radiation modes in combination with the property that each radiation mode contributes independently to the radiated sound power makes this approach useful for application in ASAC at low frequencies. When the vibrational sensor response is weighted in such a way that the contributions of the most efficient radiation modes are 'sensed', one is assured of a reduction of the radiated sound power. The idea of using so-called *radiation filters* was introduced by Baumann *et al.* [4]. The use of the radiation modes as radiation filters was introduced by Gibbs *et al.* and explained with the example of the radiation of a baffled plate [42]. Further literature concerning characteristic properties of radiation modes can be found in references [17, 18, 25, 26, 27, 107]. In the field of ASAC, the radiation modes is also an important subject in the literature, e.g. [3, 11, 12, 42, 94]. Similar techniques can be used for radiation into enclosures as shown by Cazzolato [14, 21].

C.2 Regularization

A problem that is often encountered in engineering problems, is ill-behavior of the inverse problem that is considered. When a problem is considered that is described by FRFs, it is common to write this in terms of a discrete transfer matrix approach according to:

$$\mathbf{H} \cdot \mathbf{x} = \mathbf{b}, \tag{C.6}$$

where the transfer matrix $\mathbf{H}$ relates the input vector $\mathbf{x}$ (cause, e.g. forces) to an output vector $\mathbf{b}$ (effect, e.g. accelerations). In a forward problem the input vector $\mathbf{x}$ is known and a solution of the output vector $\mathbf{b}$ is sought. In inverse problems the challenge is to obtain a meaningful solution of the unknown original input $\mathbf{x}$ of the system for a known output vector $\mathbf{b}$. The vector $\mathbf{b}$ and or the transfer matrix $\mathbf{H}$ is commonly obtained from measurements. Equation (C.7) can be rewritten for this case as:

$$\underset{\sim}{\mathbf{H}} \cdot \underset{\sim}{\mathbf{x}} = \underset{\sim}{\mathbf{b}}, \tag{C.7}$$

where $\underset{\sim}{\mathbf{H}}$ is the measured FRF matrix, $\underset{\sim}{\mathbf{b}}$ is the measured actual response and $\underset{\sim}{\mathbf{x}}$ is the reconstructed input vector. When the system shown in equation (C.7) arises from an ill-posed problem, the transfer matrix is ill-conditioned and standard inversion techniques fail to obtain a physically meaningful approximation of $\underset{\sim}{\mathbf{x}}$. The ill-conditioned transfer matrix amplifies the small measurement errors in the vector $\underset{\sim}{\mathbf{b}}$ in such a way that the solution of the vector $\underset{\sim}{\mathbf{x}}$ has

no physical meaning. The reconstructed input vector can contain large errors introduced by a combination of an ill-conditioned FRF matrix and the errors in the measurement of the operational responses ($\underset{\sim}{\mathbf{b}}$) and the FRFs (the components of $\underset{\sim}{\underset{\sim}{\mathbf{H}}}$). Regularization techniques are used to prevent the solution of $\mathbf{x}$ of a discrete ill-posed problem becoming dominated by contributions arising from noise in the right-hand side vector $\mathbf{b}$. A particularly useful numerical tool for the analysis of ill-conditioned problems is the SVD since it reveals all difficulties associated with the ill-conditioning of matrix $\mathbf{H}$ [45, 50].

The condition number of $\underset{\sim}{\underset{\sim}{\mathbf{H}}}$ equals the ratio of the largest and smallest singular values $s_1/s_{\min(m,n)}$. This ratio is a measure for the sensitivity of the solution to perturbation errors in $\underset{\sim}{\underset{\sim}{\mathbf{H}}}$ or the right-hand side $\underset{\sim}{\mathbf{b}}$; i.e. a high condition number of the transfer matrix indicates that ill-conditioned behavior may occur during inversion. In order to prevent this undesirable behavior, a class of regularization tools are available to produce a regularized solution. When the transfer matrix $\underset{\sim}{\underset{\sim}{\mathbf{H}}}$ is decomposed with an SVD, the equation can be written as:

$$\underset{\sim}{\mathbf{b}} = \underset{\sim}{\mathbf{U}} \cdot \underset{\sim}{\mathbf{S}} \cdot \underset{\sim}{\mathbf{V}}^{\mathrm{H}} \cdot \underset{\sim}{\mathbf{x}}, \qquad \text{or in components,} \qquad \underset{\sim}{\mathbf{b}} = \sum_i \underset{\sim}{s}_i (\underset{\sim}{\mathbf{v}}_i^{\mathrm{H}} \cdot \underset{\sim}{\mathbf{x}}) \underset{\sim}{\mathbf{u}}_i. \tag{C.8}$$

The solution of the inverse problem to determine the vector $\mathbf{x}$ can now be determined according to:

$$\underset{\sim}{\mathbf{x}} = \sum_i \frac{\underset{\sim}{\mathbf{u}}_i^{\mathrm{H}} \cdot \underset{\sim}{\mathbf{b}}}{\underset{\sim}{s}_i} \underset{\sim}{\mathbf{v}}_i. \tag{C.9}$$

In order to overcome the undesirable behavior of the amplification of noise in the right-hand side vector $\underset{\sim}{\mathbf{b}}$, the regularization techniques produce a regularized solution in the form:

$$\hat{\underset{\sim}{\mathbf{x}}} = \sum_i f_i \frac{\underset{\sim}{\mathbf{u}}_i^{\mathrm{H}} \cdot \underset{\sim}{\mathbf{b}}}{\underset{\sim}{s}_i} \underset{\sim}{\mathbf{v}}_i, \tag{C.10}$$

where f_i are known as the *filter factors*. In order to effectively apply regularization, these filter factors must have the important property that for decreasing values of $\underset{\sim}{s}_i$ the corresponding factor f_i approaches zero in such a way that the contributions $(\underset{\sim}{\mathbf{u}}_i^{\mathrm{H}} \cdot \underset{\sim}{\mathbf{b}}/\underset{\sim}{s}_i)\underset{\sim}{\mathbf{v}}_i$ are filtered out for the smaller $\underset{\sim}{s}_i$. There are different kinds of regularization techniques like *Truncated Singular Value Decomposition* (TSVD), *Tikhonov* regularization and *iterative* methods. In this work, only the TSVD technique is used.

Once it is known that the ill-conditioned behavior is related to the smallest singular values $\underset{\sim}{s}_i$, the most straightforward method is to reject the contribu-

tions corresponding with the smallest singular values:

$$\hat{\underset{\sim}{\mathbf{x}}} = \sum_{i}^{k} \frac{\underset{\sim}{\mathbf{u}}_i^{\mathrm{H}} \cdot \underset{\sim}{\mathbf{b}}}{\underset{\sim}{s}_i} \underset{\sim}{\mathbf{v}}_i, \quad \text{with} \quad k \leq \min(m, n), \tag{C.11}$$

or, in terms of the filter factors:

$$\hat{\underset{\sim}{\mathbf{x}}} = \sum_{i} f_i \frac{\underset{\sim}{\mathbf{u}}_i^{\mathrm{H}} \cdot \underset{\sim}{\mathbf{b}}}{\underset{\sim}{s}_i} \underset{\sim}{\mathbf{v}}_i, \quad \text{with} \quad f_i = \begin{cases} 1, & \text{if } i \leq k \\ 0, & \text{if } k < i \leq \min(m, n). \end{cases} \tag{C.12}$$

This technique is known as TSVD. The truncation eliminates the influence of all singular vectors $\underset{\sim}{\mathbf{v}}_i$ associated with singular values smaller than $\underset{\sim}{s}_k$. When the truncation number k is chosen carefully and sufficiently, the regularized solution $\hat{\underset{\sim}{\mathbf{x}}}$ is stable and smooth. The condition number for the regularized transfer matrix, given by $\underset{\sim}{s}_1/\underset{\sim}{s}_k$, increases when the number of rejected singular values increases. However, a too low number of k results in an over-regularized solution. And a too high number of k results in instable behavior due to under-regularization. The most optimal number of k is thus a trade-off and over-regularization or under-regularization has to be avoided. The problem is how to estimate the threshold value for the rejection of the singular values. In references [56, 57] norms of the FRF response matrix or operational response vector were adopted with varying degree of success. In references [129, 130] also more advanced techniques are treated such as Tikhonov regularization and iterative inversion.

Appendix D

Analytical formulation

In this appendix the dynamic behavior of the three isolation components (source, mounts and receiver) are described and analyzed in more detail. The analytical models for the mounts and receiver are compared with numerical results obtained with the finite element package ANSYS.

D.1 Dynamics of a rigid body

In general, the source of vibration in models of active isolation systems a rigid mass with external disturbance forces. Consider a rigid mass as depicted in Figure D.1. The excitation forces are assumed to act in the center of gravity (*c.o.g.*) of the rigid mass. Also a junction point of the connection between a mount and the source is depicted with its displacement components. The same sign convention is used for the force vector at this connection point. The analysis is performed in the frequency domain. The velocities at the mount location $\mathbf{v}_s$ can be expressed as a function of the velocities in the center of

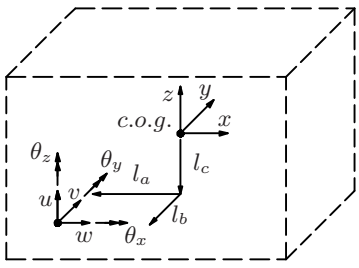

Figure D.1: Sign convention for the rigid body.

gravity of the rigid mass $\mathbf{v}_g$ according to:

$$\mathbf{v}_s = \mathbf{V}_{sg} \cdot \mathbf{v}_g, \tag{D.1}$$

where:

$$\mathbf{V}_{sg} = \begin{bmatrix} 1 & 0 & 0 & 0 & l_c & -l_b \\ 0 & 1 & 0 & -l_c & 0 & l_a \\ 0 & 0 & 1 & l_b & -l_a & 0 \\ 0 & 0 & 0 & 1 & 0 & 0 \\ 0 & 0 & 0 & 0 & 1 & 0 \\ 0 & 0 & 0 & 0 & 0 & 1 \end{bmatrix}. \tag{D.2}$$

In a similar way the forces at a junction of the source connection with a mount $\mathbf{f}_s$ are expressed as a force vector acting at the center of gravity $\mathbf{f}_g$ of the source according to:

$$\mathbf{f}_g = \mathbf{F}_{gs} \cdot \mathbf{f}_s, \tag{D.3}$$

where:

$$\mathbf{F}_{gs} = \begin{bmatrix} 1 & 0 & 0 & 0 & 0 & 0 \\ 0 & 1 & 0 & 0 & 0 & 0 \\ 0 & 0 & 1 & 0 & 0 & 0 \\ 0 & -l_c & l_b & 1 & 0 & 0 \\ l_c & 0 & -l_a & 0 & 1 & 0 \\ -l_b & l_a & 0 & 0 & 0 & 1 \end{bmatrix}. \tag{D.4}$$

The equations of motion for the rigid body mass can now be written as:

$$\mathbf{f}_g + \mathbf{f}_d = \mathrm{j}\omega\, \mathbf{M}_g \cdot \mathbf{v}_g, \tag{D.5}$$

where $\mathbf{f}_d$ is the vector with disturbance forces acting on the rigid mass. The mass matrix $\mathbf{M}_g$ can be written as

$$\mathbf{M}_g = \begin{bmatrix} m & 0 & 0 & 0 & 0 & 0 \\ 0 & m & 0 & 0 & 0 & 0 \\ 0 & 0 & m & 0 & 0 & 0 \\ 0 & 0 & 0 & I_x & 0 & 0 \\ 0 & 0 & 0 & 0 & I_y & 0 \\ 0 & 0 & 0 & 0 & 0 & I_z \end{bmatrix}, \tag{D.6}$$

where m is the mass of the rigid body and I is the rotary moment of inertia. Now the velocities at the mount location can be written in terms of the disturbance forces $\mathbf{f}_d$ and the forces at the mount location $\mathbf{f}_s$ with corresponding mobility matrices resulting in:

$$\mathbf{v}_s = \mathbf{Y}_{sd} \cdot \mathbf{f}_d + \mathbf{Y}_{ss} \cdot \mathbf{f}_s, \tag{D.7}$$

where:

$$\mathbf{Y}_{sd} = \mathbf{V}_{sg} \cdot (\mathrm{j}\omega\, \mathbf{M}_g)^{-1} \qquad \mathbf{Y}_{ss} = \mathbf{V}_{sg} \cdot (\mathrm{j}\omega\, \mathbf{M}_g)^{-1} \cdot \mathbf{F}_{gs}. \tag{D.8}$$

D.2 Dynamics of a beam

The mounts are modeled as beams for which three types of vibrations are distinguished: longitudinal or axial vibrations, bending of flexural vibrations and torsional vibrations.

D.2.1 Bending vibrations with shear and inertia effects

For bending vibrations it is often assumed that the beam is slender, which means that the length of the beam is large in comparison with its cross-sectional dimensions. For slender beams the deflection as consequence of shear can be neglected (the so-called Euler beam). However, for isolation purposes the mount supports are often short and for this reason not slender. The influence of shear effects may be considerable for slender beams and are therefore taken into account. Also the influence of the rotary inertia is taken into account, which may have considerable influence at higher frequencies.

Figure D.2: A beam element with the sign convention for bending vibration.

Consider a beam element as depicted in Figure D.2. The dynamic behavior of the beam element is described as a function of the variables at the nodal points 1 and 2. The slope of the deflection curve depends not only on the rotation of the cross sections of the beam but also on the shearing deformation. The total slope of the deflection curve is:

$$\frac{\partial w}{\partial x} = \psi + \beta, \tag{D.9}$$

where ψ is the slope of the deflection curve when the shearing force is neglected and β is the angle of shear at the neutral axis in the same cross section.

The bending moment and shearing force are:

$$M = EI\frac{\mathrm{d}\psi}{\mathrm{d}x} \qquad V = -k_s \beta AG, \tag{D.10}$$

where G is the modulus of elasticity in shear, I is the area moment of inertia and k_s is a shape factor for shear depending on the geometry of the cross-section. The nodal DOF vector $\mathbf{w}_b$ and the nodal load vector $\mathbf{f}_b$ in terms of the degrees of freedom related with the bending of the beam are defined as:

$$\mathbf{w}_b = \begin{Bmatrix} w_1 \\ \psi_1 \\ w_2 \\ \psi_2 \end{Bmatrix} \qquad \mathbf{f}_b = \begin{Bmatrix} V_1 \\ M_1 \\ V_2 \\ M_2 \end{Bmatrix}, \tag{D.11}$$

where w_1 and ψ_1 are the displacement and rotation as consequence of the deflection at node 1, respectively, and V_1 and M_1 are the corresponding nodal shear force and bending moment.

The equation of motion of a so-called Timoshenko beam (including shear and rotary inertia effects) can be written as [131]:

$$EI\frac{\partial^4 w}{\partial x^4} + \rho A\frac{\partial^2 w}{\partial t^2} - \rho I\left(1 + \frac{E}{k_s G}\right)\frac{\partial^4 w}{\partial x^2 \partial t^2} + \frac{\rho^2 I}{k_s G}\frac{\partial^4 w}{\partial t^4} = 0. \tag{D.12}$$

Assuming a harmonic excitation of the form $w(x,t) = w(x)\mathrm{e}^{\mathrm{j}\omega t}$ where ω is the angular frequency, the equation of motion becomes:

$$\frac{\partial^4 w}{\partial x^4} + c_2\frac{\partial^2 w}{\partial x^2} - c_1 w = 0, \tag{D.13}$$

where:

$$c_1 = \frac{1}{EI}\left(\omega^2\rho A - \frac{\omega^4\rho^2 I}{k_s G}\right), \tag{D.14}$$

$$c_2 = \frac{\omega^2\rho}{E}\left(1 + \frac{E}{k_s G}\right). \tag{D.15}$$

The general solution of the homogeneous equation (D.13) is:

$$w = C_1\mathrm{e}^{n_1(x-L)} + C_2\mathrm{e}^{-n_1 x} + C_3\mathrm{e}^{n_2(x-L)} + C_4\mathrm{e}^{-n_2 x}, \tag{D.16}$$

where C_1 to C_4 are the integration coefficients, and n_1 and n_2 are defined as:

$$\begin{aligned} n_1 &= \frac{1}{2}\sqrt{-2c_2 + 2\sqrt{c_2^2 + 4c_1}}, \\ n_2 &= \frac{1}{2}\sqrt{-2c_2 - 2\sqrt{c_2^2 + 4c_1}}. \end{aligned} \tag{D.17}$$

The nodal DOF vector $\mathbf{w}_b$ can be calculated in terms of the integration coefficients at the nodal locations $x = 0$ and $x = L$ with L the length of the beam element:

$$\mathbf{w}_b = \mathbf{G} \cdot \mathbf{c}\,, \tag{D.18}$$

where:

$$\mathbf{G} = \begin{bmatrix} e^{-n_1 L} & 1 & \cdots \\ \frac{\left(-k_s AG - EI\left(n_1^2 + \frac{\omega^2\rho}{k_s G}\right)\right) n_1 e^{-n1L}}{\omega^2\rho I - k_s AG} & \frac{k_s AG n_1 - EI n_1\left(-n_1^2 - \frac{\omega^2\rho}{k_s G}\right)}{\omega^2\rho I - k_s AG} & \\ 1 & e^{-n_1 L} & \\ \frac{-k_s AG n_1 - EI n_1\left(n_1^2 + \frac{\omega^2\rho}{k_s G}\right)}{\omega^2\rho I - k_s AG} & \frac{\left(k_s AG - EI\left(-n_1^2 - \frac{\omega^2\rho}{k_s G}\right)\right) n_1 e^{-n1L}}{\omega^2\rho I - k_s AG} & \\ e^{-n_2 L} & 1 & \\ \frac{\left(-k_s AG - EI\left(n_2^2 + \frac{\omega^2\rho}{k_s G}\right)\right) n_2 e^{-n2L}}{\omega^2\rho I - k_s AG} & \frac{k_s AG n_2 - EI n_2\left(-n_2^2 - \frac{\omega^2\rho}{k_s G}\right)}{\omega^2\rho I - k_s AG} & \\ 1 & e^{-n_2 L} & \\ \frac{-k_s AG n_2 - EI n_2\left(n_2^2 + \frac{\omega^2\rho}{k_s G}\right)}{\omega^2\rho I - k_s AG} & \frac{\left(k_s AG - EI\left(-n_2^2 - \frac{\omega^2\rho}{k_s G}\right)\right) n_2 e^{-n2L}}{\omega^2\rho I - k_s AG} & \end{bmatrix}, \tag{D.19}$$

and:

$$\mathbf{c} = \begin{Bmatrix} C_1 \\ C_2 \\ C_3 \\ C_4 \end{Bmatrix}. \tag{D.20}$$

In the same way the forces can be related with the integration coefficients according to:

$$\mathbf{f}_b = \mathbf{H} \cdot \mathbf{c}. \tag{D.21}$$

The matrix $\mathbf{H}$ can be calculated with equations (D.10) resulting in:

$$\mathbf{H} = \begin{bmatrix} -k_s AG\left(1 - \frac{-k_s AG - EI\left(n_1^2 + \frac{\omega^2\rho}{k_s G}\right)}{\omega^2\rho I - k_s AG}\right) n_1 \mathrm{e}^{-n_1 L} & \cdots \\ -EI\mathrm{e}^{-n_1 L}\left(n_1^2 + \frac{\omega^2\rho}{k_s G}\right) & \\ k_s AGn_1\left(1 - \frac{-k_s AG - EI\left(n_1^2 + \frac{\omega^2\rho}{k_s G}\right)}{\omega^2\rho I - k_s AG}\right) & \\ EI\left(n_1^2 + \frac{\omega^2\rho}{k_s G}\right) & \end{bmatrix}$$

$$\begin{bmatrix} -k_s AGn_1\left(-1 - \frac{k_s AG - EI\left(-n_1^2 - \frac{\omega^2\rho}{k_s G}\right)}{\omega^2\rho I - k_s AG}\right) & \cdots \\ -EI\left(n_1^2 + \frac{\omega^2\rho}{k_s G}\right) & \\ k_s AG\left(-1 - \frac{k_s AG - EI\left(-n_1^2 - \frac{\omega^2\rho}{k_s G}\right)}{\omega^2\rho I - k_s AG}\right) n_1 \mathrm{e}^{-n_1 L} & \\ EI\mathrm{e}^{-n_1 L}\left(n_1^2 + \frac{\omega^2\rho}{k_s G}\right) & \end{bmatrix}$$

$$\begin{bmatrix} -k_s AG\left(1 - \frac{-k_s AG - EI\left(n_2^2 + \frac{\omega^2\rho}{k_s G}\right)}{\omega^2\rho I - k_s AG}\right) n_2 \mathrm{e}^{-n_2 L} & \cdots \\ -EI\mathrm{e}^{-n_2 L}\left(n_2^2 + \frac{\omega^2\rho}{k_s G}\right) & \\ k_s AGn_2\left(1 - \frac{-k_s AG - EI\left(n_2^2 + \frac{\omega^2\rho}{k_s G}\right)}{\omega^2\rho I - k_s AG}\right) & \\ EI\left(n_2^2 + \frac{\omega^2\rho}{k_s G}\right) & \end{bmatrix}$$

$$\begin{bmatrix} -k_s AGn_2\left(-1 - \frac{k_s AG - EI\left(-n_2^2 - \frac{\omega^2\rho}{k_s G}\right)}{\omega^2\rho I - k_s AG}\right) \\ -EI\left(n_2^2 + \frac{\omega^2\rho}{k_s G}\right) \\ k_s AG\left(-1 - \frac{k_s AG - EI\left(-n_2^2 - \frac{\omega^2\rho}{k_s G}\right)}{\omega^2\rho I - k_s AG}\right) n_2 \mathrm{e}^{-n_2 L} \\ EI\mathrm{e}^{-n_2 L}\left(n_2^2 + \frac{\omega^2\rho}{k_s G}\right) \end{bmatrix}. \quad \text{(D.22)}$$

With the equations (D.18) and (D.21) the following relation between the nodal forces and displacements can be derived:

$$\mathbf{f}_b = \mathbf{H} \cdot \mathbf{G}^{-1} \cdot \mathbf{w}. \quad \text{(D.23)}$$

In this equation the matrix product $\mathbf{H} \cdot \mathbf{G}^{-1}$ defines the relation between the dynamic force and the dynamic displacements in the nodes and is called the dynamic stiffness matrix. Equation (D.23) can be rewritten as:

$$\begin{Bmatrix} V_1 \\ M_1 \\ V_2 \\ M_2 \end{Bmatrix} = \begin{bmatrix} \mathbf{k}_{11}^b & \mathbf{k}_{12}^b \\ \mathbf{k}_{21}^b & \mathbf{k}_{22}^b \end{bmatrix} \cdot \begin{Bmatrix} w_1 \\ \psi_1 \\ w_2 \\ \psi_2 \end{Bmatrix}. \tag{D.24}$$

The matrices $\mathbf{k}_{11}^b$ and $\mathbf{k}_{22}^b$ are the blocked dynamic driving point matrices related with the bending of the beam at node 1 and 2 respectively and relate the nodal forces with its own nodal displacements. The matrices $\mathbf{k}_{12}^b$ and $\mathbf{k}_{21}^b$ are the blocked dynamic transfer bending stiffness matrices relating the forces in one node to the displacements of the other node. For the beam depicted in Figure D.2 the bending in the $x-z$ plane can be written in terms of the total dynamic stiffness matrices:

$$\mathbf{f}_b = \begin{bmatrix} k_{11}(3,3) & k_{11}(3,5) & k_{12}(3,3) & k_{12}(3,5) \\ k_{11}(5,3) & k_{11}(5,5) & k_{12}(5,3) & k_{12}(5,5) \\ k_{21}(3,3) & k_{21}(3,5) & k_{22}(3,3) & k_{22}(3,5) \\ k_{21}(5,3) & k_{21}(5,5) & k_{22}(5,3) & k_{22}(5,5) \end{bmatrix} \cdot \mathbf{w}_b. \tag{D.25}$$

In the same way the bending of the beam in the $x-y$ plane can be determined according to:

$$\mathbf{f}_b = \begin{bmatrix} k_{11}(2,2) & k_{11}(2,6) & k_{12}(2,2) & k_{12}(2,6) \\ k_{11}(6,2) & k_{11}(6,6) & k_{12}(6,2) & k_{12}(6,6) \\ k_{21}(2,2) & k_{21}(2,6) & k_{22}(2,2) & k_{22}(2,6) \\ k_{21}(6,2) & k_{21}(6,6) & k_{22}(6,2) & k_{22}(6,6) \end{bmatrix} \cdot \mathbf{w}_b. \tag{D.26}$$

Structural damping can be introduced by assuming a complex elasticity modulus [23] according to:

$$E = E' + \mathrm{j}E'' = E'(1 + \mathrm{j}\eta), \tag{D.27}$$

where η is the structural loss factor of the material, E' and E'' are the real and imaginary part of the modulus of elasticity respectively.

D.2.2 Longitudinal vibration

In the same way as described for the bending deformation, the dynamic stiffness matrix for longitudinal vibrations can be derived. The sign convention

Figure D.3: A beam element with the sign convention for longitudinal vibration.

is shown in Figure D.3. The nodal variables are written in a vector according to:

$$\mathbf{u} = \begin{Bmatrix} u_1 \\ u_2 \end{Bmatrix} \qquad \mathbf{f}_n = \begin{Bmatrix} N_1 \\ N_2 \end{Bmatrix}, \tag{D.28}$$

where u_1 and u_2 are the axial displacements at nodes 1 and 2, respectively, and N_1 and N_2 are the corresponding nodal shear forces. The equation of motion for longitudinal vibrations is:

$$EA\frac{\partial^2 u}{\partial x^2} - m\frac{\partial^2 u}{\partial t^2} = N, \tag{D.29}$$

where E is the Young's modulus, A is the cross-sectional area and m is the mass per unit length, all assumed to be independent on coordinate x. The homogeneous form of the equation of motion can be solved in the frequency domain which yields the general displacement function:

$$w = C_1 \sin(k_l x) + C_2 \cos(k_l x), \tag{D.30}$$

where k_l the longitudinal wave number defined as:

$$k_l = \sqrt{\omega^2 \frac{m}{EA}}. \tag{D.31}$$

In the same way as described for the bending vibrations, the relations between the nodal displacements and the integration constants can be derived, which yields:

$$\mathbf{G} = \begin{bmatrix} 0 & 1 \\ \sin(k_l L) & \cos(k_l L) \end{bmatrix}, \tag{D.32}$$

With help of the relation:

$$N = EA\frac{\mathrm{d}u}{\mathrm{d}x}, \tag{D.33}$$

the relation between the nodal axial forces and the integration constants can be derived, which yields:

$$\mathbf{H} = EAk_l \begin{bmatrix} -1 & 0 \\ \cos(k_l L) & -\sin(k_l L) \end{bmatrix}. \tag{D.34}$$

The relation between the nodal forces and displacements can again be calculated according to:

$$\mathbf{f}_n = \mathbf{H} \cdot \mathbf{G}^{-1} \cdot \mathbf{u}. \tag{D.35}$$

In terms of the total dynamic stiffness matrix, equation (D.45) is written as:

$$\mathbf{f}_n = \begin{bmatrix} k_{11}(1,1) & k_{12}(1,1) \\ k_{21}(1,1) & k_{22}(1,1) \end{bmatrix} \cdot \mathbf{u}. \tag{D.36}$$

D.2.3 Torsional vibration

The sign convention to describe the torsional vibration in a beam is described in Figure D.4. The nodal variables are written in a vector according to:

Figure D.4: A beam element with sign convention for torsional deformation.

$$\boldsymbol{\theta} = \begin{Bmatrix} \theta_1 \\ \theta_2 \end{Bmatrix} \qquad \mathbf{t} = \begin{Bmatrix} T_1 \\ T_2 \end{Bmatrix}, \tag{D.37}$$

where θ_1 is the torsional rotation angle and T_1 is the torsional moment on node 1. The equation of motion for torsional vibrations is:

$$GJ\frac{\partial^2\theta}{\partial x^2} - I_{mp}\frac{\partial^2\theta}{\partial t^2} = T, \tag{D.38}$$

where G is the shear modulus, J is the polar moment of inertia of the cross-sectional area and I_{mp} is the mass polar moment of inertia per unit length. The defined parameters are assumed to be independent of x. The general solution of the equation of motion in the frequency domain is:

$$\theta = C_1 \sin(k_t)x + C_2 \cos(k_t x), \tag{D.39}$$

where k_t is the torsional wave number defined as:

$$k_t = \sqrt{\omega^2 \frac{\rho}{G}}. \tag{D.40}$$

The relation between the nodal displacements and the integration constants can be determined again, resulting in:

$$\mathbf{G} = \begin{bmatrix} 0 & 1 \\ \sin(k_t L) & \cos(k_t L) \end{bmatrix}. \tag{D.41}$$

With use of the relation:

$$T = GJ\frac{\mathrm{d}\theta}{\mathrm{d}x}, \tag{D.42}$$

the nodal torsional moments can be expressed as function of the integration constants resulting in:

$$\mathbf{H} = GJ\,k_t \begin{bmatrix} -1 & 0 \\ \cos(k_t L) & -\sin(k_t L) \end{bmatrix}. \tag{D.43}$$

The relation between the torsional moments and rotations can be calculated with:

$$\mathbf{t} = \mathbf{H} \cdot \mathbf{G}^{-1} \cdot \boldsymbol{\theta}. \tag{D.44}$$

In terms of the total dynamic stiffness matrix, equation (D.45) can be written as:

$$\mathbf{t} = \begin{bmatrix} k_{11}(4,4) & k_{12}(4,4) \\ k_{21}(4,4) & k_{22}(4,4) \end{bmatrix} \cdot \boldsymbol{\theta}. \tag{D.45}$$

D.2.4 Example and comparison with FEM

The derived analytical expressions are used to determine the dynamic behavior of an example beam and the results are compared with mobilities calculated with a harmonic analysis in the finite element package Ansys. Consider a square beam with material properties and dimensions as defined in Table D.1. In Figure D.5 the driving point stiffness component $k_{11}(2,2)$ from lateral force

Parameter	**Value**
Density	1000 kg/m^3
Modulus of elasticity	$1 \cdot 10^7$ N/m^2
Poisson's ratio	0.33
Dimensions ($b \times h \times L$)	$0.01 \times 0.01 \times 0.1$ m^3
Structural loss factor	0.01

Table D.1: Parameters for the considered beam example.

to lateral displacement and the transfer point stiffness $k_{11}(2,6)$ from lateral force to rotation are depicted. The analytical results agree very well with the numerical solution determined in ANSYS. The influence of the shear effects and rotary inertia are considerable. In Figure D.6 the driving point stiffness $k_{11}(1,1)$ in axial direction and the torsional driving point stiffness $k_{11}(4,4)$ are shown.

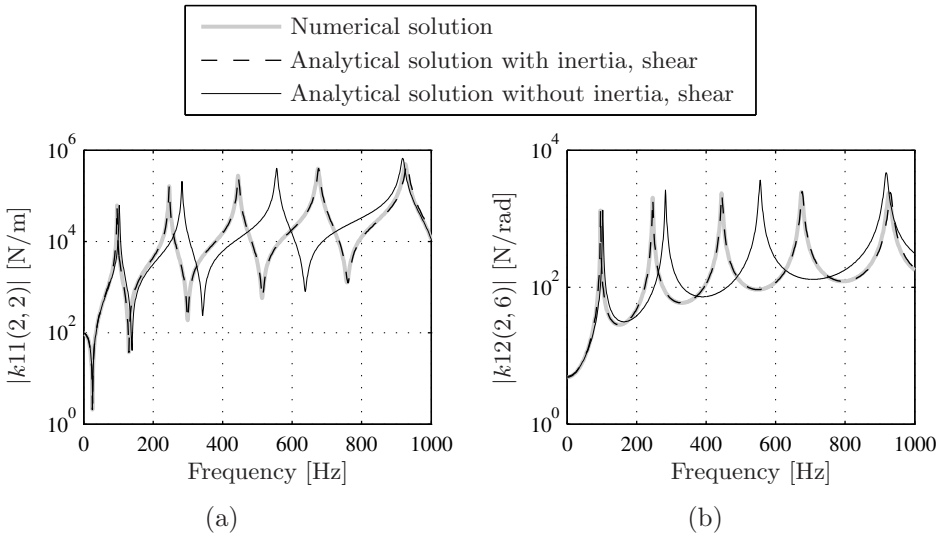

Figure D.5: Different components of the dynamic stiffness concerning the bending deformation.

D.2.5 Impedance matrices

The dynamics of the mount are described in equation (4.1) with the help of an impedance matrix approach:

$$\begin{Bmatrix} \mathbf{f}_{ms} \\ \mathbf{f}_{mr} \end{Bmatrix} = \begin{bmatrix} \mathbf{Z}_{ss} & \mathbf{Z}_{sr} \\ \mathbf{Z}_{rs} & \mathbf{Z}_{rr} \end{bmatrix} \cdot \begin{Bmatrix} \mathbf{v}_{ms} \\ \mathbf{v}_{mr} \end{Bmatrix} + \begin{bmatrix} \mathbf{T}_{as} \\ \mathbf{T}_{ar} \end{bmatrix} \cdot \mathbf{f}_a. \tag{D.46}$$

The impedance matrices are related with the described dynamic stiffness matrices by:

$$\mathbf{Z}_{ss} = \mathrm{j}\omega\, \mathbf{k}_{11} \qquad \mathbf{Z}_{sr} = \mathrm{j}\omega\, \mathbf{k}_{12}, \tag{D.47}$$

$$\mathbf{Z}_{rs} = \mathrm{j}\omega\, \mathbf{k}_{21} \qquad \mathbf{Z}_{rr} = \mathrm{j}\omega\, \mathbf{k}_{22}, \tag{D.48}$$

where 1 indicates the source side and 2 the receiver side of the mounts in terms of the dynamic stiffness matrix formulation.

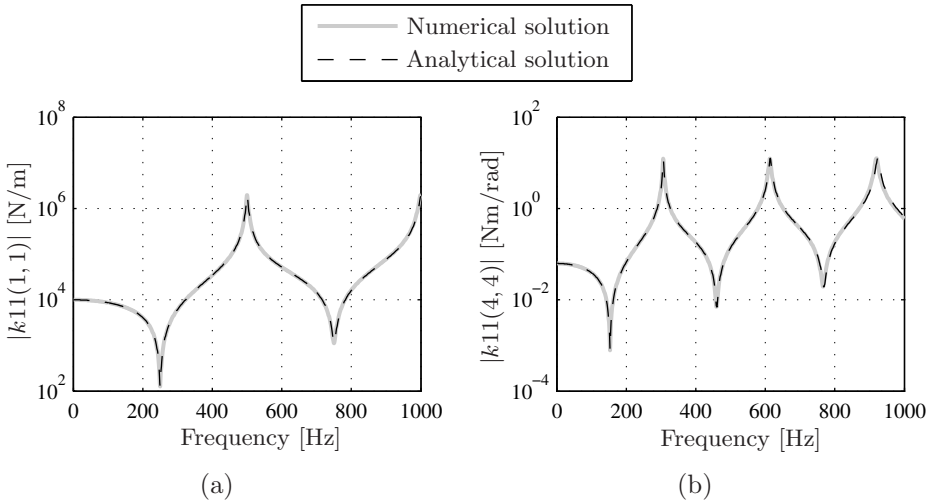

Figure D.6: Different components of the dynamic stiffness concerning the bending deformation.

D.3 Analytical model of a simply supported plate

The receiver structure is modeled as a simply supported plate with a mobility description. An approximate dynamical model is derived for transverse and in-plane vibrations of a plate and the following assumptions are used:

- The vibration amplitudes are assumed to be small and therefore the transverse and in-plane vibrations are uncoupled with respect to each other.
- Kirchhoff hypothesis: a plane through the plate and perpendicular to the mid-plane of the plate remains straight and perpendicular to the mid-plane when deformed.
- Thin plate assumption: the shear and rotary inertia effects are neglected.

The dynamic stiffness matrix method was used to describe the dynamics of a beam, but this method can not be used for plate-like structures because no exact solution of the governing equation of motion exists. For this reason the so-called modal superposition method is used. This approximate method gives a good result for the dynamic behavior at relatively low frequencies with a relatively low modal density. The transfer functions are expressed in terms

of a mobility matrix $\mathbf{Y}$ according to:

$$\mathbf{v} = \mathbf{Y} \cdot \mathbf{f}, \tag{D.49}$$

where the velocity vector $\mathbf{v}$ contains the velocities at different locations for the forces present in the force vector $\mathbf{f}$.

$$\mathbf{v}_j = \begin{Bmatrix} \dot{u} \\ \dot{v} \\ \dot{w} \\ \dot{\theta}_x \\ \dot{\theta}_y \\ \dot{\theta}_z \end{Bmatrix}_j \qquad \mathbf{f}_k = \begin{Bmatrix} f_x \\ f_y \\ f_z \\ m_x \\ m_y \\ m_z \end{Bmatrix}_k . \tag{D.50}$$

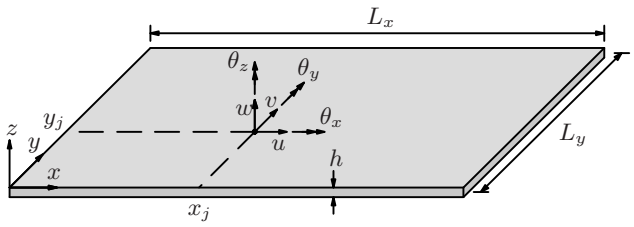

Figure D.7: Sign convention used for the calculation of the plate mobility.

The total dynamics of the receiver plate is split into transverse vibrations, in-plane vibrations and torsional vibrations. The torsional vibrations are not considered. In the end the derived analytical expressions are validated with numerical results obtained with ANSYS.

D.3.1 Transverse vibrations

The harmonic equation of motion of a plate in the normal direction of a plate can be written as [23]:

$$B(1+\mathrm{j}\eta)\left(\frac{\partial^4 w(x,y)}{\partial x^4} + \frac{\partial^4 w(x,y)}{\partial x^2 \partial y^2} + \frac{\partial^4 w(x,y)}{\partial y^4}\right) - \rho h \omega^2 w(x,y) = f_z(x,y), \tag{D.51}$$

where B is the bending stiffness of the plate, η is the structural loss factor, $w(x,y)$ is the displacement in normal direction of the plate, ρ is the density, h is the thickness and $f_z(x,y)$ is the distributed force on the plate. The influence of the rotary moment of inertia is neglected in the equation of motion, thus

the plate is considered to be stiff in shear direction. The bending stiffness is equal to:

$$B = \frac{E}{1-\nu^2}\frac{h^3}{12}, \tag{D.52}$$

where ν is the Poisson's ratio. The homogeneous solution of equation (D.51) defines the eigenfunctions (or mode shapes) $\varphi_n(x,y)$ and the undamped eigenfrequencies ω_n according to:

$$B(1+\mathrm{j}\eta)\left(\frac{\partial^4\varphi_n(x,y)}{\partial x^4}+\frac{\partial^4\varphi_n(x,y)}{\partial x^2\partial y^2}+\frac{\partial^4\varphi_n(x,y)}{\partial y^4}\right)-\rho h\omega_n^2\varphi_n(x,y)=0. \tag{D.53}$$

In general the response of a plate can be written in terms of a summation of the eigenfunctions according to:

$$w(x,y)=\sum_{n=1}^{\infty} W_n\varphi_n(x,y). \tag{D.54}$$

Substitution of equation (D.54) in equation (D.51) yields with substraction of (D.53):

$$w(x,y)=\sum_{n=1}^{\infty} W_n\rho h(\omega_n^2(1+\mathrm{j}\eta)-\omega^2)\varphi_n(x,y)=f_z(x,y). \tag{D.55}$$

Multiplication with $\varphi_m(x,y)$, integration over the whole area S of the plate and taking account of the orthogonality relation between the modes yields:

$$W_n(\omega_n^2(1+\mathrm{j}\eta)-\omega^2)\int_S \rho h\,\varphi_n^2(x,y)\,\mathrm{d}x\mathrm{d}y=\int_S f_z(x,y)\varphi_n(x,y)\,\mathrm{d}x\mathrm{d}y. \tag{D.56}$$

With combination of equation (D.54) the normal displacement of the plate is expressed as:

$$w(x,y)=\sum_{n=1}^{\infty}\frac{\varphi_n(x,y)}{\Lambda_n(\omega_n^2(1+\mathrm{j}\eta)-\omega^2)}\int_S f_z(x,y)\varphi_n(x,y)\,\mathrm{d}x\mathrm{d}y. \tag{D.57}$$

where Λ_n is the modal mass of mode n, which is defined as:

$$\Lambda_n=\int_S \rho h\,\varphi_n^2(x,y)\mathrm{d}x\mathrm{d}y. \tag{D.58}$$

With the defined expression the mobility matrix for the plate can be derived. For a point force f_z at location (x_0,y_0) the excitation term in equation (D.58) can be written as [72]:

$$f_z(x,y)=f_z\delta(x-x_0)\delta(y-y_0), \tag{D.59}$$

where $\delta(x-x_0)$ is the Dirac delta function. The mobility describing the normal velocity of the plate can now be determined by:

$$Y(3,3) = \frac{\dot{w}}{f_z} = \mathrm{j}\omega \sum_{n=1}^{\infty} \frac{\varphi_n(x,y)\varphi_n(x_0,y_0)}{\Lambda_n(\omega_n^2(1+\mathrm{j}\eta)-\omega^2)}, \tag{D.60}$$

The relation of the angles of bending with respect to the normal displacement of the plate is:

$$\theta_x = \partial w/\partial y \quad \theta_y = -\partial w/\partial x. \tag{D.61}$$

With help of the angle definitions the following mobilities are determined:

$$Y(4,3) = \frac{\dot{\theta}_x}{f_z} = \mathrm{j}\omega \sum_{n=1}^{\infty} \frac{\frac{\partial\varphi_n(x,y)}{\partial y}\varphi_n(x_0,y_0)}{\Lambda_n(\omega_n^2(1+\mathrm{j}\eta)-\omega^2)}, \tag{D.62}$$

$$Y(5,3) = \frac{\dot{\theta}_y}{f_z} = -\mathrm{j}\omega \sum_{n=1}^{\infty} \frac{\frac{\partial\varphi_n(x,y)}{\partial x}\varphi_n(x_0,y_0)}{\Lambda_n(\omega_n^2(1+\mathrm{j}\eta)-\omega^2)}. \tag{D.63}$$

For a point moment excitation in the x-direction located at the coordinates (x_0, y_0) the excitation term at the left-hand side can be written as [125]:

$$f(x,y) = \frac{\partial M_x}{\partial x}\delta(x-x_0)\delta(y-y_0). \tag{D.64}$$

The flexural displacement as result of a point moment excitation in the x-direction is determined by:

$$Y(3,4) = \frac{\dot{w}}{M_x} = \mathrm{j}\omega \sum_{n=1}^{\infty} \frac{\varphi_n(x,y)\frac{\partial\varphi_n(x_0,y_0)}{\partial x}}{\Lambda_n(\omega_n^2(1+\mathrm{j}\eta)-\omega^2)}, \tag{D.65}$$

With equation (D.61) the relations between a point moment excitation and the angle velocity are:

$$Y(4,4) = \frac{\dot{\theta}_x}{M_x} = \mathrm{j}\omega \sum_{n=1}^{\infty} \frac{\frac{\partial\varphi_n(x,y)}{\partial y}\frac{\partial\varphi_n(x_0,y_0)}{\partial x}}{\Lambda_n(\omega_n^2(1+\mathrm{j}\eta)-\omega^2)}, \tag{D.66}$$

$$Y(5,4) = \frac{\dot{\theta}_y}{M_x} = -\mathrm{j}\omega \sum_{n=1}^{\infty} \frac{\frac{\partial\varphi_n(x,y)}{\partial x}\frac{\partial\varphi_n(x_0,y_0)}{\partial x}}{\Lambda_n(\omega_n^2(1+\mathrm{j}\eta)-\omega^2)}. \tag{D.67}$$

The mobilities for a point moment excitation in the y-direction can be determined in the same way:

$$Y(3,5) = \frac{\dot{w}}{M_y} = \mathrm{j}\omega \sum_{n=1}^{\infty} \frac{\varphi_n(x,y)\frac{\partial \varphi_n(x_0,y_0)}{\partial y}}{\Lambda_n(\omega_n^2(1+\mathrm{j}\eta)-\omega^2)}, \tag{D.68}$$

$$Y(4,5) = \frac{\dot{\theta}_x}{M_y} = \mathrm{j}\omega \sum_{n=1}^{\infty} \frac{\frac{\partial \varphi_n(x,y)}{\partial y}\frac{\partial \varphi_n(x_0,y_0)}{\partial y}}{\Lambda_n(\omega_n^2(1+\mathrm{j}\eta)-\omega^2)}, \tag{D.69}$$

$$Y(5,5) = \frac{\dot{\theta}_y}{M_y} = -\mathrm{j}\omega \sum_{n=1}^{\infty} \frac{\frac{\partial \varphi_n(x,y)}{\partial x}\frac{\partial \varphi_n(x_0,y_0)}{\partial y}}{\Lambda_n(\omega_n^2(1+\mathrm{j}\eta)-\omega^2)}. \tag{D.70}$$

The mode shapes or eigenfunctions and natural frequencies can be determined by solving equation (D.53). For a simply supported plate the eigenfunctions are [15, 23]:

$$\varphi_n(x,y) = \sin\left(\frac{n_1\pi}{L_x}x\right)\sin\left(\frac{n_2\pi}{L_y}y\right), \tag{D.71}$$

with the corresponding eigenfrequencies:

$$\omega_n = \sqrt{\frac{B}{\rho h}}\left[\left(\frac{n_1\pi}{L_x}\right)^2 + \left(\frac{n_2\pi}{L_y}\right)^2\right], \tag{D.72}$$

where the index n represents the double index n_1 and n_2.

D.3.2 In-plane vibrations

In most cases only the out-of-plane response is considered for the dynamics in plates. This response is often the most dominant because the flexural or bending stiffness is much lower than the in-plane stiffness of a plate. However, for an excitation of a source in all degrees of freedom the plate is also excited in the in-plane directions. At higher frequencies resonances occur in these directions which result in a considerable contribution to the transmitted power.

The equations of motion of motion for harmonic excitation forces f_x and f_y at a point (x_0, y_0) in the middle of the plane can be written as [99]:

$$C_l^2\frac{\partial^2 u}{\partial x^2} + C_s^2\frac{\partial^2 u}{\partial y^2} + (\nu C_l^2 + C_s^2)\frac{\partial^2 v}{\partial x \partial y} + \omega^2 u = -\frac{f_x}{\rho h}\delta(x-x_0)(y-y_0), \tag{D.73}$$

$$C_s^2\frac{\partial^2 v}{\partial y^2} + C_l^2\frac{\partial^2 v}{\partial x^2} + (\nu C_l^2 + C_s^2)\frac{\partial^2 u}{\partial x \partial y} + \omega^2 v = -\frac{f_y}{\rho h}\delta(x-x_0)(y-y_0), \tag{D.74}$$

with the sign convention as displayed in Figure D.7. Notice that the two equations are coupled by the two directions of vibration. The wave speed in longitudinal direction C_l and in shear direction C_s are defined as:

$$C_l = \sqrt{\frac{E}{\rho(1-\nu^2)}} \qquad C_s = \sqrt{\frac{E}{2\rho(1+\nu)}}. \tag{D.75}$$

For a simply supported or clamped plate, the displacement fields that satisfy the boundary conditions are assumed to have the form:

$$u(x,y) = \sum_{p=1}^{\infty}\sum_{s=1}^{\infty} A_{ps} \sin\frac{p\pi x}{L_x}\sin\frac{s\pi y}{L_y}\mathrm{e}^{\mathrm{j}\omega t}, \tag{D.76}$$

$$v(x,y) = \sum_{p=1}^{\infty}\sum_{s=1}^{\infty} B_{ps} \sin\frac{p\pi x}{L_x}\sin\frac{s\pi y}{L_y}\mathrm{e}^{\mathrm{j}\omega t}. \tag{D.77}$$

Substitution into equations (D.73) and (D.74), integrating over the area of the plate and making use of orthogonality properties of the assumed mode shapes yields [36]:

$$\left[\left(\frac{p\pi C_l^2}{L_x}\right)^2 + \left(\frac{s\pi C_s^2}{L_y}\right)^2 - \omega^2\right] A_{ps} + (\nu C_l^2 + C_s^2)\frac{\pi^2}{\Lambda} I_{B_{ps}} = \frac{f_x}{\Lambda\rho h}\sin\frac{p\pi x_0}{L_x}\sin\frac{s\pi y_0}{L_y}, \tag{D.78}$$

$$\left[\left(\frac{s\pi C_l^2}{L_x}\right)^2 + \left(\frac{p\pi C_s^2}{L_y}\right)^2 - \omega^2\right] B_{ps} + (\nu C_l^2 + C_s^2)\frac{\pi^2}{\Lambda} I_{A_{ps}} = \frac{f_y}{\Lambda\rho h}\sin\frac{p\pi x_0}{L_x}\sin\frac{s\pi y_0}{L_y}, \tag{D.79}$$

where $\Lambda = L_x L_y/4$ and:

$$I_{A_{ps}} = \sum_{q=1}^{\infty}\sum_{r=1}^{\infty} \alpha_{pq,rs} A_{qr}, \tag{D.80}$$

$$I_{B_{ps}} = \sum_{q=1}^{\infty}\sum_{r=1}^{\infty} \alpha_{pq,rs} B_{qr}, \tag{D.81}$$

$$\alpha_{pq,rs} = -\frac{qr}{L_x L_y}\int_{x=0}^{L_x}\sin\frac{p\pi x}{L_x}\cos\frac{q\pi x}{L_x}\mathrm{d}x\int_{y=0}^{L_y}\sin\frac{s\pi y}{L_y}\cos\frac{r\pi y}{L_y}\mathrm{d}y. \tag{D.82}$$

The expression for α can be simplified to:

$$\alpha_{ps,qr} = -qr \left[\frac{(-1)^p (-1)^q p + p}{\pi(p+q)(p-q)} \right] \left[\frac{(-1)^s (-1)^r s + s}{\pi(s+r)(-s+r)} \right]. \tag{D.83}$$

The modal participations A_{ps} and B_{ps} are obtained by solving the coupled set of equations (D.78) and (D.79) for a reduced number of k modes. The system of equations has a total size of 2 x k x k. With the calculated modal participations, the in-plane displacements are determined by equations (D.76) and (D.77) where the assumed mode shapes are summed over k modes weighted with the modal participations. The equations can be solved for a unit excitation in the x-direction while maintaining the force in y-direction zero. With the calculated results of the displacement in x-direction and y-direction the mobilities $Y(1,1)$ and $Y(2,1)$ can be determined. In the same way the mobilities $Y(2,2)$ and $Y(1,2)$ can be determined for a unit force excitation in y-direction. Structural damping is taken into account by defining a complex modulus of elasticity.

D.3.3 Example of a receiver plate

To validate the derived analytical expressions, the mobilities are compared with the mobilities calculated with the finite element package Ansys. Consider a simply supported plate with the properties as defined in Table D.2.

Parameter	**Value**
Density	2700 kg/m^3
Modulus of elasticity	$70 \cdot 10^9$ N/m^2
Poisson's ratio	0.33
Dimensions ($L_x \times L_y \times h$)	$1.2 \times 1 \times 0.025$ m^3
Excitation location (x_0, y_0)	$(0.4, 0.4)$ m
Structural loss factor	0.01 [-]

Table D.2: Parameters for the example plate.

In Figure D.8 some mobilities are plotted for three different models: the numerical solution (FEM), the analytical solution with account of a residual mode and the analytical solution without account of a residual mode. Especially for the so-called driving point mobilities (the degree of freedom of response is the same as the excitation degree of freedom and considered in

the same point as the excitation or in other words the diagonal terms of the driving point mobility matrix) the influence of the modes in the high-frequency region is high. The frequency response function of these mobilities can be improved considerably with account of a residual mode as can be seen clearly in Figure D.8(a) and D.8(c). The point cross mobilities are described quite well without a residual mode as can be seen in Figure D.8(d). The analytically determined mobilities agree very well with the results obtained with the harmonic analysis obtained from ANSYS.

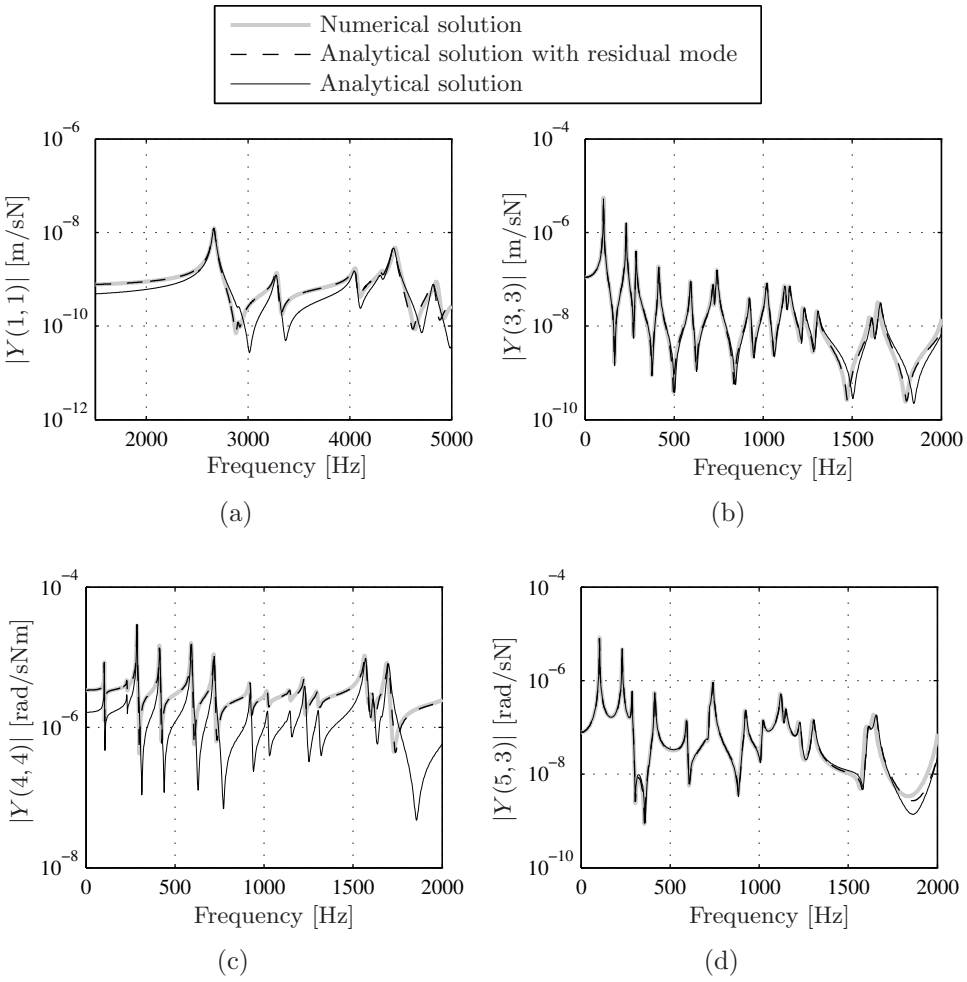

Figure D.8: Different point mobility plots of the plate with the numerical solution, the analytical solution and the analytical solution with account of a residual mode.

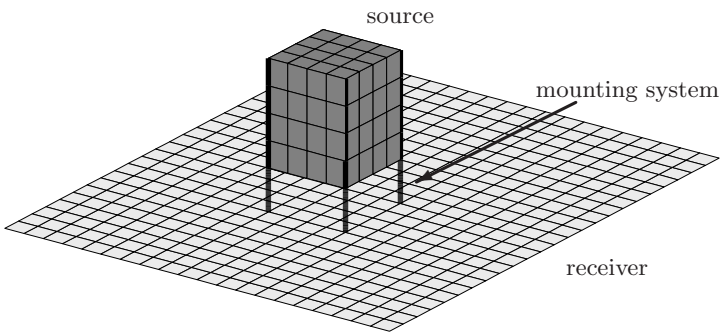

Figure D.9: Finite element model of the considered hybrid isolation system.

D.4 Total isolation model: example

With the models of the source, mounts and receiver a total isolation model can be composed by connecting the subcomponents with each other. An example of such an isolation system is shown in chapter 3, where a rigid mass source is connected to a simply supported plate as receiver structure by four mounts. The total model is connected at the junctions and ports as described in chapter 2. In this section, the passive response of the analytical isolation model is compared to the response calculated with a finite element model of this isolation system. This FEM model is shown in Figure D.9.

The same model parameters are used as described in Table 3.1 for the validation, except that the structural loss factor of the mounts is chosen equal to the loss factor of the receiver ($\eta = 0.01$) and the disturbance force is defined as a unit force in x-, y- and z-directions and a unit moment around the x- and y-axis in the center of gravity of the source. In Figure D.10 the transmitted power is plotted as a function of the frequency for both models. As can be seen the numerical calculated response resembles the analytical response well. However, for frequencies above 2500 Hz, some deviations can be observed, caused by a too coarse mesh of the finite element model, but the tendencies are still comparable.

To give some more insight in the dynamic behavior of the isolation system, the first eight peaks in the transmitted power are compared with a modal analysis and are described in Table D.3. The first three peaks correspond to modes whose shape show a 'rigid body' displacement of the source with the receiver, whereas all deformation is concentrated in the mounts. The fourth peak is the first deformation mode of the receiver structure. The fifth peak

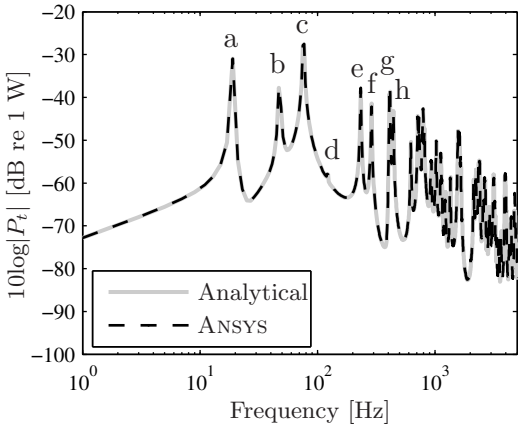

Figure D.10: Passive response of the considered hybrid isolation system in terms of the transmitted power, determined with the analytical model and with ANSYS.

correspond with the first resonance in the mounting system. Already in the first frequency band of 500 Hz a lot of different deformation shapes of the isolation system are present: global rigid body motion of the source, resonance frequencies in the mounting system and deformation modes in the receiver plate. This variety in dynamic behavior also occurs in realistic isolation systems and therefore this model is considered to be more realistic than the simple oscillator models.

Ind.	Freq. [Hz]	Mode description
a	18.8	rigid body mode: translational motion x- and y-direction
b	47.7	rigid body mode: translational motion z-direction
c	76	rigid body mode: rotational motion around x- and y-axis
d	122.2	1-1 mode receiver plate
e	233	2-1 mode receiver plate
f	288	1-2 mode receiver plate
g	401	first bending mode mounts
h	408	2-2 mode receiver plate

Table D.3: Characterization of the first 8 modes of the isolation system.

Appendix E

FEM modeling of rubber

In this appendix the theory on the finite element modeling of rubber material is briefly described. The behavior of rubber material is quite complex, and rubber has the property that it can undergo large elastic deformations. It also behaves nearly incompressibly, which means that the volume of the material does not change much during deformation. In this appendix, first the kinematics and strain definitions are treated. Then, the strain energy function is introduced, which is used to describe the behavior of hyperelastic materials such as rubbers. The virtual work equation is consequently introduced, which is solved by the FEM code in a discretized form. Finally, the theory is described to perform a frequency domain analysis, following a static analysis.

E.1 Kinematics and strain definition

The kinematics of a deformable body concerns the motion of a material from an initial configuration (reference configuration) to the final situation. Consider the vibration isolator depicted in Figure E.1, with a material particle located at position $\vec{X}$ in the reference configuration $\mathcal{B}$ that, after the deformation, is located at current position $\vec{x}$ in $\mathcal{S}$. The motion of the continuum body is a mapping of the current configuration on the initial configuration at time t:

$$\varphi_t : \mathcal{B} \rightarrow \mathcal{S} \in \mathbb{R}^3. \tag{E.1}$$

Hence, the spatial position $\vec{x}$ for the position $\vec{X} \in \mathcal{B}$ at time t becomes:

$$\vec{x} = \varphi_t(\vec{X}) = \varphi(\vec{X}, t). \tag{E.2}$$

The displacement of a material particle is written as:

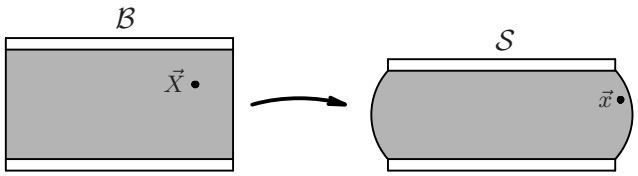

Figure E.1: Motion of a material point from the reference configuration $\mathcal{B}$ to $\mathcal{S}$.

$$\vec{u} = \vec{x} - \vec{X}. \tag{E.3}$$

The deformation gradient tensor $\mathbf{F}$ relates the current spatial configuration to the reference configuration:

$$\mathbf{F} = \frac{\partial \vec{x}}{\partial \vec{X}} = \begin{bmatrix} \frac{\partial x_1}{\partial X_1} & \frac{\partial x_1}{\partial X_2} & \frac{\partial x_1}{\partial X_3} \\ \frac{\partial x_2}{\partial X_1} & \frac{\partial x_2}{\partial X_2} & \frac{\partial x_2}{\partial X_3} \\ \frac{\partial x_3}{\partial X_1} & \frac{\partial x_3}{\partial X_2} & \frac{\partial x_3}{\partial X_3} \end{bmatrix}. \tag{E.4}$$

To describe the material behavior it is necessary to have a measure for the amount of deformation. The definition of the deformation gradient is used for this purpose:

$$\mathbf{C} = \mathbf{F}^{\mathrm{T}} \cdot \mathbf{F}, \tag{E.5a}$$

$$\mathbf{B} = \mathbf{F} \cdot \mathbf{F}^{\mathrm{T}}, \tag{E.5b}$$

where the metric tensors $\mathbf{C}$ and $\mathbf{B}$ are defined as the right Cauchy-Green tensor or Cauchy tensor and the left Cauchy-Green tensor or Finger tensor, respectively. This can be seen more clearly when the deformation of the length of a current infinitesimal vector $\mathrm{d}\vec{x}$ is considered:

$$\mathrm{d}s^2 = \mathrm{d}\vec{x} \cdot \mathrm{d}\vec{x} = \left(\mathbf{F} \cdot \mathrm{d}\vec{X}\right) \cdot \left(\mathbf{F} \cdot \mathrm{d}\vec{X}\right) = \left(\mathbf{F}^{\mathrm{T}} \cdot \mathbf{F}\right) : \mathrm{d}\vec{X}\mathrm{d}\vec{X} = \mathbf{C} : \mathrm{d}\vec{X}\mathrm{d}\vec{X}. \tag{E.6}$$

Another measure is the so-called stretch ratio, defined as the ratio between the lengths of $\mathrm{d}\vec{x}$ and $\mathrm{d}\vec{X}$:

$$\lambda = \sqrt{\frac{\mathrm{d}s^2}{\mathrm{d}S^2}} = \sqrt{\frac{\mathrm{d}\vec{x} \cdot \mathrm{d}\vec{x}}{\mathrm{d}\vec{X} \cdot \mathrm{d}\vec{X}}}. \tag{E.7}$$

Considering the deformation gradient tensor in more detail, the length of the current infinitesimal vector $\mathrm{d}\vec{x}$ is related to the original infinitesimal vector $\mathrm{d}\vec{X}$ according to:

$$\mathrm{d}\vec{x} = \mathbf{F} \cdot \mathrm{d}\vec{X}. \tag{E.8}$$

When the deformation gradient is subjected to an eigenvalue analysis, the three eigenvalues represent the three principal stretches λ_1, λ_2 and λ_3 and the three eigenvectors represent the orthogonal principal directions (referred to as the "Lagrangian triad" or 'material axes'). Subsequently the eigenvalues of the Cauchy or Finger tensor can be determined as function of the principal stretches. The invariants are:

$$I_1 = C_{11} + C_{22} + C_{33} = \lambda_1^2 + \lambda_2^2 + \lambda_3^2, \tag{E.9a}$$

$$\begin{aligned} I_2 &= C_{11}C_{22} + C_{22}C_{33} + C_{33}C_{11} - C_{12}C_{21} - C_{23}C_{32} - C_{13}C_{31} \\ &= \lambda_2^2\lambda_3^2 + \lambda_3^2\lambda_1^2 + \lambda_1^2\lambda_2^2, \end{aligned} \tag{E.9b}$$

$$\begin{aligned} I_3 &= C_{11}C_{22}C_{33} + 2C_{12}C_{23}C_{13} - C_{11}C_{23}C_{32} - C_{22}C_{13}C_{31} \\ &\quad - C_{33}C_{12}C_{21} = \lambda_1^2\lambda_2^2\lambda_3^2. \end{aligned} \tag{E.9c}$$

The principal invariants of $\mathbf{B}$ and $\mathbf{C}$ coincide and are given by:

$$I_1 = \mathrm{tr}(\mathbf{C}) = \mathrm{tr}(\mathbf{B}), \tag{E.10a}$$

$$I_2 = \frac{1}{2}(I_1^2 - \mathrm{tr}(\mathbf{C^2})) = \frac{1}{2}(I_1^2 - \mathrm{tr}(\mathbf{B^2})), \tag{E.10b}$$

$$I_3 = \det(\mathbf{C}) = \det(\mathbf{B}), \tag{E.10c}$$

where det(.) refers to the determinant. The third principal invariant can be rewritten as:

$$J = \sqrt{I_3} = \det(\mathbf{F}), \tag{E.11}$$

where J represents the ratio of the deformed volume over the undeformed (reference) volume. This expression can be used to determine the deviatoric stretches:

$$\bar{\lambda} = J^{-1/3}\lambda, \tag{E.12}$$

and are thus defined in such a way that these stretches are volume preserving:

$$\bar{J} = \bar{\lambda}_1\bar{\lambda}_2\bar{\lambda}_3 = 1. \tag{E.13}$$

With the definition for J the isochoric deformation gradient can be determined:

$$\bar{\mathbf{F}} = J^{-1/3}\,\mathbf{F}, \tag{E.14}$$

and the isochoric strain tensors can subsequently be written as:

$$\bar{\mathbf{C}} = \bar{\mathbf{F}}^{\mathrm{T}} \cdot \bar{\mathbf{F}} = J^{-2/3}\mathbf{C}, \tag{E.15a}$$

$$\bar{\mathbf{B}} = \bar{\mathbf{F}} \cdot \bar{\mathbf{F}}^{\mathrm{T}} = J^{-2/3}\mathbf{B}. \tag{E.15b}$$

With these equations, the first two deviatoric invariants in equations (E.10), can be determined:

$$\bar{I}_1 = \bar{\lambda}_1^2 + \bar{\lambda}_2^2 + \bar{\lambda}_3^2 = I_1 I_3^{-1/3} = I_1 J^{-2/3}, \tag{E.16a}$$

$$\bar{I}_2 = \bar{\lambda}_2^2\bar{\lambda}_3^2 + \bar{\lambda}_3^2\bar{\lambda}_1^2 + \bar{\lambda}_1^2\bar{\lambda}_2^2 = I_2 I_3^{-2/3} = I_2 J^{-4/3}. \tag{E.16b}$$

In order to derive the finite element equations, the time derivative of the deformation gradient is needed:

$$\dot{\mathbf{F}} = \frac{\mathrm{d}}{\mathrm{d}t}\frac{\partial \vec{x}}{\partial \vec{X}} = \frac{\partial \vec{v}}{\partial \vec{x}} \cdot \frac{\partial \vec{x}}{\partial \vec{X}} = \frac{\partial \vec{v}}{\partial \vec{x}} \cdot \mathbf{F}. \tag{E.17}$$

With help of this equation the spatial velocity gradient $\mathbf{L}$ can be written as:

$$\mathbf{L} = \frac{\partial \vec{v}}{\partial \vec{x}} = \dot{\mathbf{F}} \cdot \mathbf{F}^{-1}. \tag{E.18}$$

The velocity gradient can be decomposed into a symmetric part and a skew-symmetric part:

$$\mathbf{L} = \mathbf{D} + \mathbf{W}, \tag{E.19}$$

where $\mathbf{D}$ is the symmetric spatial rate of deformation:

$$\mathbf{D} = \frac{1}{2}\left(\mathbf{L} + \mathbf{L}^{\mathrm{T}}\right), \tag{E.20}$$

and $\mathbf{W}$ is the skew-symmetric spin tensor:

$$\mathbf{W} = \frac{1}{2}\left(\mathbf{L} - \mathbf{L}^{\mathrm{T}}\right). \tag{E.21}$$

The rate of deformation can again be decomposed in a rate of change of volume per current volume:

$$\varepsilon^v = \mathbf{I} : \mathbf{D} = \mathrm{tr}(\mathbf{D}), \tag{E.22}$$

and the deviatoric strain rate:

$$\mathbf{e} = \mathbf{D} - \frac{1}{3}\varepsilon^v \mathbf{I}. \tag{E.23}$$

Summarizing, the total spatial velocity gradient is:

$$\mathbf{L} = \mathbf{e} + \frac{1}{3}\mathrm{tr}(\mathbf{D}) + \mathbf{W}. \tag{E.24}$$

E.2 Strain energy density functions

The elastic behavior of isotropic hyperelastic material is described by means of a strain energy function or elastic potential [5, 24, 97]. The strain energy function determines the strain energy stored in the material per unit of reference volume. Many different strain energy functions are proposed in the literature. Some functions describe the strain energy in terms of the strain invariants whereas other functions are described in terms of the principle stretches. Also different approaches are chosen with respect to compressibility: sometimes fully incompressible behavior is assumed and other functions take account of some compressibility. However, all strain energy functions satisfy certain conditions. In the first place the material is assumed to be isotropic, which implies that it must be symmetric in terms of the principal stretches (λ_1, λ_2 and λ_3). Furthermore, the strain energy function must be zero for the undeformed state and must always be positive for the deformed state. The most simple form of a strain energy function in terms of the strain invariants that fulfill these conditions is the following polynomial:

$$U = \sum_{p,q,r=0}^{\infty} C_{pqr}(I_1 - 3)^p (I_2 - 3)^q (I_3 - 1)^r, \qquad \text{with } C_{000} = 0, \tag{E.25}$$

where $C_{p,q,r}$ are constant factors for $p, q, r = 1, 2, 3, ..\infty$. When further is assumed that the rubber is incompressible, meaning $J = 1$ and therefore $I_3 = 1$, this equation can be rewritten in:

$$U = \sum_{p,q=0}^{\infty} C_{pq}(I_1 - 3)^p (I_2 - 3)^q \qquad \text{with } C_{00} = 0. \tag{E.26}$$

The strain invariants can be rewritten in terms of the deviatoric invariants. However, rubber is to some extent compressible and for this reason a compressible or volumetric term is added to the strain energy function. The most general polynomial form for isothermal conditions is:

$$U = \sum_{p+q=1}^{\infty} C_{pq}(\bar{I}_1 - 3)^p (\bar{I}_2 - 3)^q + \sum_{p=1}^{\infty} \frac{1}{D_p} (J - 1)^{2p}, \tag{E.27}$$

where the D_p values determine the compressibility of the material. The initial shear modulus G_0 and bulk modulus k_0 depend only on the coefficients of order $p = 1$:

$$G_0 = 2(C_{10} + C_{01}) \qquad k_0 = \frac{2}{D_1}. \tag{E.28}$$

A lot of strain energy functions are proposed in the literature and implemented in commercial finite element packages [52] (e.g. other polynomial expressions like the Mooney-Rivlin and Neo-Hookean functions and other formulations like the Ogden, Arruda-Boyce and Van der Waals form). The most common material used for vibration isolators is carbon black reinforced natural rubber. The Yeoh form [143], a reduced expression of the general polynomial function, describes the material behavior of this type of rubber well:

$$U = C_{10}(\bar{I}_1 - 3) + C_{20}(\bar{I}_1 - 3)^2 + C_{30}(\bar{I}_1 - 3)^3 + \sum_{p=1}^{3} \frac{1}{D_1} (J-1)^{2p}. \quad \text{(E.29)}$$

The influence of the compressibility is normally not so large, and for this reason often just one term (D_1) is taken into account. The latter strain-energy function is used for the finite element analyses presented in this thesis. The coefficients are determined with the help of material experiments of defined samples of the rubber material. Possible tests are uni-axial tension or compression, biaxial tension or compression, planar tension and compression and volumetric tension and compression. The strain-stress curves of these tests are used to fit the parameters (for the Yeoh model C_{10}, C_{20} and C_{30} and D_1) of the strain energy function.

E.3 Stress definition and virtual work principle

The goal is to find an approximate solution for the displacements, deformations, stresses, forces and other state variables. The exact solution of the problem is obtained by demanding both force and moment equilibrium at all times over any arbitrary volume of the body. The displacement finite element method is based on an approximation of this equilibrium, by demanding that the equilibrium condition be maintained in an average sense over a finite number of divisions (elements) of the volume of the body; the so-called weak formulation. This weak formulation of equilibrium must be met for all velocity fields, resulting in an expression of the virtual work, which can be written for the 'virtual' velocity field $\delta\mathbf{v}$ as [52]:

$$\int_V \boldsymbol{\sigma} : \delta\mathbf{D}\, \mathrm{d}V = \int_S \delta\mathbf{v} \cdot \mathbf{t}\, \mathrm{d}S + \int_V \delta\mathbf{v} \cdot \mathbf{f}\, \mathrm{d}V, \quad \text{(E.30)}$$

where $\boldsymbol{\sigma}$ the 'true' or Cauchy stress tensor, $\mathbf{t}$ are the surface tractions per current unit area, $\mathbf{f}$ are the body forces per unit current volume and V the current volume. The term on the left-hand side of the equation represents the

internal energy variation δW_I. The stress tensor can be decomposed into an equivalent pressure stress p:

$$p = -\frac{1}{3}\mathbf{I} : \boldsymbol{\sigma} = -\frac{1}{3}\mathrm{tr}\boldsymbol{\sigma}, \tag{E.31}$$

and the deviatoric stress:

$$S = \boldsymbol{\sigma} + p\mathbf{I}. \tag{E.32}$$

The internal energy variation can subsequently be written as:

$$\delta W_I = \int_{V_0} J(\mathbf{S} : \delta\mathbf{e} - p\delta\varepsilon^v)\,\mathrm{d}V_0, \tag{E.33}$$

where V_0 is the reference volume.

The internal energy variation is by definition equal to the variation of the strain energy potential:

$$\delta W_I = \int_{V_0} J(\mathbf{S} : \delta\mathbf{e} - p\delta\varepsilon^v)\,\mathrm{d}V_0 = \int_{V_0} \delta U\,\mathrm{d}V_0. \tag{E.34}$$

With the help of this equation the deviatoric stress tensor can be derived according to:

$$\mathbf{S} = \frac{2}{J}\mathrm{dev}\left[\left(\frac{\partial U}{\partial \bar{I}_1} + \bar{I}_1\frac{\partial U}{\partial \bar{I}_2}\right)\bar{\mathbf{B}} - \frac{\partial U}{\partial \bar{I}_2}\bar{\mathbf{B}}\cdot\bar{\mathbf{B}}\right]. \tag{E.35}$$

The discretized equilibrium equation (E.30) is nonlinear and is generally solved with Newton's method. The discretized formulation of the weak equilibrium must hold for all virtual velocity fields, resulting in the following vector equation for each nodal variable:

$$\mathbf{F}_{int} = \mathbf{F}_{ext}, \tag{E.36}$$

where $\mathbf{F}_{int}$ the internal reaction force vector and $\mathbf{F}_{ext}$ the external force vector. For Newton's method, the tangent stiffness matrix must be determined for (each) iteration i:

$$K_i = \left.\frac{\mathrm{d}\mathbf{F}_{int}}{\mathrm{d}\mathbf{u}}\right|_{\mathbf{u}_i}, \tag{E.37}$$

where K_i is the tangent stiffness matrix and $\mathbf{u}_i$ is the displacement vector at iteration i. The tangent stiffness matrix is determined by taking the derivative of the internal energy.

$$\begin{aligned}\mathrm{d}\delta W_I = \int_V \Bigg[\begin{bmatrix}\delta\mathbf{e} & \delta\varepsilon^v\end{bmatrix} : \begin{bmatrix}\mathbf{C}^S & \mathbf{Q}\\ \mathbf{Q} & K\end{bmatrix} : \begin{pmatrix}\mathrm{d}\mathbf{e}\\ \mathrm{d}\varepsilon^v\end{pmatrix}\Bigg] \\ - \sigma : (2\,\delta\varepsilon\cdot\mathrm{d}\varepsilon - \delta\mathbf{L}^T\cdot\mathrm{d}\mathbf{L})\,\mathrm{d}V,\end{aligned} \tag{E.38}$$

where $\mathbf{C}^s$ is the 'effective deviatoric elasticity', $\mathbf{Q}$ is the coupling term between the deviatoric stress rate and the volumetric strain rate and K the effective bulk modulus of the material.

For almost incompressible materials, the described pure displacement formulation can behave poorly. This is due to the fact that the stiffness matrix becomes nearly singular, caused by the numerical problems involved with the relatively large effective bulk modulus compared to the effective shear modulus. Most commercial finite element programs have taken measures to circumvent this kind of problem by adjusting the formulation.

E.4 Frequency domain analysis

As explained before, the analysis of the behavior of the rubber vibration isolators is split into two parts. First the rubber isolator is preloaded statically due to the weight of the source. This pre-deformation generally involves large deformations of the rubber material, and it is assumed that this purely elastic behavior is applied for a sufficiently long time so that no viscous effects are present. Subsequently, the dynamic viscoelastic response about the pre-deformed elastic state can be determined. A condition for this approach to be valid is that the vibration amplitude is sufficiently small so that both the kinematic and material response can be treated as linear perturbations about the pre-deformed state.

The virtual work equation for the dynamic response is given by:

$$\delta W_I = \delta W_E + \delta W_D, \tag{E.39}$$

where δW_E is the virtual work of the external forces (equal to the right-hand side of equation (E.30)) and δW_D the virtual work of the d'Alembert forces, which can be determined by:

$$\delta W_D = -\int_{V_0} \rho_0 \delta \mathbf{v} \cdot \ddot{\mathbf{u}} \, \mathrm{d}V_0, \tag{E.40}$$

where ρ_0 the mass density of the material in the initial configuration. The dynamic vibrations are considered to be linear perturbations on the preloaded configuration, and therefore equation (E.39) can be linearized:

$$\triangle W_I = \triangle W_E + \triangle W_D. \tag{E.41}$$

The internal virtual work for a harmonic motion is determined with the help

of equation (E.38) according to:

$$\begin{aligned}\Delta\delta W_I = \int_V &\begin{bmatrix}\Re(\delta\mathbf{e}) & \Im(\delta\mathbf{e}) & \Re(\delta\varepsilon^{vol}) & \Im(\delta\varepsilon^{vol})\end{bmatrix} \\ &: \begin{bmatrix}\Re(\tilde{\mathbf{C}}) & \Im(\tilde{\mathbf{C}}) & \mathbf{Q}|_0 & 0 \\ \Im(\tilde{\mathbf{C}}) & -\Re(\tilde{\mathbf{C}}) & 0 & -\mathbf{Q}|_0 \\ \mathbf{Q}|_0 & 0 & \Re(\tilde{k}) & \Im(\tilde{k}) \\ 0 & -\mathbf{Q}|_0 & \Im(\tilde{k}) & -\Re(\tilde{k})\end{bmatrix} : \begin{Bmatrix}\Re(\Delta\mathbf{e}) \\ \Im(\Delta\mathbf{e}) \\ \Re(\Delta\varepsilon^{vol}) \\ \Im(\Delta\varepsilon^{vol})\end{Bmatrix} \\ - \mathbf{S}_0 : \Bigg[2\begin{bmatrix}\Re(\delta\mathbf{e}) & \Im(\delta\mathbf{e})\end{bmatrix} &: \begin{Bmatrix}\Re(\Delta\mathbf{e}) \\ \Im(\Delta\mathbf{e})\end{Bmatrix} - \begin{bmatrix}\Re(\delta\mathbf{L}) & \Im(\delta\mathbf{L})\end{bmatrix} : \begin{Bmatrix}\Re(\Delta\mathbf{L}) \\ \Im(\Delta\mathbf{L})\end{Bmatrix}\Bigg] \, \mathrm{d}V,\end{aligned} \tag{E.42}$$

where:

$$\Re(\tilde{\mathbf{C}}) = (1 - \omega\Im(g))\, \mathbf{C}^S\big|_0\,, \tag{E.43}$$

$$\Im(\tilde{\mathbf{C}}) = -\omega\Re(g)\mathbf{C}^S\big|_0\,, \tag{E.44}$$

$$\Re(\tilde{\mathbf{k}}) = (1 - \omega\Im(k))\, k|_0\,, \tag{E.45}$$

$$\Im(\tilde{\mathbf{k}}) = -\omega\Re(k)\, k|_0\,. \tag{E.46}$$

In these equations is $\mathbf{C}^S\big|_0$ the effective elasticity and is $k|_0$ the effective bulk modulus of the material after the pre-deformation and prior to the harmonic vibration. The viscous material behavior is taken into account by the definition of the terms $\Re(g)$, $\Im(g)$, $\Re(k)$ and $\Im(k)$ as a function of the frequency. The terms are related to the shear and bulk moduli according to:

$$\omega\Re(g) = \frac{G_l}{G_\infty} \qquad \omega\Im(g) = 1 - \frac{G_s}{G_\infty}, \tag{E.47}$$

$$\omega\Re(k) = \frac{k_l}{k_\infty} \qquad \omega\Im(k) = 1 - \frac{k_s}{k_\infty}, \tag{E.48}$$

where G_l is the frequency dependent loss modulus, G_s is the frequency dependent storage modulus, k_l is the frequency dependent bulk loss modulus, k_s is the frequency dependent storage modulus, G_∞ is the long-term shear modulus and k_∞ the long-term bulk modulus.

Appendix F

Flowchart for material parameters identification of rubber

The flowchart of the procedure to identify the material parameters is shown in Figure F.1. The procedure is divided into two stages, and for each stage a different measurement of the whole isolator is necessary.

- The first stage is to determine the material parameters related with the behavior of the rubber vibration isolator during static pre-deformation. This behavior is determined by the so-called strain-energy function. For filled rubbers, the Yeoh model is normally used as fitting function of the strain-energy function. It consists of three coefficients and a bulk modulus when compressibility is taken into account. The Yeoh parameters are updated in an iterative optimization process, in such a way that the numerically determined static force-displacement curve matches the experimentally determined force-displacement curve. In this work the FEM package ABAQUS is used. For this procedure it is thus necessary to perform experiments where the mount is deformed statically with different preloads after which the reaction forces are measured for each preload. When the optimization process has converged, the three Yeoh coefficients are known and all the necessary material parameters needed to calculate the static deformation are obtained.

- In the next stage the shear storage and loss modulus can be determined with the use of the already determined Yeoh parameters. As in the first stage, an optimization procedure is used. In this situation a measure-

ment of the dynamic stiffness as a function of the frequency is used to minimize the objective function. This means that for each frequency step the shear moduli are updated in the numerical model in such a way that a quadratic objective function, in terms of the difference between both the real and imaginary parts of the experimentally and numerically determined dynamic stiffnesses, is minimized. This process is repeated for each frequency step. After convergence within a frequency step, a first guess value of the shear modulus for the next frequency step can be obtained with extrapolation of the values of the current and previously determined steps. At the end of this stage all necessary material parameters are obtained to determine the dynamic stiffness of preloaded rubber vibration isolators with a harmonic calculation process.

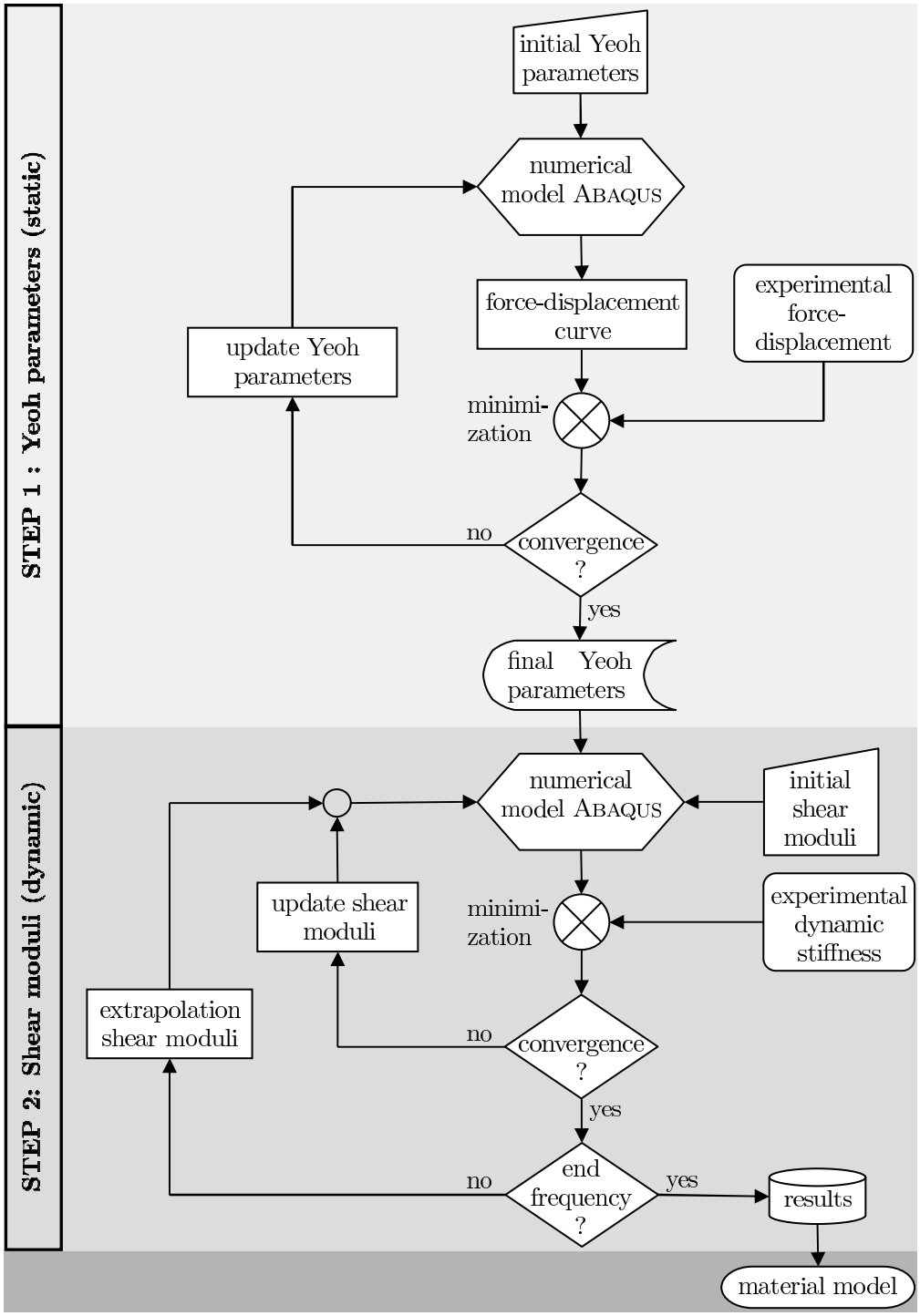

Figure F.1: Flow chart to identify the rubber material properties with the help of experimental data of the rubber isolator.

Appendix G

Applying measurement errors on FRF

The dynamic behavior of structures is normally described by Frequency Response Functions. These functions describe the response at one or more locations of the structure for a certain harmonic excitation. This representation has been used in the considered models in this work, but is also used to represent the dynamic behavior of structures with measured data. Normally, these measurements are determined by means of mobility measurements on the structure that is considered. These measurements are inevitably susceptible to small measurement errors. Mobility or admittance measurements are performed by exciting the structure with a measurable force resulting in a vibrating structure. Sensors (like acceleration pickups) are attached to the structure to measure the response at different locations. During the measurements, it is possible to measure the ratio or transfer between the force and the response for different frequencies, the so-called Frequency Response Function (FRF). However, in practice there are a number of problems that introduce errors like mechanical noise in the structure (also due to nonlinear behavior), electrical noise in the instrumentation and limited analysis resolution.

Consider the following transfer function to be measured:

$$v = Hf, \tag{G.1}$$

where v is the velocity measured at a location, f is the excitation force and H is the FRF. All measured quantities are a function of the frequency. The estimator that minimizes the effect of noise at the output (at the measured velocity response) is [10]:

$$H_1 = \frac{G_{fv}}{G_{ff}}, \tag{G.2}$$

where H_1 is the estimator of the FRF, G_{fv} is the cross spectrum between the force and response and G_{ff} is the auto spectrum of the force. The FRF and both spectra are a function of the frequency. The spectra are determined by an averaging procedure:

$$G_{fv} = \frac{1}{n_a} \sum_{n=1}^{n_a} f^* v, \tag{G.3}$$

$$G_{ff} = \frac{1}{n_a} \sum_{n=1}^{n_a} f^* f, \tag{G.4}$$

where n_a is the number of averages and $(.)^*$ indicates the complex conjugate. The auto spectrum is real, whereas the cross spectrum is complex, showing the phase shift between the output and input.

During mobility measurements two types of errors occur:

- Random errors caused by noise, which are visible as random scatter in the data,
- Bias errors caused by systematic errors, which appear in the measured FRF as a deviation with the same magnitude and phase for each frequency component.

When the FRF is determined according the procedure described by equation (G.2), the random noise in the output v decreases during the average procedure and as the number of averages increases, H_1 converges to the true H. However, bias errors are not removed during this averaging process.

The procedure described above is simulated for the purpose of a sensitivity analysis of the error criteria with weighting matrices for active isolation. The 'exact' FRF's are determined as described in the previous sections with the Finite Element model by using a unit force at each frequency. Both velocity and force spectra are corrupted by adding a complex noise signal in the frequency domain. The velocity vector is corrupted in the following way:

$$\underset{\sim}{v} = v + e = Hf + e, \tag{G.5}$$

where v is the 'true' response, $\tilde{v}$ the operational response and e the error. In the simulations, 'measurement noise' was added to each response signal based on a Gaussian additive noise model [129]:

$$\underset{\sim}{v} = v + c\ n_n\, \mathrm{e}^{\mathrm{j}\, 2\pi n_u}, \tag{G.6}$$

where $\tilde{v}$ is the corrupted velocity response component, v is the true velocity response component, c is a constant, n_n is a normally distributed random number with mean value 0 and standard deviation 1 and n_u is a uniformly distributed random number in the range $0-1$. The exponent with the random number n_u acts on the normally distributed error, and results in an arbitrary complex disturbance signal. The corrupted response signals (indicated by $\widetilde{(.)}$) are used to determine the cross spectrum and auto spectrum, after which the FRF is calculated with the average procedure shown in equation (G.2).

Bibliography

[1] T.G.H. Basten. *Noise reduction by viscothermal acousto-elastic interaction in double wall panels*. PhD dissertation, University of Twente, The Netherlands, 2001. ISBN 90-365-1597-1.

[2] T.G.H. Basten and J.W. Verheij. Actuator and sensor configurations in hybrid isolation of machinery vibration. In *Proceedings of the Tenth International Congress on Sound and Vibration*, Stockholm, Sweden, 2003.

[3] W.T. Baumann, F.-S. Ho, and H.H. Robertshaw. Active structural acoustic control of broadband disturbances. *Journal of the Acoustical Society of America*, 92(4):1998–2005, 1992.

[4] W.T. Baumann, W.R. Saunders, and H.H. Robertshaw. Active suppression of acoustic radiation from impulsively excited structures. *Journal of the Acoustical Society of America*, 90(6):3202–3208, 1991.

[5] H. Bechir, K. Boufala, and Y. Chevalier. Strain energy density function for carbon black filled rubber vulcanized for industrial applications. *Méchanique & Industries*, 3:245–252, 2002.

[6] C.A.J. Beijers, T.G.H. Basten, D.R. van den Brink, J.W. Verheij, and A. de Boer. Near-source error sensor strategies for active vibration isolation of machines. In *Proceedings of ISMA 2004*, Leuven, Belgium, 2004.

[7] C.A.J. Beijers and A. de Boer. Hybrid isolation of structure-borne sound. In *Proceedings of Active 2002*, Southampton, UK, 2002.

[8] C.A.J. Beijers and A. de Boer. Numerical modelling of rubber vibration isolators. In *Proceedings of the Tenth International Congress on Sound and Vibration*, Stockholm, Sweden, 2003.

[9] C.A.J. Beijers, B.A.T. Noordman, and A. de Boer. Numerical modelling of rubber vibration isolators: identification of material parameters. In *Proceedings of the Eleventh International Congress on Sound and Vibration*, St. Petersburg, Russia, 2004.

[10] J.S. Bendat and A.G. Piersol. *Engineering Applications of Correlation and Spectral Analysis*. John Wiley & Sons, 2nd edition, 1993. ISBN 0-471-57055-9.

[11] A.P. Berkhoff. Sensor scheme design for active structural acoustic control. *Journal of the Acoustical Society of America*, 108(3):1037–1045, 2000.

[12] A.P. Berkhoff. Broadband radiation modes: estimation and active control. *Journal of the Acoustical Society of America*, 111(3):1295–1305, 2002.

[13] A.P. Berkhoff. Control strategy for active noise barriers using nearfield error sensing. Patent EP 04076031.6, 2004.

[14] A.P. Berkhoff, E. Sarajlic, B.S. Cazzolato, and C.H. Hansen. Inverse and reciprocity methods for experimental determination of radiation modes. In *Proceedings of the Eighth International Congress on Sound and Vibration*, Hong Kong, 2001.

[15] R.D. Blevins. *Formulas for Natural Frequency and Mode Shape*. Van Nostrand Reinhold, 1979. ISBN 0-89874-791-0.

[16] G.V. Borgiotti. The power radiated from a vibrating body in an acoustic fluid and its determination from boundary measurements. *Journal of the Acoustical Society of America*, 88(4):1884–1893, 1990.

[17] G.V. Borgiotti and K.E. Jones. The determination of the acoustic far field of a radiating body in an acoustic fluid from boundary measurements. *Journal of the Acoustical Society of America*, 93(5):2788–2797, 1993.

[18] G.V. Borgiotti and K.E. Jones. Frequency independence property of radiation spatial filters. *Journal of the Acoustical Society of America*, 96(6):3516–3524, 1994.

[19] B.S. Cazzolato. *Sensing systems for active control of sound transmission into cavities*. PhD dissertation, University of Adelaide, Australia, 1999.

[20] B.S. Cazzolato and C.H. Hansen. Active control of sound transmission using structural error sensing. *Journal of the Acoustical Society of America*, 104(5):2878–2889, 1998.

[21] B.S. Cazzolato and C.H. Hansen. Structural radiation mode sensing for active control of sound radiation into enclosed spaces. *Journal of the Acoustical Society of America*, 106(6):3732–3735, 1999.

[22] R.R. Craig. *Structural Dynamics: An Introduction to Computer Methods*. Wiley, 1981. ISBN 0-471-04499-7.

[23] L. Cremer and M. Heckl. *Körperschall: Physikalische Grundlagen und Technische Anwendungen*. Springer Verlag, 2nd-revised edition, 1996. In German, ISBN 3-540-54631-6.

[24] M.A. Crisfield. *Nonlinear Finite Element Analysis of Solids and Structures, Volume 2 Advanced Topics*. John Wiley & Sons, 1997. ISBN 0-471-95649-X.

[25] K.A. Cunefare and M.N. Currey. On the exterior acoustic radiation modes of structures. *Journal of the Acoustical Society of America*, 96(4):2302–2312, 1994.

[26] M.N. Currey and K.A. Cunefare. The radiation modes of baffled finite plates. *Journal of the Acoustical Society of America*, 98(3):1570–1580, 1995.

[27] M.N. Currey, K.A. Cunefare, M.E. Johnson, and S.J. Elliott. The radiation efficiency grouping of free-space acoustic radiation modes. *Journal of the Acoustical Society of America*, 109(1):203–215, 2001.

[28] J. Dato, W.F. Cousins, W. von Hellens, and D. Wall. Elastomers for Engine Mounts. *Presented at a meeting of the American Chemical Society, Rubber Division Anaheim, California*, (27), 1997.

[29] A. de Boer. *Mechanical behaviour of the periodontal ligament in-vivo; measurements and numerical analyses*. PhD dissertation, Utrecht University, The Netherlands, Utrecht, The Netherlands, 1987.

[30] J.D. Dickens. Dynamic model of vibration isolator under static load. *Journal of Sound and Vibration*, 236(2):323–337, 2000.

[31] J.D. Dickens. Phase velocity of rubber element in vibration isolator under static load. *Journal of Sound and Vibration*, 234(1):21–42, 2000.

[32] J.D. Dickens and C.J. Norwood. Universal method to measure dynamic performance of vibration isolators under static load. *Journal of Sound and Vibration*, 244(4):685–696, 2001.

[33] D.J. Ewins. *Modal Testing: Theory and Practice*. Research Studies Press Ltd., 1986. ISBN 0-86380-036-X.

[34] F.J. Fahy. *Sound and Structural Vibration: Radiation, Transmission and Response*. Academic Press, 1985. ISBN 0-12-247670-0.

[35] F.J. Fahy. *Foundations of Engineering Acoustics*. Academic Press, 2001. ISBN 0-12-247665-4.

[36] N.A. Farag and J. Pan. Free and forced in-plane vibration of rectangular plates. *Journal of the Acoustical Society of America*, 103(1):408–413, 1998.

[37] J.D. Ferry. *Viscoelastic Properties of Polymers*. John Wiley & Sons, 3rd edition, 1980. ISBN 0-471-04894-1.

[38] C.R. Fuller, S.J. Elliott, and P.A. Nelson. *Active Control of Vibration*. Academic Press, 1996. ISBN 0-12-269440-6.

[39] P. Gardonio and S.J. Elliott. Passive and active isolation of structural vibration transmission between two plates connected by a set of mounts. *Journal of Sound and Vibration*, 237(3):483–511, 2000.

[40] P. Gardonio, S.J. Elliott, and R.J. Pinnington. Active isolation of structural vibration on a multiple-degree-of-freedom system, part I: the dynamics of the system. *Journal of Sound and Vibration*, 207(1):61–93, 1997.

[41] P. Gardonio, S.J. Elliott, and R.J. Pinnington. Active isolation of structural vibration on a multiple-degree-of-freedom system, part II: effectiveness of active control strategies. *Journal of Sound and Vibration*, 207(1):95–121, 1997.

[42] G.P. Gibbs, R.L. Clark, D.E. Cox, and J.S. Vipperman. Radiation modal expansion: application to active structural control. *Journal of the Acoustical Society of America*, 107(1):332–339, 2000.

[43] G.M.L. Gladwell and U.C. Tahbildar. Finite element analysis of the axisymmetric vibrations of cylinders. *Journal of Sound and Vibration*, 22(2):143–157, 1972.

[44] G.M.L. Gladwell and D.K. Vijay. Vibration analysis of axisymmetric resonators. *Journal of Sound and Vibration*, 42(2):137–145, 1975.

[45] G.H. Golub and C.F. van Loan. *Matrix Computations*. The John Hupkins University Press, 2nd edition.

[46] H.G.D. Goyder and R.G. White. Vibrational power flow from machines into built-up structures, part I: introduction and approximate analyses of beam and plate-like structures. *Journal of Sound and Vibration*, 69:59–75, 1980.

[47] H.G.D. Goyder and R.G. White. Vibrational power flow from machines into built-up structures, part II: wave propagation and power flow in beam-stiffened plates. *Journal of Sound and Vibration*, 69:77–96, 1980.

[48] H.G.D. Goyder and R.G. White. Vibrational power flow from machines into built-up structures, part III: power flow through isolation system. *Journal of Sound and Vibration*, 69:97–117, 1980.

[49] R.T. Haftka and Zafer Gürdal. *Elements of Structural Optimization*. Kluwer Academic Publishers, 3rd revised and expanded edition, 1999.

[50] P.C. Hansen. Regularization tools: a Matlab package for analysis and solution of discrete ill-posed problems. *Numerical Algorithms*, 6(1-2):1–35, 1994.

[51] C.M. Harris. *Shock and Vibration Handbook*. McGraw-Hill, 3rd edition.

[52] Karlsson & Sorensen Hibbit. *Abaqus theory manual*. Abaqus.

[53] C.Q. Howard. *Active isolation of machinery vibration from flexible structures*. PhD dissertation, University of Adelaide, Australia, 1999.

[54] C.Q. Howard, C.H. Hansen, and J. Pan. Power transmission from a vibrating body to a circular cylindrical shell through passive and active isolators. *Journal of the Acoustical Society of America*, 101(3):1479–1491, 1997.

[55] X. Huang, S.J. Elliott, and M.J. Brennan. Active isolation of a flexible structure from base vibration. *Journal of Sound and Vibration*, 263:357–376, 2003.

[56] M.H.A. Janssens, J.W. Verheij, and T. Loyau. Experimental example of the pseudo-forces method used in characterisation of a structure-borne sound source. *Applied Acoustics*, 63(1):9–34, 2002.

[57] M.H.A. Janssens, J.W. Verheij, and D.J. Thompson. The use of an equivalent forces method for the experimental quantification of structural sound transmission in ships. *Journal of Sound and Vibration*, 226(2):305–328, 1999.

[58] J.V. Jayachandran, S.M. Hirsch, and J.Q. Sun. On the numerical modelling of interior sound fields by the modal function expansion approach. *Journal of Sound and Vibration*, 210(2):243–254, 1998.

[59] M.D. Jenkins, P.A. Nelson, R.J. Pinnington, and S.J. Elliott. Active isolation of periodic machinery vibrations. *Journal of Sound and Vibration*, 166(1):117–140, 1993.

[60] L. Ji, B.R. Mace, and R.J. Pinnington. Estimation of power transmission to a flexible receiver from a stiff source using a power mode approach. *Journal of Sound and Vibration*, 268(3):525–542, 2003.

[61] L. Ji, B.R. Mace, and R.J. Pinnington. A power mode approach to estimating vibrational power transmitted by multiple sources. *Journal of Sound and Vibration*, 265(2):387–399, 2003.

[62] S. Jianxin, A.T. Moorhouse, and B.M. Gibbs. Towards a practical characterization for structure-borne sound sources based on mobility techniques. *Journal of Sound and Vibration*, 185(4):737–741, 1995.

[63] L. Kari. *Structure-borne sound properties of vibration isolators*. PhD dissertation, Kungl Tekniska Höskolan (KTH), Sweden, Stockholm, Sweden, 1998. ISSN 1103-470X, ISNR KTH/FKT/DA–98/02-SE.

[64] L. Kari. The audible stiffness of preloaded vibration isolators. In *Proceedings of the Sixth International Congress on Sound and Vibration*, pages 2081–2090, Copenhagen, Denmark, 1999.

[65] L. Kari. Dynamic transfer stiffness measurements of vibration isolators in the audible frequency range. *Noise Control Engineering Journal*, 49(2):88–102, 2001.

[66] L. Kari. On the waveguide modelling of dynamic stiffness of cylindrical vibration isolators. Part I: the model, solution and experimental comparison. *Journal of Sound and Vibration*, 244(2):211–233, 2001.

[67] L. Kari. On the dynamic stiffness of preloaded vibration isolators in the audible frequency range: modeling and experiments. *Journal of the Acoustical Society of America*, 113(4):1909–1921, 2003.

[68] L. Kari and M. Sjöberg. Audible stiffness of a preloaded vibration isolator at different temperatures. In *Proceedings of the Tenth International Congress on Sound and Vibration*, Stockholm, Sweden, 2003.

[69] D. Karnopp. Active and semi-active vibration isolation. *Transactions of the ASME*, 117:177–185, 1995.

[70] S. Kim and R. Singh. Vibration transmission through an isolator modelled by continuous system theory. *Journal of Sound and Vibration*, 248(5):925–953, 2001.

[71] S.-M. Kim and M.J. Brennan. Active control of harmonic sound transmission into an acoustic enclosure using both structural and acoustic actuators. *Journal of the Acoustical Society of America*, 170(4):451–472, 1994.

[72] Y.K. Koh and R.G. White. Analysis and control of vibrational power transmission to machinery supporting structures subjected to a multi-excitation system, part I: driving point mobility matrix of beams and rectangular plates. *Journal of Sound and Vibration*, 196(4):469–493, 1996.

[73] Y.K. Koh and R.G. White. Analysis and control of vibrational power transmission to machinery supporting structures subjected to a multi-excitation system, part II: vibration power analysis and control schemes. *Journal of Sound and Vibration*, 196(4):495–508, 1996.

[74] Y.K. Koh and R.G. White. Analysis and control of vibrational power transmission to machinery supporting structures subjected to a multi-excitation system, part III: vibrational power cancellation. *Journal of Sound and Vibration*, 196(4):495–508, 1996.

[75] Usik Lee. Vibration analysis of one-dimensional structures using the spectral transfer matrix method. *Engineering Structures*, 22:681–690, 2000.

[76] W.L. Li and M. Daniels. Vibrational power transmission from a machine to its supporting cylindrical shell. *Journal of Sound and Vibration*, 257(2):283–299, 2002.

[77] W.L. Li and P. Lavrich. Prediction of power flows through machine vibration isolators. *Journal of Sound and Vibration*, 224(4):757–774, 1999.

[78] P.B. Lindley. *Engineering Design with Natural Rubber*. The Malaysian Rubber Producers' Research Association, 4th edition, 1974.

[79] P. Lueg. Process of silencing sound oscillations. US Patent No. 2043416, 1936.

[80] S. Johansson M. Winberg and T.L. Lagö. Control approaches for active noise and vibration control in a naval application. In *Proceedings of the Seventh International Congress on Sound and Vibration*, Garmisch-Partenkirchen, Germany, 2000.

[81] S. Mahajan and R. Redfield. Power flow in linear, active vibration isolation systems. *Journal of Vibration and Acoustics*, 120(2):571–578, 1998.

[82] Ansys Theory Manual. *Ansys 7.0*. Ansys Inc.

[83] N.G. McCrum, B.E. Read, and G. Williams. *Anelastic and Dielectric Effects in Polymeric Solids*. John Wiley & Sons, 1967.

[84] A.I. Medalia. Effect of carbon black on dynamic properties of rubber vulcanizates. *Rubber Chemistry and Technology*, 51:437–523, 1978.

[85] L. Meirovitch. *Elements of Vibration Analysis*. McGraw-Hill Book Company, 2nd edition, 1986. ISBN 0-07-100271-5.

[86] D.W. Miller, S.R. Hall, and A.H. von Flotow. Optimal control of power flow at structural junctions. *Journal of Sound and Vibration*, 140(4):475–497, 1990.

[87] C.T. Molloy. Use of four-pole parameters in vibration calculations. *Journal of the Acoustical Society of America*, 29:842–853, 1957.

[88] A.T. Moorhouse and B.M. Gibbs. Prediction of the structure borne noise emission of machines: development of a methodology. *Journal of Sound and Vibration*, 167(2):223–237, 1993.

[89] P.M. Morse and K.U. Ingard. *Theoretical Acoustics*. McGraw-Hill, 1968.

[90] A.T. Naatje. Active isolation of structure-borne sound from machinery: actuator and sensor configurations. Master's thesis, University of Twente, Faculty of Mechanical Engineering, Enschede, The Netherlands, 2001.

[91] A.M. Nanning. Hybrid isolation of structure borne sound from resiliently mounted machinery. Master's thesis, University of Twente, Faculty of Mechanical Engineering, Enschede, The Netherlands, 2002.

[92] P.A. Nelson and S.J. Elliott. *Active Control of Sound*. Academic Press, 1992. ISBN 0-12-515425-9.

[93] V.H. Neubert. *Mechanical Impedance: Modeling/Analysis of Structures*. Josten Printing and Publishing, 1987.

[94] M.H.H. Oude Nijhuis. *Analysis tools for the design of active structural acoustic control systems*. PhD dissertation, University of Twente, The Netherlands, 2003. ISBN 90-365-1983-7.

[95] G. Nijsse, H. Super, J. van Dijk, and J.B. Jonker. A robust subspace based approach to feedforward control of broadband disturbances on a novel six-degrees-of-freedom vibration isolation set-up. *Submitted to Noise Control Engineering Journal*.

[96] G. Nijsse, H. Super, J. van Dijk, and J.B. Jonker. Subspace based identification and control of a six-degrees-of-freedom vibration isolation set-up. In *Proceedings of Euronoise 2003*, Naples, Italy, 2003.

[97] J.W.M. Noordermeer. *Industriële Elastomeren*. University of Twente, 2000. In Dutch.

[98] B.A.T. Noordman. Rubber engine mounts: a characterization of passive vibration isolator. Master's thesis, University of Twente, Faculty of Mechanical Engineering, Enschede, The Netherlands, 2004.

[99] B.A. Ovunc. Inplane vibration of plates under external disturbances applied at singular points. *Journal of Sound and Vibration*, 18(1):83–95, 1994.

[100] J. Pan and C.H. Hansen. Active control of power flow from a vibrating rigid body to a flexible panel through two active isolators. *Journal of the Acoustical Society of America*, 93(4):1947–1953, 1993.

[101] J. Pan and C.H. Hansen. Power transmission from a vibrating source through an intermediate flexible panel to a flexible cylinder. *Journal of Vibration of Acoustics*, 116(4):496–505, 1994.

[102] J. Pan, C.H. Hansen, and J. Pan. Active isolation of a vibration source from a thin beam using a single active mount. *Journal of the Acoustical Society of America*, 94(3):1425–1434, 1993.

[103] J. Pan, J. Pan, and C.H. Hansen. Total power flow from a vibrating rigid body to a thin panel through multiple elastic mounts. *Journal of the Acoustical Society of America*, 92(2):895–907, 1992.

[104] A.R. Payne and R.E. Whittaker. Low strain dynamic properties of filled rubber. *Rubber Chemistry and Technology*, 44:440–478, 1971.

[105] B.A.T. Petersson. Structural acoustic power transmission by point moment and force excitation, part I: beam- and frame-like structures. *Journal of Sound and Vibration*, 160(1):43–66, 1993.

[106] B.A.T. Petersson. Structural acoustic power transmission by point moment and force excitation, part II: plate-like structures. *Journal of Sound and Vibration*, 160(1):67–91, 1993.

[107] D.M. Photiadis. The relationship of singular value decomposition to wave-vector filtering in sound radiation problems. *Journal of the Acoustical Society of America*, 88(2):1152–1159, 1990.

[108] A.D. Pierce. *Acoustics: An Introduction to its Physical Principles and Applications*. McGraw-Hill, 2nd edition, 1991. ISBN 0-88318-612-8.

[109] R.J. Pinnington. Vibrational power transmission to a seating of a vibration isolated motor. *Journal of Sound and Vibration*, 118(3):515–530, 1987.

[110] R.J. Pinnington and R.G. White. Power flow through machine isolators to resonant and non-resonant beams. *Journal of Sound and Vibration*, 75(2):179–197, 1981.

[111] A.J. Pretlove. Free vibrations of a rectangular panel backed by a close rectangular cavity. *Journal of Sound and Vibration*, 2(3):179–209, 1965.

[112] A. Preumont. *Vibration Control of Active Structures*. Kluwer Academic Publishers, 1999. ISBN 0-7923-4392-1.

[113] T.J. Royston and R. Singh. Vibratory power flow through a nonlinear path. *Journal of the Acoustical Society of America*, 101(4):2059–2069, 1997.

[114] M.A. Sanderson. Vibration isolation: moments and rotations included. *Journal of Sound and Vibration*, 198(2):171–191, 1996.

[115] D. Sciulli and D.J. Inman. Isolation design for a flexible system. *Journal of Sound and Vibration*, 216(2):251–267, 1998.

[116] K.B. Scribner, L.A. Stevens, and A.H. von Flotow. Active narrow-band vibration isolation of machinery noise from resonant substructures. *Journal of Sound and Vibration*, 167(1):17–40, 1993.

[117] M. Sjöberg. Dynamic behaviour of a rubber component in the low frequency range - measurements and modelling. In *Proceedings of the Seventh International Congress on Sound and Vibration*, Garmisch-Partenkirchen, Germany, 2000.

[118] M. Sjöberg and L. Kari. Nonlinear behavior of a rubber isolator system using fractional derivatives. *Vehicle System Dynamics*, 37(3):217–236, 2002.

[119] M. Sjöberg and L. Kari. Measurements of rubber isolator stiffness at non-sinusoidal excitation. In *Proceedings of the Tenth International Congress on Sound and Vibration*, Stockholm, Sweden, 2003.

[120] M. Sjöberg and L. Kari. Testing of nonlinear interaction effects of sinusoidal and noise excitation on rubber isolator stiffness. *Polymer Testing*, 22:343–351, 2003.

[121] J.C. Snowdon. Mechanical four-pole parameters and their applications. *Journal of the Acoustical Society of America*, 15(3):307–323, 1971.

[122] J.C. Snowdon. Vibration isolation: use and characterization. *Journal of the Acoustical Society of America*, 66(5):1245–1274, 1979.

[123] S.D. Snyder and C.H. Hansen. The design of systems to control actively periodic sound transmission into enclosed spaces, part I: analytical models. *Journal of Sound and Vibration*, 170(4):433–449, 1994.

[124] S.D. Snyder and C.H. Hansen. The design of systems to control actively periodic sound transmission into enclosed spaces, part II: mechanisms and trends. *Journal of Sound and Vibration*, 170(4):451–472, 1994.

[125] W. Soedel. *Vibrations of Shells and Plates*. Marcel Dekker, 1981. ISBN 0-8247-1193-9.

[126] S.D. Sommerfeldt and J. Tichy. Adaptive control of a two-stage vibration isolation mount. *Journal of the Acoustical Society of America*, 88(2):938–944, 1990.

[127] H. Super, G. Nijsse, J. van Dijk, and J.B. Jonker. Design of a hybrid six-degrees-of-freedom vibration isolation set-up. In *Proceedings of Euronoise 2003*, Naples, Italy, 2003.

[128] H. Super, J. van Dijk, and J.B. Jonker. Experimental set-up for hybrid isolation of structure borne sound. In *Proceedings of Mechatronics 2002*, Enschede, The Netherlands, 2002.

[129] A.N. Thite and D.J. Thompson. The quantification of structure-borne transmission paths by inverse methods. part 1: improved singular value rejection methods. *Journal of Sound and Vibration*, 264(2):411–431, 2003.

[130] A.N. Thite and D.J. Thompson. The quantification of structure-borne transmission paths by inverse methods. part 2: use of regularization techniques. *Journal of Sound and Vibration*, 264(2):433–451, 2003.

[131] S. Timoshenko, D.H. Young, and W. Weaver. *Vibration Problems in Engineering*. John Wiley & Sons, 4$^{\text{th}}$ edition, 1974. ISBN 0-471-87315-2.

[132] D.R. van den Brink. Numerical evaluation of a near source cost function for hybrid isolation of structure borne sound. Master's thesis, University of Twente, Faculty of Mechanical Engineering, Enschede, The Netherlands, 2003.

[133] W.L. van Hof. Hybrid isolation with a weighed near-source sensor approach. Master's thesis, University of Twente, Faculty of Mechanical Engineering, Enschede, The Netherlands, 2005.

[134] J.W. Verheij. *Multi-path sound transfer from resiliently mounted shipboard machinery*. PhD dissertation, 2$^{\text{nd}}$ edition, Institute of Applied Physics TNO-TH, Delft, The Netherlands.

[135] J.W. Verheij. *Basiskennis Geluidsarm Construeren*. Technical University of Eindhoven, Netherlands, 1996. In Dutch.

[136] R. Vermeulen, R. Lemmen, A.P. Berkhoff, and J.W. Verheij. Active cancellation of unwanted excitation when measuring dynamic stiffness

of resilient elements. In *Proceedings of Internoise 2001*, The Hague, The Netherlands, 2001.

[137] R. Visser. *A boundary element approach to acoustic radiation and source identification*. PhD dissertation, University of Twente, The Netherlands, 2004. ISBN 90-365-2051-7.

[138] R.L. Willis, T.S. Stone, and Y.H. Berthelot. An experimental-numerical technique for evaluating the bulk and shear dynamic moduli of viscoelastic materials. *Journal of the Acoustical Society of America*, 102(6):3549–3555, 1997.

[139] R.L. Willis, L. Wy, and Y.H. Berthelot. Determination of the complex young and shear dynamic moduli of viscoelastic materials. *Journal of the Acoustical Society of America*, 109(2):611–621, 2001.

[140] Y.P. Xiong, J.T. Xing, and W.G. Price. A general linear mathematical model of power flow analysis and control for integrated structure-control systems. *Journal of Sound and Vibration*, 267:301–334, 2003.

[141] Y.P. Xiong, J.T. Xing, and W.G. Price. Power flow analysis of complex coupled systems by progressive approaches. *Journal of Sound and Vibration*, 239(2):275–295, 2003.

[142] Y.P. Xiong, J.T. Xing, W.G. Price, and X.P. Wang. Hybrid active and passive control of vibratory power flow in flexible isolation system. *Shock and Vibration*, 7(3):139–148, 2000.

[143] O.H. Yeoh. Characterization of elastic properties of carbon-black-filled rubber vulcanizates. *Rubber Chemistry and Technology*, 63:792–805, 1990.

Nawoord

Eindelijk, het heeft een tikkeltje langer geduurd dan 'gepland' maar het is klaar. Dat betekent dat of de tijd snel gaat of dat ik niet kan plannen. Voor mijn gevoel is de tijd in ieder geval erg snel gegaan, en dat is over het algemeen een goed teken. Ik heb een interessant onderzoek mogen uitvoeren bij de vakgroep Technische Mechanica, een leuke en dynamische groep, en bovendien in goede samenwerking met TNO. En hoewel alleen mijn naam op het boekje staat, is dat onterecht, omdat veel andere mensen (in)direct hebben bijgedragen.

Eerst wil ik mijn beide promotoren bedanken. André de Boer wil ik bedanken voor de begeleiding, steun en hulp gedurende het onderzoek. Zeker het vertrouwen dat hij in mij had als het wat minder ging waardeer ik erg. Verder wil ik Jan Verheij bedanken voor het 'sturen' van het onderzoek en de begeleiding bij het schrijven van het proefschrift. De bijdrage van de technisch inhoudelijke discussies bij TNO hebben enorm aan dit proefschrift bijgedragen. Ook wil ik Henk Tijdeman bedanken voor de begeleiding tijdens de start van het project en voor het feit dat hij me heeft weten te strikken voor deze promotie plaats. Tom Basten dank ik als begeleider vanuit TNO. Gelukkig had hij al wat ervaring met het begeleiden van mij gedurende mijn afstuderen en als collega-promovendus. Ook wil ik René Lemmen bedanken voor de begeleiding vanuit TNO gedurende de beginfase van het projekt.

Verder hebben de medewerkers van de dynamica groep een belangrijke bijdrage geleverd: Ruud Spiering, Peter van der Hoogt, Bert Wolbert en Ysbrand Wijnant, bedankt. De samenwerking met de vakgroep Werktuigbouwkundige Automatisering in het kader van het onderzoeksproject was erg waardevol. Daarvoor dank ik Ben Jonker, Johannes van Dijk en collega-promovendus Hiddo Super.

Zoals gezegd is het me prima bevallen in de vakgroep Technische Mechanica, en dat komt vooral door de goede sfeer met enthousiaste collega's dat vooral tot uiting kwam tijdens de koffie pauzes, lunchwandelingen maar ook in de kroeg. Laat ik een poging doen om ze te noemen: Frits van der Eerden,

Tom Basten, Hedzer Tillema, Marco Oude Nijhuis, René Visser, Rob Huls, Marieke Hannink, Ekke O, Marten Nijhof, Peter Sloetjes, Martijn Bonte, Bert K, Jaap van Kampen, Loes van Haren en Richard Loendersloot. René, het is voor mij een raadsel hoe je het als kamer/projectgroep-genoot het met mij hebt kunnen uithouden, maar uiteindelijk hebben we toch als een soort 'brothers in arms' de studie en promotieonderzoek afgerond. Een aantal van deze mensen kom ik nog wel eens tegen in een kroeg of op een festival. Ik hoop dat dat zo blijft. Ook bedank ik de collega-promovendi van de dynamica-groep voor alle hulp en correcties van het proefschrift.

Ook wil ik Arthur Berkhoff van harte bedanken voor deelname aan de technisch inhoudelijke discussies en wijze adviezen. Ook Ruud Vermeulen bedank ik voor de hulp bij de experimenten.

De bijdrage van de secretaresses Debbie Vrieze en Tanja van Scherpenzeel is erg belangrijk geweest, niet alleen voor de koffie en allerlei zaken en rompslomp dat geregeld moet worden, maar vooral voor de ondersteuning en sociale rol die ze vervullen in de vakgroep. Bedankt!

Aan het project hebben de volgende afstudeerders meegewerkt en een waardevolle bijdrage geleverd aan het onderzoek waarvoor ik erg dankbaar ben: Jasper Peen, Alexander Naatje, Allard Nanning, Bram Noordman en Wouter van Hof.

I also would like to thank Leif Kari from the KTH, who helped me very much to gain knowledge in the world of passive isolation. Ook wil ik de vakgroep Rubbertechnologie onder leiding van Jacques Noordermeer bedanken voor de hulp bij de fabricatie van de 'silica' isolator.

Ten slotte wil ik mijn vrienden en familie bedanken. Hoewel ze over het algemeen weinig wisten waar ik precies mee bezig was, hadden zij de volste vertrouwen in mij, meer nog dan ik zelf had. Ik wil Maarten, Hans, Sebastiaan en Evelien, Werner, Jacco en Stijn bedanken. También quiero dar gracias a Andrea Sanchez, muchas gracias. Tenslotte wil ik mijn ouders en mijn broers Freek en Joris bedanken voor de onvoorwaardelijke steun. Hulde.

Iedereen hartelijk dank!

Enschede, mei 2005